The Dissertation Committee for Sophie Shiting Yi Certifies that this is the approved version of the following dissertation:

Development of Computationally Efficient 2D and Pseudo-3D Multi-Fracture Models with Applications to Fracturing and Refracturing

Committee:

Mukul M. Sharma, Supervisor

Nicolas P. Roussel

Spyros A. Kinnas

John T. Foster Jr.

Jon E. Olson

Development of Computationally Efficient 2D and Pseudo-3D Multi-Fracture Models with Applications to Fracturing and Refracturing

by

Sophie Shiting Yi

Dissertation

Presented to the Faculty of the Graduate School of

The University of Texas at Austin

in Partial Fulfillment

of the Requirements

for the Degree of

Doctor of Philosophy

The University of Texas at Austin

August 2018

Dedication

To my family, for their unconditional love and support.

Acknowledgements

I would like to thank all those made this dissertation possible.

I am especially grateful to my advisor, Dr. Mukul M. Sharma for his guidance and encouragement throughout my study. Despite his busy schedule, he has always been available to his students and enthusiastic about sharing his experience and ideas. His ingenious perspective, valuable suggestions, and the opportunities he gave me to present my work to industry partners and sponsors helped my research in so many ways. I would also like to express my sincere appreciation to my committee members, Dr. Nicolas Roussel, Dr. Spyros Kinnas, Dr. John Forster and Dr. Jon Olson, for their kind advice and help during the completion of this work.

This work would not have been possible without the financial support of the Hydraulic Fracturing and Sand Control JIP at the University of Texas at Austin. I am also grateful to the following university staff: Jin Lee, Amy Stewart, Frankie Hart, John Cassibry and Tim Guinn for their day-to-day contributions to the success of students.

I benefited greatly from the collaborative atmosphere in the group. Discussions and collaborations with my friends and colleagues shaped this work in so many wonderful ways. In particular, I would like to thank Chu-Hsiang Wu, Ripudaman Manchanda, Jongsoo Hwang, Hanyi Wang, and Sho Hiroshi, whose advice and help has been crucial in the development of the dissertation. I am also grateful for the moral support and help of my friends: Haotian Wang, Peng Zhang, Hisanao Ouchi, Emmanouil Karantinos, Deepen Gala, Ashish Kumar, Murtada Tammar, Kaustubh Shrivastava, Min Zhang, Shuang Zheng, Javid Shiriyev, Puneet Seth, Shivam Agrawal, Rodney Russel, Ajeetha Kamilla, Alex Chong, and many others whom I did not cite explicitly.

Finally, I would like to thank my parents, whose love and support are with me in whatever I pursue. I owe special thanks to my husband, Ye Yuan, for his patience, encouragement, moral support and companionship. The five years we spent together in Austin are memories I will always cherish.

Development of Computationally Efficient 2D and Pseudo-3D Multi-Fracture Models with Applications to Fracturing and Refracturing

Sophie Shiting Yi, Ph.D.

The University of Texas at Austin, 2018

Supervisor: Mukul M. Sharma

Multi-stage hydraulic fracturing is one of the key technologies of the U.S. tight oil and shale gas revolution. Recently, fracture diagnostic methods revealed that the fracture propagation could be quite uneven when stimulating multiple fractures simultaneously. As a result, only 64% of the perforated clusters contribute to production. Promoting uniform fracture propagation, ensuring that all perforation clusters receive treatment would be a big step in improving oil recovery in shale reservoirs.

The dissertation reports the development of computationally efficient, 2D and Pseudo-3D multi-fracture models. Novel methods are developed to solve the dynamic fluid and proppant partitioning among multiple perforation clusters. The Resistance Method is developed to distribute fluid among fractures. This new method could be more computationally efficient than the widely adopted Newton-Raphson Method. The Particle Transport Efficiency (PTE) correlations are implicitly incorporated into the multi-fracture models to compute proppant distribution among the fractures. It is shown that the inertial effect tends to accumulate proppant particles downstream in the wellbore while fluid leaks off from the perforations, leading to pre-mature screen out of toe-side clusters, and the heel-biased final treatment distribution.

The model has been applied to two important unconventional reservoir stimulation technologies: the plug-and-perf operation and horizontal well refracturing.

We investigate how parameters including the number of perforations, the size of the perforation, the injection rate and so on affect the final fluid and proppant distribution. Directional suggestions are provided regarding each parameter. An automated process to search for the optimum plug-and-perf design within the user-specified parameter range was developed. It is shown that when multiple parameters are optimized together, the propped surface area can be improved greatly.

We simulated horizontal well refracturing operations employing diverting agents with the model. Two field cases were studied, and the simulation workflow of initial completion – pore pressure depletion – refracturing was carried out for both cases. Our simulation results match the field diagnostic observations well. We successfully captured the heel-biased refrac treatment distribution, and showed that both new and existing perforations can effectively break down during refrac. Strategies have been developed to improve refrac success.

Table of Contents

List of Tables

List of Figures

MAJOR SECTION 1: INTRODUCTION

Chapter 1: Background and Scope of the Dissertation

The dissertation reports the development of a computationally efficient multi-fracture model. The model has been applied to two important unconventional reservoir stimulation technologies: the plug-and-perf operation and horizontal well refracturing.

1.1. BACKGROUND

We have known for some time that shales contain a remarkable amount of hydrocarbons. Economic production of oil embedded in these low-permeable reservoirs started about three decades ago. In the 1990s, Mitchell Energy successfully fractured the Barnet Shale and demonstrated the feasibility of extracting natural gas from the formation economically (Gold, 2014). Since then, many producers have entered the unconventional plays, and the oil and gas production has boomed in North America.

The U.S. tight oil and shale gas revolution is a technology-driven success. The key technologies for the development of unconventional reservoirs include horizontal well drilling (Azar & Samuel, 2007) and multi-stage hydraulic fracturing (Cipolla et al., 2009, McDaniel, 2010). Longer horizontal well sections and higher-intensity completion designs have helped improve production rates and EURs. Novel diagnostic technologies have been applied to help guide the field development, such as microseismic fracture diagnostics (Fisher et al., 2004; Le Calvez et al., 2007), proppant tracers (Leonard et al., 2015; Leonard et al., 2016), dynamic acoustic sensing (DAS) and dynamic temperature sensing (DTS) (Molenaar & Cox, 2013; Somanchi et al., 2016; Ugueto et al., 2016). As some of the

unconventional plays mature, refracturing and infill well drilling will play important roles in further field development (Strother et al., 2013; Indras et al., 2015; Safari et al., 2017). Producers are maximizing oil recovery on the field scale, considering fracture interference, wellbore interference, pad arrangement and well stacking in multiple layers.

In 2017, the U.S. Energy Information Administration (EIA) estimated that tight oil resources produced about 4.67 million barrels of crude oil per day, which was equal to about 50% of the total crude oil produced in the US. Tight oil production is predicted to increase to beyond 8.2 million barrels per day in the 2040s and make up 70% of total crude oil production in the US (EIA, 2018). The major shale reservoirs in the lower 48 states include Permian, Eagle Ford, Barnett, Haynesville and Bakken, as shown in Fig. 1.1. The Permian Basin contributed more than 36% of U.S. tight oil production in 2017. Other major contributors include the Bakken and Eagle Ford formations.

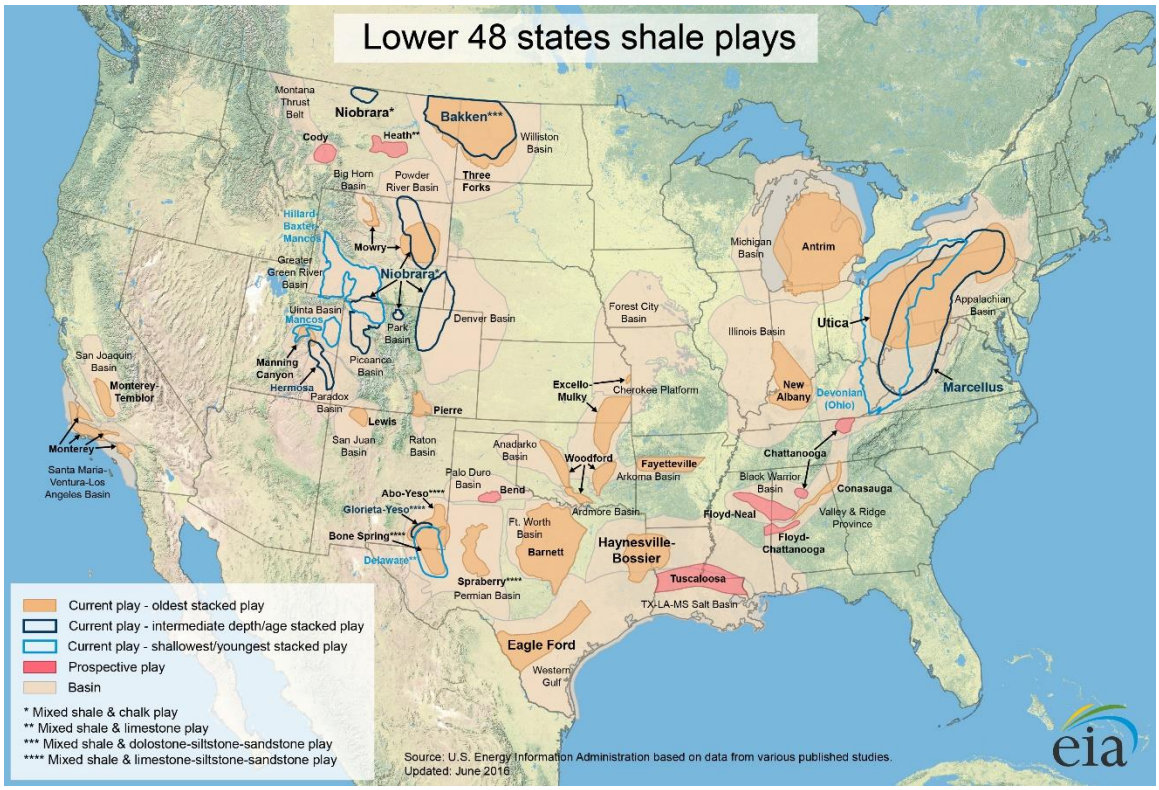

Figure 1.1: Shale plays in the lower 48 states. (U.S. EIA., 2016, Retrieved from https://www.eia.gov/maps/maps.htm)

The potential of improving oil and gas recovery from shale wells is significant. Production logging has shown that typically only 64% of the perforated clusters contribute to production. This leaves 40% of the wellbore as a potential target for improvement by refracturing (Fragachan et al., 2015; Denney, 2011; Sinha & Ramakrishnan, 2011). Furthermore, advanced fracture diagnostic methods such as proppant tracers, microseismic, DAS, and DTS revealed that when multiple fractures are stimulated simultaneously, the fluid and proppant placement among the fractures can be quite uneven. The heel side clusters are often dominant (Molenaar & Cox, 2013; Leonard et al., 2015; Ugueto et al., 2016). Promoting uniform fracture propagation to ensure that all perforation

clusters receive fluid and proppant would be a big step in ensuring improved oil recovery in shale reservoirs.

The present study focuses on the simulation of multi-fracture stimulation and to introduce strategies that can help promote even fluid and proppant distribution among multiple fractures during fracturing and refracturing.

1.2. OBJECTIVES

The main objective of this dissertation is to simulate the simultaneous propagation of multiple fractures, to calculate the dynamic fluid and proppant partitioning among multiple perforation clusters during fracturing, and to provide strategies that promote uniform fracture propagation. This overall objective can be achieved by addressing the following:

1. Develop computationally efficient fracture models.
2. Calculate fluid distribution among multiple fractures during stimulation.
3. Calculate proppant transport into multiple perforated clusters. Account for the difference between the proppant and fluid distribution due to the inertia of proppant particles.
4. Apply the model to plug-and-perf stages and provide recommendations to improve plug-and-perf operations.
5. Simulate horizontal well refracturing and work on strategies to improve refrac success.

1.3. STRUCTURE OF THE DISSERTATION

The core of the dissertation is divided into three major sections. Each major section includes two chapters. The first major section focuses on the development of single fracture models. The second major section solves the problem of dynamic fluid and proppant partitioning among multiple fractures and builds multi-fracture models based on the single fracture models developed in the previous major section. Following that, the last major section applies the multi-frac models to plug-and-perf as well as horizontal well refracturing simulations. New completion and re-stimulation strategies are proposed that prevent the heel-biased treatment distribution and promotes uniform fracture propagation.

1.3.1. Major Section 2: Single Fracture Modeling

Computationally efficient 2D-PKN type (Chapter 2) and Pseudo-3D (Chapter 3) single fracture models are developed. These models incorporate fracture mechanics, fluid flow, and mass balance. They capture major features of fracture propagation with minimum computational cost. Both models have been validated with available solutions.

1.3.2. Major Section 3: Multi-Frac Simulation

Novel methods are developed to solve the dynamic fluid and proppant distribution among perforation clusters when multiple fractures are stimulated simultaneously.

In Chapter 4, the Resistance Method is developed to distribute fluid among fractures. It is shown that this new method could be more computationally efficient than the widely adopted Newton-Raphson Method. The convergence of this new method was proved. Multi-fracture simulators are developed by combining the fluid distribution calculation and the single fracture models developed in the last major section.

In Chapter 5, the Particle Transport Efficiency (PTE) correlations are implicitly incorporated into the multi-fracture models to compute proppant distribution among the fractures. It is shown that the proppant partitioning could be quite different from that of the fluid. The inertial effect tends to accumulate proppant particles downstream in the wellbore while fluid leaks off from the perforations, resulting in a high slurry concentration in the toe side clusters that increase the risk of premature screen out. When the toe side clusters screen out, the remainder of the treatment is transported into the heel side clusters, and the final treatment distribution is heel biased.

1.3.3. Major Section 4: Applications of the Model

In this section, we apply the multi-fracture models developed in the last two major sections to the simulation of plug-and-perf operations and horizontal well refracturing.

In Chapter 6, we investigate how parameters including the number of perforations per cluster, the size of the perforation, the injection rate and so on affect the final fluid and proppant distribution. We found that, as a rule of thumb, when the fluid and proppant distribution is more even, more propped surface area is created. Directional suggestions are provided regarding each parameter for promoting a more uniform treatment distribution. An automated process to search for the optimum plug-and-perf design within the user-specified parameter range was developed. It is shown that when multiple parameters are optimized at the same time, the propped surface area can be improved greatly.

Chapter 7 presents the application of our models to the simulation of horizontal well refracturing. Two field cases were studied, and the workflow of initial completion –

pore pressure depletion – refracturing was carried out for both cases. Our simulation results match field diagnostic observations. Strategies are developed to improve refrac success.

REFERENCES

Azar, J.J. and Samuel, G.R., 2007. *Drilling engineering*. PennWell Books.

Cipolla, C.L., 2009. Modeling production and evaluating fracture performance in unconventional gas reservoirs. *Journal of Petroleum Technology*, 61(09), pp.84-90.

Daneshy, A.A., 2011. Hydraulic Fracturing of Horizontal Wells: Issues and Insights. Paper SPE 140134 presented at the *SPE Hydraulic Fracturing Technology Conference and Exhibition* held in The Woodlands, Texas, USA, 24-26 January 2011.

Denney, D., 2011. Screening Method To Select Horizontal-Well Refracturing Candidates in Shale-Gas Reservoirs. *Journal of Petroleum Technology*,63(11), pp.102-106.

Fisher, M.K., Heinze, J.R., Harris, C.D., Davidson, B.M., Wright, C.A. and Dunn, K.P., 2004, January. Optimizing horizontal completion techniques in the Barnett shale using microseismic fracture mapping. In *SPE Annual Technical Conference and Exhibition*. Society of Petroleum Engineers.

Fragachan, F.E., Babey, A.G., Arnold, D.M., Heminway, E.M. and Yuan, F., 2015, September. Secret Weapon Against the Red Queen: Using Chemical Packers and Degradable Mechanical Diverters in Refracturing Operations. In *SPE Annual Technical Conference and Exhibition*. Society of Petroleum Engineers.

Gold, R., 2014. *The boom: How fracking ignited the American energy revolution and changed the world*. Simon and Schuster.

Mcdaniel, B.W., 2010, January. Horizontal Wells with Multi-Stage Fracs Provide Better Economics for Many Lower Permeability Reservoirs. In *SPE Asia Pacific Oil and Gas Conference and Exhibition*. Society of Petroleum Engineers.

Le Calvez, J.H., Craven, M.E., Klem, R.C., Baihly, J.D., Bennett, L.A. and Brook, K., 2007, January. Real-time microseismic monitoring of hydraulic fracture treatment: A tool to improve completion and reservoir management. In *SPE Hydraulic Fracturing Technology Conference*. Society of Petroleum Engineers.

Leonard, R.S., Moore, C.P., Woodroof, R.A. and Senters, C.W., 2015, September. Refracs-Diagnostics provide a second chance to get it right. In *SPE Annual Technical Conference and Exhibition*. Society of Petroleum Engineers.

Leonard, R.S., Woodroof, R.A., Senters, C.W., Wood, T.M. and Drylie, S.W., 2016, September. Evaluating and optimizing refracs-what the diagnostics are telling us. In *SPE Annual Technical Conference and Exhibition*. Society of Petroleum Engineers.

Indras, P. and Blankenship, C., 2015, September. A Commercial Evaluation of Refracturing Horizontal Shale Wells. In *SPE Annual Technical Conference and Exhibition*. Society of Petroleum Engineers.

Molenaar, M.M. and Cox, B.E., 2013, January. Field cases of hydraulic fracture stimulation diagnostics using fiber optic distributed acoustic sensing (DAS) measurements and Analyses. In *SPE Unconventional Gas Conference and Exhibition*. Society of Petroleum Engineers.

Safari, R., Lewis, R., Ma, X., Mutlu, U. and Ghassemi, A., 2017. Infill-Well Fracturing Optimization in Tightly Spaced Horizontal Wells. *SPE Journal*, 22(02), pp.582-595.

Sinha, S. and Ramakrishnan, H., 2011, January. A novel screening method for selection of horizontal refracturing candidates in shale gas reservoirs. In *North American Unconventional Gas Conference and Exhibition*. Society of Petroleum Engineers.

Somanchi, K., O'Brien, C., Huckabee, P. and Ugueto, G., 2016. Insights and observations into limited entry perforation dynamics from fiber-optic diagnostics. *Unconventional Resources Technology Conference* (URTEC).

Strother, D., Valadares, R., Nakhwa, A.D. and Pitcher, J.L., 2013, November. Challenges of refracturing horizontal wells in unconventional and tight reservoirs. In *SPE Unconventional Resources Conference and Exhibition-Asia Pacific*. Society of Petroleum Engineers.

Ugueto, C., Gustavo, A., Huckabee, P.T., Molenaar, M.M., Wyker, B. and Somanchi, K., 2016, February. Perforation cluster efficiency of cemented plug and perf limited entry completions; Insights from fiber optics diagnostics. In *SPE Hydraulic Fracturing Technology Conference*. Society of Petroleum Engineers.

U.S. Energy Information Administration. 2016. from, https://www.eia.gov/maps/maps.htm

U.S. Energy Information Administration. 2018. *Annual Energy Outlook 2018 with projections to 2050*.

MAJOR SECTION 2: COMPUTATIONALLY EFFICIENT SINGLE HYDRAULIC FRACTURE MODELS

This major section discusses the development of computationally efficient single hydraulic fracture models. Two fracture models are developed: the 2D PKN-Type model (Chapter 2) and the Pseudo-3D model (Chapter 3). In the first model, the fracture is assumed to be contained within the reservoir layer with a constant height. In the second model, fracture height growth is accounted for, and many reservoir and fluid properties can vary with depth. Both models are solved with a moving mesh algorithm, where the mesh grows with the fracture, and the number of elements remains constant throughout the simulation.

Both the 2D and the Pseudo-3D fracture models are computationally efficient and capture major features of hydraulic fracture propagation. They are further developed to multi-cluster hydraulic fracture models in the next major section. Such models can be used for the efficient and rapid simulation of plug-and-perf stages as well as horizontal well refracturing.

Chapter 2: A 2D PKN-Type Fracture Model

2.1. INTRODUCTION

From the late 1950s to the early 1970s, several key papers developed the foundation of modeling hydraulic fractures (Economides & Nolte, 1989). The early works either simplified the fluid flow and focused on fracture mechanics (Khristianovich & Zheltov, 1955), or focused on fluid flow and simplified fracture mechanics (Perkins & Kern, 1961). Carter (1957) developed a model for fluid leak-off calculation based on volume balance

considerations. The classic PKN (Nordgren, 1972) and KGD (Geertsma & De Klerk, 1969) models were the first to integrate fracture mechanics, fluid flow, and fluid volume balance, capturing many of the major features of hydraulic fracture propagation.

Both PKN and KGD models are 2D fracture models that assume constant fracture height. The KGD model assumes plane strain in the horizontal direction and is more suitable for fractures with a height greater than the length. The PKN model assumes plane strain in the vertical direction and is more suitable for fractures with a length larger than the height. For our applications, the fracture usually grows more in the length dimension than the height dimension. Therefore, a PKN-Type fracture model is more suitable.

Today, fracture modeling has developed far beyond 2-D fracture models. However, the sophisticated models are usually computationally expensive and require a lot more information about the reservoir. The PKN fracture model is the simplest model that can capture major features of hydraulic fracture propagation. It is very computationally efficient and is suitable for applications that involve simultaneous propagation of many fractures, such as refracturing horizontal wells. Therefore, for this chapter, we focus on developing a PKN fracture model for single fracture propagation. Proppant transport in the fracture is simulated. And the entire system is solved with a moving mesh algorithm.

2.2. MODEL FORMULATION

In this section, we first introduce the five governing equations for the classic PKN fracture model. Next, we explain the simulation of proppant transport in the fracture. Finally, we present the explicit moving mesh strategy and the solution algorithm of the governing equations.

2.2.1. Governing Equations for PKN Fracture Propagation

The classic PKN fracture model describes a vertical hydraulic fracture confined in the reservoir layer with a constant height (see Fig. 2.1). The stress contrasts between the reservoir layer and the layers surrounding it are sufficiently high that the fracture remains confined to the reservoir layer while it propagates laterally. The vertical cross-section of a PKN fracture is elliptical with the maximum width at the center.

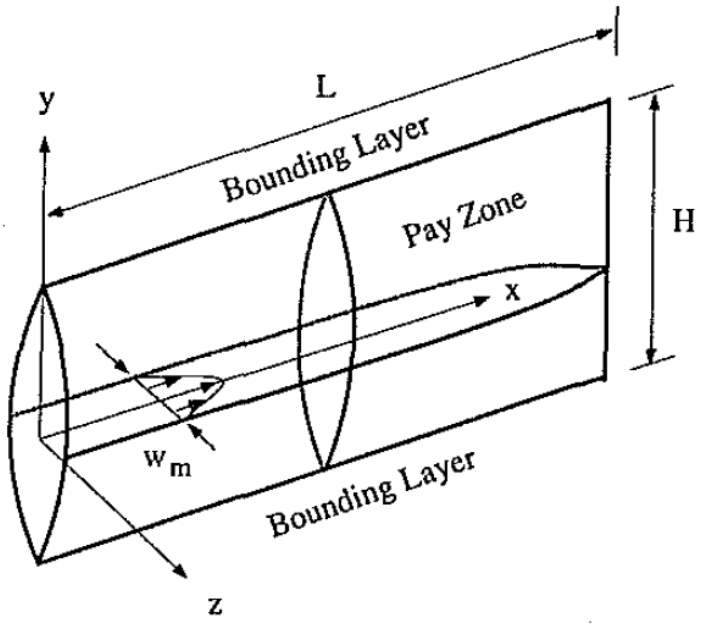

Figure 2.1: Classic PKN fracture geometry. (Detournay et al., 1990)

Given the reservoir properties, the injection schedule, and the injected fluid properties, the PKN fracture model calculates the dynamic evolution of the fracture by solving five governing equations. The main assumptions of the PKN fracture model include:

1). Constant fracture height;

2). Plane strain;

3). Constant fluid pressure along vertical cross-sections of the fracture;

4). Incompressible, Newtonian fluid.

The governing equations for the classic PKN fracture model are summarized below. All the equations are in SI units.

2.2.1.1. Local Fluid Mass Balance

If we divide a PKN fracture into many small cells along the fracture length direction, a local fluid mass balance equation can be written for each cell, taking into account the fracture volume change and leak-off, as shown in Equation 2.1.

$$\frac{\partial q}{\partial x} + \frac{\partial w}{\partial t} + u_L = 0 \tag{2.1}$$

Note that Equation 2.1 is formulated per unit height of the fracture, where q is the flow rate per unit height of the fracture, w is average width of the fracture, and u_L is the velocity of fluid leaking off from both walls per unit height of the fracture.

2.2.1.2. Fluid Momentum Equation

The fluid pressure in the fracture is assumed to only vary in the longitudinal direction (the fracture length direction). The momentum equation for laminar flow in a fracture can be derived from the lubrication theory (Lamb, 1932)

$$\frac{\partial P_f}{\partial x} = -\frac{\pi^2 \mu q}{w^3} \tag{2.2}$$

Where P_f is the fluid pressure in the fracture and μ is the viscosity of the fracturing fluid.

2.2.1.3. Pressure-Fracture Width Relation

Following Sneddon and Elliot (1946), fractures of fixed height are elliptical. And the maximum width is

$$w_{max} = -\frac{2P_{net}h_f(1-v^2)}{E} \tag{2.3}$$

Where w_{max} is the maximum fracture width, P_{net} is the net pressure in the fracture, h_f is the fracture height, v is Poisson's Ratio and *E* is Young's Modulus. To be consistent with the fluid momentum equation (Equation 2.2) and local fluid mass balance equation (Equation 2.1) above, we rewrite Equation 2.3 in terms of the average fracture width *w*

$$w = -\frac{\pi P_{net}h_f(1-v^2)}{2E} = -\frac{\pi P_{net}h_f(1-v)}{4G} \tag{2.4}$$

Where *G* is Shear Modulus.

2.2.1.4. Carter's Leak-Off Equation.

The fluid-loss in the fracturing treatment is controlled by three mechanisms as shown in Fig. 2.2: (1) the compression of the reservoir fluids, (2) the invaded zone filled with the fracturing fluid, and (3) the filter cake that may or may not exist depending on the additives of fracturing fluid (Schechter, 1992). In this study, the fluid pressure drop due to the filter cake is ignored, and only the first two mechanisms are considered in the leak-off calculation.

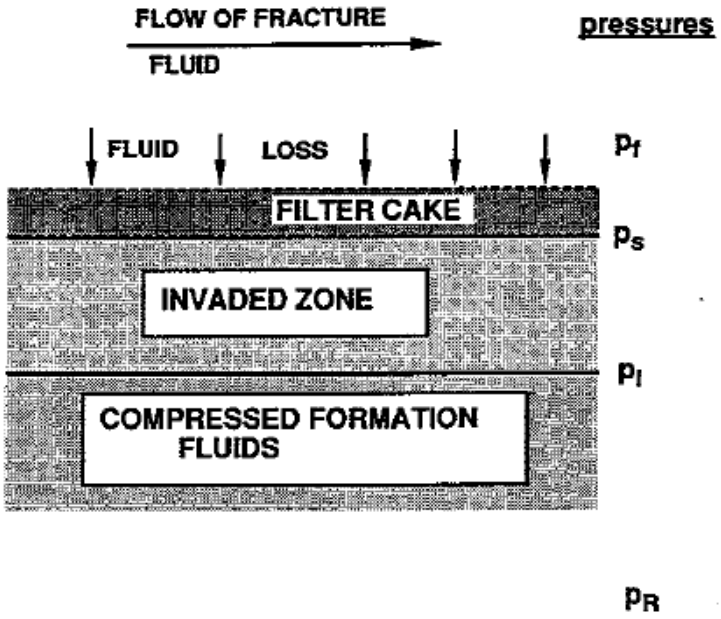

Figure 2.2: Processes related to fluid-loss from the fracture. (Schechter, 1992)

The high pressure in the hydraulic fracture forces fluid into the formation and compresses the formation fluid. If P_R represents the reservoir fluid pressure, and P_I is the pressure at the interface between the invaded zone and the compressed formation fluid, then the flux at the interface may be expressed as (Schechter, 1992)

$$u_N = \sqrt{\frac{\varphi \kappa_{fl} k}{\pi \mu_{fl}}} \frac{(P_I - P_R)}{\sqrt{t}} = \alpha_c \frac{(P_I - P_R)}{\sqrt{t}} \tag{2.5a}$$

$$P_I - P_R = \frac{u_N}{\alpha_c} \sqrt{t} \tag{2.5b}$$

Where u_N is the flux at the interface, φ is the reservoir porosity, κ_{fl} is the isothermal compressibility of the formation fluid, k is the formation permeability, μ_{fl} is the formation fluid viscosity and t is time.

Similarly, the flux at the interface between fracture face and the invaded zone can be written as (Schechter, 1992)

$$u_N = \sqrt{\frac{\varphi k}{2\mu}}\sqrt{\frac{P_f - P_I}{t}} = \alpha_v\sqrt{\frac{P_f - P_I}{t}} \tag{2.6a}$$

$$P_f - P_I = (\frac{u_N}{\alpha_v}\sqrt{t})^2 \tag{2.6b}$$

Where P_f is fluid pressure in the fracture. Note that capillary pressure between the oil or gas phase and the water phase is ignored. If a sharp interface can be assumed between the fracturing fluid and the reservoir fluid, the capillary pressure can be estimated at the water saturation of the reservoir and be added to the equation above.

The overall leak-off coefficient can be derived by combining Equation 2.5 and Equation 2.6 as below

$$\Delta P = P_f - P_R = \left(\frac{u_N}{\alpha_v}\sqrt{t}\right)^2 + \frac{u_N}{\alpha_c}\sqrt{t} \tag{2.7}$$

Dividing both sides of Equation 2.7 by ΔP we get

$$1 = \left(\frac{u_N}{C_v}\sqrt{t}\right)^2 + \frac{u_N}{C_c}\sqrt{t} \tag{2.8}$$

Where C_v is the viscous fluid-loss coefficient ($C_v = \alpha_v\sqrt{\Delta P} = \sqrt{\frac{\varphi k}{2\mu}\Delta P}$), and C_c is the compressibility fluid-loss coefficient ($C_c = \alpha_c\Delta P = \sqrt{\frac{\varphi\kappa_{fl}k}{\pi\mu_{fl}}}\Delta P$). Solving for $u_N\sqrt{t}$ using Equation 2.8, we get

$$u_N\sqrt{t} = \frac{-\frac{1}{C_c} + \sqrt{\frac{1}{C_c^2} + 4\frac{1}{C_v^2}}}{2\frac{1}{C_v^2}} = C_l \tag{2.9}$$

Where C_l is the overall fluid-loss coefficient that we simply refer to as fluid-loss coefficient in the forthcoming.

Finally, we get the fluid leak-off equation as

$$u_L = 2u_N = \frac{2C_l}{\sqrt{t - \tau(x)}} \tag{2.10}$$

Where $\tau(x)$ is the time the fracture tip arrives location x.

2.2.1.5. Total Fluid Mass Balance

For a PKN fracture discretized along the length, the four equations explained above apply to each cell. The fracture length L is an unknown that we can determine using the total fluid mass balance. The overall fluid mass balance for incompressible fluid states that the injected fluid volume is equal to the sum of fracture volume and the leak-off volume, as shown in Equation 2.11.

$$\int_0^{L(t)} w(x,t)dx + \int_0^t \int_0^{L(t')} u_L(x,t')\,dxdt' = \int_0^t q_o(t')dt' \tag{2.11}$$

Note that this is a global fluid mass balance per unit fracture height and that $q_o = Q_o/h_f$ is the fluid injection rate per unit fracture height.

2.2.1.6. Initial and Boundary Conditions.

The initial condition for the PKN fracture model is given in Equation 2.12. And the boundary conditions are summarized in Equation 2.13.

$$L(t=0) = 0 \tag{2.12}$$

$$P_{net}(x=0, t=0) = 0 \tag{2.13a}$$

$$q(x=0,t) = q_o(t);\ \ (t>0) \tag{2.13b}$$

$$P_{net}(x=L(t),t) = 0;\ \ \ (t>0) \tag{2.13c}$$

Now, Equation 2.1, 2.2, 2.4, 2.10, 2.11, together with the initial and boundary conditions in Equation 2.12 and 2.13, represent a complete and consistent mathematical model to calculate fracture geometry evolution during the hydraulic fracturing treatment.

The governing equations introduced in this section describe a fluid-driven fracture. When proppant is introduced into the system, the fluid becomes a two-phase slurry. The simulation of proppant transport in the PKN fracture is discussed in the next section.

2.2.2. Simulation of Proppant Transport in the PKN Fracture

Proppant transport in the fracture is governed by the local mass balance for the slurry and proppant in the fracture. Recall the local fluid mass balance equation (Equation 2.1), the local slurry and proppant mass balance equations can be written in an analogous manner

$$\frac{\partial w}{\partial t} + \frac{\partial q_s}{\partial x} + u_L = 0 \tag{2.14}$$

$$\frac{\partial w\bar{\emptyset}}{\partial t} + \frac{\partial q_p}{\partial x} = 0 \tag{2.15}$$

In Equation 2.15, $\bar{\emptyset}$ is the averaged proppant volume concentration normalized by maximum proppant volume concentration ($\emptyset_{\max} = 0.585$) as shown below

$$\bar{\emptyset} = \frac{\emptyset_{avg}}{\emptyset_{\max}} = \frac{2}{w}\int_0^{\frac{w}{2}} \frac{\emptyset}{\emptyset_{\max}} dz \ , \bar{\emptyset} \in [0,1] \tag{2.16}$$

Dontsov and Peirce's (2014) proppant transport model is adopted to describe the slurry flow and proppant transport in the fracture. The model is based on a constitutive continuum model for a slurry and describes a smooth transition from Poiseuille flow to Darcy flow when proppant concentration increases from low to high. The slurry flux in a fracture is described by

$$q^s = -\frac{w^3}{12\mu}\hat{Q}^s(\bar{\emptyset}, \frac{w}{a})\frac{\partial P_f}{\partial x} \tag{2.17}$$

$$\hat{Q}^s\left(\bar{\emptyset}, \frac{w}{a}\right) = Q^s\left(\bar{\emptyset}\right) + \frac{a^2}{w^2}\bar{\emptyset}D(1) \tag{2.18}$$

$$D(1) = \frac{8\left(1-\bar{\emptyset}_{\max}\right)^{\bar{\alpha}}}{3\bar{\emptyset}_{\max}} \tag{2.19}$$

Where $\bar{\alpha} = 4.1$ is a constant, a is the proppant radius, and $Q^s\left(\bar{\emptyset}\right)$ is a function of normalized proppant concentration as shown in Fig. 2.3. The term Q^s can be interpreted as the inverse of effective viscosity of the slurry. As $\bar{\emptyset}$ approaches 0, Q^s is close to 1. And as $\bar{\emptyset}$ approaches 1, the effective viscosity goes to infinity and Q^s is close to 0.

For a slurry with low proppant concentration, $\overline{\emptyset} \approx 0$ and $Q^s(\overline{\emptyset}) \approx 1$, Equation 2.17 describes Poiseuille flow. For a highly concentrated slurry, $Q^s(\overline{\emptyset}) \approx 0$ and Equation 2.17 is governed by Darcy's law.

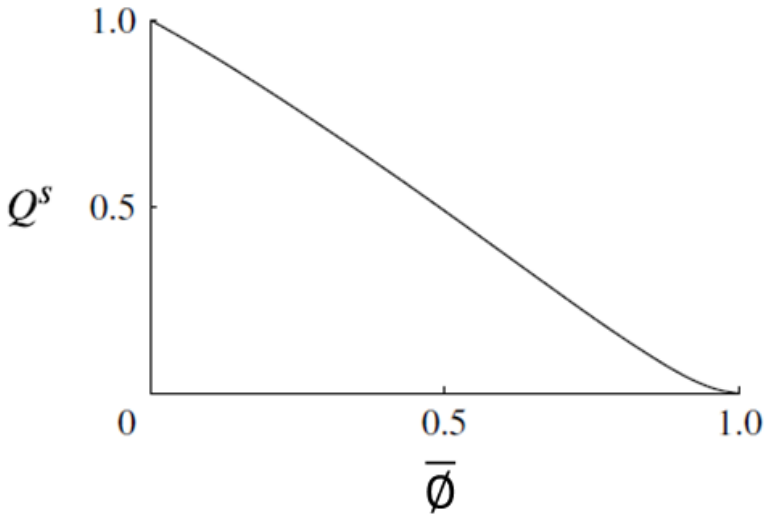

Figure 2.3: Function Q^s versus normalized average proppant concentration $\overline{\emptyset}$. (Dontsov & Peirce, 2014)

The proppant flux in the fracture is given by

$$\boldsymbol{q^p} = B\left(\frac{w}{a}\right)\hat{Q}^P\left(\overline{\emptyset},\frac{w}{a}\right)\boldsymbol{q^s} - B\left(\frac{w}{a}\right)\frac{a^2 w}{12\mu}(\rho_p - \rho_f)g\boldsymbol{e}_z\hat{G}^p\left(\overline{\emptyset},\frac{w}{a}\right) \tag{2.20}$$

$$\hat{Q}^P\left(\overline{\emptyset},\frac{w}{a}\right) = \frac{w^2 Q^p(\overline{\emptyset})}{w^2 Q^s(\overline{\emptyset}) + a^2\overline{\emptyset}D(1)} \tag{2.21}$$

$$\hat{G}^P\left(\overline{\emptyset},\frac{w}{a}\right) = G^p(\overline{\emptyset}) - \frac{w^2 G^s(\overline{\emptyset})Q^p(\overline{\emptyset})}{w^2 Q^s(\overline{\emptyset}) + a^2\overline{\emptyset}D(1)} \tag{2.22}$$

$$B\left(\frac{w}{a}\right) = \frac{1}{2}H\left(\frac{w}{2a} - N\right)H\left(\frac{w_B - w}{2a}\right)\left[1 + \cos\left(\frac{\pi(w_B - w)}{2a}\right)\right] + H\left(\frac{w - w_B}{2a}\right) \tag{2.23}$$

$B\left(\frac{w}{a}\right)$ is the "blocking" function that prevents proppant from entering narrow regions where the fracture width is smaller than N times of the proppant diameter. A

typical value for N is 3. H is the Heaviside step function and $w_B = 2a(N+1)$. These two functions provide a smooth vanishing of proppant flux and helps the stability of the simulation. Proppant retardation is captured by the parameter $\hat{Q}^P\left(\overline{\emptyset}, \frac{w}{a}\right)$, which is a function of proppant concentration and the ratio of fracture width versus proppant size. The variable Q^p in Equation 2.21 and 2.22 is a function of normalized proppant concentration as shown in Fig. 2.4.

The last term of Equation 2.20 describes the effect of gravity. Proppant settling due to gravity is ignored in the PKN fracture model. In the Pseudo-3D fracture model developed in the next chapter, proppant settling is accounted for.

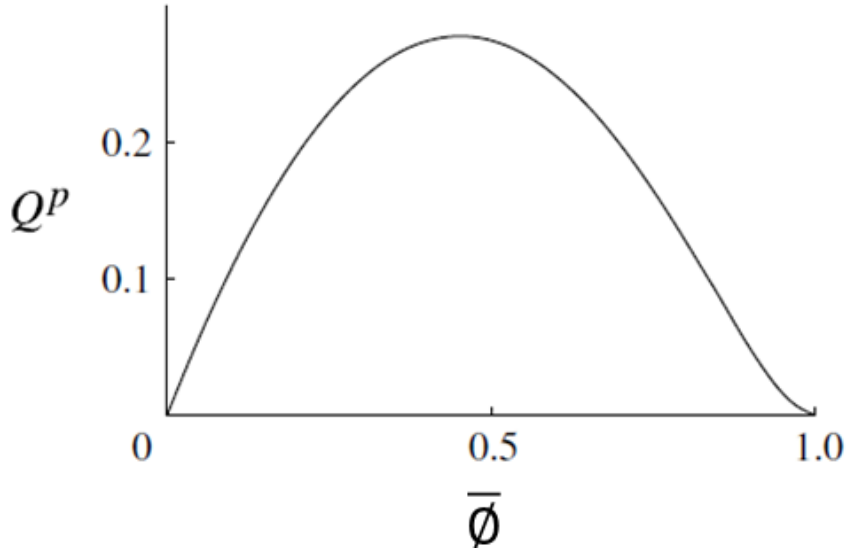

Figure 2.4: Function Q^p versus normalized average proppant concentration $\overline{\emptyset}$. (Dontsov & Peirce, 2014)

The local fluid mass balance equation in the PKN fracture model presented in Section 2.2.1 is now replaced by the local slurry mass balance equation (Equation 2.14) and proppant transport equation (Equation 2.15). And the slurry flux (Equation 2.17) and

proppant flux (Equation 2.20) are functions of parameters such as proppant concentration, fracture width, proppant radius and so on. All governing equations are solved simultaneously on a moving mesh. The mesh grows as the fracture propagates and the total number of elements in the mesh remains constant throughout the simulation. The algorithms for solving the fracture propagation and proppant transport in the fracture are presented in the next section.

2.2.3. Explicit Moving Mesh Strategy

The governing equations introduced in the last two sections describe PKN fracture propagation and proppant transport in the fracture. These equations consist of a system of non-linear equations that need to be solved simultaneously with a moving boundary. As the fracture propagates, the fracture length discretization needs to be updated by either re-meshing or adding new elements.

Several methods may be used to solve these coupled equations. In this work, we adopt the explicit finite-difference method with a dynamic grid that evolves in such a way that the fracture is always divided into a fixed number of elements (stretching coordinate system). The advantage of this method is that the number of computational elements for one fracture remains constant as the fracture grows longer and wider. The constant number of elements helps keep the computation efficient. In addition, the explicit moving mesh algorithm is very suitable for solving non-linear, moving boundary problems (such as fracture propagation). It has been shown that a small number of elements (about 10 to 20) is enough to capture hydraulic fracture propagation accurately (Economides & Nolte, 1989; Xiang 2012). The derivation of the moving mesh algorithm for solving the fracture geometry evolution follows that of Detournay et al. (1990).

2.2.3.1. The Stretching Coordinate System

The governing equations are valid in the range of $0 \leq x \leq L(t)$, with $L(t)$ being the length of the fracture at time t. The non-dimensional form of the equations can help avoid updating the mesh as the fracture grows. In other words, the governing equations can be reformulated in terms of a moving coordinate θ defined as:

$$\theta = \frac{x}{L(t)}, \qquad (0 \leq \theta \leq 1) \tag{2.24}$$

By adopting the dimensionless coordinate θ, a constant number of nodes at fixed locations in the θ coordinate can be used throughout the simulation.

The dimensionless fracture length $0 \leq \theta \leq 1$ is discretized into N nodes with a geometric progression that refines the mesh at the tip of the fracture. For an expansion ratio equal to 1, the mesh is uniform. For typical PKN fracture simulations, a small number of nodes (about 11 to 20) is sufficient to obtain a reasonably accurate solution for the equations described above.

Fig. 2.5 is an illustration of fracture discretization with the first node being at the perforation (Node 1) and the last node being at the fracture tip (Node N). Variables including $P_f(\theta_i, t), w(\theta_i, t), \tau(\theta_i, t), u_L(\theta_i, t)$ are stored at fracture nodes 1 to N. The fracture nodes are marked by hourglasses in Fig. 2.5. And N-1 auxiliary nodes at the center of fracture cells (i+1/2) are introduced for slurry flow rate in the fracture $q_s\left(\theta_{i\pm\frac{1}{2}}, t\right)$ and proppant concentration $\overline{\emptyset}\left(\theta_{i\pm\frac{1}{2}}, t\right)$. The auxiliary nodes are marked by circles in Fig. 2.5.

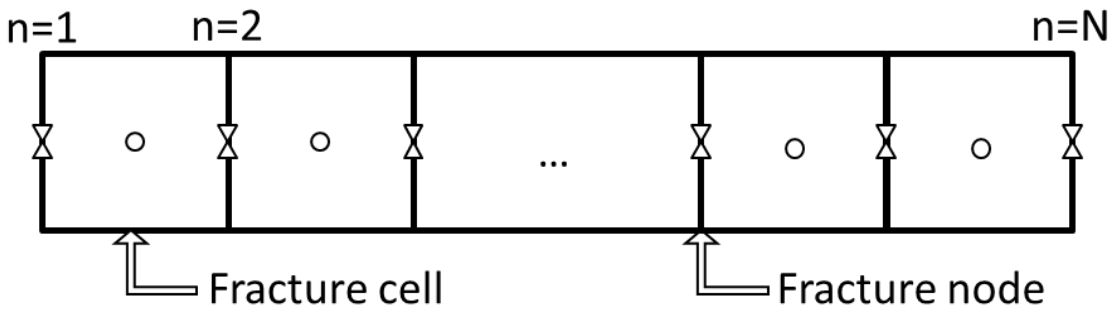

Figure 2.5: Illustration of fracture discretization.

All variables and equations are now expressed in θ and t, instead of x and t. The conversion of spatial and time derivatives from x to θ is shown in Equation 2.25.

$$\left.\frac{\partial}{\partial x}\right|_t = \frac{1}{L}\left.\frac{\partial}{\partial \theta}\right|_t \tag{2.25a}$$

$$\left.\frac{\partial}{\partial t}\right|_x = \left.\frac{\partial}{\partial t}\right|_\theta - \theta\frac{\dot{L}}{L}\left.\frac{\partial}{\partial \theta}\right|_t \tag{2.25b}$$

Where $\dot{L}$ is the fracture propagation rate ($\dot{L} = \frac{dL}{dt}$).

With the transformation shown in Equation 2.25, Equation 2.4, 2.10, 2.11, 2.14 and 2.17 can be re-written as:

$$\frac{1}{L}\frac{\partial P_{net}}{\partial \theta} = -\frac{12\mu q_s}{w^3 \hat{Q}^s(\bar{\emptyset}, \frac{w}{a})} \tag{2.26}$$

$$\dot{w} = \frac{\theta\dot{L}}{L}\frac{\partial w}{\partial \theta} - \frac{1}{L}\frac{\partial q_s}{\partial \theta} - u_L \tag{2.27}$$

$$w = \frac{\pi P_{net} h_f (1-v)}{4G} \tag{2.28}$$

$$u_L = \frac{2C_l}{\sqrt{t-\tau(x)}} \tag{2.29}$$

$$L\int_0^1 w(\theta,t)d\theta + \int_0^t L(t')\int_0^1 u_L(\theta,t')\,d\theta dt' = \int_0^t q_o(t')dt' \tag{2.30a}$$

$$\dot{L} = \frac{L_{t+dt} - L_t}{dt} \tag{2.30b}$$

And the boundary and initial conditions are transformed to be

$$L(0) = 0 \tag{2.31}$$

$$P_{net}(0,0) = 0 \tag{2.32a}$$

$$q_s(0,t) = q_o(t);\ \ (t > 0) \tag{2.32b}$$

$$P_{net}(1,t) = 0;\quad (t > 0) \tag{2.32c}$$

The fracture propagation is solved on the θ coordinate and the results are transformed back to real dimensions by multiplying by the fracture length. An explicit finite-difference scheme is adopted. The local fluid mass balance equation is discretized with a forward Euler difference in time. And an upwind differentiation scheme is used for the $\partial w/\partial\theta$ term to reduce the "advection error" introduced by the moving mesh. After that, the fracture pressure is calculated using the updated fracture width. Then, flow rate in the fracture is solved using the lubrication theory and the updated fracture pressure and width. Leak off is then calculated. Finally, the fracture length and propagation speed are updated using the total mass balance equation.

2.2.3.2. Upwind Scheme for Proppant Transport Simulation

At each time step, fracture propagation is determined prior to the proppant transport calculation. When solving for proppant distribution in the fracture, the fracture geometry is fixed.

The local proppant mass balance equation is both nonlinear and heterogeneous. Dontsov and Peirce (2015) have done an in-depth analysis of solving the nonlinear conservation laws on a moving mesh. Their analysis suggests implementing an upwind scheme for proppant transport in the fracture.

First, the local proppant mass balance equation is converted to the θ coordinate

$$\frac{\partial(w\bar{\phi})}{\partial t} - \theta\frac{\dot{L}}{L}\frac{\partial\left(w\bar{\phi}\right)}{\partial\theta} + \frac{1}{L}\frac{\partial q_p}{\partial\theta} \tag{2.33}$$

A parameter $\widetilde{q_p}$ is defined as

$$\widetilde{q_p} = q_p - \theta \dot{L}(w\bar{\emptyset}) \tag{2.34}$$

Then Equation 2.33 becomes

$$\frac{\partial(w\bar{\emptyset})}{\partial t} + \frac{\dot{L}}{L}\left(w\bar{\emptyset}\right) + \frac{1}{L}\frac{\partial \widetilde{q_p}}{\partial \theta} = 0 \tag{2.35}$$

A forward Euler scheme is adopted for the time derivative and a central differencing scheme is adopted for the special derivative, the discrete equation becomes

$$\frac{\left(w\bar{\emptyset}\right)_{j+\frac{1}{2}}^{t+\Delta t} - \left(w\bar{\emptyset}\right)_{j+\frac{1}{2}}^{t}}{\Delta t} + \frac{\dot{L}}{L}\left(w\bar{\emptyset}\right)_{j+\frac{1}{2}}^{t} + \frac{1}{L}\frac{(\widetilde{q_p}_{j+1}^{t} - \widetilde{q_p}_{j}^{t})}{\theta_{j+1} - \theta_j} = 0 \tag{2.36}$$

Note that $\left(w\bar{\emptyset}\right)$ is calculated at fracture cell centers by

$$\left(w\bar{\emptyset}\right)_{j+\frac{1}{2}} = 0.5 * \left(w_j + w_{j+1}\right) * \bar{\emptyset}_{j+\frac{1}{2}} \tag{2.37}$$

And $\widetilde{q_p}$ is first calculated at cell centers as

$$\widetilde{q_p}_{j+\frac{1}{2}} = q_{p\,j+\frac{1}{2}} - \theta \dot{L}\left(w\bar{\emptyset}\right)_{j+\frac{1}{2}} \tag{2.38}$$

The value of $\widetilde{q_p}$ needs to be interpolated to the fracture cell nodes for the central differencing term in Equation 2.36. An upwind scheme is adopted for the interpolation of $\widetilde{q_p}$. The Wind is calculated at each cell center (Equation 2.39), and the Velocity is calculated at each cell node (Equation 2.40)

$$Wind_{j+\frac{1}{2}} = \left(\frac{\partial \widetilde{q_p}}{\partial\left(w\bar{\emptyset}\right)}\right)_{j+\frac{1}{2}} = \frac{\widetilde{q_p}_{j+\frac{3}{2}} - \widetilde{q_p}_{j+\frac{1}{2}}}{\left(w\bar{\emptyset}\right)_{j+\frac{3}{2}} - \left(w\bar{\emptyset}\right)_{j+\frac{1}{2}}} \tag{2.39}$$

$$Vel_j = \left(\frac{\partial \widetilde{q_p}}{\partial\left(w\bar{\emptyset}\right)}\right)_j = \frac{\widetilde{q_p}_{j+\frac{1}{2}} - \widetilde{q_p}_{j-\frac{1}{2}}}{\left(w\bar{\emptyset}\right)_{j+\frac{1}{2}} - \left(w\bar{\emptyset}\right)_{j-\frac{1}{2}}} \tag{2.40}$$

Fig. 2.6 illustrates how the interpolation of $\widetilde{q_p}$ from the cell center to the cell nodes is done according to the direction of the Wind and the Velocity. And finally, the proppant distribution in the fracture is updated by solving Equation 2.36.

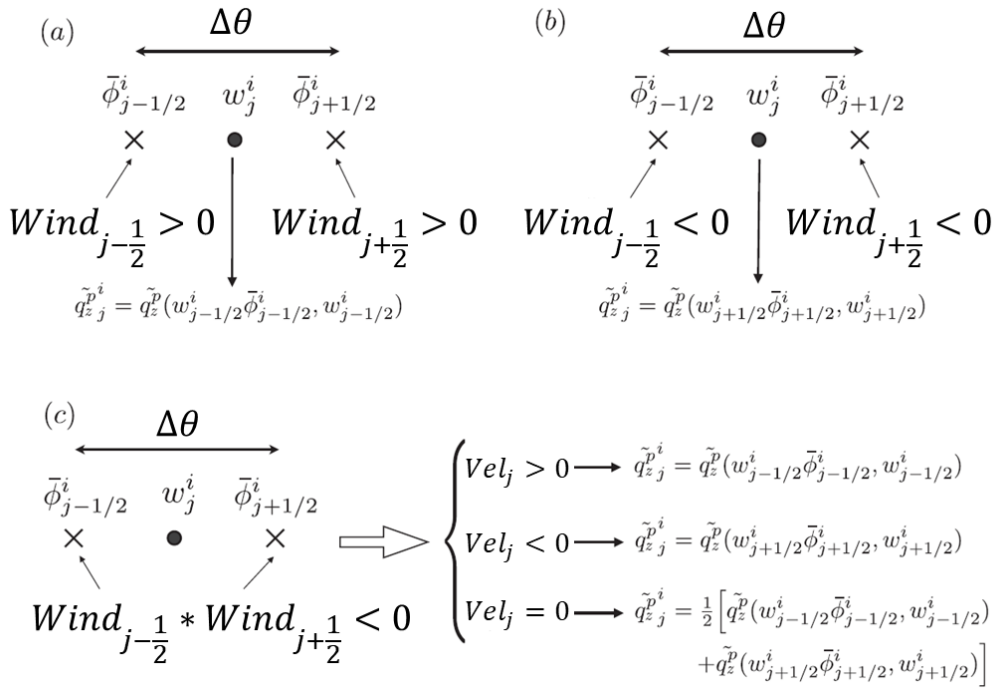

Figure 2.6: Upwind scheme for proppant transport in the fracture. (Dentsov & Peirce, 2015)

2.2.3.3. Stability Criterion.

A forward Euler scheme is adopted for the time derivatives in both the fracture propagation and the proppant transport equations. One of the limitations of adopting this explicit method is that the time step may not exceed a critical value to keep the calculation stable. A well-known approach for determining critical time step for explicit finite difference scheme is the von Neumann analysis, also known as the CFL criterion (Ferziger & Peric, 2012). This analysis needs to be applied to both the local slurry mass balance equation (Equation 2.27) and the proppant transport equation (Equation 2.35) for finding the maximum stable time step.

The local slurry mass balance equation, together with the fluid momentum equation and fracture pressure-width relation, form the stiff part of the problem, which would require a time step restriction $\Delta t \sim O(\Delta\theta^3)$, while the proppant transport equation is less stiff and would require a time step restriction $\Delta t \sim O(\Delta\theta)$ (Dontsov & Peirce, 2015). Therefore, the maximum stable time step is determined by applying the von Neumann analysis to the stiffer part of the problem. The derivation is shown below (Detournay et al., 1990).

Ignoring the leak-off term in Equation 2.27, assume $q_s = q$, and substituting Equation 2.26 and 2.28 in to 2.27, we can get Equation 2.41.

$$\dot{w} = c_w \frac{\partial^2 w}{\partial \theta^2} + \frac{3c_w}{w}\left(\frac{\partial w}{\partial \theta}\right)^2 + \frac{\theta \dot{L}}{L}\frac{\partial w}{\partial \theta} \tag{2.41}$$

Equation 2.41 is in the form of a diffusion equation, and the "diffusivity coefficient":

$$c_w = \frac{4Gw^3}{\pi^3(1-\nu)\mu h_f L^2} \tag{2.42}$$

Assume that the stability condition can be estimated by the high order term and that c_w can be approximated from fracture geometry of the previous time step, then the critical time step can be derived by the von Neumann analysis:

$$\Delta t_{critical}^{k+1} = \min\left[\frac{\Delta\theta_{\mathrm{i}}^2}{2c_{\mathrm{w,i}}^{\mathrm{k}}}\right]; \mathrm{i} = 1,2,\ldots,\mathrm{N}-1 \tag{2.43}$$

Equation 2.43 shows that: (1) If the fracture is discretized uniformly, the critical time step is determined by the fracture node with the smallest dimensions. And in a case where multiple fractures propagate simultaneously, the critical time step is restricted by the fracture with the smallest dimensions. (2) For a PKN geometry with no leak-off, the critical time step increases linearly with time (Detournay et al., 1990). Fluid leak off in unconventional reservoir stimulation is small and as a rule of thumb, the increasing of the critical time step is an indication of a stable simulation.

2.2.3.4. Initialization of the Fracture.

Although the initial condition of the fracture is *L=0*, it is not possible to start the simulation with zero fracture length. Instead, the fracture starts from a small length with initial values of $\Delta P_{net}, w, q, u_L, \tau$ at each node. In this work, the fractures are initialized using the approximate analytical solution of PKN fracture with no leak-off (Nordgren, 1972).

Initialize fracture length at a small time ($t_{initial}$) using

$$L(t_{initial}) = 0.68\left[\frac{GQ_{inj}^3}{(1-\nu)\mu h_f^4}\right]^{\frac{1}{5}} {t_{initial}}^{\frac{1}{4}} \tag{2.44}$$

Initialize fracture width at a small time using

$$w(0, t_{initial}) = 2.5\left[\frac{(1-\nu)\mu Q_{inj}^2}{G h_f}\right]^{\frac{1}{5}} {t_{initial}}^{\frac{1}{5}} \tag{2.45}$$

Initialize fracture net pressure

$$P_{net}(0, t_{initial}) = 2.5\left[\frac{G^4 \mu Q_{inj}^2}{(1-\nu)^4 h_f^6}\right]^{\frac{1}{5}} {t_{initial}}^{\frac{1}{5}} \tag{2.46}$$

And the initial fracture propagation speed:

$$\dot{L}(t_{initial}) = 0.17\left[\frac{GQ_{inj}^3}{(1-\nu)\mu h_f^4}\right]^{\frac{1}{5}} {t_{initial}}^{-\frac{3}{4}} \tag{2.47}$$

2.2.4. Solution Algorithm

The numerical solution of the fracture starts from an initial state of a small fracture described by Equation 2.44 to 2.47. With known nodal quantities at time t^k ($w_i^k, P_{net,i}^k, q_{s,i+\frac{1}{2}}^k, q_{p,i+\frac{1}{2}}^k, \overline{\emptyset}_{i+\frac{1}{2}}^k, u_{L,i}^k, L^k$), the following procedure is followed to advance to t^{k+1}:

(1). The maximum time step Δt^{k+1} is calculated using the stability criterion (Equation 2.43).

(2). Fracture widths at cell nodes w_i^{k+1} are calculated using the Euler explicit finite difference scheme by solving the local slurry mass balance (Equation 2.27).

(3). The net pressure in the fracture $P_{net,i}^{k+1}$ are calculated assuming plane strain (Equation 2.28).

(4). The slurry flux rate at cell centers $q_{s,i+\frac{1}{2}}^{k+1}$ are updated using the slurry momentum (Equation 2.17).

(5). The proppant flux at cell centers $q_{p,i+\frac{1}{2}}^{k+1}$ are updated (Equation 2.20).

(6). The normalized proppant concentration at cell centers $\overline{\emptyset}_{i+\frac{1}{2}}^{k+1}$ are calculated using the local proppant mass balance (Equation 2.36).

(7). The leak-off velocity $u_{L,i}^{k+1}$ at cell nodes are evaluated using Equation 2.29.

(8). The fracture length L^{k+1} and the fracture propagation velocity $\dot{L}^{k+1}$ are updated using the global mass balance (Equation 2.30).

The steps (1) through (8) are repeated until the whole treatment is complete.

2.3. RESULTS AND DISCUSSION

In this section, we first present the validation of the model with an analytical solution (Nordgren, 1972). After that, a sensitivity study of mesh density is shown. Finally, simulations of proppant transport in the fracture are presented.

2.3.1. Model Validation.

The analytical solution of a fracture driven by Newtonian fluid pumped at a constant rate in an impermeable medium (no leak off) was obtained by Nordgren (1972).

This solution is used to validate the moving mesh PKN fracture model developed in this chapter.

The analytical solution is summarized below:

$$L = 0.68\left[\frac{GQ_{inj}^3}{(1-\nu)\mu h_f^4}\right]^{0.2} t^{0.8} \tag{2.48}$$

$$w(0,t) = 2.5\left[\frac{(1-\nu)\mu Q_{inj}^2}{G h_f}\right]^{0.2} t^{0.2} \tag{2.49}$$

$$P_{net}(0,t) = 2.5\left[\frac{G^4 \mu Q_{inj}^2}{(1-\nu)^4 h_f^6}\right]^{0.2} t^{0.2} \tag{2.50}$$

All the parameters are in SI units.

Parameters used for the validation case are summarized in Table 2.1. And the results are summarized in Fig. 2.7, Fig. 2.8 and Fig. 2.9. The simulated fracture growth (fracture with, length and net pressure) show good agreement with the analytical solution.

Parameter	**Value**	**Parameter**	**Value**
Young's Modulus (GPa)	24	Fluid Viscosity (Pa·s)	0.56
Poisson's Ratio	0.2	Injection Rate (bpm)	3.02
Fracture Height (m)	10	Injection Time (s)	1000
Pore Pressure (psi)	3000	Min Hz Stress (psi)	4000

Table 2.1: Parameters for the moving mesh 2D PKN fracture validation case.

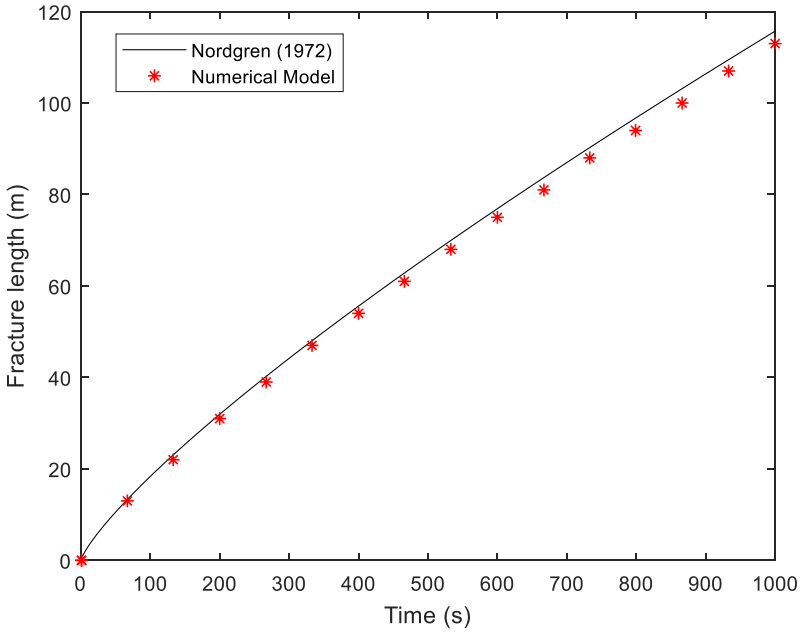

Figure 2.7: Fracture length history for the PKN fracture validation case.

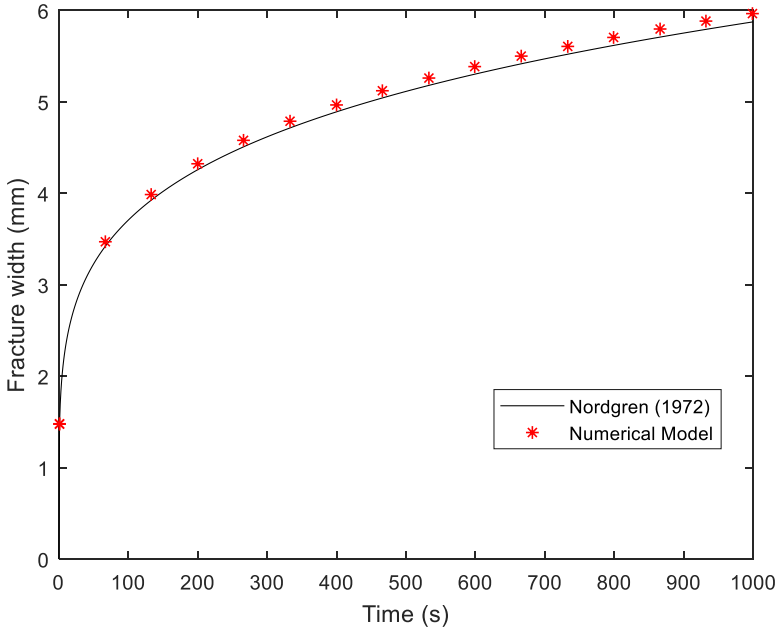

Figure 2.8: Fracture maximum width history for the PKN fracture validation case.

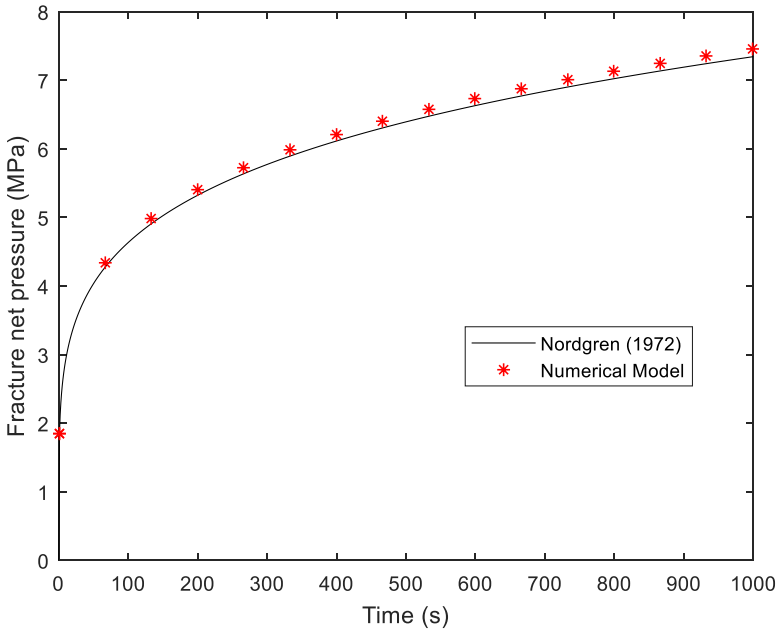

Figure 2.9: Fracture net pressure history for the PKN fracture validation case.

A visualization of the fracture geometry is shown in Fig. 2.10. This file is generated in VTK format (Avila et al., 2010) and is visualized in the open source software ParaView. The VTK files allow us to visualize information including fracture geometry, proppant concentration, relative location of the fracture and so on.

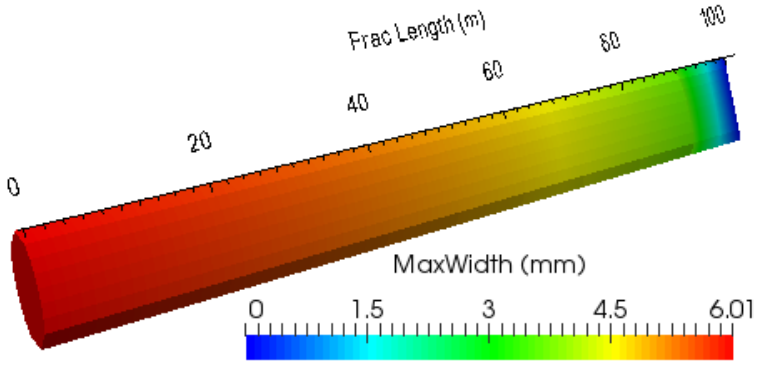

Figure 2.10: VTK file visualization of the fracture geometry.

2.3.2. Mesh Density Study.

The governing equations for fracture propagation are solved on a moving mesh. The number of mesh elements remains constant as the fracture grows wider and longer. Usually a small number of cells (Economides & Nolte, 1989; Xiang 2012) is enough to acquire reasonably accurate solution. A sensitivity study of mesh density is performed, to estimate the minimum number of elements needed for one fracture.

Parameters used for the mesh density study case are summarized in Table 2.2. And the results are summarized in Fig. 2.11 to Fig. 2.14. It is shown that 11 nodes are enough to provide reasonable accuracy.

Parameter	Value	Parameter	Value
Young's Modulus (GPa)	24	Res. Permeability (mD)	1
Poisson's Ratio	0.2	Res. Fluid Vis. (cp)	2
Fracture Height (m)	10	Res. Fluid Comp. (Pa^{-1})	9.7e-10
Pore Pressure (psi)	3000	Fluid Viscosity (cp)	560
Min. Hz Stress (psi)	4000	Injection Rate (bpm)	3.02
Reservoir Porosity	0.1	Injection Time (s)	1000

Table 2.2: Parameters for the mesh density study.

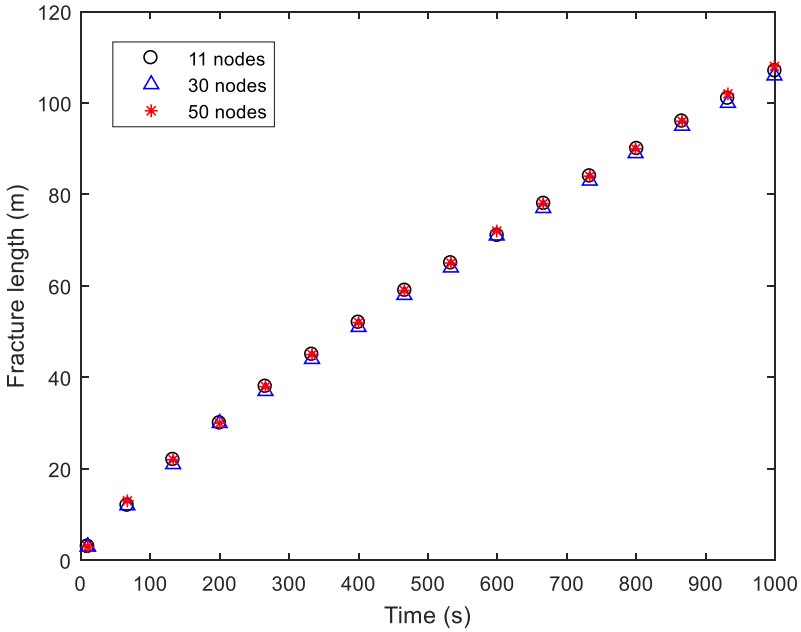

Figure 2.11: Fracture length history for the PKN fracture mesh density study.

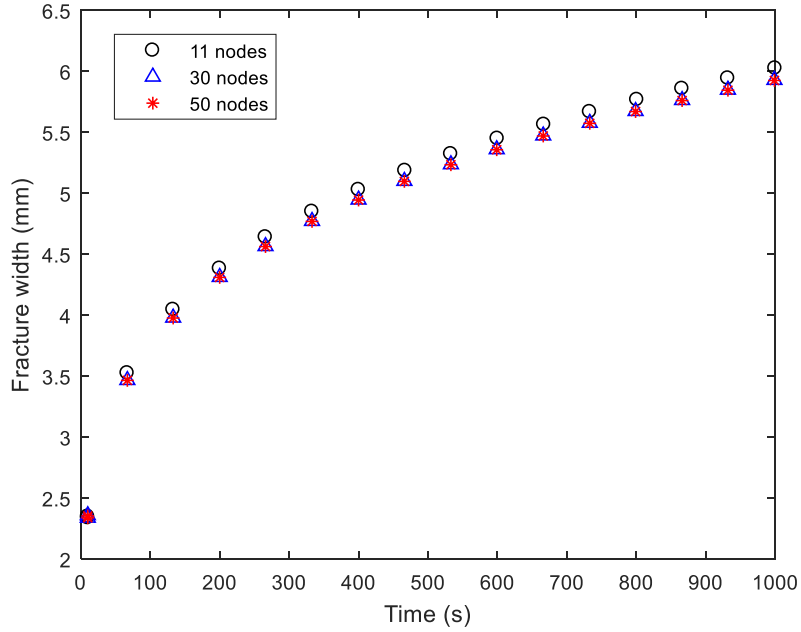

Figure 2.12: Fracture maximum width history for the PKN fracture mesh density study.

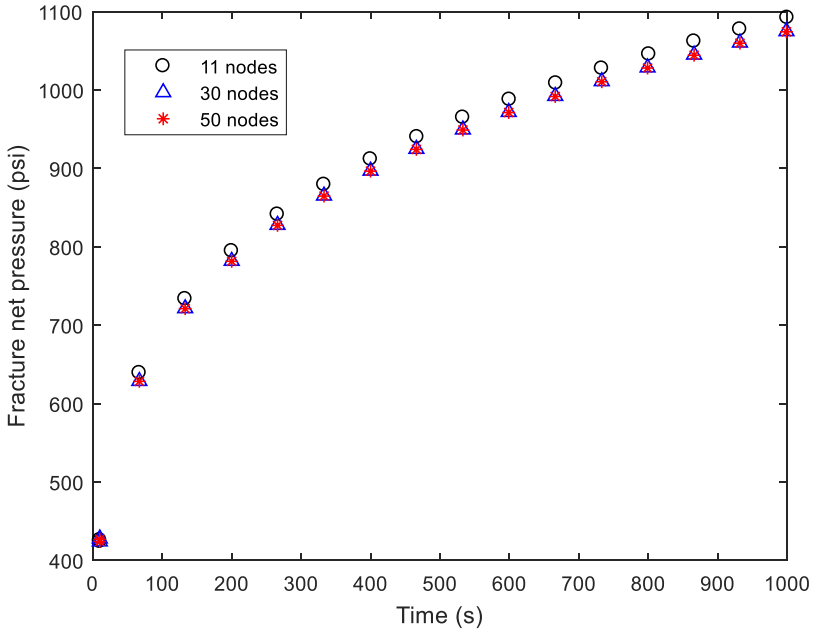

Figure 2.13: Fracture net pressure history for the PKN fracture mesh density study.

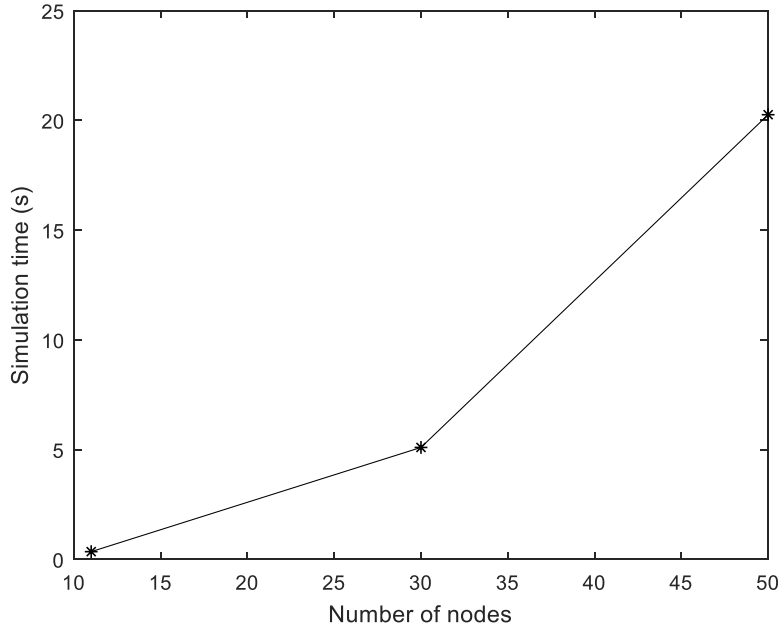

Figure 2.14: Computation time for the PKN fracture mesh density study.

2.3.3. Proppant Transport in the Fracture.

Proppant is added in the pumping schedule to demonstrate the calculation of proppant transport in the fracture. Parameters used for this case is the same as in Table 2.1. Proppant is added to the pumping fluid starting from 6.7 minutes for 5 minutes with a concentration of 2 ppa, and then 5 ppa for 2 minutes.

The final proppant concentration in the fracture is shown in Fig. 2.15. The proppant concentration is low close to the wellbore due to the flush stage. Deeper in the fracture, proppant concentration increases, and the max proppant concentration is about 20.5% (volume percentage). Close the tip of the fracture, the proppant concentration is low. The total proppant mass is conserved.

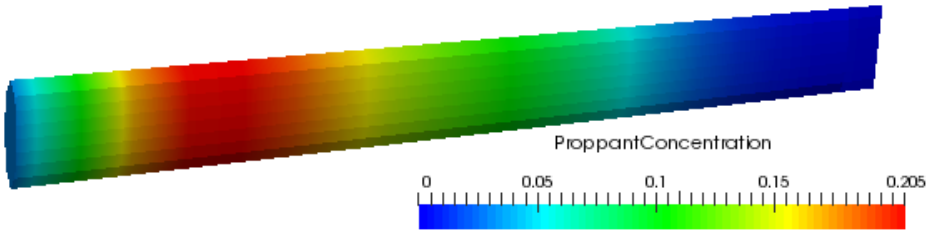

Figure 2.15: Proppant distribution in the fracture.

2.4. Conclusions

In this chapter, a PKN fracture model for single fracture propagation is developed. The governing equations for fracture propagation and proppant transport are solved simultaneously with a moving boundary. A moving mesh algorithm is adopted where the mesh grows with the fracture, and the number of elements remains constant through the fracture simulation. Proppant transport in the fracture is simulated using the proppant transport model developed by Dontsov and Peirce (2014). A smooth transition from Poiseuille flow to Darcy flow is described for low to high proppant concentration.

The model is validated with the analytical solution of Nordgren (1972). A mesh density study has been performed to validate the model further and to study the minimum number of nodes (11 nodes) needed for reasonable accuracy. The simulation of proppant transport in the fracture has been demonstrated. Parameters including fracture geometry and proppant concentration in the fracture are visualized with VTK files.

The PKN fracture model developed in this chapter is a simple and computationally efficient model that captures the primary features of fracture propagation, including fracture mechanics, fluid and proppant mass balance and fluid flow in the fracture. This model can be extended to simulate simultaneous propagation of multiple fractures as shown in Chapter 4. It can also be used to estimate the non-uniform fluid and proppant placement among multiple clusters as shown in Chapter 5. For applications that require great computational efficiency (such as re-fracturing horizontal wells as discussed in Chapter 7), or simulations with limited reservoir information, this model can be readily applied.

NOMENCLATURE

B	=	Blocking function for proppant transport
C_c	=	Compressibility fluid-loss coefficient, L/√T, m/√s
C_l	=	Overall fluid-loss coefficient, L/√T, m/√s
C_v	=	Viscous fluid-loss coefficient, L/√T, m/√s
D	=	Function related to the permeability of the packed particles
E	=	Young's Modulus, M/LT^2, Pa
G	=	Shear Modulus, M/LT^2, Pa
G^p	=	Function numerically calculated
$\hat{G}^P$	=	Function controlling proppant settling in the slurry
G^s	=	Function numerically calculated
H	=	Heaviside step function
L	=	Fracture length, L, m
$\dot{L}$	=	Fracture propagation rate, L/T, m/s
P_f	=	Fluid pressure in fracture, M/LT^2, Pa
P_{net}	=	Net pressure in the fracture, M/LT^2, Pa
P_I	=	Pressure at the interface between the invaded zone and the formation fluid, M/LT^2, Pa
P_R	=	Reservoir fluid pressure, M/LT^2, Pa
Q_{inj}	=	Initial injection rate, L^3/T, m^3/s
Q_o	=	Fluid injection rate, L^3/T, m^3/s
Q^p		Function numerically calculated
$\hat{Q}^P$	=	Function controlling volumetric concentration of proppant in the slurry
Q^s	=	Function numerically calculated
$\hat{Q}^s$	=	Function representing transition of flow
a	=	Proppant radius, L, m
g	=	Gravitational acceleration, L/T^2, m/s^2
c_w	=	The diffusivity coefficient for time step calculation, T^{-1}, s^{-1}
h_f	=	Fracture height, L, m
k	=	Formation permeability, L^2, m^2
q	=	Fluid flow rate per unit fracture height, L^2/T, m^2/s
q_o	=	Fluid injection rate per unit fracture height, L^2/T, m^2/s
q_p	=	Proppant flow rate per unit fracture height, L^2/T, m^2/s
q_s	=	Slurry flow rate per unit fracture height, L^2/T, m^2/s
$\widetilde{q_p}$	=	Function defined for proppant transport calculation, L^2/T, m^2/s
t	=	Time, s
$t_{initial}$	=	Initial time step, T, s
u_L	=	Fluid leak off velocity from both walls per unit fracture height, L/T, m/s
u_N	=	Fluid leak off velocity, L/T, m/s
w	=	Average width of the fracture, L, m
w_B	=	Function of proppant radius, L, m

w_{max}	=	Maximum fracture width, L, m
$\Delta t_{critical}^{k+1}$	=	Critical time step, T, s
$\bar{\emptyset}$	=	Normalized proppant volume concentration
$\emptyset_{\max}$	=	Maximum proppant volume concentration
$\bar{\alpha}$	=	Constant in the proppant transport model
θ	=	Dimensionless x-coordinate
κ_{fl}	=	Isothermal compressibility of the formation fluid, LT^2/M, Pa^{-1}
μ	=	Fracturing fluid viscosity, M/LT, Pa·s
μ_{fl}	=	Formation fluid viscosity, M/LT, Pa·s
ν	=	Poisson's Ratio
ρ_f	=	Fluid density, M/L^3, kg/m^3
ρ_p	=	Proppant density, M/L^3, kg/m^3
$\tau(x)$	=	Time when fracture tip arrives location x, T, s
φ	=	Reservoir porosity

REFERENCES

Avila, L.S., Barre, S., Blue, R., Geveci, B., Henderson, A., Hoffman, W.A., King, B., Law, C.C., Martin, K.M. and Schroeder, W.J., 2010. *The VTK User's Guide*. New York: Kitware.

Carter, R.D., 1957. Derivation of the general equation for estimating the extent of the fractured area. *Appendix I of "Optimum Fluid Characteristics for Fracture Extension," Drilling and Production Practice, GC Howard and CR Fast, New York, New York, USA, American Petroleum Institute*, pp.261-269.

Detournay, E., Cheng, A.D. and McLennan, J.D., 1990. A poroelastic PKN hydraulic fracture model based on an explicit moving mesh algorithm. *Journal of energy resources technology*, *112*(4), pp.224-230.

Dontsov, E.V. and Peirce, A.P., 2014. Slurry flow, gravitational settling and a proppant transport model for hydraulic fractures. *Journal of Fluid Mechanics*, *760*, pp.567-590.

Dontsov, E.V. and Peirce, A.P., 2015. Proppant transport in hydraulic fracturing: crack tip screen-out in KGD and P3D models. *International Journal of Solids and Structures*, *63*, pp.206-218.

Economides, M.J. and Nolte, K.G., 1989. *Reservoir stimulation* (Vol. 2). Englewood Cliffs, New Jersey: Prentice Hall.

Ferziger, J.H. and Peric, M., 2012. *Computational methods for fluid dynamics*. Springer Science & Business Media.

Geertsma, J. and De Klerk, F., 1969. A rapid method of predicting width and extent of hydraulically induced fractures. *Journal of Petroleum Technology*, *21*(12), pp.1-571.

Khristianovic, S. and Zheltov, Y., 1955, June. Formation of vertical fractures by means of highly viscous fluids. In *Proc. 4th world petroleum congress, Rome* (Vol. 2, pp. 579-586).

Lamb, H., 1932. *Hydrodynamics*. Cambridge university press.

Nordgren, R.P., 1972. Propagation of a vertical hydraulic fracture. *Society of Petroleum Engineers Journal*, *12*(04), pp.306-314.

Perkins, T.K. and Kern, L.R., 1961. Widths of hydraulic fractures. *Journal of Petroleum Technology*, *13*(09), pp.937-949.

Schechter, R.S., 1992. Oil well stimulation.

Sneddon, I.N. and Elliot, H.A., 1946. The opening of a Griffith crack under internal pressure. *Quarterly of Applied Mathematics*, *4*(3), pp.262-267.

Xiang, J., 2012. *A PKN hydraulic fracture model study and formation permeability determination* (Master Thesis, Texas A & M University).

Chapter 3: Pseudo-3D Fracture Propagation Model

3.1. INTRODUCTION

For the PKN-Type fracture model developed in the last chapter, the fracture height is assumed to be constant. This assumption could be a significant limitation because fractures are not always well-contained, and sometimes estimates of fracture height are required from the simulation. In addition, when the height is assumed constant, the fracture height variation from the wellbore to the fracture tip is not captured.

To estimate the fracture height growth in layered formations, Simonson et al. (1978) developed a solution to model fracture height growth in three layers with a symmetric stress barrier. Fung et al. (1987) extended the concept to non-symmetric, multiple layers. Solutions of fracture height growth through reservoir layers with dissimilar confining stresses are the basis for the development of Pseudo-3D fracture models.

Developed in the 1980s, Pseudo-3D fracture models are "a crude, yet effective, attempt to capture the physical behavior of a planar 3D hydraulic fracture at minimal computational cost" (Adachi et al., 2007). Compared to fully 3D fracture models, the Pseudo-3D model captures many of the major features of hydraulic fracture propagation with a fraction of computation time.

There are two main types of Pseudo-3D fracture models: the "lumped" and cell-based (Economides & Nolte, 1989). The "lumped" Pseudo-3D model consists of two half-ellipses, as shown in Fig. 3.1 (a). In each time step, the fracture length and the fracture height near the wellbore are calculated, and the fracture shape is interpolated. Usually, some empirical correlations are implemented in the "lumped" Pseudo-3D model to calculate fracture geometry and fluid flow in the fracture.

Cell-based Pseudo-3D models discretize the fracture to be a series of connected vertical cells, as shown in Fig.1 (b). Plane strain is usually assumed, and the fracture cells are decoupled laterally. Parameters including fracture height, width, flow rate and proppant concentration are solved on each fracture cell.

Both "lumped" and cell-based Pseudo-3D fracture models have been useful for completion designs in the oil and gas industry. Today, some of the most popular commercial hydraulic fracturing modeling tools are based on the Pseudo-3D methodology. In this chapter, we work on developing a cell-based Pseudo-3D fracture model for single fracture simulation.

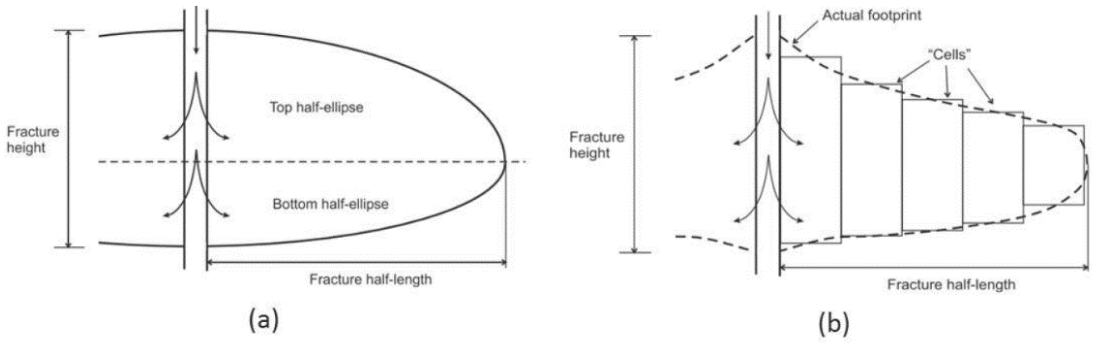

Figure 3.1: Illustration for "lumped" (a), and cell-based (b) Pseudo-3D fracture models. (Adachi et al., 2007)

3.2. PSEUDO-3D FRACTURE MODEL FORMULATION

In this section, we present the formulation used for modeling the propagation of a Pseudo-3D fracture. First, the solid mechanics solution for the fracture height and width profile of the Pseudo-3D fracture in multiple, non-symmetric layers is discussed. Next, the governing equations for the propagation of Pseudo-3D fracture and proppant transport are

presented. Then, the fracture propagation is solved on a moving mesh that grows with the fracture, and proppant settling is solved on a separate, fixed mesh. Finally, the solution algorithm is explained.

3.2.1. Solid Mechanics Solution for Pseudo-3D Fracture Model

This section presents the solid mechanics solution for the calculation of the Pseudo-3D fracture height and width profile. It is an exact, analytical solution for a 2D elastic fracture under arbitrary internal load. And the solution is applied to every vertical cell of the Pseudo-3D fracture assuming plane strain. The validity of the plane strain assumption compared to fully 3D solutions is studied and presented later in this chapter

Using this fundamental solution, many properties including minimum horizontal stress, pore pressure, rock flow properties (porosity and permeability) and formation fluid properties (formation fluid viscosity and density) can vary with depth. But the mechanical properties including Young's Modulus and Poisson's Ratio must be constant. Fung et al. (1987) have shown that the effect of Young's Modulus contrast on fracture height growth is not significant, even for modulus contrasts as large as 5. Yue et al. (2018) derived approximations of effective modulus of multiple layers. The impact of layer heterogeneity on planar fracture width has been studied by many researchers (Van Eekelen, 1982; Thiercelin et al., 1987; Gu and Siebrits, 2006; Yue et al., 2018). More complicated fracture behavior at layer interface has been investigated in the literature, such as fracture crossing, bending, kinking and offsetting (Fisher & Warpinski, 2012; Ouchi et al., 2017).

Main assumptions related to the calculation of the Pseudo-3D fracture height and width profile are summarized below:

1. Planar fracture;

2. Elastic material;
3. Equilibrium fracture height ($K_I = K_{I_c}$);
4. Plane strain.
5. Homogeneous mechanical properties (Young's Modulus and Poisson's Ratio)

3.2.1.1. Solid Mechanics Solution for Load in One Layer

Exact, analytical solution exists for the stress intensity factor and the width profile of a Pseudo-3D fracture created by arbitrary internal pressure. It is the fundamental solution of an infinite line crack subjected to an internal load. This fundamental solution is obtained by finding the corresponding Airy Stress Function.

The use of Airy Stress Function is a powerful technique for solving 2D equilibrium elasticity problems. After determining the Airy Stress Function for a specific problem, all the stress field and displacement are known. The basic idea of Airy Stress Function is explained briefly below (Tada et al., 1973; Wang et al., 2018).

The stress equilibrium equations in a 2D domain can be expressed as

$$\frac{\partial \sigma_x}{\partial x} + \frac{\partial \sigma_{xy}}{\partial y} = 0 \tag{3.1a}$$

$$\frac{\partial \sigma_y}{\partial y} + \frac{\partial \sigma_{yx}}{\partial x} = 0 \tag{3.1b}$$

Assume that a scalar function Φ exists, and is related to the stresses by

$$\sigma_x = \frac{\partial^2 \Phi}{\partial y^2} \tag{3.2a}$$

$$\sigma_y = \frac{\partial^2 \Phi}{\partial x^2} \tag{3.2b}$$

$$\sigma_{xy} = -\frac{\partial^2 \Phi}{\partial x \partial y} \tag{3.2c}$$

Then, the stress equilibrium equations shown in Equation 3.1a and 3.1b are always satisfied, regardless of the specific format of Φ. Therefore, the choice of Φ is the solution

to some problem (although we don't always know what that problem is). And the scalar function, Φ, is termed the Airy Stress Function.

One constraint on the selection of the Airy Stress Function is the Biharmonic Equation:

$$\frac{\partial^4\Phi}{\partial x^4} + 2\frac{\partial^4\Phi}{\partial x^2\partial y^2} + \frac{\partial^4\Phi}{\partial y^4} = 0 \tag{3.3}$$

The Biharmonic Equation can be abbreviated as

$$(\nabla^4\Phi) = 0 \tag{3.4}$$

Westergaard (1939) found that an Airy Stress Function of complex numbers can be the solution for the stress field in an infinite plate containing a crack. He discussed several Mode I crack problems that could be solved using:

$$\Phi = Re\{\bar{\bar{Z}}(z)\} + yIm\{\bar{Z}(z)\} \tag{3.5}$$

Where *Re* and *Im* denote the real and imaginary part respectively, and *z* is a complex number. The derivatives of the function $\bar{\bar{Z}}(z)$ is defined as

$$\bar{Z}(z) = \frac{d(\bar{\bar{Z}}(z))}{dz} \tag{3.6}$$

$$Z(z) = \frac{d(\bar{Z}(z))}{dz} \tag{3.7}$$

And the stresses can be calculated by taking derivatives of the Airy Stress Function in Equation 3.5:

$$\sigma_x = ReZ - yImZ' \tag{3.8a}$$

$$\sigma_y = ReZ + yImZ' \tag{3.8b}$$

$$\sigma_{xy} = -yReZ' \tag{3.8c}$$

Where,

$$Z'(z) = \frac{d(Z(z))}{dz} \tag{3.9}$$

The displacements are given by

$$2Gu_x = (1-2v)Re\bar{Z} - yImZ \tag{3.10a}$$

$$2Gu_y = 2(1-\upsilon)Im\bar{Z} - yReZ \tag{3.10b}$$

Finally, the width of a fracture can be calculated by setting y=0 (assuming the fracture is along the y=0 line) in Equation 3.10b

$$w_f(x, y=0) = 2u_y\big|_{y=0} = \frac{2(1-\upsilon)}{G} Im\bar{Z} \tag{3.11}$$

Many researchers have worked on obtaining analytical solutions for various kinds of fracture problems. Tada et al. (1973) compiled many useful solutions into a handbook. The solution we used for stress intensity factor and fracture width profile of the Pseudo-3D fracture is discussed below.

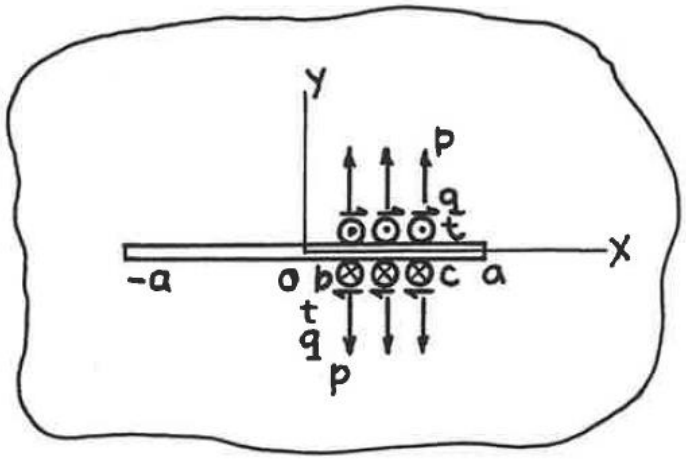

Figure 3.2: An infinite line crack subjected to a partial load. (Tara et al., 1973)

Fig. 3.2 shows a line crack $(-a \le x \le a)$ in an infinite elastic plate. Normal traction p is applied to part of the fracture from $x = b$ to $x = c$. The Westergaard's solution, function $\mathrm{Z(z)}$ for Mode I fracture is given as (Tara et al., 1973)

$$Z(\mathrm{z}) = \frac{1}{\pi} p \left\{ \begin{array}{c} sin^{-1}\dfrac{a^2 - cz}{a(z-c)} - sin^{-1}\dfrac{a^2 - bz}{a(z-b)} \\ + \dfrac{sin^{-1}\dfrac{c}{a} - sin^{-1}\dfrac{b}{a}}{\sqrt{1-\left(\dfrac{a}{z}\right)^2}} - \dfrac{\sqrt{a^2-c^2} - \sqrt{a^2-b^2}}{\sqrt{z^2-a^2}} \end{array} \right\} \tag{3.12}$$

And the imaginary part of $\bar{Z}(z)$ is:

$$Im\left(\bar{Z}(z)\right) = \frac{1}{\pi}p\left\{\begin{matrix}(c-x)cosh^{-1}\dfrac{a^2-cx}{a|x-c|} - (b-x)cosh^{-1}\dfrac{a^2-bx}{a|x-b|} \\ +(sin^{-1}\dfrac{c}{a} - sin^{-1}\dfrac{b}{a})\sqrt{a^2-x^2}\end{matrix}\right\} \quad (3.13)$$

Finally, the stress intensity factor and the fracture width profile due to the partial load from $x = b$ to $x = c$ are

$$K_{I_{\pm a}} = \frac{1}{\pi}p\sqrt{\pi a}\left[sin^{-1}\frac{c}{a} - sin^{-1}\frac{b}{a} \mp \left(\sqrt{1-\left(\frac{c}{a}\right)^2} - \sqrt{1-\left(\frac{b}{a}\right)^2}\right)\right] \quad (3.14)$$

$$w_f(x)_{|x|\le a} = \frac{2(1-v)}{G}Im\left(\bar{Z}(z)\right) \quad (3.15)$$

For the special case of uniform net pressure in the fracture (when $b = -a$ and $c = a$), Eq.3.15 reduces to the Sneddon and Elliot's (1946) solution:

$$w_f(x) = \frac{4p}{E'}\sqrt{a^2-x^2} \quad (3.16)$$

Where E' is the plane strain Young's Modulus. Further uses of the Westgaard's function includes the evaluation of stress intensity factor for Mode II and III cracks (Tara et al., 1973).

Now, for a line crack ($-a \le x \le a$) in an infinite elastic plate subjected to normal traction p from $x = b$ to $x = c$, we can calculate the stress intensity factor at fracture tips and the fracture width profile using Equation 3.14 and 3.15. These analytical solutions are exact.

3.2.1.2. Solution for Multiple Layers and Validation

The solutions introduced in the last section applies for a fracture subjected to load in one reservoir layer. These solutions can be superposed to calculated stress intensity factor and fracture width profile due to loads in multiple layers.

The equilibrium fracture height is calculated using the criteria

$$K_{I_{\pm a}} = K_{I_c} \tag{3.17}$$

Where $K_{I_{\pm a}}$ is the calculated stress intensity factor at the fracture tips, and K_{I_c} is the local critical stress intensity factor of the material.

The calculated equilibrium fracture height is validated with the results of Fung et al. (1987). They used both analytical and finite element method to solve fracture equilibrium height in asymmetrically layered formation. The analytical method assumes constant Young's Modulus while the finite element method allows the Young's Modulus to vary for each layer. Their results show that the Young's Modulus contrast is not a significant containment mechanism for fracture height. The analytical solution is very accurate even for the modulus contrast as large as 5.

We were able to repeat their fracture containment calculation with the same parameters as shown in Table 3.1. The critical stress intensity factor is assumed to be 0. And the results are shown in Fig. 3.3.

Layer Description	Thickness(m)	E/E_{pay}	Stress in Layer (MPa)	
			Case 1	Case 2
Lower Layer	∞	2	5	10
Pay	100	1	0	0
First Upper Layer	60	2	5	5
Second Upper Layer	∞	2	10	10

Table 3.1: Parameters for the fracture height containment validation case.

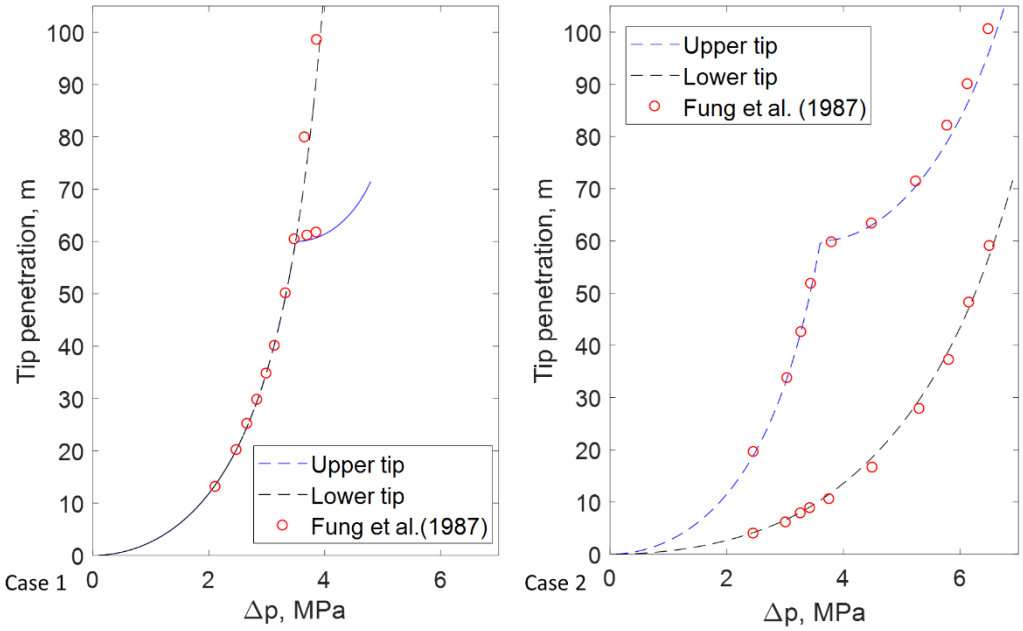

Figure 3.3: Validation of fracture height calculation.

The fracture width calculation is validated with the integral method (England & Green, 1963) and the 2D Displacement Discontinuity Method (DDM) (Crouch & Starfield, 1983). The integral method assumes symmetric pressure with respect to the center of the fracture. The 2D DDM method and the superposition method can be applied to arbitrary pressure distribution.

For the validation case, six symmetric layers of non-uniform pressure are applied to the fracture. And the fracture width is calculated with all three methods. The Young's modulus is 3 MMpsi, the Poisson's ratio is 0.25, and the total fracture height is 60.96 m. The fracture width profile is plotted in Fig. 3.4. As shown in the figure, the fracture width profile calculated with the three methods agrees well with each other.

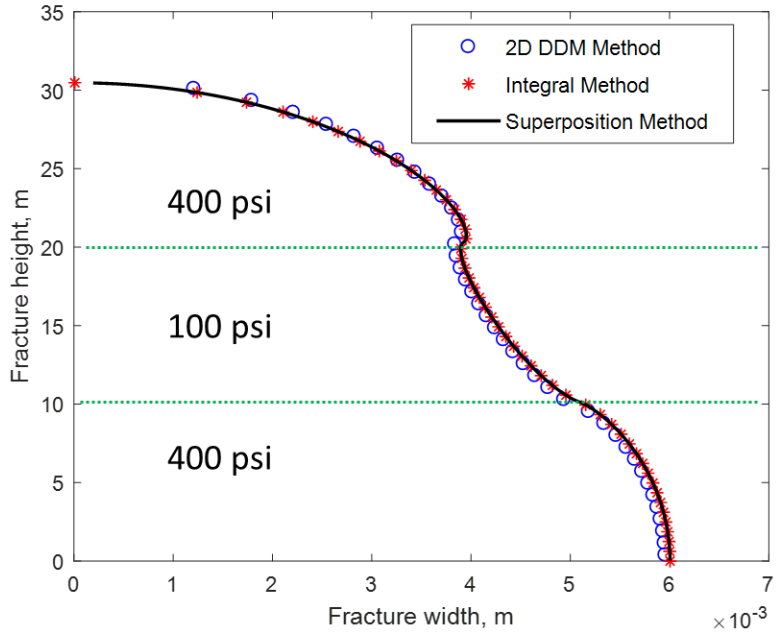

Figure 3.4: Validation of fracture width profile calculation.

3.2.1.3. Computational Efficiency of the Solution

The superposition method developed in the last section is very fast compared to the 2D DDM method and the integral method for solving the same problem. All three methods are solved with MATLAB. The interaction coefficient matrix of DDM is inverted using the backslash operator.

Fig. 3.5 plots the comparison of computation time of the three methods versus the number of layers. The number of elements is set to be constant for all cases (2048 elements). It is shown that the 2D DDM and the superposition method are not sensitive to the number of layers if the number of elements is constant, while the integral method takes longer as the number of layers increases even with a constant number of elements. The superposition method is much faster than the other two methods.

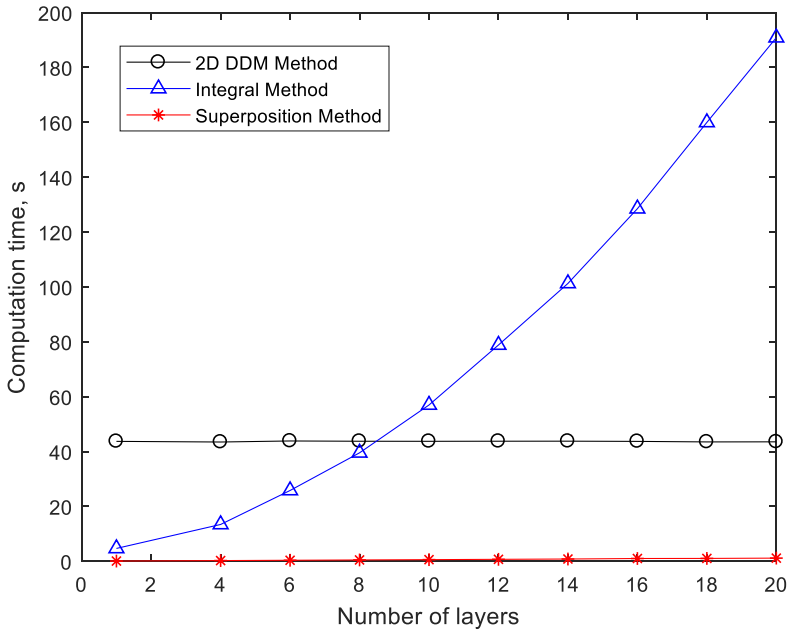

Figure 3.5: Computation time versus the number of layers for the superposition, 2D DDM, and the integral method.

Fig. 3.6 plots computation time of the three methods versus the number of elements. It is shown that for all three methods, computation time increases with the number of elements, and the 2D DDM method has the steepest slope. Both axes are on 10-based log scales. For three to four thousand elements, the superposition method is about 1000 times faster than the 2D DDM method.

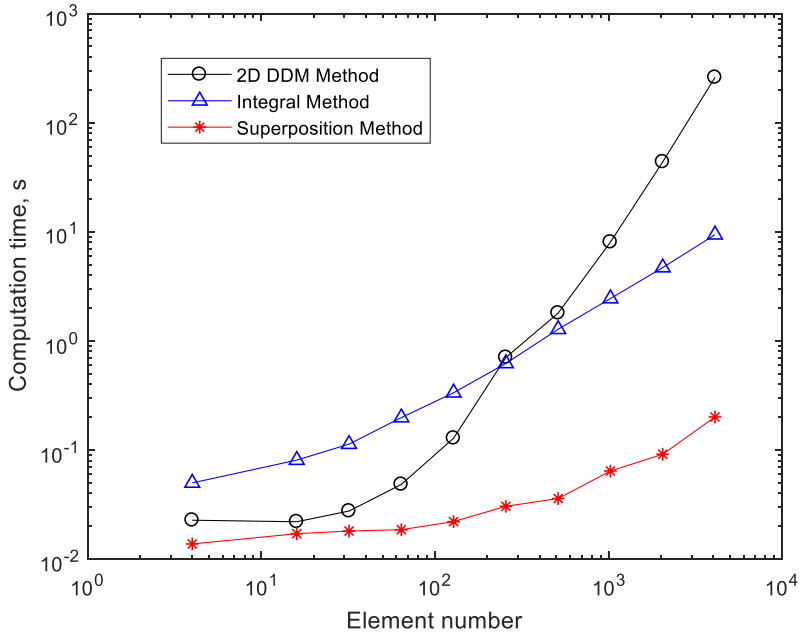

Figure 3.6: Computation time versus the number of elements for the superposition, 2D DDM, and the integral method.

3.2.1.4. Validity of the Plane Strain Assumption

The Pseudo-3D fracture model assumes plane strain. This assumption means that the fracture cells are decoupled laterally, and the fracture width profile of each cell is only dependent on the local net pressure profile in the same cell. For fully 3D solutions, fracture width at any point of the fracture is calculated considering the pressure distribution everywhere in the fracture. In other words, fully 3D solutions are vertically and laterally coupled.

A study has been performed to test the validity of the plane strain assumption of the Pseudo-3D fracture model. The fracture width profile is calculated for the same set of parameters using the Pseudo-3D model, the open source fully 3D finite volume model

(Cardiff et al., 2015; Manchanda et al., 2016; Hwang et al., 2018), and a fully 3D DDM model (Shrivastava et al., 2017).

The fracture is rectangular. In the first case, the fracture length to height ratio is 10:1, with fracture length being 100 meters (tip to tip) and fracture height being 10 meters. In the second case, the fracture length to height ratio is 1:1, with both fracture length and height being 10 meters. Symmetric, linear net pressure is applied to the fracture with 100 psi at the fracture center and 0 psi at fracture tips.

The results from the three different methods are summarized in Fig. 3.7. The plot on the top of Fig. 3.7 shows results for fracture length to length ratio being 10 and the plot on the bottom shows results for the ratio being 1. The three groups of fracture width profile curves on both plot correspond to fracture width close to fracture tip (the group of curves on the left), close to the center of one fracture wing (the group of curves in the middle), and close to the center of the fracture (the group of curves on the right).

When the fracture length is much larger than the fracture height, the fracture width profile calculated using the Pseudo-3D method, with the plane strain assumption, is quite accurate compared to the fully 3D solutions. The maximum difference between the Pseudo-3D solution and the fully 3D finite volume solution is smaller than 1%. On the other hand, when the fracture length is close to the fracture height, the Pseudo-3D model overestimates the fracture width compared to the fully 3D solution.

This conclusion is consistent with the observation of some other researchers (Barree, 1983; Economides & Nolte, 1989; Valko & Economides, 1995). When the fracture length is close to the fracture height, the plane strain assumption overestimates the fracture width because it sees the restrictive effect of fracture tips on the height direction, while it does not see the restriction from the fracture length direction (Barree, 1983). When the fracture length is much longer than the fracture height, this effect decreases and the fracture

width calculated with the plane strain assumption gets closer to the fully 3D solutions. As a rule of thumb, for fractures with length (tip to tip) versus height ratio larger than 3, the results from the plane strain assumption is fairly accurate (Economides & Nolte, 1989).

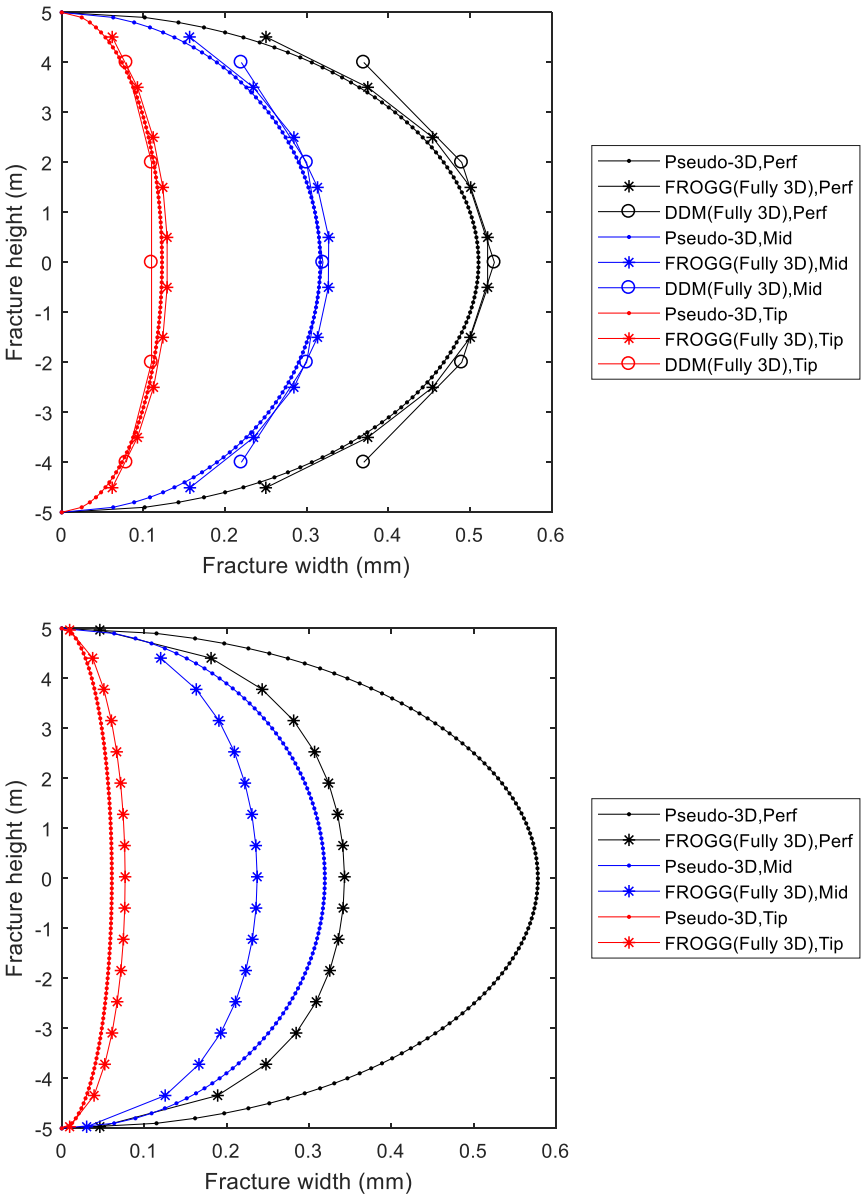

Figure 3.7: Validity of the plane strain assumption. The length to height ratio is 10:1 (top) and 1:1 (bottom) respectively.

In fact, the pressure-displacement calculation is the most computationally expensive part of fully 3D fracture models. A large fraction of computation time is spent on this calculation. The Pseudo-3D method solves the fracture width profile within a small fraction of computation time compared to fully 3D models and gets almost accurate solutions. This is a big advantage for the Pseudo-3D fracture model in terms of computational efficiency and makes it suitable for everyday industrial use.

3.2.2. Governing Equations for Pseudo-3D Fracture Propagation

In the last section, we showed how the Pseudo-3D fracture model calculates fracture height and width profile under arbitrary load (multiple layers). In this section, we present the governing equations of the cell-based Pseudo-3D fracture model.

The fracture is discretized as a series of connected cells, as shown in Fig. 3.1b. Plane strain is assumed, and each vertical cross-section of the fracture acts independently in terms of pressure-displacement relation.

Given the reservoir properties (with multiple layers), the pumping schedule and the fluid and proppant properties, the Pseudo-3D fracture model simulates the dynamic evolution of the fracture and the treatment pressure by solving all the governing equations simultaneously.

The main assumptions of the Pseudo-3D fracture model include:

1. Planar fracture;
2. Plane strain;
3. Homogeneous mechanical properties (Young's Modulus and Poisson's Ratio);
4. Incompressible fluid and proppant.

5. The fracture model is able to account for power-law fluid. But the proppant transport model and the Proppant Transport Efficiency (PTE) correlations (Chapter 5) are limited to Newtonian fluids.

The governing equations for the Pseudo-3D fracture model are summarized below. All the equations are in SI units.

3.2.2.1. Local Fluid Mass Balance.

The local fluid mass balance is satisfied at each fracture cell. Considering fracture volume change, leak off and flow rate change, the local mass balance equation for incompressible fluid can be written as

$$\frac{\partial Q}{\partial x} + \frac{\partial A}{\partial t} + u_L H = 0 \tag{3.18}$$

Where Q is flow rate in one wing of the fracture, A is the cross-sectional area, u_L is the velocity of fluid leaking off from both walls per unit height of fracture, and H is fracture height. The cross-sectional area A is calculated by integration of the fracture width profile

$$A(x,t) = \int_{-\frac{H}{2}}^{\frac{H}{2}} w_f(x,z,t)dz \tag{3.19}$$

3.2.2.2. Fluid Momentum Equation.

The fluid momentum equation inside the fracture is derived by considering the fracture cross section as a combination of slit flow ducts (Perkins & Kern, 1961; Nolte, 1979). The derivation is explained below.

For power law fluids, the relation between shear stress and shear rate is

$$\tau = k\left(-\frac{du}{dy}\right)^n \tag{3.20}$$

Where τ is shear stress, u is fluid velocity, k is the flow consistency index and n is the flow behavior index.

For isothermal, steady, uniform, laminar flow of incompressible power-law fluid between parallel plates as shown in Fig. 3.8, the force balance can be expressed as:

$$y\Delta P = L\tau \tag{3.21}$$

Equation 3.21 shows that the force per unit height acting towards the right on the fluid element of thickness y and length L may be equated to the force per unit height acting towards the left.

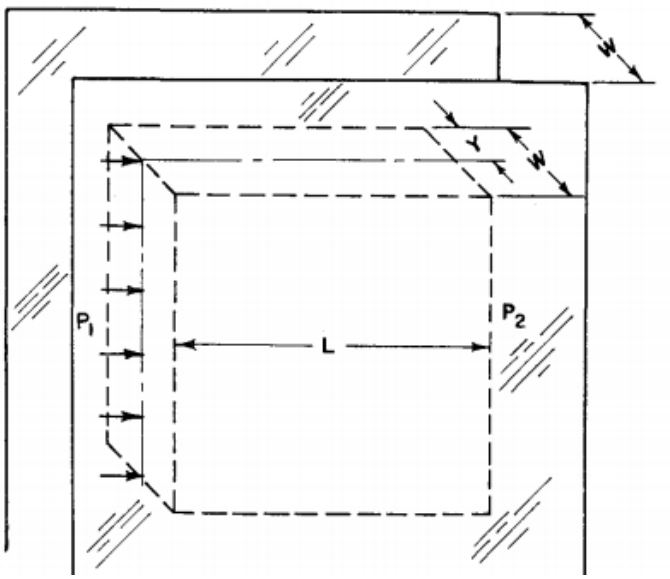

Figure 3.8: Illustration of laminar flow between two plates. (Perkins & Kern, 1961)

Substitute Equation 3.20 into 3.21

$$\frac{\partial u}{\partial y} = -\left(\frac{y\Delta P}{kL}\right)^{\frac{1}{n}} \tag{3.22}$$

Integrate Equation 3.22, with velocity being zero at the wall, we get Equation 3.23

$$u = \frac{n}{n+1}\left(\frac{\Delta P}{kL}\right)^{\frac{1}{n}}\left[\left(\frac{w}{2}\right)^{\frac{n+1}{n}} - y^{\frac{n+1}{n}}\right] \tag{3.23}$$

Integrate Equation 3.23 to get flow rate per unit height of the channel

$$q = 2\int_0^{\frac{w}{2}} u dy = \frac{n}{2(2n+1)}\left(\frac{w^{2n+1}}{2k}\frac{\partial P}{\partial x}\right)^{\frac{1}{n}} \tag{3.24}$$

Equation 3.24 applies for fracture cross section of parallel walls with distance w per unit height. For fracture cross section considered as a combination of several slit flow ducts, we can integrate Equation 3.24 with two assumptions: 1). *k* and *n* are constant across the vertical section, and 2). *dp/dx* is constant across the vertical section.

$$Q = \int_{-\frac{H}{2}}^{\frac{H}{2}} q dy = \frac{n}{2(2n+1)}\left(\frac{1}{2k}\frac{dP}{dx}\right)^{\frac{1}{n}}\int_{-\frac{H}{2}}^{\frac{H}{2}} w^m dy \tag{3.25}$$

We further define functions $m(n)$, $\varphi(x,n)$ and $M(m,\varphi(x,n))$ to simplify and re-organize Equation 3.25

$$\frac{dP}{dx} = -\frac{2kM(x,n)(Q)^n}{w(x,avg)^{2n+1}} \tag{3.26a}$$

$$m = \frac{2n+1}{n} \tag{3.26b}$$

$$M = \left(\frac{2m}{\varphi(x,n)}\right)^n \tag{3.26c}$$

$$\varphi(x,n) = \int_{-\frac{H}{2}}^{\frac{H}{2}} \left(\frac{w(x,z)}{w(x,avg)}\right)^m dz \tag{3.26d}$$

Where $\varphi(x,n)$ is the fracture shape factor (dimensionless).

Equation 3.26 is used to solve for the fluid pressure drop in the Pseudo-3D fracture.

3.2.2.3. Fluid Leak-Off Equation.

The fluid leak-off calculation is similar to that of Chapter 2, except that non-uniform rock flow properties (formation porosity and permeability) and reservoir fluid properties (reservoir fluid viscosity and compressibility) are considered for the Pseudo-3D fracture model. It is assumed that the leak-off into each formation layer is independent. For

each layer, leak off coefficient and leak off velocity is calculated using the same equations as in Chapter 2. And the total leak-off volume is the summation of leak-off into each formation layer.

3.2.2.4. Pressure and Fracture Height and Width Relation.

The equilibrium fracture height and width profile are calculated using the superposition method introduced in the last section. In the Pseudo-3D fracture simulation, a table of fracture geometry solutions (fracture height and width versus fluid pressure in the fracture) can be calculated prior to the simulation of fracture propagation. And table lookup, rather than solving the solid mechanics equation during the simulation, can greatly speed up the fracture propagation simulation.

3.2.2.5. Total Fluid Mass Balance.

The four governing equations introduced above applies to each cell. The total fracture length L_f can be determined by the total fluid mass balance. For incompressible fluids, the total fluid mass balance states that the injected fluid volume is equal to the fracture volume and the total leak-off volume. The total fluid mass balance is described by Equation 3.27.

$$\int_0^{L_f(t)} A(x,t)dx + \int_0^t \int_0^{L_f(t')} u_L(x,t')\,H(x)dxdt' = \int_0^t Q_o(t')dt' \qquad (3.27)$$

Where Q_o is the injection fluid rate for one wing of the fracture.

3.2.2.6. Initial and Boundary Conditions.

The initial condition for the Pseudo-3D fracture is given in Equation 3.28. And the boundary conditions are given in Equation 3.29.

$$L_f(t=0)=0 \tag{3.28a}$$

$$P_{net}(x,t=0)=0 \tag{3.28b}$$

$$Q(x=0,t)=Q_o(t);\ \ (t>0) \tag{3.29a}$$

$$P_{net}\big(x=L_f(t),t\big)=0;\quad (t>0) \tag{3.29b}$$

Now, the five governing equations: (1) solid mechanics solution of fracture width and height (Equation 3.14 and 3.15); (2) the local fluid mass balance (Equation 3.18); (3) the fluid momentum equation (Equation 3.26); (4) the carter's leak off calculation; and (5) the total mass balance equation (Equation 3.27), together with the initial and boundary conditions (Equation 3.28 and 3.29), consist of a complete mathematical model to calculate the propagation of a Pseudo-3D fracture.

3.2.3. Simulation of Proppant Transport in the Pseudo-3D Fracture

During the hydraulic fracturing process, the slurry (a mixture of fluid and proppant) is injected from the wellbore into the fracture. As the slurry flows towards the tip of the fracture, proppant settles downwards due to gravity. A mound of proppant starts to develop at the bottom of the fracture. And as the proppant mound grows, the height of the slurry region decreases, the slurry flow velocity increases, and more proppant gets transported further in the fracture. The proppant bank grows higher and spreads laterally until it reaches an equilibrium state with the slurry flow above it. Fig. 3.9 shows an illustration of this process.

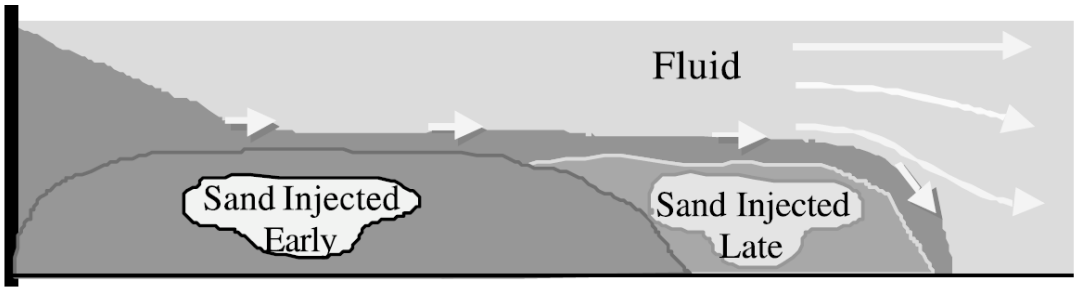

Figure 3.9: Illustration of proppant transport and proppant bank development in a fracture. (Patankar et al., 2002)

We try to simulate the proppant transport and the proppant bank development in the fracture by assuming two regions in each fracture cell: the slurry region and the settled proppant bed region as shown in Fig. 3.10. The slurry flow is solved on moving mesh fracture cells, and the settled proppant bank is solved on a separate, fixed mesh. In the slurry region, the proppant concentration is assumed to be uniform.

The proppant transport and placement in the Pseudo-3D fracture is calculated by solving the local mass conservation and momentum balance of the slurry, and the volumetric distribution of proppant. The "slip" between the proppant and the carrying fluid includes (1) proppant settling, (2) proppant retardation, and (3) proppant bridging when fracture width is narrow (usually near the fracture tip).

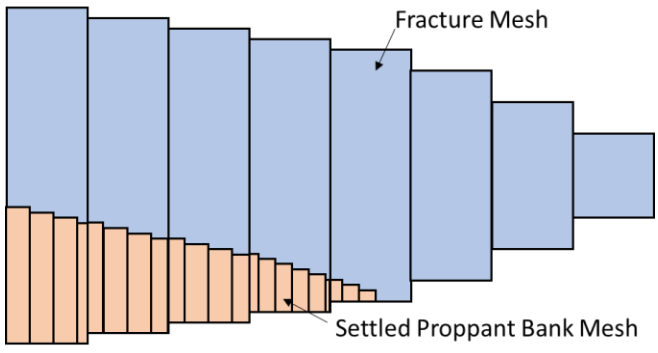

Figure 3.10: Illustration of the fracture mesh and the proppant bank mesh.

3.2.3.1. Local Mass Balance for Slurry and Proppant.

For every fracture cell, the local slurry and proppant mass balance equation for the slurry region can be written as

$$\frac{\partial A}{\partial t} + \frac{\partial Q_s}{\partial x} + u_L H = 0 \tag{3.30}$$

$$\frac{\partial A' \overline{\emptyset}}{\partial t} + \frac{\partial Q_p}{\partial x} = 0 \tag{3.31}$$

Where A is the vertical cross-sectional area of the fracture. Q_s and Q_p are the volumetric flow rate of the slurry and the proppant respectively. A' is the cross-sectional area for the slurry region, which is equal to the fracture cross sectional area minus the settled bank cross sectional area. $\overline{\emptyset}$ is the averaged proppant volume concentration normalized by maximum proppant volume concentration (i.e. $\emptyset_{\max} = 0.585$) as shown below ($\overline{\emptyset} \in [0,1]$).

$$\overline{\emptyset} = \frac{\emptyset_{avg}}{\emptyset_{\max}} = \frac{2}{w} \int_0^{\frac{w}{2}} \frac{\emptyset}{\emptyset_{\max}} dz \tag{3.32}$$

The volumetric flow rate of slurry (Q_s) and proppant (Q_p) are functions of pressure gradient, proppant concentration, proppant size, fracture width and so on. The same model as in Chapter 2 (Dontsov & Peirce, 2014) is applied to calculate Q_s and Q_p. It is a constitutive continuum model that describes a smooth transition from Poiseuille flow to Darcy flow when proppant concentration increases from low to high. Please refer to Chapter 2 for the details of the model and the calculation of Q_s and Q_p.

3.2.3.2. Modeling the Settled Proppant Bank

The settled proppant bank grows until it reaches an equilibrium with the slurry flow above it. The equilibrium height of the proppant bank is a function of fluid and proppant

density, proppant diameter, fracture width and so on. Wang et al. (2003) developed empirical correlations for the equilibrium proppant bank height between two parallel plates. Four dimensionless parameters are defined to describe the problem.

The Gravity Reynolds number:

$$R_G = \frac{\rho_f[\rho_p - \rho_f]gd^3}{\mu^2} \tag{3.33}$$

Where ρ_f is the fluid density, ρ_p is the proppant density, g is the gravitational acceleration, d is the particle diameter and μ is the fluid viscosity.

The Fluid Gravity Reynolds number:

$$R_{FG} = \frac{\frac{\mu}{\rho_f}}{w_f^{3/2}\sqrt{g}} \tag{3.34}$$

Fluid Reynolds number:

$$R_F = \frac{\rho_f Q}{w\mu} \tag{3.35}$$

Proppant Reynolds number:

$$R_P = \frac{\rho_p Q_p}{w\mu} \tag{3.36}$$

For erosion case, where the clean fluid is injected, the equilibrium proppant bank height can be written as:

$$H_{equil} = H - w * a(R_G)R_F^{m(R_G)} \tag{3.37}$$

Values of $a(R_G)$ and $m(R_G)$ are summarized in Table 3.2.

	Range of R_G		
	86.8	521-2.03×10^4	1.00×10^5
$\boldsymbol{a(R_G)}$	0.0294	9.36×10^{-4}	5.52×10^{-4}
$\boldsymbol{m(R_G)}$	0.618	0.914	0.878

Table 3.2: Values of $a(R_G)$ and $m(R_G)$ for the erosion case. (Wang et al., 2003)

For bed load transport case, where slurry (with proppant concentration > 0) is injected, the equilibrium proppant bank height can be written as:

$$H_{equil} = H - w_f * c_1(R_G) R_F^{m_1(R_G)} R_P^{n_1(R_G)} \tag{3.38}$$

Where $c_1(R_G)$, $m_1(R_G)$ and $n_1(R_G)$ are functions of R_G as shown below:

$$c_1(R_G) = -2.30 \times 10^{-4} \ln(R_G) + 2.92 \times 10^{-3} \tag{3.39}$$

$$m_1(R_G) = 1.2 - 1.26 \times 10^{-3} R_{FG}^{-0.428} [15.2 - \ln(R_G)] \tag{3.40}$$

$$n_1(R_G) = -0.0172 \ln(R_G) - 0.120 \tag{3.41}$$

When the proppant bed height is smaller than the equilibrium bank height, proppant settles, and the proppant bank grows. The deposition velocity ($V_{Deposition}$) is calculated from proppant settling velocity ($u_{settling}$). Liu (2006) proposed a corrected proppant settling velocity modifying the stokes settling velocity (u_{Stokes}) to include inertial, concentration and wall effects. The corrected correlation for proppant settling velocity is

$$u_{settling} = u_{Stokes} \left(\frac{a_s \mu^{0.57}}{\rho_f^{0.29} (\rho_P - \rho_f)^{0.29} d^{0.86}} \right) (1 - 4.8\overline{\emptyset} + 8.8\overline{\emptyset}^2 - 5.9\overline{\emptyset}^3) \left[1 - 1.563 \left(\frac{d}{w_f} \right) + 0.563 \left(\frac{d}{w_f} \right)^2 \right] \tag{3.42}$$

$$u_{Stokes} = \frac{d^2 (\rho_P - \rho_f) g}{18\mu} \tag{3.43}$$

And the proppant deposition velocity is

$$V_{Deposition} = u_{settling} * w_f * dx * \emptyset_{avg} \tag{3.44}$$

The parameter a_s in Equation 3.42 is a constant for unit conversion purpose. For SI units, the value of a_s is 1.4535.

3.2.4. Meshing Algorithm

The five governing equations and the proppant transport equations presented in previous sections need to be solved simultaneously with a moving boundary, in order to

simulate the Pseudo-3D fracture evolution. The mesh can either be fixed or moving. As the fracture propagates, the discretization along the fracture length direction needs to be updated by either re-meshing or adding new elements.

In this work, we adopt the explicit finite-difference method with a grid that moves at a reasonable speed so that the fracture is always divided into a fixed number of elements (the stretching coordinate system). The advantage of using this mesh is that the number of computational elements for one fracture remains constant as the fracture propagates. Compared to re-meshing or adding new elements every time step, the moving mesh algorithm keeps the simulation efficient. The explicit moving mesh algorithm is suitable for solving non-linear, moving boundary problems like fracture propagation.

One of the primary limitations of the explicit scheme is that the time step may not exceed a critical value to keep the calculation stable. This limitation can be eliminated by adopting implicit schemes with no time step restriction. However, for non-linear problems like fracture propagation, the non-linear system needs to be linearized and the error introduced by linearization needs to be corrected and re-calculated. Iterations are frequently required. Using implicit methods to solve such non-linear problem can be complex and not always much more computationally efficient than explicit methods. It will be shown later in this Chapter that a small number of elements (about 10 to 20) is enough to capture the evolution of the Pseudo-3D fracture accurately with the explicit method.

The fracture propagation and proppant transport in the longitudinal direction (fracture length direction) is solved with the explicit moving mesh algorithm. And a secondary, fixed mesh is used to store the settled proppant bank. This mesh is uniform, and elements are added as the fracture propagates and as the proppant bank develops.

Before the simulation start, a table of the fracture pressure-width-height relation is obtained using the solid mechanics solution. During the simulation, the fracture width,

height, and pressure relations are calculated by a table lookup. This is a way to speed up the Pseudo-3D fracture modeling (Economides & Nolte, 1989).

3.2.4.1. Moving Mesh for Fracture Propagation

The governing equations are reformulated with a moving coordinate θ

$$\theta = \frac{x}{L_f(t)}, \quad (0 \le \theta \le 1) \tag{3.45}$$

In the θ coordinate, a constant number of nodes at fixed locations can be used throughout the simulation.

The dimensionless fracture length $0 \le \theta \le 1$ is discretized into N nodes with either a uniform mesh or a geometric progression that refine the mesh at the tip of the fracture. The first node is at the perforation (Node 1), and the last node is the fracture tip (Node N). Variables including $P_f(\theta_i, t), w_f(\theta_i, t), H(\theta_i, t), A(\theta_i, t), \tau(\theta_i, t), u_L(\theta_i, t)$ are stored at fracture nodes 1 to N. And a system of N-1 auxiliary nodes at the center of fracture cells (i+1/2) is introduced for flow rate in the fracture $Q_s\left(\theta_{i\pm\frac{1}{2}}, t\right)$, $Q_p\left(\theta_{i\pm\frac{1}{2}}, t\right)$ and proppant concentration $\overline{\emptyset}\left(\theta_{i\pm\frac{1}{2}}, t\right)$.

All variables are now expressed in terms of time t and dimensionless coordinate θ. The conversion of the partial differential equations from x to θ

$$\left.\frac{\partial}{\partial x}\right|_t = \frac{1}{L_f}\left.\frac{\partial}{\partial \theta}\right|_t \tag{3.46}$$

$$\left.\frac{\partial}{\partial t}\right|_x = \left.\frac{\partial}{\partial t}\right|_\theta - \theta\frac{\dot{L_f}}{L_f}\left.\frac{\partial}{\partial \theta}\right|_t \tag{3.47}$$

Where $\dot{L}_f$ is the fracture propagation rate ($\dot{L_f} = \frac{dL_f}{dt}$).

The equations transformed on the dimensionless coordinate θ is summarized below

$$\frac{1}{L_f}\frac{dP}{d\theta} = -\frac{2kM(\theta, n)(Q)^n}{w(\theta, avg)^{2n+1}} \tag{3.48}$$

$$\dot{A} = \frac{\theta \dot{L_f}}{L_f}\frac{\partial A}{\partial \theta} - \frac{1}{L_f}\frac{\partial Q_s}{\partial \theta} - u_L H \tag{3.49}$$

$$u_L = \frac{2C_l}{\sqrt{t - \tau(\theta)}} \tag{3.50}$$

$$\int_0^t Q_o(t')dt' = L_f \int_0^1 A(\theta, t)d\theta + \int_0^t L_f(t') \int_0^1 Q_L(\theta, t')\, d\theta dt' \tag{3.51a}$$

$$\dot{L_f} = \frac{L_{f,t+dt} - L_{f,t}}{dt} \tag{3.51b}$$

3.2.4.2. Secondary Fixed Mesh for Settled Proppant Bank

At each time step, fracture propagation is determined prior to the proppant transport calculation. When solving for proppant distribution in the fracture, the fracture geometry is fixed. And the proppant transport calculation is done in two steps. First, the local mass balance of proppant is solved on the moving fracture mesh, to get the updated proppant volumetric concentration distribution in the fracture. And then, proppant settling is solved, and the proppant transport between the slurry region and the proppant bank region is calculated.

For the first step, the local proppant mass balance equation is re-formulated to the θ coordinate

$$\frac{\partial(A'\overline{\emptyset})}{\partial t} - \theta\frac{\dot{L_f}}{L_f}\frac{\partial\left(A'\overline{\emptyset}\right)}{\partial \theta} + \frac{1}{L_f}\frac{\partial Q_p}{\partial \theta} = 0 \tag{3.52}$$

Where *A'* is the cross-sectional area for the slurry region.

A similar upwind scheme as that in Chapter 2 is used to solve Equation 3.52. The definition of "Wind" and "Velocity", and the interpolation of the proppant volumetric flow rate is the same, except that the fracture width (w_f) in Chapter 2 is replaced with the cross-sectional area for the slurry region (A').

Next, proppant settling is solved. The settled proppant bank mesh is fixed and uniform. As the fracture propagates, new elements are added to the proppant bank mesh.

Parameters including settled proppant volume and mass, proppant bank height and so on are stored in the proppant bank mesh.

At every time step, after solving equation 3.52, the updated proppant volumetric concentration is interpolated from the fracture mesh to the proppant bank mesh. Then, the equilibrium proppant bank height is calculated with Equation 3.37 or 3.38 depending on the injection condition. If the height of the proppant bank has not reached the equilibrium height, the proppant deposition rate is calculated with Equation 3.44. The deposited proppant is transported from the slurry to the settled proppant bank. The height of the proppant bank, and the proppant concentration in the slurry are updated.

3.2.5. Solving Algorithm

3.2.5.1. Fracture Initialization

The initialization of the fracture is similar to that in Chapter 2. The Pseudo-3D fracture is initialized using the analytical solution of Nordgren (1972) at a small time step.

Initialize fracture length at a small time ($t_{initial}$)

$$L(t_{initial}) = 0.68\left[\frac{GQ_{inj}^3}{(1-\nu)\mu h_f^4}\right]^{\frac{1}{5}} {t_{initial}}^{\frac{1}{4}} \qquad t_{initial}$$

Initialize fracture width at a small time

$$w_f(0, t_{initial}) = 2.5\left[\frac{(1-\nu)\mu Q_o^2}{GH}\right]^{\frac{1}{5}} {t_{initial}}^{\frac{1}{5}} \tag{3.54}$$

Initialize fracture net pressure

$$P_{net}(0, t_{initial}) = 2.5\left[\frac{G^4\mu Q_o^2}{(1-\nu)^4 H^6}\right]^{\frac{1}{5}} {t_{initial}}^{\frac{1}{5}} \tag{3.55}$$

And the initial fracture propagation speed:

$$\dot{L_f}(t_{initial}) = 0.17\left[\frac{GQ_o^3}{(1-\nu)\mu H^4}\right]^{\frac{1}{5}} {t_{initial}}^{-\frac{3}{4}} \tag{3.56}$$

For the PKN-Type fracture in Chapter 2, the fracture height is the height of the reservoir layer. For the Pseudo-3D fracture model, the fracture height used for the initialization is the minimum fracture height between two bounding layers. In other words, the initial fracture height is between the closest layers above and below the perforation with minimum horizontal stress larger than that of the perforated layer.

3.2.5.2. Stability of the Simulation

The time step of the explicit finite-difference scheme cannot exceed a critical value to ensure the stability of the simulation. And in this section, we try to determine the expression for the critical time step.

The local slurry mass balance equation, the fluid momentum equation, and fracture pressure-width-height relation form the stiff part of the problem, which requires a time step restriction $\Delta t \sim O(\Delta\theta^3)$, while the proppant transport equation is less stiff and requires a time step restriction $\Delta t \sim O(\Delta\theta)$ (Dontsov & Peirce, 2015). Therefore, von Neumann analysis is applied to find the critical time step (Ferziger & Peric, 2012) of the stiffer part of the problem.

Ignoring the leak-off term in the discretized local slurry mass balance equation (Equation 3.49), we get

$$\dot{A} = \frac{\theta \dot{L}_f}{L_f}\frac{\partial A}{\partial \theta} - \frac{1}{L_f}\frac{\partial Q_s}{\partial \theta} \tag{3.57}$$

We can get an estimation of the term $\frac{\partial Q_s}{\partial \theta}$ in Equation 3.57 from the slurry momentum equation (assume $\hat{Q}^s = 1$)

$$\frac{1}{L_f}\frac{dP}{d\theta} = -\frac{2kM(Q_s)^n}{w_{avg}^{2n+1}} = -2kMQ_s^n\left(\frac{H}{A}\right)^{2n+1} \tag{3.58}$$

We reformulate Equation 3.58 to get

$$Q_s = \left[-\frac{1}{2kML_f} \left(\frac{A}{H}\right)^{2n+1} \frac{dP}{d\theta} \right]^{\frac{1}{n}} \tag{3.59}$$

Assuming

$$\frac{dP}{d\theta} = c_p \frac{dA}{d\theta} \tag{3.60}$$

Where c_p is a dummy variable. Then Equation 3.59 becomes

$$Q_s = \left[-\frac{c_p}{2kML_f} \left(\frac{A}{H}\right)^{2n+1} \frac{dA}{d\theta} \right]^{\frac{1}{n}} \tag{3.61}$$

Substitute Equation 3.61 into Equation 3.57, we get

$$\dot{A} = \frac{\theta \dot{L_f}}{L_f} \frac{\partial A}{\partial \theta} + \frac{1}{L_f} \left(\frac{c_p}{2kML_f}\right)^{\frac{1}{n}} \left(\frac{1}{H}\right)^{2+\frac{1}{n}} \left[\left(2 + \frac{1}{n}\right) A^{1+\frac{1}{n}} \left(\frac{dA}{d\theta}\right)^{1+\frac{1}{n}} + \frac{1}{n} A^{2+\frac{1}{n}} \left(\frac{dA}{d\theta}\right)^{\frac{1}{n}-1} \left(\frac{d^2A}{d\theta^2}\right) \right] \tag{3.62}$$

We postulate that the stability condition can be assessed by the highest order term, then Equation 3.62 becomes

$$\dot{A} = \frac{1}{nL_f} \left(\frac{c_p}{2kML_f}\right)^{\frac{1}{n}} \left(\frac{A}{H}\right)^{2+\frac{1}{n}} \left(\frac{dA}{d\theta}\right)^{\frac{1}{n}-1} \left(\frac{d^2A}{d\theta^2}\right) + O(\frac{dA}{d\theta}) \tag{3.63}$$

Equation 3.63 can be simplified by the slurry momentum Equation 3.59 to get

$$\dot{A} = \frac{1}{nL_f} Q_s \left(\frac{dA}{d\theta}\right)^{-1} \left(\frac{d^2A}{d\theta^2}\right) + O(\frac{dA}{d\theta}) \tag{3.64}$$

Equation 3.64 is in the form of a diffusivity equation, and the critical time step is:

$$\Delta t_{critical}^{k+1} = \min \left[\frac{\Delta\theta^2 \left(\frac{dA}{d\theta}\right) nL_f}{2Q_s} \right]_i , \qquad i = 1,2,\dots,n \tag{3.65}$$

As the Pseudo-3D fracture propagates, the increase in the critical time step is usually an indication of a stable simulation.

3.2.5.3. Solving Algorithm

A table of the fracture pressure-width-height relation is obtained using the fundamental solid mechanics solution, prior to starting the simulation. In each time step, fracture propagation is determined before the proppant transport calculation. When solving for proppant distribution in the fracture, the fracture geometry is fixed. With known nodal quantities at time t^k, the following steps are followed to advance to t^{k+1}:

(1) Calculate stable time step Δt^{k+1} (Equation 3.65)

(2) Solve local slurry mass balance equation with Euler explicit finite difference scheme for updated cross-sectional area A^{k+1} (Equation 3.49)

(3) Look up the fracture pressure-width-height table for updated pressure P^{k+1}, fracture height h_f^{k+1}, and average fracture width w_f^{k+1}

(4) Calculate leak-off (Equation 3.50)

(5) Calculate fracture length and propagation rate (Equation 3.51)

(6) Update volumetric slurry and proppant rate (Equation 3.33, and 3.36)

(7) Solve local proppant mass balance equation in the slurry region for updated volumetric proppant concentration $\overline{\emptyset}^{k+1}$(Equation 3.52)

(8) Calculate proppant settling, update proppant bank height and volumetric proppant concentration in the slurry

These steps are repeated until the desired treatment time is complete.

3.3. RESULTS AND DISCUSSION

In this section, we first present the validation of the Pseudo-3D fracture model with published results. After that, we show a sensitivity study for mesh density. Finally, results showing proppant transport and settling in the fracture are presented.

3.3.1. Model Validation

The Pseudo-3D fracture model developed in this Chapter has been validated against the one presented by Dotsov and Peirce (2015). Parameters used for the validation case are summarized in Table 3.3. These parameters are not in the range of realistic field values. It is a synthetic case we use to validate the model. The results are shown in Fig. 3.11, and 3.12. A visualization of the fracture geometry is shown in Fig. 3.13. The simulated results agree well with the published results.

Parameter	Value	Parameter	Value
Young's Modulus (GPa)	3.3	Fluid Viscosity (Pa s)	30.2
Poisson's Ratio	0.4	Injection Rate (mm^3/s)	1.7
Reservoir Layer Height (m)	0.05	Injection Time (s)	604
Stress Barrier $\Delta\sigma$ (MPa)	4.3	K_{Ic} (MPa $m^{0.5}$)	0.16

Table 3.3: Parameters for the Pseudo-3D fracture validation case.

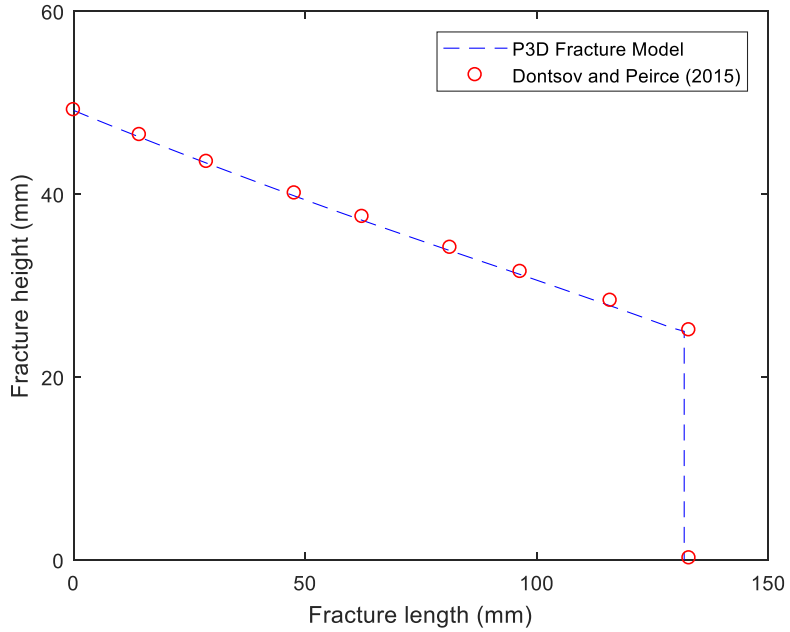

Figure 3.11: Fracture height versus fracture length for the P3D fracture validation case.

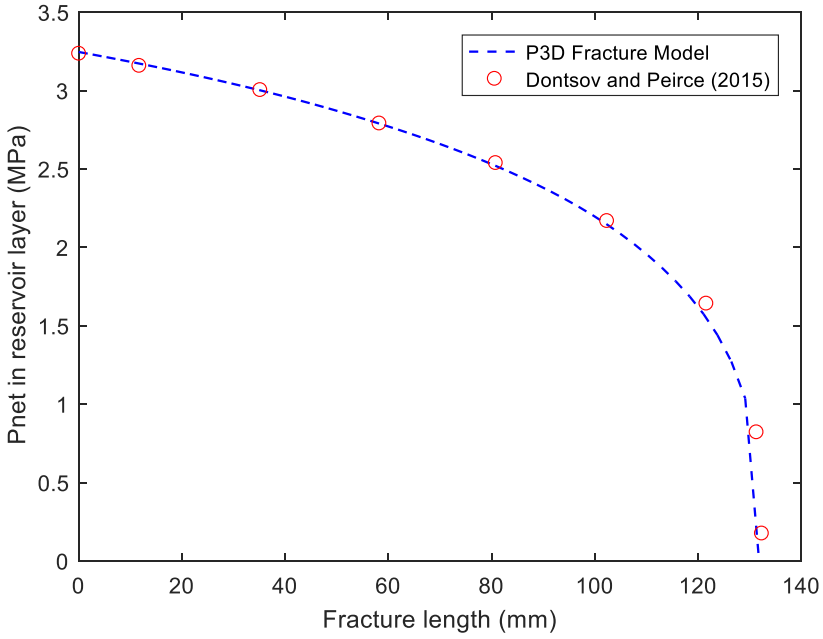

Figure 3.12: Net pressure in the fracture versus fracture length for the P3D fracture validation case.

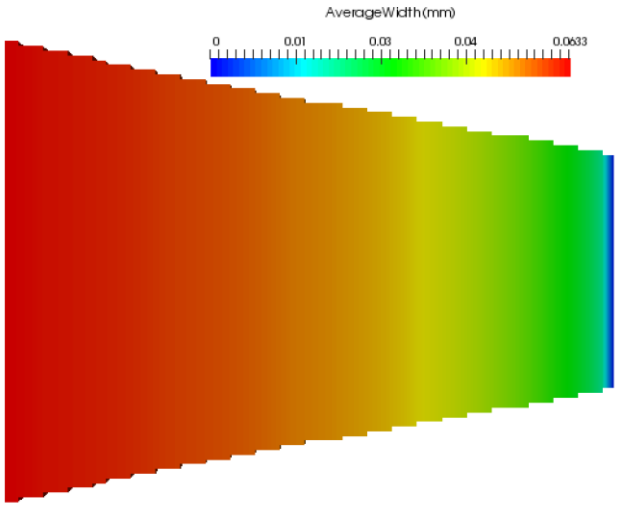

Figure 3.13: Visualization of the P3D fracture for the validation case.

3.3.2. Sensitivity of Mesh Density Study

A sensitivity study for mesh density has been performed to estimate the minimum number of elements needed for the Pseudo-3D fracture simulation. Parameters used for this study are summarized in Table 3.4, and the results are shown in Fig. 3.14 to Fig. 3.18. It is shown that the results calculated by using 11, 20, 40 and 60 nodes are fairly close to each other. However, the computation time increases a lot from 20 to 60 nodes. Therefore, the recommended number of nodes to use for the Pseudo-3D fracture is 11 to 20 nodes, to get a good estimation of fracture propagation with minimum computational cost.

Parameter	Value	Parameter	Value
Young's Modulus (GPa)	20.68	Reservoir Porosity	0.08
Poisson's Ratio	0.25	Res. Fluid Viscosity (cp)	5
Res. Layer Height (m)	30	Res. Fluid Comp. (Pa^{-1})	5e-10
Stress Barrier $\Delta\sigma$ (psi)	100	Fracturing Fluid Viscosity (cp)	1
K_{Ic} (Pa $m^{0.5}$)	1e6	Fracturing Fluid n	1
Res. P_{pore} (psi)	180	Injection Rate (bpm)	5
Res. Permeability (μD)	1	Injection Time (min)	10

Table 3.4: Parameters for the Pseudo-3D fracture mesh density study.

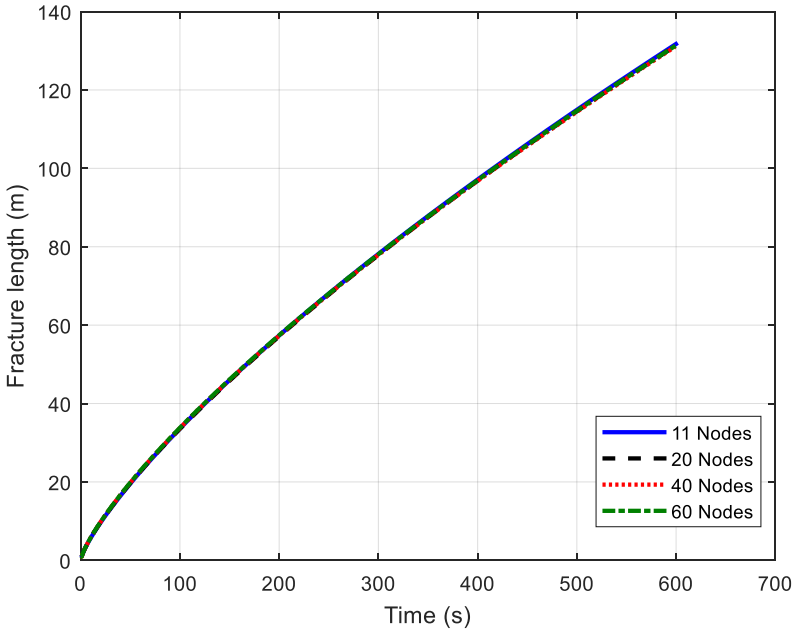

Figure 3.14: Fracture length history for the Pseudo-3D fracture mesh density study.

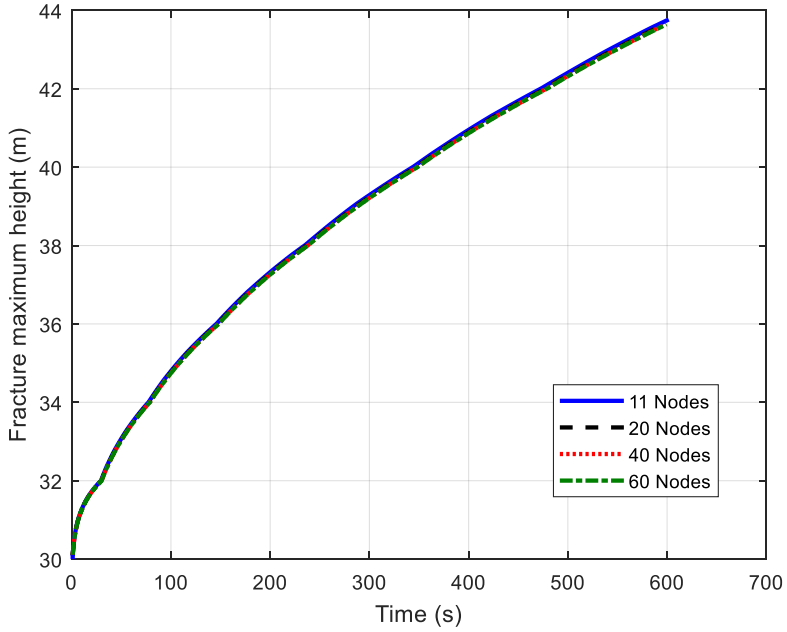

Figure 3.15: Fracture maximum height history for the Pseudo-3D fracture mesh density study.

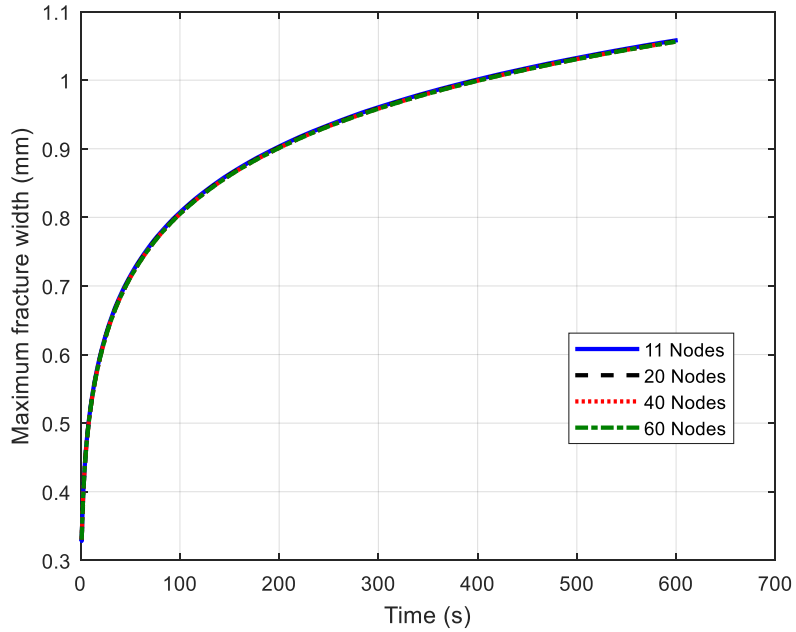

Figure 3.16: Average fracture width history for the Pseudo-3D fracture mesh density study.

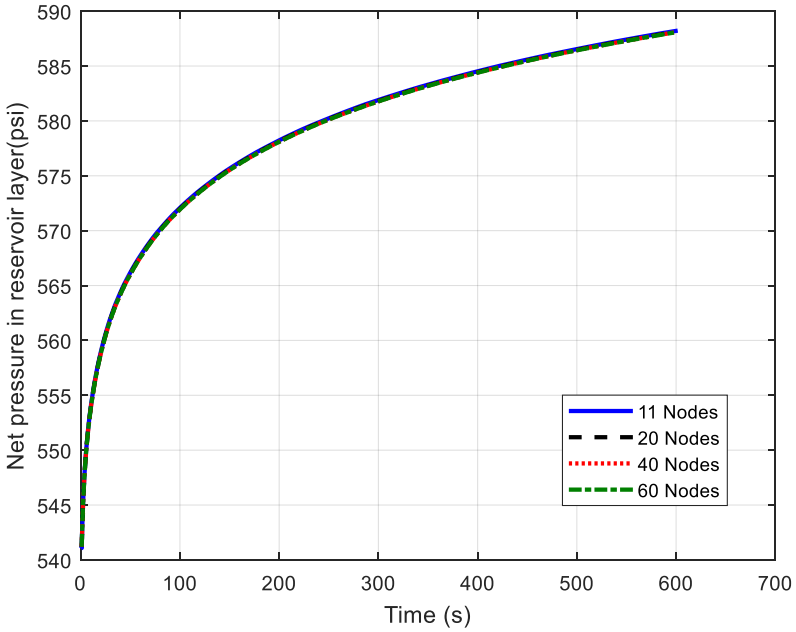

Figure 3.17: History of net pressure in the reservoir layer for the Pseudo-3D fracture mesh density study.

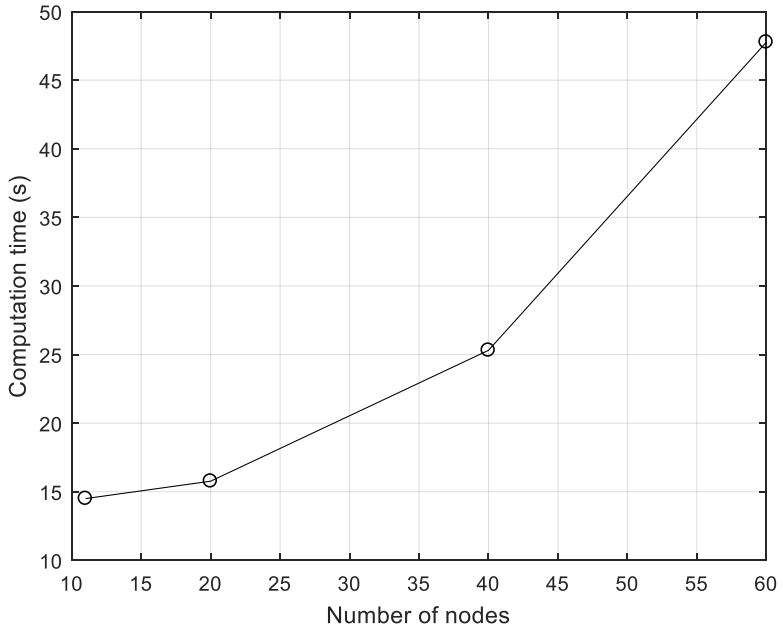

Figure 3.18: Computation time for the P3D fracture mesh density study.

3.3.3. Proppant Transport in the Pseudo-3D Model

In this section, proppant is added in the slurry to present the results of proppant transport calculation (both convection and settling) in the fracture. Reservoir parameters used for the simulation are the same as in Table 3.4. Parameters of the proppant and fluid properties, as well as the injection rate are summarized in Table 3.5.

Parameter	Value	Parameter	Value
Frac Fluid ρ (kg/m^3)	1000	Injection Rate (bpm)	5
Frac Fluid Viscosity (cp)	1	Proppant Conc. (ppa)	5
Proppant ρ (kg/m^3)	3100	Injection Time (min)	20
Proppant Diameter (m)	0.0006	Proppant Bridging (N)	1

Table 3.5: Parameters for the Pseudo-3D fracture proppant transport case.

Fig. 3.19 shows the simulated fracture width and proppant concentration in the fracture at the end of the treatment. This case assumes no proppant settling. It is shown that the fracture width decreases from the injection point to the tip. The proppant is restrained by the narrow fracture width and accumulates where the fracture width is close to the proppant diameter. It is shown that the hydraulic fracture length is over 180 meters, while the propped fracture length is about 2/3 of the hydraulic length. Other than that, the bridging of proppant in the fracture could cause pre-mature screen-out in the fracture.

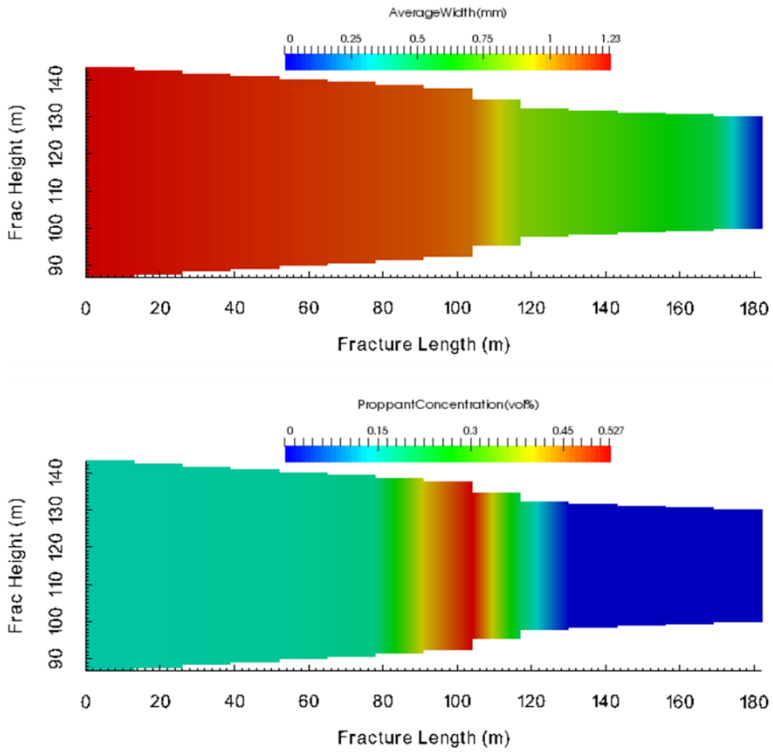

Figure 3.19: Fracture width and proppant concentration in the Pseudo-3D fracture (no proppant settling).

Fig. 3.20 shows the simulated fracture width and proppant concentration in the fracture at the end of the treatment, with proppant settling. It is shown that a proppant bank

has formed at the bottom of the fracture. This is an optimistic estimation of proppant transport in the fracture with little settling during the treatment. Some other researchers (Shiozawa & McClure, 2016; Cohen et al., 2017) observed similar proppant concentration profile in the fracture using a similar proppant transport model. The proppant settling might be under-estimated because the proppant concentration is assumed uniform in the slurry region. If the proppant concentration gradient in the vertical direction is captured, more settling may be observed.

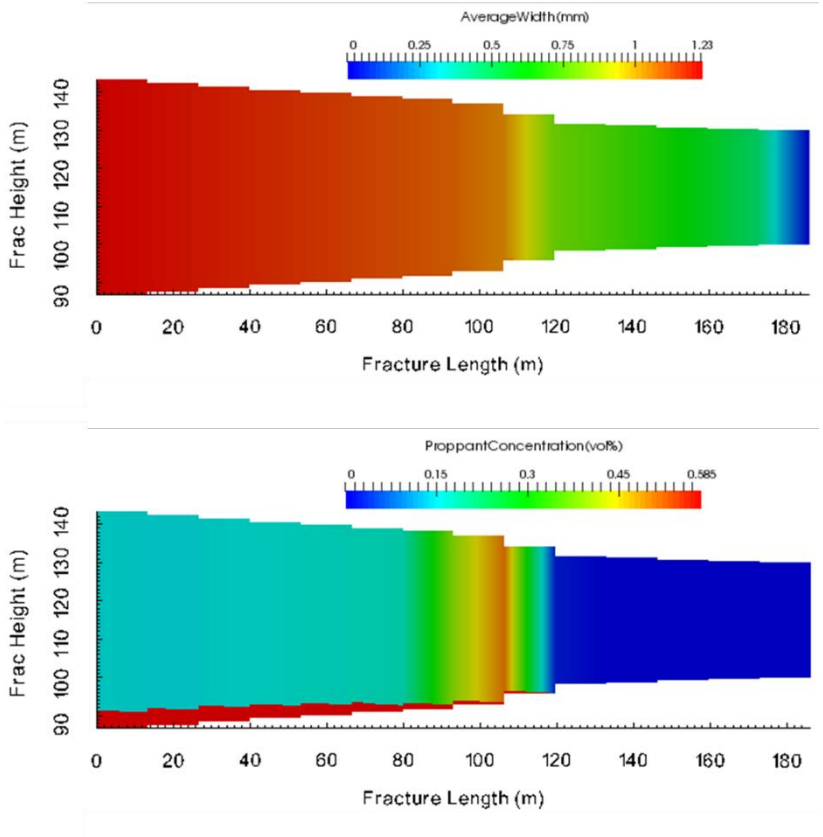

Figure 3.20: Fracture width and proppant concentration from the Pseudo-3D fracture model (with proppant settling).

Like the last case, the proppant accumulates where the fracture width is close to the proppant diameter. In this case, because some proppant settled out from the slurry, the proppant concentration in the slurry appears lower than the last case. In both cases, the total proppant mass is conserved.

After injection stopped, the proppant settles to the bottom of the fracture. Fig. 3.21 is the proppant concentration in the fracture after 30 minutes of shut in. It is shown that as proppant settles from the slurry, the proppant concentration in the slurry decreases and the proppant bank on the bottom of the fracture grows. Most proppant ends up at the bottom of the fracture.

In the development of unconventional reservoirs, water-fracs are commonly applied to create long fractures (Britt et al., 2006). The proppant settling velocity in the slick water is much larger than that in the gel (Gadde et al., 2004; Liu & Sharma, 2005). The proppant could form a dune at the bottom of the fracture before the fracture closes, resulting in reduced propped fracture height (Warpinski 2009; Cipolla et al., 2008). The fracture model developed in this chapter can be integrated with a contact model to further study the fracture closure process and the impact of final proppant placement in the fracture on the production.

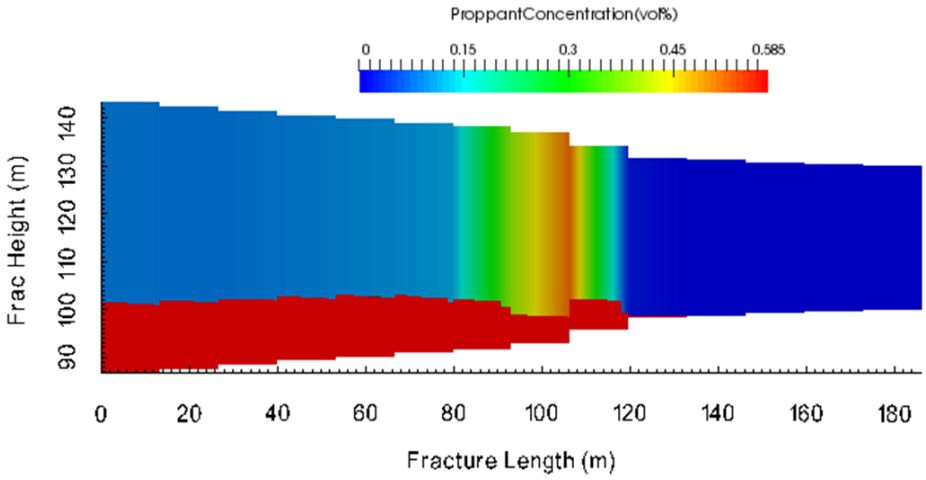

Figure 3.21: Proppant concentration after 30 minutes of shut in.

3.4. CONCLUSIONS

In this chapter, a Pseudo-3D fracture model for simulating single fracture propagation is developed. This model allows a series of reservoir and fluid properties to vary with depth, including minimum horizontal stress, pore pressure, reservoir porosity and permeability, reservoir fluid viscosity and compressibility. The mechanical properties such as Young's Modulus and Poisson's Ratio must be constant.

The equilibrium height and the width profile of the fracture are calculated using superposition of an exact, analytical solid mechanics solution. This method is much faster than the integral method or the 2D DDM method. Plane strain is assumed. This assumption is fairly accurate when the fracture length (tip to tip) is larger than three times the fracture height.

Fracture propagation is solved on a moving mesh. The mesh grows with the fracture, and the number of elements remains constant throughout the simulation. Proppant

convection in the fracture length direction is solved on the same moving mesh. Proppant settling, and the development of a proppant bank is solved on a separate, fixed mesh.

The model has been validated with published Pseudo-3D fracture modeling results. A sensitivity study has been applied to estimate the minimum number of elements needed. Simulation results for proppant transport and settling have been presented.

The Pseudo-3D fracture model developed in this Chapter captures major features of fracture propagation including fracture height growth, slurry flow in the fracture, proppant convection and settling. This fracture model can be extended to simulate simultaneous propagation of multiple fractures as shown in Chapter 4. It can also be used to estimate non-uniform fluid and proppant placement among multiple clusters as shown in Chapter 6.

NOMENCLATURE

A	=	Fracture cross-sectional area, L^2, m^2
A'	=	Cross-sectional area for the slurry region, L^2, m^2
C_l	=	Leak off coefficient, $L/\sqrt{T}$, $m/\sqrt{s}$
E'	=	Plane strain Young's Modulus, M/LT^2, Pa
G	=	Shear modulus, M/LT^2, Pa
H	=	Fracture height, L, m
H_{equil}	=	Equilibrium proppant bank height, L, m
Im	=	Imaginary part of a complex number
K_I	=	Stress intensity factor, $M/\sqrt{LT^2}$, $Pa\cdot\sqrt{m}$
K_{Ic}	=	Critical stress intensity factor, $M/\sqrt{LT^2}$, $Pa\cdot\sqrt{m}$
$K_{I_{\pm a}}$	=	Stress intensity factor at fracture tips, $M/\sqrt{LT^2}$, $Pa\cdot\sqrt{m}$
L	=	Length of laminar flow between two plates, L, m
L_f	=	Fracture length, L/T, m/s
$\dot{L_f}$	=	Fracture propagation velocity, L/T, m/s
M	=	Function of the flow behavior index and fracture shape factor
P_f	=	Hydraulic pressure in fracture, M/LT^2, Pa
P_{net}	=	Net pressure in the fracture, M/LT^2, Pa
Q	=	Fluid Flow rate in one wing of the fracture, L^3/T, m^3/s
Q_o	=	Fluid injection rate for one wing of the fracture, L^3/T, m^3/s
Q_p	=	Proppant flow rate in one fracture wing, L^3/T, m^3/s
Q_s	=	Slurry flow rate in one fracture wing, L^3/T, m^3/s
R_F	=	Fluid Reynolds number
R_{FG}	=	Fluid Gravity Reynolds number
R_G	=	Gravity Reynolds number
R_P	=	Proppant Reynolds number
Re	=	Real part of a complex number
$V_{Deposition}$	=	Proppant deposition velocity, L^3/T, m^3/s
$\mathrm{Z}(\mathrm{z})$	=	Second derivative of $\bar{\bar{\mathrm{Z}}}(\mathrm{z})$ over z
$\bar{\mathrm{Z}}(\mathrm{z})$	=	First derivative of $\bar{\bar{\mathrm{Z}}}(\mathrm{z})$ over z
$\bar{\bar{\mathrm{Z}}}(\mathrm{z})$	=	Function of a complex number z
$\mathrm{Z}'(\mathrm{z})$	=	Third derivative of $\bar{\bar{\mathrm{Z}}}(\mathrm{z})$ over z
a	=	Line crack half length, L, m
a_s	=	Constant in proppant settling velocity calculation
$a(R_G)$	=	Function of Gravity Reynolds number
b	=	Lower boundary of the partial load applied to the line crack, L, m
c	=	Upper boundary of the partial load applied to the line crack, L, m
$c_1(R_G)$	=	Function of Gravity Reynolds number
c_p	=	Dummy variable in the derivation of critical time step
d	=	Proppant diameter, L, m
g	=	Gravitational acceleration, L/T^2, m/s^2

k = Flow consistency index, MT^{n-2}/L, $Pa \cdot s^n$
m = Function of the flow behavior index
$m(R_G)$ = Function of Gravity Reynolds number
$m_1(R_G)$ = Function of Gravity Reynolds number
n = Flow behavior index
$n_1(R_G)$ = Function of Gravity Reynolds number
p = Normal traction applied to part of the line crack, M/LT^2, Pa
q = Flow rate per unit height of the channel, L^2/T, m^2/s
t = Time, s
$t_{initial}$ = Initial time step, T, s
u = Fluid velocity between two parallel plates, L/T, m/s
u_L = Leak off velocity from both fracture walls, L/T, m/s
u_{Stokes} = Stokes proppant settling velocity, L/T, m/s
$u_{settling}$ = Proppant settling velocity, L/T, m/s
u_x = Component of displacement, L, m
u_y = Component of displacement, L, m
w = Width of the channel, m
w_f = Fracture width, L, m
ΔP = Pressure difference for laminar flow between two plates, M/LT^2, Pa
$\Delta t_{critical}$ = Critical time step, T, s
Φ = Airy Stress Function, ML/T^2, $Pa \cdot m^2$
$\emptyset_{max}$ = Maximum proppant volume concentration
$\overline{\emptyset}$ = Normalized proppant volume concentration
θ = Dimensionless coordinate
μ = Fluid viscosity, M/LT, Pa·s
υ = Poisson's ratio
ρ_f = Fluid density, M/L^3, kg/m^3
ρ_p = Proppant density, M/L^3, kg/m^3
σ_x = Stress component, M/LT^2, Pa
σ_{xy} = Stress component, M/LT^2, Pa
σ_y = Stress component, M/LT^2, Pa
σ_{yx} = Stress component, M/LT^2, Pa
τ = Shear stress on fracture walls, M/LT^2, Pa
$\tau(\theta, t)$ = Fracture arrival time at location θ, T, s
$\varphi(x, n)$ = Fracture shape factor

REFERENCES

Adachi, J., Siebrits, E., Peirce, A. and Desroches, J., 2007. Computer simulation of hydraulic fractures. *International Journal of Rock Mechanics and Mining Sciences*, *44*(5), pp.739-757.

Barree, R.D., 1983. A practical numerical simulator for three-dimensional fracture propagation in heterogeneous media. In *SPE Reservoir Simulation Symposium*. Society of Petroleum Engineers.

Britt, L.K., Smith, M.B., Haddad, Z.A., Lawrence, J.P., Chipperfield, S.T. and Hellman, T.J., 2006, January. Waterfracs: We do need proppant after all. In *SPE Annual Technical Conference and Exhibition*. Society of Petroleum Engineers.

Cardiff, P., Manchanda, R., Bryant, E.C., Lee, D., Ivankovic, A. and Sharma, M.M., 2015. Simulation of fractures in OpenFOAM: from adhesive joints to hydraulic fractures. In *10th OpenFOAM Workshop*.

Cipolla, C. L., Lolon, E., Mayerhofer, M. J., & Warpinski, N. R., 2009. The Effect of Proppant Distribution and Un-Propped Fracture Conductivity on Well Performance in Unconventional Gas Reservoirs. Society of Petroleum Engineers. doi:10.2118/119368-MS

Cohen, C.E., Kresse, O. and Weng, X., 2017, January. Stacked height model to improve fracture height growth prediction, and simulate interactions with multi-layer DFNs and ledges at weak zone interfaces. In *SPE Hydraulic Fracturing Technology Conference and Exhibition*. Society of Petroleum Engineers.

Crouch, S.L., Starfield, A.M. and Rizzo, F.J., 1983. Boundary element methods in solid mechanics. *Journal of Applied Mechanics*, *50*, p.704.

Dontsov, E.V. and Peirce, A.P., 2014. Slurry flow, gravitational settling and a proppant transport model for hydraulic fractures. *Journal of Fluid Mechanics*, 760, pp.567-590.

Dontsov, E.V. and Peirce, A.P., 2015. Proppant transport in hydraulic fracturing: crack tip screen-out in KGD and P3D models. *International Journal of Solids and Structures*, 63, pp.206-218.

Economides, M.J. and Nolte, K.G., 1989. *Reservoir stimulation* (Vol. 2). Englewood Cliffs, New Jersey: Prentice Hall.

England, A.H. and Green, A.E., 1963, April. Some two-dimensional punch and crack problems in classical elasticity. In *Mathematical Proceedings of the Cambridge Philosophical Society* (Vol. 59, No. 2, pp. 489-500). Cambridge University Press.

Ferziger, J.H. and Peric, M., 2012. *Computational methods for fluid dynamics*. Springer Science & Business Media.

Fisher, M.K. and Warpinski, N.R., 2012. Hydraulic-fracture-height growth: Real data. *SPE Production & Operations*, *27*(01), pp.8-19.

Fung, R.L., Vilayakumar, S. and Cormack, D.E., 1987. Calculation of vertical fracture containment in layered formations. *SPE formation evaluation*, *2*(04), pp.518-522.

Gadde, P.B., Liu, Y., Norman, J., Bonnecaze, R. and Sharma, M.M., 2004, January. Modeling proppant settling in water-fracs. In *SPE annual technical conference and exhibition*. Society of Petroleum Engineers.

Gu, H. and Siebrits, E., 2006, January. Effect of formation modulus contrast on hydraulic fracture height containment. In *International Oil & Gas Conference and Exhibition in China*. Society of Petroleum Engineers.

Liu, Y., 2006. *Settling and hydrodynamic retardation of proppants in hydraulic fractures* (Doctoral dissertation).

Liu, Y. and Sharma, M.M., 2005, January. Effect of fracture width and fluid rheology on proppant settling and retardation: an experimental study. In *SPE Annual Technical Conference and Exhibition*. Society of Petroleum Engineers.

McDaniel, B.W., 2012, March. Can We Achieve Acceptable Fracture Conductivity Using WaterFracs?. In *SPE/EAGE European Unconventional Resources Conference & Exhibition-From Potential to Production*.

Nolte, K.G., 1979, January. Determination of fracture parameters from fracturing pressure decline. In *SPE Annual Technical Conference and Exhibition*. Society of Petroleum Engineers.

Nordgren, R.P., 1972. Propagation of a vertical hydraulic fracture. Society of Petroleum Engineers Journal, 12(04), pp.306-314.

Ouchi, H., Foster, J.T. and Sharma, M.M., 2017. Effect of reservoir heterogeneity on the vertical migration of hydraulic fractures. *Journal of Petroleum Science and Engineering*, *151*, pp.384-408.

Patankar, N.A., Joseph, D.D., Wang, J., Barree, R.D., Conway, M. and Asadi, M., 2002. Power law correlations for sediment transport in pressure driven channel flows. *International Journal of Multiphase Flow*, *28*(8), pp.1269-1292.

Perkins, T.K. and Kern, L.R., 1961. Widths of hydraulic fractures. *Journal of Petroleum Technology*, 13(09), pp.937-949.

Shiozawa, S. and McClure, M., 2016, February. Comparison of pseudo-3D and fully-3D simulations of proppant transport in hydraulic fractures, including gravitational settling, formation of proppant banks, tip-screen out, and fracture closure. In *SPE hydraulic fracturing technology conference*. Society of Petroleum Engineers.

Shrivastava, K., Blyton, C.A. and Sharma, M.M., 2017. Local Linearization Method for Efficient Solution of Coupled Fluid Flow and Geomechanics Problem. In *51st US*

Rock Mechanics/Geomechanics Symposium. American Rock Mechanics Association.

Simonson, E.R., Abou-Sayed, A.S. and Clifton, R.J., 1978. Containment of massive hydraulic fractures. *Society of Petroleum Engineers Journal*, *18*(01), pp.27-32.

Sneddon, I.N. and Elliot, H.A., 1946. The opening of a Griffith crack under internal pressure. *Quarterly of Applied Mathematics*, 4(3), pp.262-267.

Tada, H., Paris, P.C. and Irwin, G.R., 1973. The stress analysis of cracks. *Handbook, Del Research Corporation*.

Thiercelin, M., Jeffrey, R.G. and Naceur, K.B., 1987, January. The Influence of Fracture Toughness on the Geometry of Hydraulic Fractures. In *Low Permeability Reservoirs Symposium*. Society of Petroleum Engineers.

Valko, P. and Economides, M.J., 1995. *Hydraulic fracture mechanics* (Vol. 28). Chichester: Wiley.

Van Eekelen, H.A.M., 1982. Hydraulic fracture geometry: fracture containment in layered formations. *Society of Petroleum Engineers Journal*, *22*(03), pp.341-349.

Wang, H., Yi, S. and Sharma, M.M., 2018. A computationally efficient approach to modeling contact problems and fracture closure using superposition method. *Theoretical and Applied Fracture Mechanics*, *93*, pp.276-287.

Wang, J., Joseph, D.D., Patankar, N.A., Conway, M. and Barree, R.D., 2003. Bi-power law correlations for sediment transport in pressure driven channel flows. *International journal of multiphase flow*, *29*(3), pp.475-494.

Warpinski, N.R., 2009, January. Stress amplification and arch dimensions in proppant beds deposited by waterfracs. In *SPE Hydraulic Fracturing Technology Conference*. Society of Petroleum Engineers.

Westergaard, H.M., 1939. Bearing pressures and cracks. *Journal of applied mechanics*, *6*(2), pp.A49-A53.

Yue, K., Olson, J. and Schultz, R., 2018, July. Layered Modulus Effect on Fracture Modeling and Height Containment. In *SPE/AAPG/SEG Unconventional Resources Technology Conference*. Unconventional Resources Technology Conference.

MAJOR SECTION 3: SIMULTANEOUS PROPAGATION OF MULTIPLE FRACTURES

In this Major Section, we extend the single fracture models developed in Major Section 2 to simulate simultaneous propagation of multiple fractures.

We present novel methods to calculate dynamic fluid and proppant partitioning among multiple clusters. The interaction between fractures due to stress shadow effects is considered through analytical solutions or the DDM calculation.

The most widely adopted method to solve for fluid distribution among multiple fractures is the Newton-Raphson Method. Although this method can be computationally efficient, it requires an evaluation of the Jacobian matrix for every iteration in each time step. Inaccuracy in the evaluation of the Jacobian matrix can cause instability and even divergence in the computation. In Chapter 4, we present a new approach to calculate fluid distribution. This new approach does not require an evaluation of the Jacobian matrix, is computationally efficient and has been successfully applied to fracturing and refracturing simulations.

Chapter 5 discusses the proppant distribution in multiple perforation clusters. In almost all multi-fracture models, it is assumed that the proppant distribution among multiple fractures is the same as that of the fluid. In our recent work, we have shown that this assumption is not valid (Wu & Sharma, 2016; Wu et al., 2017; Yi et al., 2018). The inertia and gravity of the proppant cause separation between the proppant and the fluid when the slurry flows into a fracture from the wellbore. And this separation can cause significant changes in the final fluid and proppant placement.

The fluid and proppant distribution methods developed in this Major Section have been applied to both the 2D and Pseudo-3D fracture models. These new methods are not

limited to the fracture model developed in this research. They can be applied to almost any fracture models with minor modifications.

Chapter 4: A Novel Method for Dynamic Fluid Partitioning Among Multiple Fractures.[1]

4.1. INTRODUCTION

Simultaneous stimulation of multiple fractures has become a common practice in the development of unconventional reservoirs. For example, Plug-and-perf completion designs stimulate the well with isolated treatment stages. Each stage stimulates 3 to 10 clusters at the same time. In horizontal well refrac operations, all clusters along the wellbore are open and accepting treating fluid at the same time. Diverting agents are applied to plug the depleted fractures and promote the stimulation of new/not depleted clusters.

In the simulation of multi-fracture stimulation, it is crucial to determine the transient fluid partitioning among the fractures accurately. Early work of fluid distribution calculation was based on steady-state fluid partitioning, where a constant rate was assumed for each fracture (Siriwardane and Layne 1991, Elbel 1993). To solve the transient fluid distribution among multiple fractures, Elbel et al. (1992) introduced a method to model the stimulation of multilayer formations. In their model, an analytical PKN model was applied for each fracture, and the Newton-Raphson Method was used to solve the system of non-linear equations for fluid partitioning. Later, the fracture model of this multilayer

[1]Parts of this chapter have been published in Journal of Petroleum Science and Engineering: Yi, S.S. and Sharma, M.M., 2018. A new method to calculate slurry distribution among multiple fractures during fracturing and refracturing. Journal of Petroleum Science and Engineering.

stimulation simulator was updated to a Pseudo-3D model with capabilities including proppant transport and heat transfer calculation (Mack et al. 1992, Gu et al. 2000), and the fluid distribution model remained the same. This fluid distribution model has also been adopted by some other researchers to build multi-fracture propagation simulators (Wu & Olson 2015b, Lecampion & Desroches. 2015). We will refer to this fluid distribution calculation method as the Newton-Raphson Method.

Although the Newton-Raphson Method can be efficient for solving multi-variable nonlinear equation systems like fluid distribution, it requires an evaluation of the Jacobian matrix for every iteration in each time step. For most fracture models, derivatives in the Jacobian matrix have to be evaluated numerically. Therefore, to solve a system of N fractures, numerical evaluation of (N+1)*(N+1) derivatives needs to be carried out for every iteration, which implies solving the fracture model multiple times. Inaccuracy in the evaluation of the Jacobian matrix can cause instability and even divergence in the computation.

In this chapter, we present a new approach to calculate fluid distribution (Yi & Sharma, 2018). This new approach does not require the evaluation of the Jacobian matrix. It is computationally efficient and has been successfully applied to fracturing and refracturing simulations.

4.2. Model Formulation

In this section, we present the formulation of the novel dynamic fluid partitioning method. The fracture interaction due to stress shadow effect could also impact fluid distribution and should be considered. Two methods are adopted to estimate the stress shadow effect: an analytical solution and the DDM method.

4.2.1. Dynamic Fluid Partitioning Among Multiple Fractures

In this section, we present the mathematical derivation and the final formulation of the new fluid distribution method.

Fluid distribution among multiple fractures is controlled by the conservation of mass (Equation 4.1) and the continuity of pressure (Equation 4.2).

$$Q_T = \sum_{i=1}^{n} Q_i \tag{4.1}$$

$$BHP = S_{hmin,i} + \Delta p_{f,i} + \Delta p_{pf,i} + \Delta p_{w,i} \tag{4.2}$$

Where Q_T is the total fluid injection rate and Q_i is the fluid injection rate into fracture i; BHP is the bottom hole pressure; $S_{hmin,i}$ is the closure stress of fracture i; $\Delta p_{f,i}$ is pressure drop in the fracture for fracture i; $\Delta p_{pf,i}$ is the pressure drop in the perforations of fracture i; and $\Delta p_{w,i}$ is pressure drop in the wellbore for fracture i.

Equation 4.2 represents one equation for each fracture. Therefore, for a multi-fracture system with N fractures, Equation 4.1 and Equation 4.2 consist of a system of N+1 non-linear equations with N+1 unknowns $(Q_1, Q_2, \dots, Q_N, BHP)$ for the fluid distribution calculation.

4.2.1.1. The Newton-Raphson Method

For completeness, we first describe the commonly adopted Newton-Raphson Method for solving fluid distribution. First, an unknown vector $\boldsymbol{Q}$ consisting of the N+1 unknown variables (Equation 4.3) and a function vector $\boldsymbol{f}$ (Equation 4.4) is defined.

$$\boldsymbol{Q}^T = [Q_1, Q_2, \dots, Q_n, BHP] \tag{4.3}$$

$$\boldsymbol{f}^T = [f_1, f_2, \dots, f_n, f_{n+1}] \tag{4.4a}$$

$$f_i = BHP - (S_{hmin,i} + \Delta p_{f,i} + \Delta p_{pf,i} + \Delta p_{w,i}) \quad (i = 1,2,\dots,n) \tag{4.4b}$$

$$f_{n+1} = Q_T - \sum_{i=1}^{n} Q_i \tag{4.4c}$$

The function vector $\boldsymbol{f}$ is a measure of error associated with the current guess of $\boldsymbol{Q}$. If the current estimation of $\boldsymbol{Q}$ is the solution to the nonlinear equation system, then $|\boldsymbol{f}| = 0$. If $|\boldsymbol{f}| > 0$, a new guess of $\boldsymbol{Q}$ can be obtained by Equation 4.5.

$$\boldsymbol{Q}_{(t+1)}{}^{T} = \boldsymbol{Q}_{(t)}{}^{T} - [\boldsymbol{J}]_{(t)}{}^{-1}\boldsymbol{f}_{(t)}{}^{T} \tag{4.5}$$

The Jacobian matrix $[\boldsymbol{J}]$ in Equation 4.5 is defined by Equation 4.6.

$$[\boldsymbol{J}] = \begin{bmatrix} \frac{\partial f_1}{\partial Q_1} & \cdots & \frac{\partial f_1}{\partial Q_n} & \frac{\partial f_1}{\partial BHP} \\ \frac{\partial f_2}{\partial Q_1} & \cdots & \frac{\partial f_2}{\partial Q_n} & \frac{\partial f_2}{\partial BHP} \\ \vdots & \ddots & \vdots & \vdots \\ \frac{\partial f_{n+1}}{\partial Q_1} & \cdots & \frac{\partial f_{n+1}}{\partial Q_n} & \frac{\partial f_{n+1}}{\partial BHP} \end{bmatrix} \tag{4.6}$$

The new guess of $\boldsymbol{Q}$ is used to update $\boldsymbol{f}$ and $[\boldsymbol{J}]$, which are substituted into Equation 4.5 in the next iteration. This process is repeated until convergence.

The Newton-Raphson Method is of quadratic convergence and can be efficient for some cases. However, for most fracture models, the derivatives in the Jacobian matrix cannot be expressed analytically. Each fracture needs to be solved at least twice to estimate the corresponding derivative in the Jacobian matrix numerically. This process can be time-consuming and sometimes cause instabilities in the calculation. Next, we propose a new approach to calculate fluid distribution, which does not require the evaluation of the Jacobian matrix.

4.2.1.2. A Novel Approach: the Resistance Method

The N fracture system resembles an electrical circuit network with N branches as shown in Fig. 4.1. And we use a similar idea of electrical resistance to calculate fluid distribution among multiple fractures. Assume that each fracture has a certain resistance, then the amount of fluid a fracture receives is inversely proportional to its resistance.

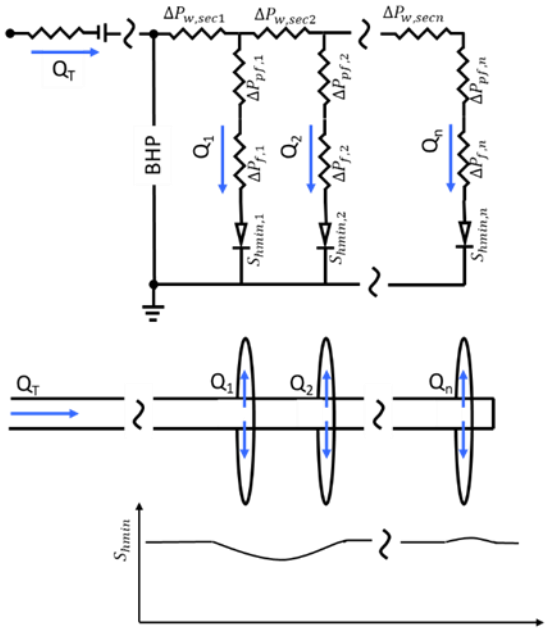

Figure 4.1: Schematic illustration of multi-fracture stimulation in a horizontal wellbore and the analogy with an electrical circuit network. (Elbel et al., 1992)

The resistance of each fracture (R_i) is defined by rewriting Equation 4.2 as Equation 4.7.

$$R_i = \frac{BHP - S_{hmin,i}}{Q_i} = \frac{\Delta p_{f,i} + \Delta p_{pf,i} + \Delta p_{w,i}}{Q_i} \tag{4.7}$$

According to Equation 4.7, the resistance of a fracture is the total pressure drop per unit flow rate. Following Equation 4.7, the fluid injection rate of each fracture can be written as Equation 4.8.

$$Q_i = \frac{BHP - S_{hmin,i}}{R_i} \tag{4.8}$$

Substitute Equation 4.8 into Equation 4.1, we get Equation 4.9.

$$Q_T = \sum_{i=1}^{n} Q_i = \sum_{i=1}^{n} \frac{BHP - S_{hmin,i}}{R_i} = BHP \sum_{i=1}^{n} \frac{1}{R_i} - \sum_{i=1}^{n} \frac{S_{hmin,i}}{R_i} \tag{4.9}$$

We define the total resistance (R_{tot}) in the same way as the electrical circuit, as shown in Equation 4.10.

$$\frac{1}{R_{tot}} = \sum_{i=1}^{n} \frac{1}{R_i} \tag{4.10}$$

Substitute equation 4.10 to equation 4.9 we get Equation 4.11.

$$BHP = R_{tot}(Q_T + \sum_{i=1}^{n} \frac{S_{hmin,i}}{R_i}) \tag{4.11}$$

For the special case of homogeneous closure stress ($S_{hmin,1} = S_{hmin,2} = \cdots = S_{hmin,N} = S_{hmin}$), Equation 4.11 simplifies to Equation 4.12.

$$BHP = Q_T R_{tot} + S_{hmin} \tag{4.12}$$

Now the original N+1 equations are reformed into a new set of N+1 equations consisting of Equation 4.8 and Equation 4.11 (or Equation 4.8 and Equation 4.12 for the special case). Since the unknown variable BHP is explicitly expressed in Equation 4.11, it can be substituted into Equation 4.8 to finally get equation 4.13.

$$Q_i = \frac{R_{tot}(Q_T + \sum_{i=1}^{n} \frac{S_{hmin,i}}{R_i}) - S_{hmin,i}}{R_i} \tag{4.13}$$

In Equation 4.13, The fracture resistance (R_i) is defined by Equation 4.7 and the total resistance (R_{tot}) is defined by Equation 4.10. They are both functions of fracture injection rates (Q_i). For an N fracture system, Equation 4.13 represents a fixed point iteration formulation of N equations with N unknowns ($Q_i, i = 1,2, \dots, n$). It can be proved with map contraction theory that this system of non-linear equations converges locally at least linearly (see **Appendix A**).

Fig. 4.2 shows the algorithm for computing the dynamic fluid distribution with the new fluid distribution method. Starting from a first guess of the fluid distribution, pressure drops in the wellbore, in the perforations, fracture propagation and proppant transport for each fracture are calculated. Next, R_i, R_{tot} and BHP are evaluated using Equation 4.7, 4.10 and 4.11. After that, a new guess of fluid distribution can be obtained using Equation 4.13. This iteration process is repeated until convergence. The outer loop in Fig. 4.2 is the fluid distribution loop and the inner loop is the calculation for each fracture. Therefore, the fracture model (which solves fracture propagation, proppant transport etc.) is implicitly incorporated with the fluid distribution model. This algorithm can be applied to almost any fracture model with minor alteration.

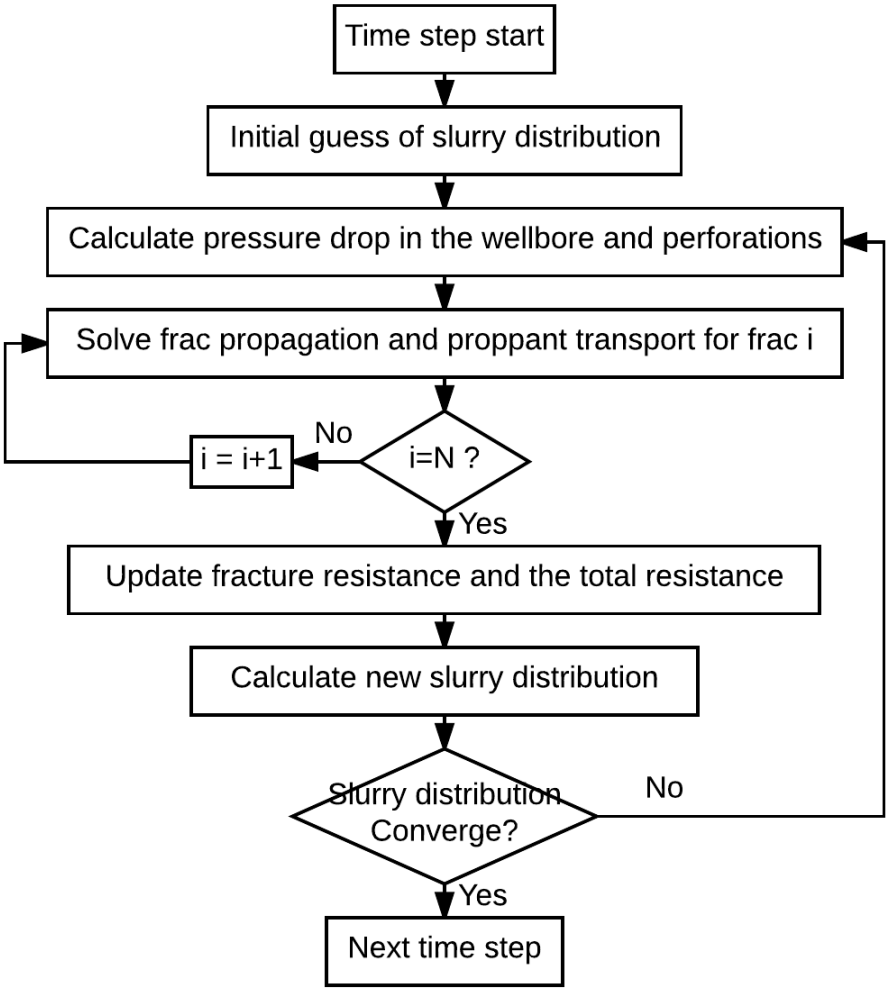

Figure 4.2: The computation algorithm for solving fluid distribution among multiple fractures using the Resistance Method.

4.2.2. Modeling Stress Shadow Effect

When modeling the simultaneous propagation of multiple fractures, it is important to consider the interaction among the fractures. There are two main mechanisms of hydraulic fracture interaction: 1). the mechanical stress shadow effect and 2) the poro-elastic effect.

The poro-elastic effect describes the stress change in the reservoir caused by production or injection of fluids (Roussel & Sharma 2010; Roussel 2011; Bhardwaj et al., 2016). In applications such as re-fracturing and infill well stimulation, the poro-elastic effect can be dominant in terms of stress reduction and reorientation in the reservoir (Roussel & Sharma 2012; Manchanda et al., 2018; Gala et al., 2018). However, for the stimulation of unconventional reservoirs, fluid leak-off from the fracture face is insignificant due to the ultra-low permeability and the poro-elastic effect is less important in the fracture treatment.

The mechanical effect describes the stress change in the reservoir caused by the dilation of the fracture. The mechanical opening of a fracture induces deformation and additional stress in the reservoir, which affects the propagation of other fractures. The mechanical effect is sometimes referred to as the stress shadow effect (Fisher et al., 2004; Roussel & Sharma, 2011), and it can be important in multiple fracture propagation. For example, in a plug-and-perf stage, the fractures in the middle can be restricted due to the stress shadow from the outside fractures (Roussel & Sharma, 2011; Wu, 2014). The stress in the vicinity of a fracturing stage will be elevated, causing an increase of the shut-in pressures (ISIP) in following stages (Manchanda et al., 2012; Roussel et al., 2012). And the ISIP increase may be used to help quantify the geometry of the dilated fractures (Roussel, 2017).

Many different methods may be adopted to simulate stress shadow effect during fracture propagation, such as Finite-Volume based general 3D fracture model (Bryant et al., 2015; Manchanda, 2015), DDM fracture models (Wu, 2014; Shrivastava et al., 2017), Peridynamics-based hydraulic fracture model (Ouchi et al., 2015a; Ouchi et al., 2015b) and so on. Kresse et al. (2013) tested both analytical and DDM methods to account for stress

shadow effect in Pseudo-3D fracture modeling, and the results showed good agreement with 2D DDM fracture simulator.

In this section, we used both analytical and DDM methods to calculate the stress shadow induced by open fractures. The stress shadow effect affects the fracture propagation in two ways in our simulation: 1). the additional stress caused by the opening of nearby fractures affects the pressure, width and height of the fracture; 2). the modified stress field and fracture pressure affect the fluid distribution among multiple fractures.

4.2.2.1. The Analytical Method

The first method superposes an analytical solution. Sneddon (1946) obtained Westgaard's solution (please refer to Chapter 3) for the stress field induced by a 2D fracture opened by uniform internal pressure.

Figure 4.3 plots the induced stress versus distance from fracture face. The fracture cross section is elliptical in the x-z plane. And the fracture length is infinite along the y-coordinate. It is shown that the incremental stress due to the mechanical fracture opening is the highest near the fracture face and decreases as the distance increases.

For the 2D multi-fracture model, the stress field is updated by the summation of induced stress of all fractures. In other words, stress shadow effect is calculated by the superposition of the analytical solution.

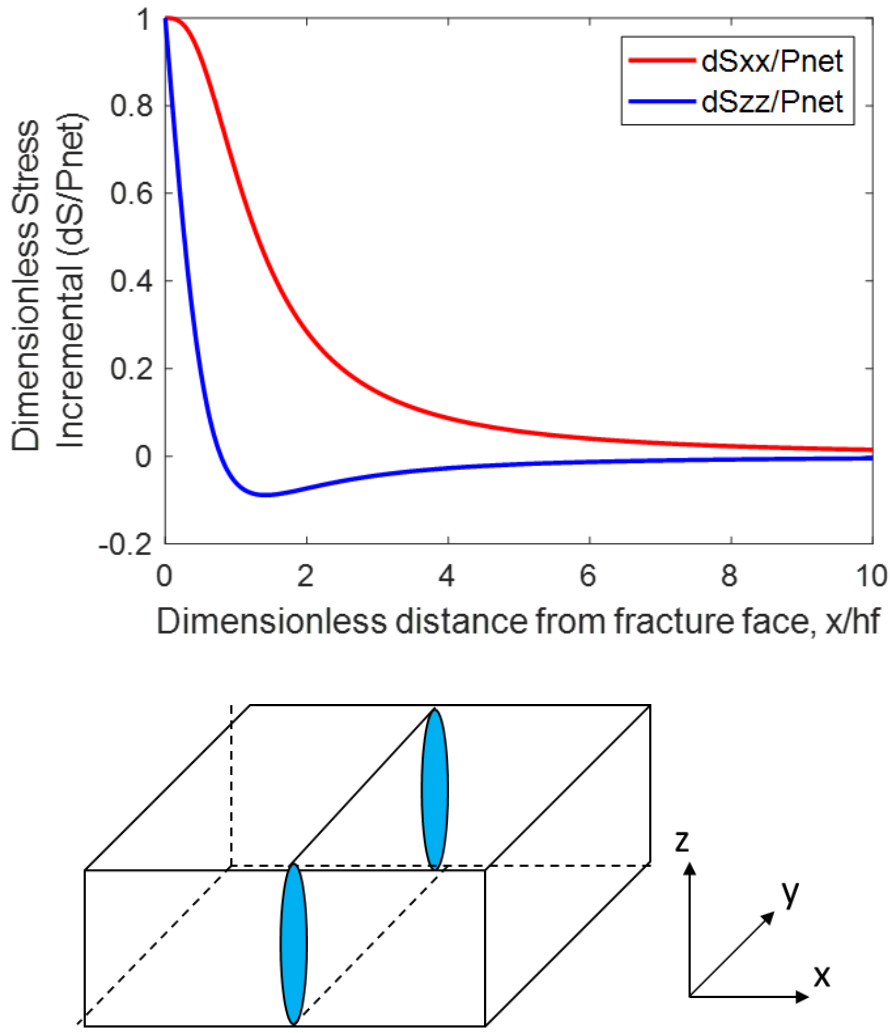

Figure 4.3: The stress induced by the opening of a 2D fracture under uniform internal pressure.

4.2.2.2. The DDM Method

A more sophisticated way to simulate the stress shadow effect is based on the Displacement Discontinuity Method. DDM is a type of Boundary Element Method (BEM) developed by Crouch and Starfield (1983) to handle fracture problems. Displacement

discontinuities D_x and D_y are defined as the difference in displacements between the two sides of the segment as shown in Equation 4.14 and Fig. 4.4.

$$D_{\bar{x}} = u_{\bar{x}}(\bar{x}, 0_-) - u_{\bar{x}}(\bar{x}, 0_+) \tag{4.14a}$$

$$D_{\bar{y}} = u_{\bar{y}}(\bar{x}, 0_-) - u_{\bar{y}}(\bar{x}, 0_+) \tag{4.14b}$$

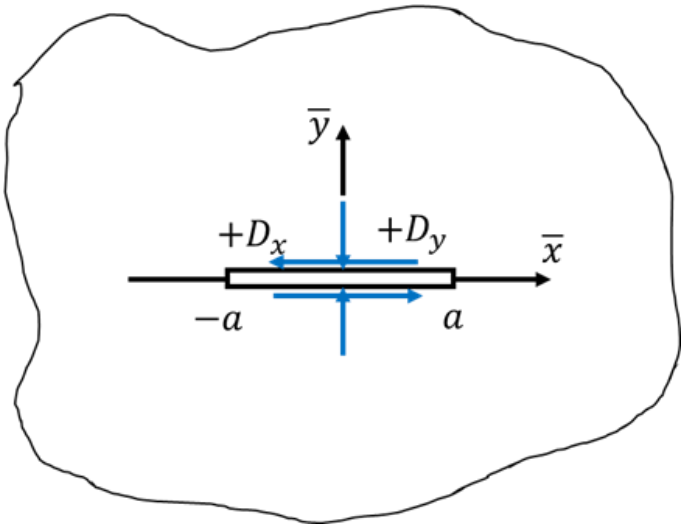

Figure 4.4: Displacement discontinuities in the local coordinate system $\bar{x}$-$\bar{y}$.

Where $u_{\bar{x}}, u_{\bar{y}}$ are positive in the positive x and y coordinate directions and $D_{\bar{x}}, D_{\bar{y}}$ are positive as illustrated by blue arrows in Fig. 4.4. Positive $D_{\bar{y}}$ suggests that two sides of the crack overlap and negative $D_{\bar{y}}$ represents a finite width of the crack.

For any point $(\overline{x}, \overline{y})$ in the local coordinate system shown in Figure 4.4, solutions for displacements and stresses are given by Crouch and Starfield (1983)

$$u_{\overline{x}} = D_{\bar{x}}\left[2(1-\nu)f_{,\overline{y}} - \overline{y}f_{,\overline{xx}}\right] + D_{\bar{y}}[-(1-2\nu)f_{,\overline{x}} - \overline{y}f_{,\overline{xy}}] \tag{4.15a}$$

$$u_{\overline{y}} = D_{\bar{x}}\left[(1-2\nu)f_{,\overline{x}} - \overline{y}f_{,\overline{xy}}\right] + D_{\bar{y}}[2(1-\nu)f_{,\overline{y}} - \overline{y}f_{,\overline{yy}}] \tag{4.15b}$$

And

$$\sigma_{\overline{xx}} = 2GD_{\bar{x}}\left[+2f_{,\overline{xy}} + yf_{,\overline{xyy}}\right] + 2GD_{\bar{y}}[f_{,\overline{yy}} + \overline{y}f_{,\overline{yyy}}] \tag{4.16a}$$

$$\sigma_{\overline{yy}} = 2GD_{\bar{x}}\left[-\overline{y}f_{,\overline{xyy}}\ \right] + 2GD_{\bar{y}}[f_{,\overline{yy}} - \overline{y}f_{,\overline{yyy}}] \tag{4.16b}$$

$$\sigma_{\overline{xy}} = 2GD_{\bar{x}}\left[f_{,\overline{yy}} + \overline{y}f_{,\overline{yyy}}\right] + 2GD_{\bar{y}}[-\overline{y}f_{,\overline{xyy}}] \tag{4.16c}$$

Where G is shear modulus and function $f(\overline{x},\overline{y})$ is defined as:

$$f(\overline{x},\overline{y}) = \frac{-1}{4\pi(1-\nu)}\left[\overline{y}\left(\arctan\frac{\overline{y}}{\overline{x}-a} - \arctan\frac{\overline{y}}{\overline{x}+a}\right)\right.$$
$$- (\overline{x}-a)ln\sqrt{\left[(\overline{x}-a)^2+\overline{y}^2\right]} \tag{4.17}$$
$$\left. + (\overline{x}+a)ln\sqrt{\left[(\overline{x}+a)^2+\overline{y}^2\right]}\right]$$

The derivatives of the function $f(\overline{x},\overline{y})$ used in the DDM formulation (Equation 4.15 and 4.16) are given below

$$f_{,\overline{x}} = \frac{1}{4\pi(1-\nu)}\left[ln\sqrt{[(\overline{x}-a)^2+\overline{y}^2]} - ln\sqrt{[(\overline{x}+a)^2+\overline{y}^2]}\right] \tag{4.18a}$$

$$f_{,\overline{y}} = \frac{-1}{4\pi(1-\nu)}\left[\arctan\frac{\overline{y}}{\overline{x}-a} - \arctan\frac{\overline{y}}{\overline{x}+a}\right] \tag{4.18b}$$

$$f_{,\overline{xy}} = \frac{1}{4\pi(1-\nu)}\left[\frac{\overline{y}}{(\overline{x}-a)^2+\overline{y}^2} - \frac{\overline{y}}{(\overline{x}+a)^2+\overline{y}^2}\right] \tag{4.18c}$$

$$f_{,\overline{xx}} = -f_{,\overline{yy}} = \frac{1}{4\pi(1-\nu)}\left[\frac{\overline{x}-a}{(\overline{x}-a)^2+\overline{y}^2} - \frac{\overline{x}+a}{(\overline{x}+a)^2+\overline{y}^2}\right] \tag{4.18d}$$

$$f_{,\overline{xyy}} = -f_{,\overline{xxx}} = \frac{1}{4\pi(1-\nu)}\left[\frac{(\overline{x}-a)^2-\overline{y}^2}{\left\{(\overline{x}-a)^2+\overline{y}^2\right\}^2} - \frac{(\overline{x}+a)^2-\overline{y}^2}{\left\{(\overline{x}+a)^2+\overline{y}^2\right\}^2}\right] \tag{4.18e}$$

$$f_{,\overline{yyy}} = -f_{,\overline{xxy}} = \frac{2\overline{y}}{4\pi(1-\nu)}\left[\frac{\overline{x}-a}{\left\{(\overline{x}-a)^2+\overline{y}^2\right\}^2} - \frac{\overline{x}+a}{\left\{(\overline{x}+a)^2+\overline{y}^2\right\}^2}\right] \tag{4.18f}$$

If the fracture faces are discretized into small boundary elements, then for each element, Equation 4.15 and 4.16 applies, and a matrix for displacements or stresses in the reservoir can be formed. Note that all the equations introduced above (Equation 4.14 to Equation 4.18) are defined in a local coordinate system for each boundary element. And transformations between the local coordinate systems and the global coordinate system is needed to form the matrix that includes all the elements.

The solution introduced above is 2D and implies infinite fracture height. To account for the 3D aspect of finite fracture height, a 3D correction factor G^{ij} derived by Olson (2004) is applied to the influence coefficients:

$$G^{ij} = 1 - \frac{d_{ij}^{\beta}}{\left[d_{ij}^2 + \left(\frac{h_f}{\alpha}\right)^2\right]^{\frac{\beta}{2}}} \tag{4.19}$$

Where h_f is the fracture height, d_{ij} is the distance between the center of element i and element j, α and β are empirical constants: $\alpha = 1$ and $\beta = 2.3$. Wu and Olson (2015a) developed a new set of height correction coefficients. These new coefficients are of higher accuracy for multi-fracture interaction that can be applied to simplified 3D DDM simulations.

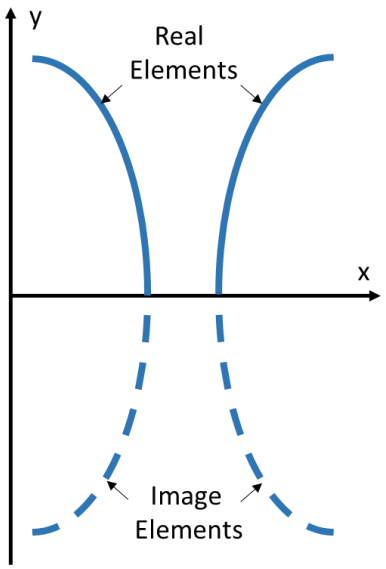

Figure 4.5: Illustration of real and image elements in the DDM calculation

Assuming the two wings of a fracture are symmetric as shown in Fig. 4.5, then image boundary elements can be used in the DDM formulation to simplify the calculation.

For a line of symmetry: $y^* = 0$, the relations between the real element and the image elements are summarized in Table 4.1.

	Global Coordinates	Orient Angle	Normal Displacement	Shear Displacement
Real Element (i)	(x_i, y_i)	β_i	D_n^i	D_s^i
Image Element(i')	$(x_i, -y_i)$	$-\beta_i + \pi$	D_n^i	$-D_s^i$

Table 4.1: Relations between the real element and the corresponding image element.

We represent a real element with *i* (*i=1, 2, ..., n*) and the corresponding image element with i' (i' *=1, 2, ..., n*), the complete matrix including all elements in terms of the global coordinates can be written as

$$\begin{bmatrix} \sigma_x^1 \\ \sigma_y^1 \\ \sigma_x^2 \\ \sigma_y^2 \\ \vdots \\ \sigma_x^n \\ \sigma_y^n \\ \sigma_x^{1'} \\ \sigma_y^{1'} \\ \sigma_x^{2'} \\ \sigma_y^{2'} \\ \vdots \\ \sigma_x^{n'} \\ \sigma_y^{n'} \end{bmatrix}_{4n} = \begin{bmatrix} A_{00}^{11} & A_{01}^{11} & & A_{00}^{1n} & A_{01}^{1n} & A_{00}^{11'} & A_{01}^{11'} & & A_{00}^{1n'} & A_{01}^{1n'} \\ A_{10}^{11} & A_{11}^{11} & \cdots & A_{10}^{1n} & A_{11}^{1n} & A_{10}^{11'} & A_{11}^{11'} & \cdots & A_{10}^{1n'} & A_{11}^{1n'} \\ A_{00}^{21} & A_{01}^{21} & & A_{00}^{2n} & A_{01}^{2n} & A_{00}^{21'} & A_{01}^{21'} & & A_{00}^{2n'} & A_{01}^{2n'} \\ A_{10}^{21} & A_{11}^{21} & & A_{10}^{2n} & A_{11}^{2n} & A_{10}^{21'} & A_{11}^{21'} & & A_{10}^{2n'} & A_{11}^{2n'} \\ \vdots & & \ddots & \vdots & & \vdots & & \ddots & \vdots & \\ A_{00}^{n1} & A_{01}^{n1} & \cdots & A_{00}^{nn} & A_{01}^{nn} & A_{00}^{n1'} & A_{01}^{n1'} & \cdots & A_{00}^{nn'} & A_{01}^{nn'} \\ A_{10}^{n1} & A_{11}^{n1} & & A_{10}^{nn} & A_{11}^{nn} & A_{10}^{n1'} & A_{11}^{n1'} & & A_{10}^{nn'} & A_{11}^{nn'} \\ A_{00}^{1'1} & A_{01}^{1'1} & & A_{00}^{1'n} & A_{01}^{1'n} & A_{00}^{1'1'} & A_{01}^{1'1'} & & A_{00}^{1'n'} & A_{01}^{1'n'} \\ A_{10}^{1'1} & A_{11}^{1'1} & \cdots & A_{10}^{1'n} & A_{11}^{1'n} & A_{10}^{1'1'} & A_{11}^{1'1'} & \cdots & A_{10}^{1'n'} & A_{11}^{1'n'} \\ A_{00}^{2'1} & A_{01}^{2'1} & & A_{00}^{2'n} & A_{01}^{2'n} & A_{00}^{2'1'} & A_{01}^{2'1'} & & A_{00}^{2'n'} & A_{01}^{2'n'} \\ A_{10}^{2'1} & A_{11}^{2'1} & & A_{10}^{2'n} & A_{11}^{2'n} & A_{10}^{2'1'} & A_{11}^{2'1'} & & A_{10}^{2'n'} & A_{11}^{2'n'} \\ \vdots & & \ddots & \vdots & & \vdots & & \ddots & \vdots & \\ A_{00}^{n'1} & A_{01}^{n'1} & \cdots & A_{00}^{n'n} & A_{01}^{n'n} & A_{00}^{n'1'} & A_{01}^{n'1'} & \cdots & A_{00}^{n'n'} & A_{01}^{n'n'} \\ A_{10}^{n'1} & A_{11}^{n'1} & & A_{10}^{n'n} & A_{11}^{n'n} & A_{10}^{n'1'} & A_{11}^{n'1'} & & A_{10}^{n'n'} & A_{11}^{n'n'} \end{bmatrix}_{4n\times 4n} \begin{bmatrix} D_x^1 \\ D_y^1 \\ D_x^2 \\ D_y^2 \\ \vdots \\ D_x^n \\ D_y^n \\ D_x^{1'} \\ D_y^{1'} \\ D_x^{2'} \\ D_y^{2'} \\ \vdots \\ D_x^{n'} \\ D_y^{n'} \end{bmatrix}_{4n} \quad (4.20)$$

Where A_{ab}^{ij} (a=0,1; b= 0,1; i = 1-n'; j = 1-n') represents the influence coefficient calculated using Equation 4.16 and coordinate transformation.

We can simplify the matrix in Equation 4.20 in two steps. First, split the shear (x) and normal (y) components. Then, use the relations between the real and image elements in Table 4.1 to eliminate the image elements in the matrix. Finally, we get Equation 4.21.

$$\begin{bmatrix}\sigma_x^1\\ \sigma_x^2\\ \vdots\\ \sigma_x^n\end{bmatrix}_n = \begin{bmatrix}A_{00}^{11}-A_{00}^{11'} & \cdots & A_{00}^{1n}-A_{00}^{1n'}\\ A_{00}^{21}-A_{00}^{21'} & \cdots & A_{00}^{2n}-A_{00}^{2n'}\\ \vdots & \ddots & \vdots\\ A_{00}^{n1}-A_{00}^{n1'} & \cdots & A_{00}^{nn}-A_{00}^{nn'}\end{bmatrix}_{n\times n}\begin{bmatrix}D_x^1\\ D_x^2\\ \vdots\\ D_x^n\end{bmatrix}_n + \begin{bmatrix}A_{01}^{11}+A_{01}^{11'} & \cdots & A_{01}^{1n}+A_{01}^{1n'}\\ A_{01}^{21}+A_{01}^{21'} & \cdots & A_{01}^{2n}+A_{01}^{2n'}\\ \vdots & \ddots & \vdots\\ A_{01}^{n1}+A_{01}^{n1'} & \cdots & A_{01}^{nn}+A_{01}^{nn'}\end{bmatrix}_{n\times n}\begin{bmatrix}D_y^1\\ D_y^2\\ \vdots\\ D_y^n\end{bmatrix}_n \tag{4.21a}$$

$$\begin{bmatrix}\sigma_y^1\\ \sigma_y^2\\ \vdots\\ \sigma_y^n\end{bmatrix}_{2n} = \begin{bmatrix}A_{10}^{11}-A_{10}^{11'} & \cdots & A_{10}^{1n}-A_{10}^{1n'}\\ A_{10}^{21}-A_{10}^{21'} & \cdots & A_{10}^{2n}-A_{10}^{2n'}\\ \vdots & \ddots & \vdots\\ A_{10}^{n1}-A_{10}^{n1'} & \cdots & A_{10}^{nn}-A_{10}^{nn'}\end{bmatrix}_{n\times n}\begin{bmatrix}D_x^1\\ D_x^2\\ \vdots\\ D_x^n\end{bmatrix}_n + \begin{bmatrix}A_{11}^{11}+A_{11}^{11'} & \cdots & A_{11}^{1n}+A_{11}^{1n'}\\ A_{11}^{21}+A_{11}^{21'} & \cdots & A_{11}^{2n}+A_{11}^{2n'}\\ \vdots & \ddots & \vdots\\ A_{11}^{n1}+A_{11}^{n1'} & \cdots & A_{11}^{nn}+A_{11}^{nn'}\end{bmatrix}_{n\times n}\begin{bmatrix}D_y^1\\ D_y^2\\ \vdots\\ D_y^n\end{bmatrix}_n \tag{4.21b}$$

Three steps are followed to calculate the stress shadow effect. First, matrixes in Equation 4.21a and 4.21b are calculated according to the relative location of the elements. Then, the normal displacement D_y^i is equal to fracture width with a negative sign, and the shear stress on the fracture faces (σ_x^1) is 0. The shear displacement D_x^i is obtained using Equation 4.21a. After that, the normal and shear displacements are substituted into Equation 4.21b to calculate the stress shadow on each element.

The DDM calculation is applied to the Pseudo-3D multi-fracture simulator to quantify the stress shadow on each element of the fracture. The Pseudo-3D fracture model is solved on a moving mesh as explained in Chapter 3. Therefore, the relative location of

the elements changes in every time step. And the influence coefficients in the matrixes in Equation 4.21a and 4.21b needs to be updated every time step. The size of the matrixes remains constant. On the other hand, if a fixed mesh is used instead, and new elements are added every time step, then the influence coefficients evaluated in the last time step remains the same, but the matrices grow larger and larger as new elements are added. Another way to improve the computation efficiency is to create a large mesh at the beginning and calculate all influence coefficients. As the fracture propagates, the fracture cells in the mesh gets connected and the corresponding pre-calculated influence coefficients are used.

4.3. RESULTS AND DISCUSSION

In this section, we first validate the Resistance Method with the results of the Newton-Raphson Method. The computation efficiency of these two methods are compared. It is shown that the Resistance Method can be more computationally efficient than the Newton-Raphson Method. After that, an example case showing the influence of layer heterogeneity and wellbore trajectory on fracture geometry is performed with the Pseudo-3D multi-fracture model.

4.3.1. Validation and Efficiency of the Resistance Method

The new fluid distribution method has been compared with the Newton-Raphson Method regarding convergence and speed by applying both methods to the same analytical PKN fracture model.

The analytical PKN model assumes plane strain, constant fracture height, Newtonian fluid and no leak off. The momentum equation for laminar flow in a fracture is approximated by the lubrication theory as shown in Equation 4.22.

$$\frac{dP}{dx} = -\frac{64q\mu}{\pi h_f w^3} \tag{4.22}$$

Where P is the pressure in the fracture, x is distance along the fracture length, q is flow rate in one wing of the fracture, μ is fluid viscosity, h_f is fracture height, and w is fracture maximum width.

The pressure-width relation for plan strain is shown in Equation 4.23 (Economides & Nolte, 1989).

$$w = \frac{2P_{net}h_f}{E_p} \tag{4.23}$$

Where P_{net} is the net pressure in the fracture and E_p is the plane strain Young's modulus ($E_p = \frac{E}{1-v^2}$).

Substituting Equation 4.23 into Equation 4.22 and integrating over the length of the fracture (assuming $P_{net} = 0$ at fracture tip and q is constant in the fracture), one can get Equation 4.24.

$$P_{net} = \left[\frac{16Q_i\mu E_p^3}{\pi h_f^4} L\right]^{\frac{1}{4}} \tag{4.24}$$

Where Q_i is the injection rate ($Q_i = 2q$) into the fracture and L is the length of one wing of the fracture.

After that, one can change the fracture half-length in Equation 4.24 to be the total fracture volume (V_i) and get Equation 4.25 and 4.26 below.

$$P_{net} = \left[\frac{20Q_i\mu V_i E_p^4}{\pi^2 h_f^6}\right]^{\frac{1}{5}} \tag{4.25}$$

$$V_{i(t+1)} = V_{i(t)} + Q_{i(t+1)}dt \tag{4.26}$$

The five equations above form a complete system of equations for solving the analytical PKN fracture propagation. The fracture geometry is solved by first calculating

the new fracture volume using Equation 4.26, and then calculating P_{net}, fracture width and fracture length using Equation 4.25, 4.23, and 4.24.

The pressure drop in the perforations is calculated using Equation 4.27 below (Romero et al., 1995)

$$\Delta p_{pf,i} = 0.2369 \frac{{Q_i}^2 \rho}{{n_{perf}}^2 D_{perf}^4 C^2} \tag{4.27a}$$

$$C = 0.56 + 1.65 \times 10^{-4} M, \qquad (C \leq 0.89) \tag{4.27b}$$

Where Q_i is the fluid injection rate into fracture i (total flow rate through perforations), in bbl/min; ρ is fluid density, (lbm/gal); n_{perf} is number of perforations in the cluster; D_{perf} is the perforation diameter (in); C is discharge coefficient and M is the total mass of proppant that has passed through the perforations (lbm). Equation 4.27-a shows that the perforation pressure drop is proportional to the square of the flow rate and is strongly influenced by the number of active perforations in a cluster.

Perforation erosion is considered in two ways in the simulation. First, perforation friction reduction due to sand erosion is accounted for in Equation 4.27b by the discharge coefficient. Second, as perforation diameter is enlarged, it impacts the proppant transport as shown in Chapter 5. The perforation diameter is updated in the simulation using the same discharge coefficient shown in Equation 4.27b.

The pressure drop in the wellbore is calculated using the friction factor as shown in Equation 4.28 (Bird et al., 2007).

$$f_r = \frac{1}{4} \left(\frac{D_{well}}{L_{well}}\right) \left(\frac{\Delta p_{sec}}{\frac{1}{2}\rho {v_f}^2}\right) \tag{4.28a}$$

$$f_r = \frac{16}{Re}, \quad Re \leq 2100 \tag{4.28b}$$

$$f_r = \frac{0.0791}{Re^{1/4}}, \quad 2100 < Re \leq 10^5 \tag{4.28c}$$

$$\frac{1}{\sqrt{f_r}} = 3.6\log_{10}[\frac{6.9}{Re} + \left(\frac{k/D_{well}}{3.7}\right)^{10/9}], \quad 10^5 < Re < 10^8 \tag{4.28d}$$

Where f_r is friction factor defined by Equation 4.28a; D_{well} is wellbore diameter; L_{well} is length of the wellbore interval; ΔP_{sec} is pressure drop in the wellbore interval; v_f is flow velocity in the wellbore; Re is Reynolds number; k is roughness of the pipe surface. Equation 4.28, Equation 4.27, the analytical PKN fracture model, together with mass conservation and pressure continuity equations, make up of a closed system for simulating multiple fracture propagation. The calculation algorithm follows that shown in Fig. 4.2.

Parameter	**Value**	**Parameter**	**Value (frac 1,2,3)**
Wellbore Inner Diameter (in.)	5.5	Min Hz Stress (psi)	3000, 3000, 3000
Young's Modulus (GPa)	28	Fracture Height (ft)	100, 100, 100
Poisson's Ratio	0.2	Distance to Heel Frac (ft)	0, 15, 30
Fluid Density (g/cm^3)	1	Perforation Number	30, 20, 10
Fluid Viscosity (cp)	1	Perforation Diameter (in.)	3/8, 3/8, 3/8
Relative Tolerance	1e-3	Time step (s)	60

Table 4.2: Parameters for the validation case of the Resistance Method.

A synthetic simulation with three fractures has been carried out with parameters in Table 4.2. Fracture 1 is the heel side fracture, and fracture 3 is the toe side fracture. The main difference among the three fractures is perforation number: fracture 1, 2, 3 has 30, 20 and 10 perforations respectively. Fluid is injected at an injection rate up to 30 bpm. The relative error is defined as in Equation 4.29 below. The convergence criterion for this case is relative error $\leqslant$ 1e-3.

$$relative\ error = \sqrt{\sum_{i=0}^{n}\left(\frac{\left(q_{i(t+1)} - q_{i(t)}\right)}{\min(q_{i(t+1)}, q_{i(t)})}\right)^2} \tag{4.29}$$

The simulated fluid distribution among the three fractures is shown in Fig. 4.6. The solid green line is the total injection rate. The red stars, black circles, and blue triangles are injection rate into fracture 1, 2 and 3 calculated by the Newton-Raphson Method. The red dash-dot line, the black dash line and the blue dot line are the injection rate into fracture 1, 2 and 3 calculated by the new Resistance Method. Due to the friction pressure drop in the perforations, the fracture that has the most perforations (fracture 1) receives most treating fluid, and the fracture that has the least perforations (fracture 3) receives least treating fluid. It is seen that both methods can solve fluid distribution accurately.

The computation efficiency is roughly estimated by the number of loops taken to reach convergence. Numbers of iteration loops per time step for both methods are shown in Table 4.3 to compare the efficiency of the two methods.

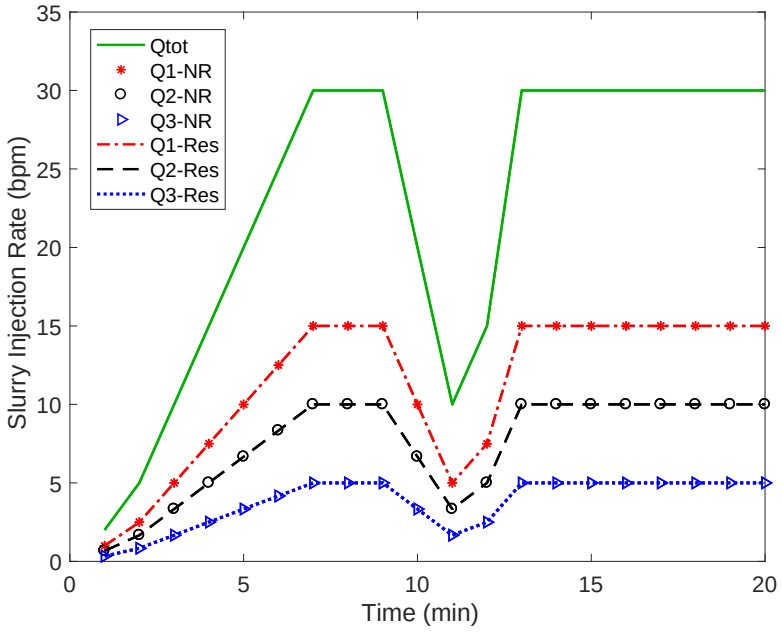

Figure 4.6: Total injection rate (green line) and fluid partitioning among three fractures calculated by the Newton-Raphson Method and the Resistance Method.

Time Step	1	2	3	4	5	6	7	8	9	10
N-R	4	2	2	2	2	2	2	1	1	2
Res, 0	106	142	205	1	1	1	1	1	1	1
Res, 0.5	5	2	2	1	1	1	1	1	1	1
Time Step	11	12	13	14	15	16	17	18	19	20
N-R	2	2	2	1	1	1	1	1	1	1
Res, 0	1	124	359	5	1	1	1	1	1	1
Res, 0.5	2	2	1	1	1	1	1	1	1	1

Table 4.3: Iterative loop numbers of the Newton Raphson Method and the Resistance Method.

The results in Table 4.3 provide several interesting learnings.

For the Newton-Raphson Method, all derivatives in the Jacobian matrix have been obtained analytically to avoid any instability caused by numerical evaluation. Therefore, the results in Table 4.3 represent the best performance of the Newton-Raphson Method. If

the numerical evaluation of the Jacobian matrix is required, more iteration loops are needed.

For the new fluid distribution approach, it is found that adopting a relaxation factor can greatly improve calculation efficiency. Without relaxation, it could take more than 300 iteration loops to converge. With a relaxation factor of 0.5, the number of iteration loops is reduced to 1 or 2 for most time steps.

The reason for this improvement is that the self-correcting nature of the Resistance Method can over-correct the solution and cause the guess of the unknown variable to oscillate around the solution before reaching convergence. In this case, using a relaxation factor of 0.5 can greatly improve the efficiency of the calculation.

Convergence of Q_1 in the first time step of Table 4.3 for the new fluid distribution method is shown in Fig. 4.7. Black dots show the error of Q_1 after each iteration with no relaxation, and red stars show the error of Q_1 with a relaxation factor of 0.5. Adopting a relaxation factor of 0.5, which takes 50% from the old guess and 50% of the new guess, greatly improved the convergence speed.

The Resistance Method has been applied to the simulations of plug-and-perf stages and horizontal well refracturing as shown in Chapter 6 and 7. A relaxation factor of 0.5 is used for all cases. For most time steps, 1 to 2 iterations are enough. In all cases tested, iteration loops seldom exceed 4.

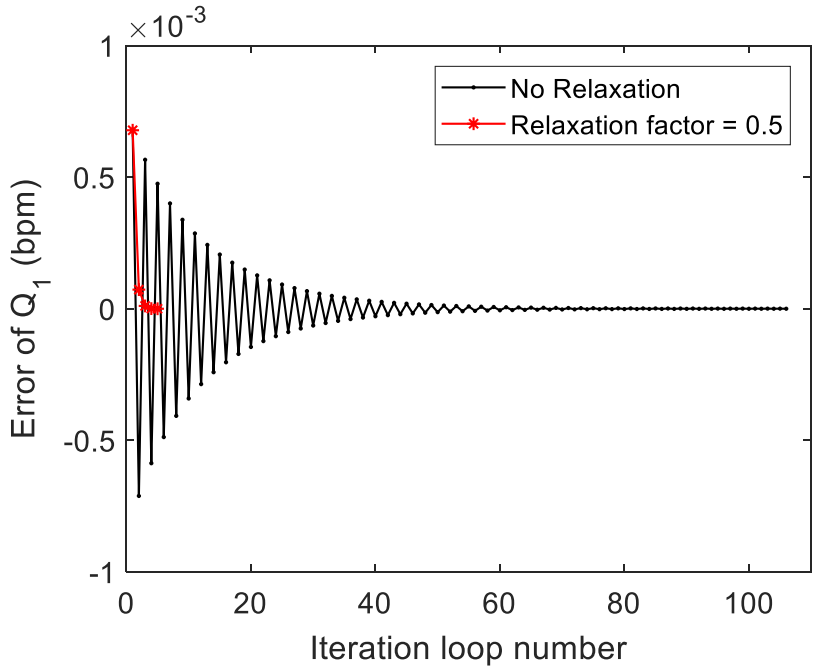

Figure 4.7: Errors of Q_1 after each iteration of the Resistance Method without relaxation and with a relaxation factor of 0.5.

With comparable iteration loop number, the new fluid distribution method is more computationally efficient than the Newton-Raphson method, because in each time step, the Newton-Raphson Method has additional steps of evaluating each derivative in the Jacobian matrix, forming and inverting the (N+1) by (N+1) Jacobian matrix. Therefore, the new method can be more computationally efficient than the Newton-Raphson Method for solving fluid distribution among multiple fractures.

4.3.2. The Pseudo-3D Multi-Fracture Model

The Resistance Method has been applied to both the 2D PKN-Type fracture model and the Pseudo-3D fracture model to simulate simultaneous propagation of multiple

fractures. In this section, we present an example application of the Pseudo-3D multi-fracture simulator.

The development of seismology and well logging technology over the past decades allows geologists to describe more details of the reservoir. The layers are divided finer to capture the influence of heterogeneity on oil and gas recovery. A synthetic case with 9 layers is simulated with the Pseudo-3D multi-fracture model. The pore pressure and minimum horizontal stress of the 9 layers are summarized in Figure 4.8 a). Figure 4.8 b) shows a horizontal wellbore that is not fully horizontal. The up and downs of the wellbore trajectory goes through the layers. In a plug-and-perf stage, 6 clusters were perforated along the wellbore, with cluster 1 being the toe side cluster and cluster 6 being the heel side cluster. The properties of the layers are summarized in Table 4.4. Note that all the properties in Table 4.4 are allowed to vary along the depth. But the Young's Modulus and Poisson's Ratio must be constant. In this case, the Young's Modulus equals to 25 GPa, and the Poisson's Ratio equals to 0.23.

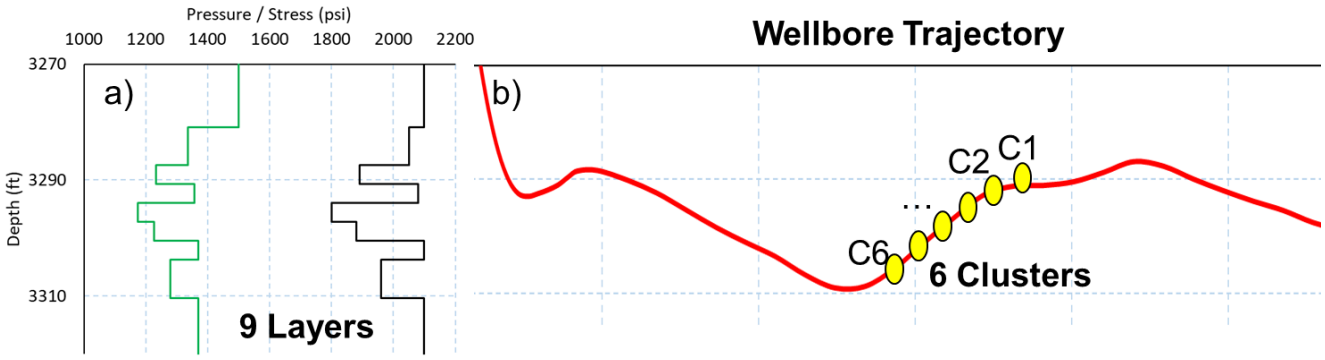

Figure 4.8: a) Pore pressure and stress of the 9 layers. b) The wellbore trajectory and the relative location of the 6 clusters.

Type	Thickness (m)	top (m)	bottom (m)	Shmin (psi)	Ppore (psi)	Klc (Pa)	Perm (mD)	Fluid Comp. (Pa-1)	Fluid Vis. (cp)	Porosity
sand	1000	0	1000	2100	1500	1E+06	13.0	5E-10	2	0.12
shale	2	1000	1002	2050	1337	1E+06	0.1	5E-10	2	0.08
Shale	1	1002	1003	1890	1233	1E+06	0.1	5E-10	2	0.08
Shale	1	1003	1004	2080	1357	1E+06	0.1	5E-10	2	0.08
Shale	1	1004	1005	1800	1174	1E+06	0.1	5E-10	2	0.08
Shale	1	1005	1006	1880	1226	1E+06	0.1	5E-10	2	0.08
Shale	1	1006	1007	2099.5	1369	1E+06	0.1	5E-10	2	0.08
Shale	2	1007	1009	1960	1278	1E+06	0.1	5E-10	2	0.08
sand	1000	1009	2009	2100	1370	1E+06	13.0	5E-10	2	0.12

Table 4.4: Layer properties.

A Newtonian fluid with viscosity of 1 cp is injected into the wellbore at 3, 5, 7, 9 bpm for 3 minutes each, and then 10 minutes with 10 bpm. The fracture geometry after injection is shown in Fig. 4.9. It is shown that cluster 2 and cluster 5 were perforated in layers with higher stress, and fracture propagation from these two clusters is restrained. Note that stress shadow effect is considered in this case using the DDM method. But it is not the primary factor in the results.

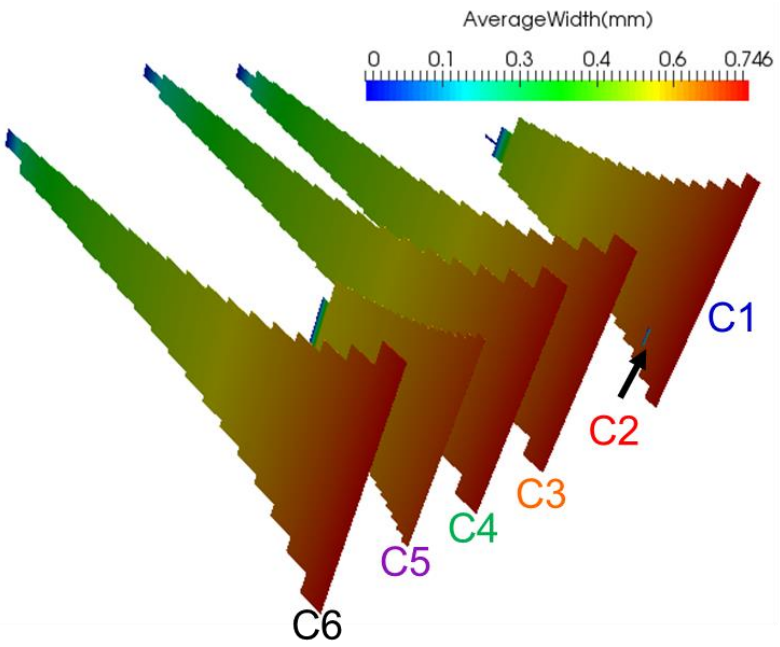

Figure 4.9: Fracture geometry after injection.

4.4. CONCLUSIONS

For the development of unconventional reservoirs, simultaneous stimulation of multiple fractures has become a widespread practice. It is very important to obtain an accurate estimation of treating fluid partitioning among multiple fractures in multi-fracture modeling. The fluid distribution among clusters is controlled by mass balance and pressure continuity, which forms a non-linear equation system with N+1 equations and N+1 unknowns ($Q_1, Q_2, \dots, Q_n, BHP$).

In previous work, researchers solved the problem using the Newton-Raphson Method. This method is of quadratic convergence in theory and can be efficient sometimes. But it requires the evaluation of the Jacobian matrix in every iteration of each time step. For most fracture models, the derivatives in the Jacobian matrix must be evaluated

numerically, which means solving the fracture model twice for the evaluation of one relevant derivative. This process can be time consuming and inefficient. Moreover, inaccuracy in the Jacobian matrix calculation can cause instability and even divergence of the calculation.

In this chapter, we proposed a new approach to calculate fluid distribution among multiple fractures: The Resistance Method. This new method defines a fracture resistance, and distribute fluid among fractures reversely proportional to fracture resistance, using an analogy of current distribution in circuit network. In the new method, the original N+1 non-linear equations are reformulated to eliminate one unknown and form system of N non-linear equations with N unknowns ($Q_1, Q_2, \dots, Q_n$). And the new system of N equations has been proved to converge locally at least linearly.

The modeling of stress shadow effect is also discussed. Two methods can be applied to calculate the stress shadow: 1) analytical solution and 2). DDM method. We applied the first method to the 2D multi-fracture model and the DDM method to the Psedueo-3D multi-fracture model.

The Resistance Model can be applied to almost any fracture models to build a multi-fracture simulator with minor alteration. A comparison between the Resistance Method and the Newton-Raphson Method regarding convergence and speed has been presented. It is shown that both methods can solve fluid distribution accurately. A relaxation factor of 0.5 can greatly improve the computation efficiency of the Resistance Method. And the Resistance Method can be more computationally efficient than the Newton-Raphson Method.

We applied The Resistance Model to both the 2D and Pseudo-3D fracture models to develop multi-fracture simulators. An example case showing the influence of layer

heterogeneity and wellbore trajectory on fracture geometry is demonstrated with the Pseudo-3D multi-fracture model.

To summarize, a new approach for the calculation of dynamic fluid distribution among multiple fractures is presented. This new method: 1) has been proved to converge locally at least linearly; 2) has been compared with the Newton-Raphson Method with respect to convergence and speed; 3) has been successfully applied in several fracture modeling applications. The impact of stress shadow effect on fluid distribution is considered using either an analytical solution or the DDM method.

The advantage of this new fluid distribution method includes: 1) it is easy to implement; 2) does not require the evaluation of a Jacobian matrix; 3) computationally efficient; 4) can be implicitly integrated with almost any fracture model to create multi-fracture simulators.

NOMENCLATURE

A_{ab}^{ij}	=	Influence Coefficient in the DMM matrix
BHP	=	Bottom hole pressure, M/LT^2, Pa
C	=	Discharge coefficient
D_{perf}	=	Perforation diameter, L, m
D_{well}	=	Wellbore diameter, L, m
D_x^i	=	Shear displacement discount in global coordinates for element i, L, m
D_y^i	=	Normal displacement discount in global coordinates for element i, L, m
$D_{\bar{x}}$	=	Shear displacement discontinuity in local coordinates, L, m
$D_{\bar{y}}$	=	Normal displacement discontinuity in local coordinates, L, m
E	=	Young's Modulus, M/LT^2, Pa
E_p	=	Plane strain Young's modulus, M/LT^2, Pa
G	=	Shear Modulus, M/LT^2, Pa
G^{ij}	=	Height correction factor for DDM
L	=	Fracture length (one wing), L, m
L_{well}	=	Length of the wellbore interval, L, m
M	=	Total mass of proppant passed through perforations, M, kg
P	=	Pressure in the fracture, M/LT^2, Pa
P_{net}	=	Net pressure in the fracture, M/LT^2, Pa
$\boldsymbol{Q}$	=	Unknown vector for the Newton-Raphson Method
Q_i	=	Fluid injection rate into fracture i, L^3/T, m^3/s
Q_T	=	Total fluid injection rate into the well, L^3/T, m^3/s
Re	=	Reynolds number
R_i	=	Fracture resistance for fracture i, M/(L^{4}T), Pa·s/m^3
R_{tot}	=	Total resistance of all the fractures, M/(L^{4}T), Pa·s/m^3
$S_{hmin,i}$	=	Closure stress for fracture i, M/LT^2, Pa
V_i	=	Total fracture volume, L^3, m^3
a	=	Half length of the DDM element
d_{ij}	=	Distance between the center of element i and element j
$\boldsymbol{f}$	=	Function vector for the Newton-Raphson Method
f_i	=	Components of the function vector for the Newton-Raphson Method
f_r	=	Friction factor
$f(\overline{x},\overline{y})$	=	Function in the DDM formulation
$f,$	=	Derivatives of function $f(\overline{x},\overline{y})$
h_f	=	Fracture height, L, m
k	=	Roughness of the pipe surface
n_{perf}	=	Number of perforations
q	=	Flow rate in the fracture (one wing), L^3/T, m^3/s
$u_{\bar{x}}$	=	Shear displacement in local coordinates
$u_{\bar{y}}$	=	Normal displacement in local coordinates
v_f	=	Flow velocity in the wellbore, L/T, m/s

w	=	Maximum fracture width, L, m
x	=	Distance along fracture length, L, m
$\Delta p_{f,i}$	=	Pressure drop in fracture i, M/LT^2, Pa
$\Delta p_{pf,i}$	=	Pressure drop in perforations of fracture i, M/LT^2, Pa
Δp_{sec}	=	Pressure drop in wellbore interval, M/LT^2, Pa
$\Delta p_{w,i}$	=	Pressure drop in the wellbore for fracture i, M/LT^2, Pa
α	=	Empirical constants for DDM height correction
β	=	Empirical constants for DDM height correction
β_j	=	Orient angle with respect to x-axis for DDM element j
σ_x^i	=	Shear stress for DDM element i in global coordinates
σ_y^i	=	Normal stress for DDM element i in global coordinates
μ	=	Fracturing fluid viscosity, M/LT, Pa·s
ν	=	Poisson's Ratio
ρ	=	Slurry density, M/L^3, kg/m^3
$\sigma_{\overline{xx}}$	=	Stress component in local coordinates, M/LT^2, Pa
$\sigma_{\overline{yy}}$	=	Stress component in local coordinates, M/LT^2, Pa
$\sigma_{\overline{xy}}$	=	Stress component in local coordinates, M/LT^2, Pa
$[\boldsymbol{J}]$	=	Jacobian matrix for the Newton-Raphson Method

REFERENCES

Bhardwaj, P., Hwang, J., Manchanda, R. and Sharma, M.M., 2016, September. Injection Induced Fracture Propagation and Stress Reorientation in Waterflooded Reservoirs. In *SPE Annual Technical Conference and Exhibition*. Society of Petroleum Engineers.

Bird, R.B., Stewart, W.E. and Lightfoot, E.N. 2007. Interphase Transport in Isothermal Systems. In *Transport Phenomena*, Revised 2nd ed, Chap 6, 177-196. New York: Wiley.

Bryant, E.C., Hwang, J. and Sharma, M.M., 2015, February. Arbitrary fracture propagation in heterogeneous poroelastic formations using a finite volume-based cohesive zone model. In *SPE Hydraulic Fracturing Technology Conference*. Society of Petroleum Engineers.

Crouch, S.L., Starfield, A.M. and Rizzo, F.J., 1983. Boundary element methods in solid mechanics. *Journal of Applied Mechanics*, 50, p.704.

Economides, M.J. and Nolte, K.G., 1989. *Reservoir stimulation* (Vol. 2). Englewood Cliffs, New Jersey: Prentice Hall.

Elbel, J.L. 1993. A method to estimate multizone injection profiles during hydraulic fracturing. *SPE Prod & Fac* 8 (02): 117-122. SPE-21869-PA. https://doi.org/10.2118/21869-PA

Elbel, J.L., Piggott, A.R. and Mack, M.G. 1992. Numerical modeling of multilayer fracture treatments. Presented at the *Permian Basin Oil and Gas Recovery Conference*, Midland, Texas, 18-20 March. SPE-23982-MS. https://doi.org/10.2118/23982-MS

Fisher, M.K., Heinze, J.R., Harris, C.D., Davidson, B.M., Wright, C.A. and Dunn, K.P., 2004, January. Optimizing horizontal completion techniques in the Barnett shale using microseismic fracture mapping. In *SPE Annual Technical Conference and Exhibition*. Society of Petroleum Engineers.

Gala, D.P., Manchanda, R., Sharma, M.M., 2018. Modeling of Fluid Injection in Depleted Parent Wells to Minimize Damage due to Frac-Hits. In *Unconventional Resources Technology Conference*. URTeC: 2881265

Gruesbeck, C. and Collins, R.E. 1982. Particle Transport Through Perforations. *Society of Petroleum Engineers Journal* 22, no. 06, pp. 857-865. doi: 10.2118/7006-PA

Gu, H., Desroches, J. and Elbel, J.L. 2000. Computer simulation of multilayer hydraulic fractures. Presented at the *International Oil and Gas Conference and Exhibition* in China, Beijing, 7-10 November. SPE-64789-MS. https://doi.org/10.2118/64789-MS

Kresse, O., Weng, X., Gu, H. and Wu, R., 2013. Numerical modeling of hydraulic fractures interaction in complex naturally fractured formations. *Rock mechanics and rock engineering*, *46*(3), pp.555-568.

Lecampion, B. and Desroches, J. 2015. Simultaneous initiation and growth of multiple radial hydraulic fractures from a horizontal wellbore. *Journal of the Mechanics and Physics of Solids*, 82: 235-258.

Mack, M.G., Elbel, J.L. and Piggott, A.R. 1992. Numerical representation of multilayer hydraulic fracturing. Presented at the *33rd US Symposium on Rock Mechanics (USRMS)*, Santa Fe, New Mexico, 3-5 June. ARMA-92-0355.

Manchanda, R., 2015, A general poro-elastic model for pad-scale fracturing of horizontal wells. (Doctoral dissertation).

Manchanda, R., Bhardwaj, P., Hwang, J. and Sharma, M.M., 2018, January. Parent-Child Fracture Interference: Explanation and Mitigation of Child Well Underperformance. In *SPE Hydraulic Fracturing Technology Conference and Exhibition*. Society of Petroleum Engineers.

Manchanda, R., Roussel, N.P. and Sharma, M.M., 2012, June. Factors influencing fracture trajectories and fracturing pressure data in a horizontal completion. In *Paper ARMA 12-633 presented at the 46th US Rock Mechanics/Geomechanics Symposium, Chicago, Illinois* (pp. 24-27).

Olson, J.E., 2004. Predicting fracture swarms—The influence of subcritical crack growth and the crack-tip process zone on joint spacing in rock. *Geological Society, London, Special Publications*, *231*(1), pp.73-88.

Ortega, J.M., 1990. *Numerical analysis: a second course*. Society for Industrial and Applied Mathematics.

Ouchi, H., Katiyar, A., Foster, J. and Sharma, M.M., 2015a, February. A peridynamics model for the propagation of hydraulic fractures in heterogeneous, naturally fractured reservoirs. In *SPE Hydraulic Fracturing Technology Conference*. Society of Petroleum Engineers.

Ouchi, H., Katiyar, A., York, J., Foster, J.T. and Sharma, M.M., 2015b. A fully coupled porous flow and geomechanics model for fluid driven cracks: a peridynamics approach. *Computational Mechanics*, *55*(3), pp.561-576.

Romero, J., Mack, M.G. and Elbel, J.L., 1995. Theoretical model and numerical investigation of near-wellbore effects in hydraulic fracturing. Presented at the *SPE Annual Technical Conference and Exhibition*, Dallas, Texas, 22-25 October. SPE-30506-MS. http://dx.doi.org/10.2118/30506-MS

Roussel, N.P., 2011. Stress reorientation in low permeability reservoirs. (Doctoral dissertation).

Roussel, N.P., 2017, January. Analyzing ISIP Stage-by-Stage Escalation to Determine Fracture Height and Horizontal-Stress Anisotropy. In *SPE Hydraulic Fracturing Technology Conference and Exhibition*. Society of Petroleum Engineers.

Roussel, N.P., Manchanda, R. and Sharma, M.M., 2012, January. Implications of fracturing pressure data recorded during a horizontal completion on stage spacing design. In *SPE Hydraulic Fracturing Technology Conference*. Society of Petroleum Engineers.

Roussel, N.P. and Sharma, M.M., 2010. Quantifying transient effects in altered-stress refracturing of vertical wells. *SPE Journal*, 15(03), pp.770-782.

Roussel, N.P. and Sharma, M.M., 2011. Optimizing fracture spacing and sequencing in horizontal-well fracturing. *SPE Production & Operations*, 26(02), pp.173-184.

Roussel, N.P. and Sharma, M.M., 2012. Role of stress reorientation in the success of refracture treatments in tight gas sands. *SPE Production & Operations*, 27(04), pp.346-355.

Shrivastava, K., Blyton, C.A. and Sharma, M.M., 2017, August. Local Linearization Method for Efficient Solution of Coupled Fluid Flow and Geomechanics Problem. In 51st *US Rock Mechanics/Geomechanics Symposium*. American Rock Mechanics Association.

Siriwardane, H.J. and Layne, A.W. 1991. Improved model for predicting multiple hydraulic fracture propagation from a horizontal well. Presented at the *SPE Eastern Regional Meeting*, Lexington, Kentucky, 22-25 October. SPE-23448-MS. https://doi.org/10.2118/23448-MS

Sneddon, I., 1946. The distribution of stress in the neighbourhood of a crack in an elastic solid. *Proc. R. Soc. Lond. A*, *187*(1009), pp.229-260.

Ugueto, C., Gustavo, A., Huckabee, P.T., Molenaar, M.M., Wyker, B. and Somanchi, K., 2016, February. Perforation cluster efficiency of cemented plug and perf limited entry completions; Insights from fiber optics diagnostics. In *SPE Hydraulic Fracturing Technology Conference*. Society of Petroleum Engineers.

Wheaton, B., Haustveit, K., Deeg, W., Miskimins, J. and Barree, R., 2016, February. A case study of completion effectiveness in the eagle ford shale using DAS/DTS observations and hydraulic fracture modeling. In *SPE Hydraulic Fracturing Technology Conference*. Society of Petroleum Engineers.

Wu, K., 2014. Numerical modeling of complex hydraulic fracture development in unconventional reservoirs (Doctoral dissertation).

Wu, K. and Olson, J.E., 2015a. A simplified three-dimensional displacement discontinuity method for multiple fracture simulations. *International Journal of Fracture*, *193*(2), pp.191-204.

Wu, K. and Olson, J.E., 2015b. Simultaneous multifracture treatments: fully coupled fluid flow and fracture mechanics for horizontal wells. *SPE J.* 20 (02): 337-346. SPE-167626-PA. https://doi.org/10.2118/167626-PA

Yi, S.S., and Sharma, M.M., 2018. A New Method to Calculate Slurry Distribution Among Multiple Fractures During Fracturing and Refracturing. *Journal of Petroleum Science and Engineering*.

Chapter 5: Non-Uniform Proppant Transport into Multiple Clusters[2]

5.1. INTRODUCTION

In almost all multi-fracture simulators, it is assumed that there is no separation between fluid and proppant regarding distribution among multiple clusters. This assumption means that the proppant distribution is the same as the fluid distribution. For example, if a fracture receives 20% of the injected fluid, it also receives 20% of the injected proppant. We have shown in our recent publications that this assumption is not valid (Wu & Sharma 2016; Wu et al., 2017; Yi et al., 2018). The distribution of fluid and proppant among multiple clusters can be quite different from each other. And the separation of fluid and proppant during the transport from the wellbore into perforated clusters can have a significant impact on final fracture geometry.

Plug-and-perf is the most commonly adopted completion method for horizontal wells in unconventional reservoirs. Multiple isolated plug-and-perf stages are performed to stimulate the whole wellbore. Each fracturing stage stimulates 3 to 8 perforation clusters simultaneously. The completion starts from the toe of a well and proceeds towards the heel. Drillable plugs are placed between each stage for zonal isolation. After all the stages are completed, the plugs are drilled and circulated out of the well before the well is put on production.

When multiple fractures are treated simultaneously, it is frequently observed that the treatment distribution among the fractures is non-uniform. Some dominant fractures receive more fluid and proppant than planned. Sometimes one or two fractures receive

[2]This Chapter is based on joint work with Wu Chu-Hsiang, who contributed greatly to the PTE correlation. Parts of this chapter have been published in the SPE Production & Operations: Yi, S.S., Wu, C.H. and Sharma, M.M., 2018. Proppant Distribution among Multiple Perforation Clusters in Plug-and-Perforate Stages. SPE Production & Operations.

more than 90% of the whole treatment. The dominant clusters are over-stimulated, leaving other clusters under-stimulated.

Usually, the over-stimulated clusters are the heel side clusters, and the treatment is said to be heel-biased. The heel-biased treatment distribution has been reported by many independent field studies. For example, Ugueto et al. (2016) published a field study of treatment distribution among multiple clusters for plug-and-perf stages. The treatment distribution is evaluated by Distributed Acoustic Sensing (DAS) and Distributed Temperature Sensing (DTS) technology. They studied 8 three-cluster stages, 18 four-cluster stages, and 4 six-cluster stages. The heel biased treatment distribution is observed in all three kinds of stages, as shown in Fig. 5.1.

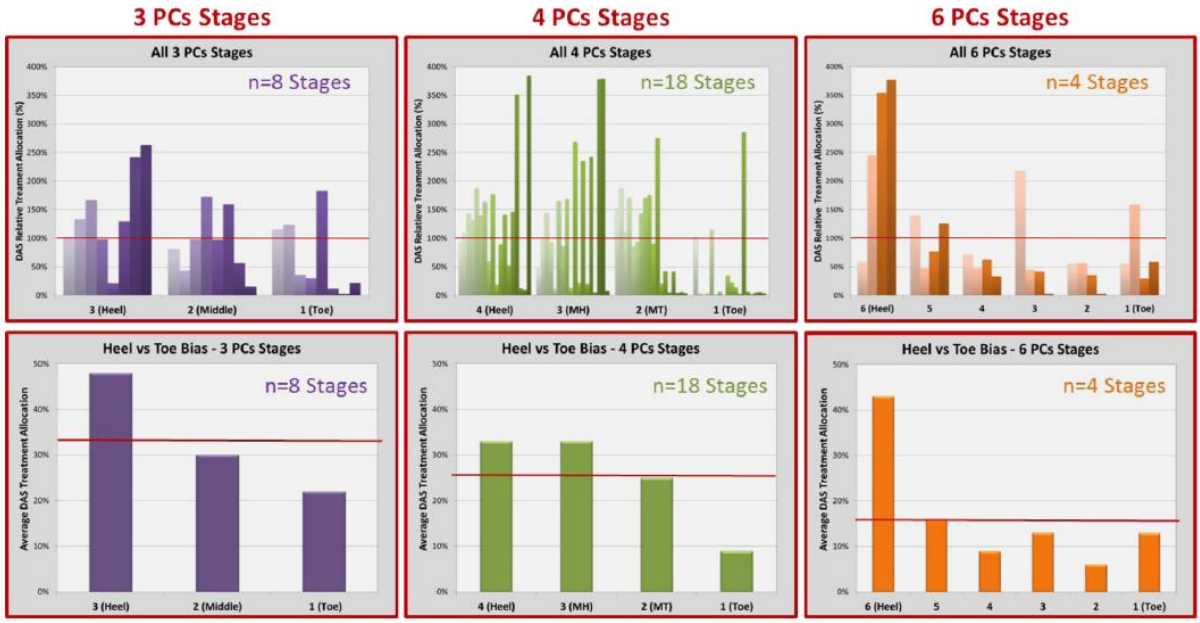

Figure 5.1: Field observation of treatment distribution. (Ugueto et al., 2016)

Wheaton et al. (2016) studied 14 plug-and-perf stages with 3 to 6 clusters per stage. And the heel biased treatment distribution trend has been observed consistently. In some

cases, the heel cluster takes most of the treatment. In other cases, the second cluster from the heel takes most treatment. Their results are shown in Fig. 5.2.

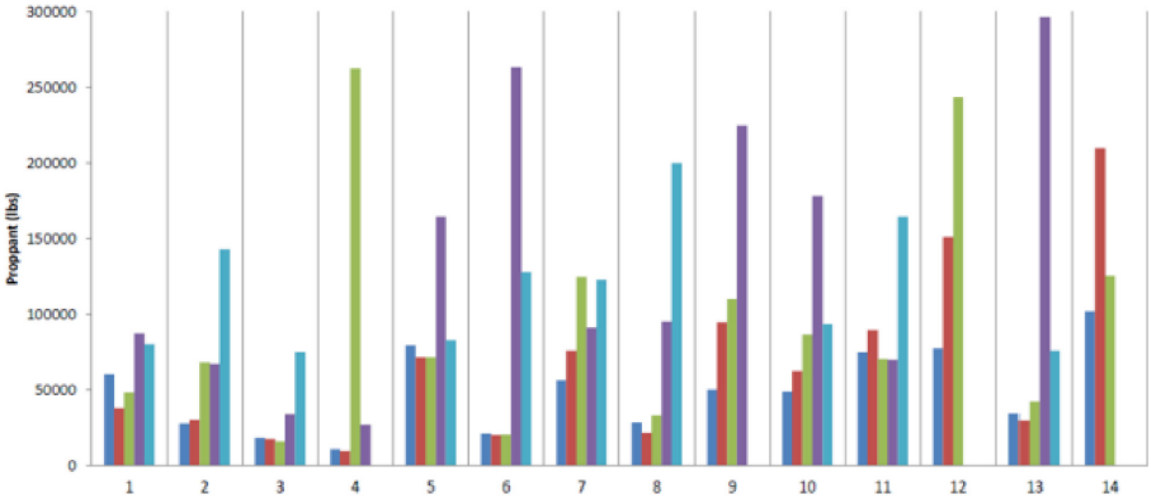

Figure 5.2: Field observation of treatment distribution. The bars on the right are the heel clusters for each stage. (Wheaton et al., 2016)

Many possible reasons can help explain the non-uniform treatment distribution: fracture interference, reservoir heterogeneity, natural fractures, stimulation design and so on. Although all these reasons can lead to the uneven stimulation of multiple clusters in plug-and-perf stages, it is difficult to explain why most of the dominant clusters are at the heel-side of a stage.

In this chapter, we work on modeling the non-uniform treatment distribution among multiple fractures with our newly developed fluid and proppant distribution model. Our results provide an alternate physical reason for the heel biased treatment distribution.

5.2. METHODOLOGY

The study of non-uniform proppant transport into multiple perforated clusters is performed following three steps: 1). Simulate proppant transport from the wellbore into perforations using coupled Computational Fluid Dynamics - Discrete Element Method (CFD-DEM); 2). Obtain Proppant Transport Efficiency (PTE) correlations through statistical analysis, and 3). Apply the PTE correlations to multi-fracture modeling. The first two steps are accomplished by Wu Chu-Hsiang. And they are explained briefly for ease of understanding of this Chapter. For more details of the CFD-DEM work, please refer to Wu and Sharma (2016).

5.2.1. Simulation of Proppant Transport

In the first step, simulation of proppant transport in the wellbore and into a single perforation is carried out using the CFD-DEM simulator (Goniva et al. 2012; Mondal et al. 2016). The simulation set up is shown in Fig. 5.3. The simulation domain includes a section of a wellbore (approximately 1 ft) and a perforation on one side of the wellbore. Slurry (a mixture of fluid and proppant) is injected from one end of the wellbore. When the slurry passes by the perforation, part of the fluid and proppant exit from the perforation, the remaining fluid and proppant flow downstream of the wellbore.

We define two parameters: Perforation Flow Ratio (PFR) is defined as the ratio of volumetric fluid rate exit from the perforation versus volumetric fluid rate injected into the wellbore, as shown in Equation 5.1. Proppant Transport Efficiency (PTE) is defined as the ratio of proppant mass rate exit from the perforation versus the proppant mass rate injected upstream of the perforation, as shown in Equation 5.2.

$$PFR = \frac{q_{perf}}{q_{upstream}} \tag{5.1}$$

$$PTE = \frac{m_{perf}}{m_{upstream}} \tag{5.2}$$

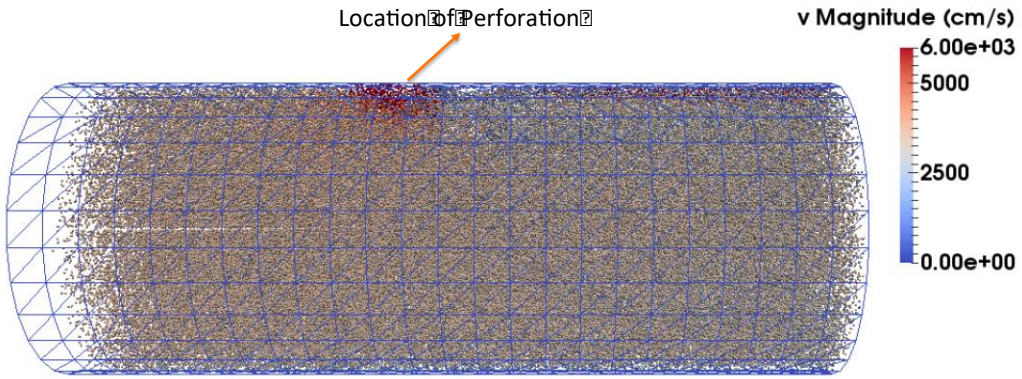

Figure 5.3: The CFD-DEM simulation domain. (Wu & Sharma, 2016).

Both PFR and PTE are computed and recorded after the simulation reaches equilibrium. These results have been validated against experiments as shown in Wu and Sharma (2016). A series of simulations have been carried out to obtain the PTE, with parameters close to field conditions. Some of the results plotted as PTE versus PFR are shown in Fig. 5.4.

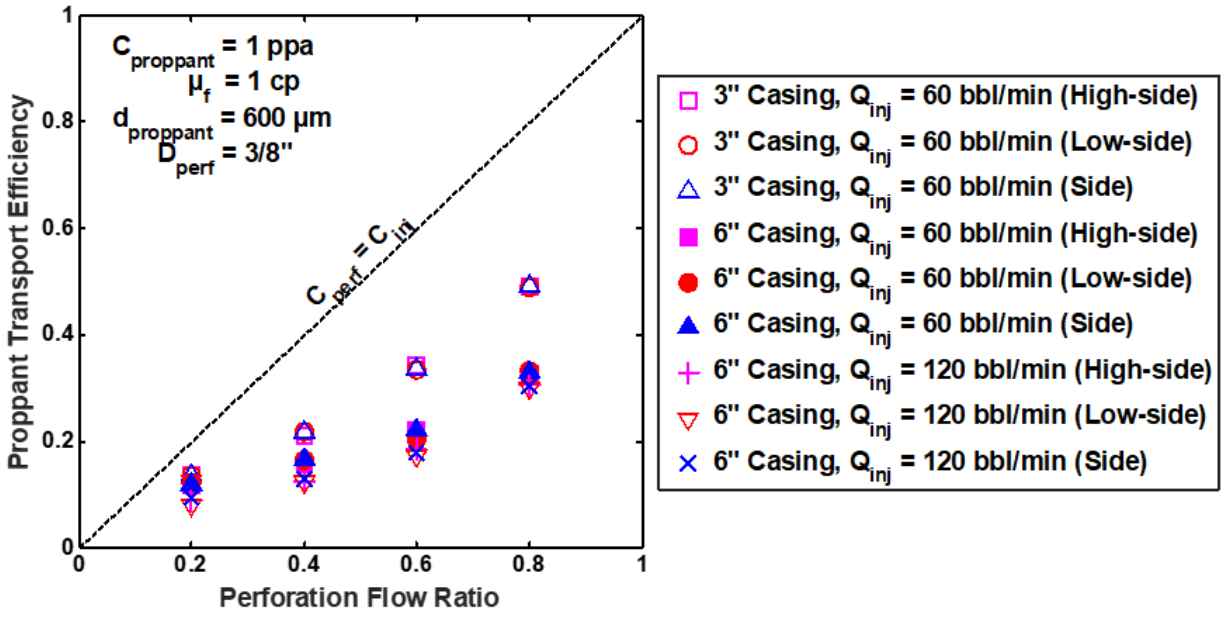

Figure 5.4: Some results of the CFD-DEM simulation. (Wu & Sharma, 2016).

In Fig. 5.4, the diagonal dashed line indicates PTE = PFR, which means that the proppant follows the fluid ratio to exit the perforation. It is shown from the simulation that this is not always the case.

Sometimes, the results are below the dashed line, meaning that less proppant exits the perforation than fluid, due to the inertia of the proppant. Therefore, the slurry that exits from the perforation has a lower proppant concentration than the slurry upstream of the perforation. And the slurry downstream the perforation will then have a higher proppant concentration. This is the most common case under field conditions.

Sometimes, the results are above the dashed line, meaning that more proppant exits the perforation than fluid. This happens mostly for low rate (< 6 bpm) and when the perforation is at the low side of the wellbore. Proppant settles due to gravity and exits from the perforation.

5.2.2. PTE versus PFR Correlations

The results from the last section are statistically analyzed to obtain curves of PTE versus PFR as a function of a series of parameters. In total, 180 simulations were used, and 45 correlations were generated. The correlations are in a format of fourth order polynomials as shown in Equation 5.3.

$$PTE = C_1(PFR)^4 + C_2(PFR)^3 + C_3(PFR)^2 + C_4(PFR) \quad (5.3)$$

Where C_1 to C_4 are fitted coefficients that are functions of upstream flow rate, upstream proppant concentration, wellbore diameter, perforation diameter, flow properties, proppant properties and so on as shown in Equation 5.4.

$$C_i = f(D_{well}, D_{perf}, c_{proppant}, d_{proppant}, \rho_{proppant}, Q_f) \quad (5.4)$$

Where D_{well} is wellbore inner diameter, D_{perf} is perforation diameter, $c_{proppant}$ is the proppant concentration, $d_{proppant}$ is the proppant diameter, Q_f is the wellbore fluid flow rate at the upstream of the perforation. An example set of C_1 to C_4 is shown in Table 5.1.

Parameter	Value	Parameter	Value
Casing Diameter (in.)	3	Perforation Diameter (in.)	3/8
Proppant Concentration (ppa)	3	Proppant Diameter (μm)	600
Proppant Density (g/cm^3)	2.65	Wellbore Flowrate (bpm)	30
PTE Curve Parameters			
C1	4.06	C2	-5.79
C3	2.43	C4	0.30

Table 5.1: PTE Correlation Example.

The PTE correlation in Table 5.1 is plotted in Fig. 5.5. It is shown that, under the condition of Table 5.1, the PTE versus PFR curve is under the diagonal line at all PFR values, which means that under this condition, due to the inertial effect of proppant, the ratio of proppant entering the perforation would always be lower than that of fluid. If the fluid ratio entering the perforation is known, the proppant ratio can be read from the Fig. 5.5.

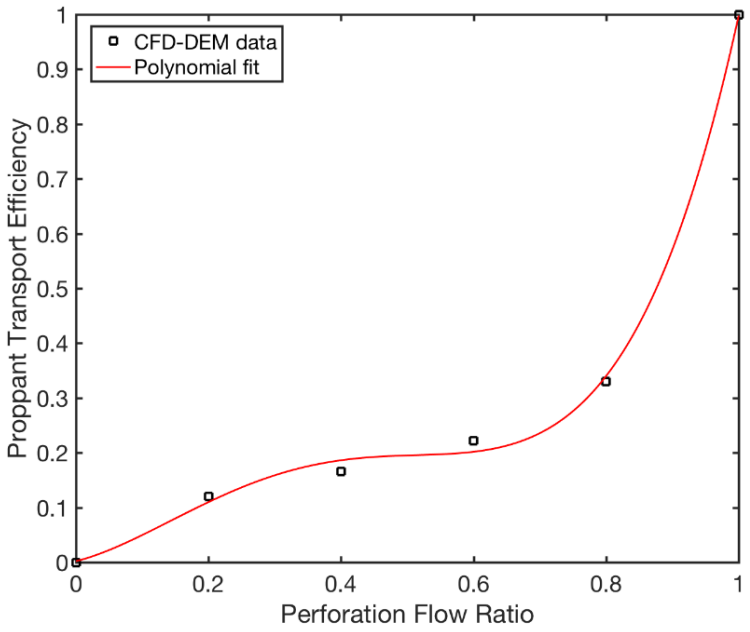

Figure 5.5: An example of the PTE versus PFR correlation.

The ranges of parameters the correlations apply are summarized in Table 5.2. The impact of perforation phasing was also investigated. We observe that when the flow rate in the wellbore is above 6 bbl/min, the PTE is not sensitive to the perforation orientation. When the flow rate is below 6 bbl/min, settling becomes important, and perforations at the low side of the wellbore tend to receive more proppant than those at other orientations.

Parameter	Range
Casing Diameter (in.)	3, 6
Perforation Orientation	High-side, Low-side, Side
Perforation Diameter (in.)	3/8, 1/2
Proppant Diameter (μm)	600, 1260
Proppant Density (g/cm^3)	1.54, 2.65, 3.56
Proppant Concentration (ppa)	1, 3
Wellbore Flow Rate (bbl/min)	6, 15, 30, 60, 120
Fluid Density (g/cm^3)	1
Fluid Viscosity (cp)	0.1, 1, 100 (Newtonian)

Table 5.2: Range of parameters the PTE correlations apply.

5.2.3. Non-Uniform Proppant Distribution among Multiple Clusters

The PTE correlations are incorporated in the multi-fracture model developed in Chapter 2, 3 and 4 to calculate dynamic proppant transport into multiple clusters. The total mass balance of proppant is conserved, as shown in Equation 5.5.

$$m_{inj} = \sum_{i=1}^{k} m_{perf,i} = \sum_{i=1}^{k} m_{upstream,i} \times PTE_{perf,i} \tag{5.5}$$

The PTE at each perf ($PTE_{perf,i}$) is calculated using local conditions of the wellbore and perforation, fluid and proppant properties, as well as the PFR value, as shown in Equation 5.3 and 5.4.

It is helpful to discuss the physical implications of incorporating the PTE versus PFR curves with the multi-fracture model. As shown in Fig. 5.4 and Fig. 5.5, the PTE

results are below the diagonal line under most field conditions. Proppant tends to accumulate in the wellbore as fluids leak off from the perforation, and proppant concentration in the wellbore increases. Regarding stimulation treatment involving multiple fractures, the PTE curve implies that the upstream/heel side fractures will receive slurry with lower proppant concentration than the injection, and the downstream/toe side fractures will receive slurry with higher proppant concentration.

Fig. 5.6 is an illustration of this phenomenon. There are 3 clusters, each with 4 perforations. The injection slurry rate is 30 bbl/min, and the injected proppant concentration is 3 ppa. It is assumed that the fluid is evenly distributed among the three clusters. And Fig. 5.6 plots the proppant concentration flows into each perforation. It is shown that for the first cluster, the proppant concentration is below the injected 3 ppa. And at the last perforation, the proppant concentration can become several times higher than the injected value. This high concentration at the toe side clusters increases the risk of pre-mature screen out.

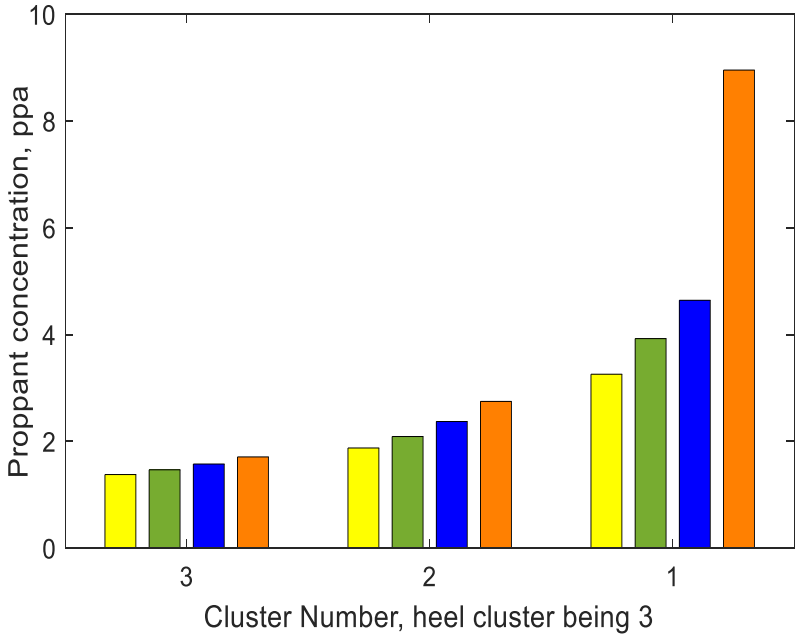

Figure 5.6: Implications of the PTE versus PFR curves.

In the multi-frac simulation, the near wellbore screen out caused by highly concentrated slurry is considered. It is worth pointing out that, screen out due to the high proppant concentration is not likely to occur in the perforation tunnel (Tran et al. 2009; Lafond et al. 2013). Instead, it is more likely to happen in the complex near-wellbore fractures in the near-wellbore region. And then the perforation loses connection to the reservoir, and fluid and proppant are re-distributed into the other active perforations. This process of screen-out and re-distribution continues until no perforation reaches the screen out criterion.

In this work, we assumed a simple criterion of a critical proppant concentration of 7.35 ppa (25% volumetric fraction) to be the screen out criterion. If the proppant concentration at a perforation exceeds the critical, screen out happens. The critical concentration is an empirical criterion, and a sensitivity study has been performed to

investigate the impact of the critical concentration. The results are presented later in this Chapter.

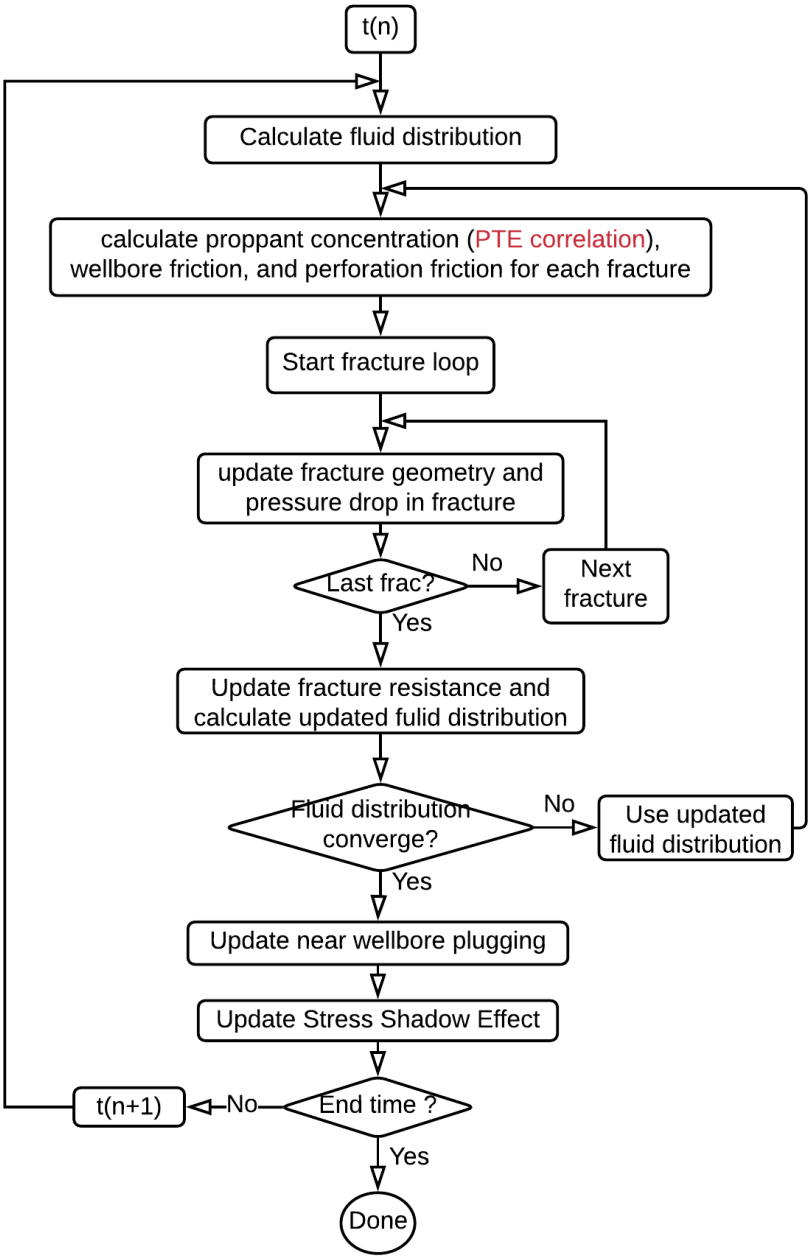

Figure 5.7: Calculation flow chart of the multi-cluster hydraulic fracturing model.

The calculation flow chart of the multi-fracture model is shown in Fig. 5.7. The fluid distribution is calculated using the Resistance Model developed in Chapter 4. And the fracture model can be either the PKN-Type 2D fracture model developed in Chapter 2 or the Pseudo-3D fracture model developed in Chapter 3. Modeling of the stress shadow effect has been discussed in Chapter 4. The calculation of the perforation and wellbore pressure drop are the same as the ones used in Chapter 4.

Note that the fluid distribution is the outside loop, and some other components of the model such as proppant distribution, fracture propagation and so on are solved inside the loop. Therefore, the dynamic fluid and proppant distribution and the fracture modeling are implicitly coupled. When the computation converges, both the slurry distribution and the fracture model are solved. The near-wellbore plugging and the stress shadow effect are evaluated explicitly after solving the fracture system in each time step.

5.3. RESULTS AND DISCUSSION

In this section, we try to capture the frequently observed heel-biased treatment distribution, using our multi-cluster hydraulic fracturing model, and the newly developed algorithms of dynamic fluid and proppant partitioning.

We set up a plug-and-perf stage based on information in Molenaar and Cox (2013). It is a multi-stage cemented liner completion in “a low permeability over-pressured sand/siltstone reservoir”, monitored by fiber optic DAS and DTS. The fracturing stage was completed with 4 clusters with 50 m spacing. Each cluster has 5 perforations. During the treatment, the two clusters close to the toe were found to screen out early in the proppant stage. And the heel-side two clusters ended up receiving most of the treatment. The final sand placement was severely heel-biased.

Set up of the simulation is shown in Fig. 5.8. The heel-side fracture from the previous stage was included for stress shadow effect considerations. The distance between the toe cluster of the current stage to the heel fracture of the previous stage is 50 m. Simulation parameters not given in Molenaar and Cox (2013) are estimated. The estimated simulation parameters are shown in Table 5.3. A typical pumping schedule is used for the simulation, as shown in Fig. 5.9. The maximum slurry injection rate is 44 bbl/min. The proppant concentration ramps up from 0 to 3 ppa. The whole treatment lasted for about 115 minutes. The total proppant amount designed to pump is 100,000 lbm per cluster, or 610 lbm/ft. Some parameters not given in the paper are assumed. Our goal is not to numerically match the data, but rather to show that the proppant placement trends are consistent.

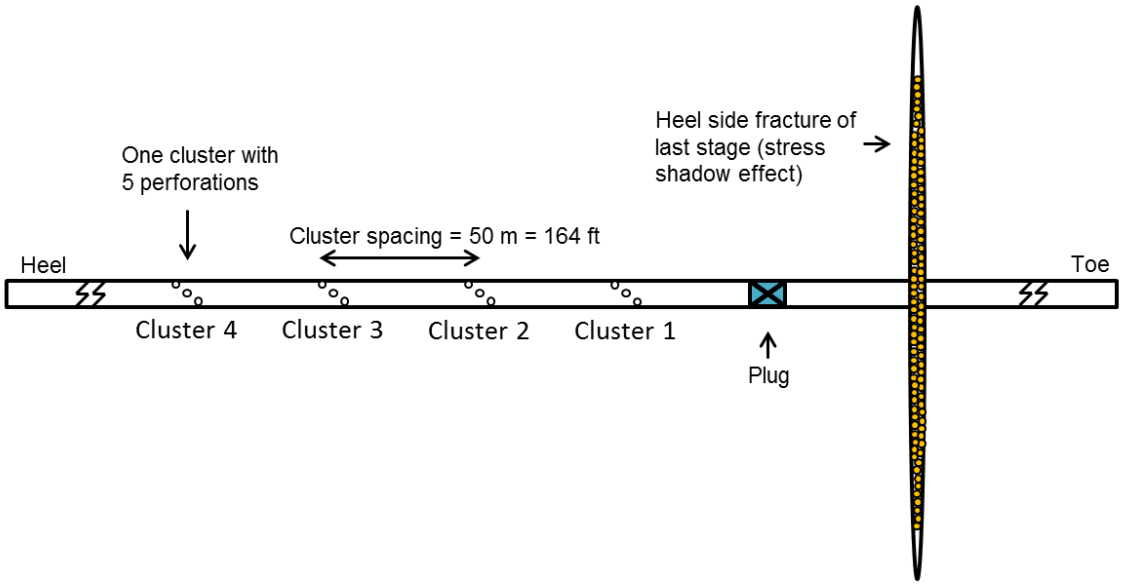

Figure 5.8: Simulation case set up.

Parameter	Value	Parameter	Value
Wellbore ID (in.)	3	Stimulation Depth (ft)	6818
Perforation Diameter (in.)	3/8	Pore Pressure (psi/ft)	0.44
Proppant Diameter (μm)	600	Min Hz Stress (psi/ft)	0.62
Proppant Density (g/cm^3)	2.65	Poisson's Ratio	0.23
Fluid Density (g/cm^3)	1	Young's Modulus (GPa)	5
Fluid Viscosity (cp)	1	Fracture Half Height (ft)	82

Table 5.3: Simulation parameters.

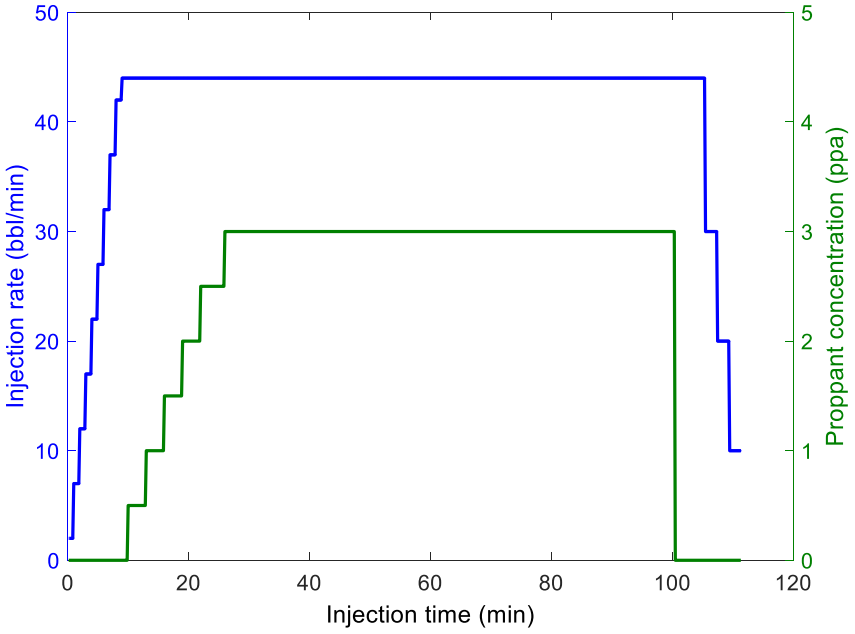

Figure 5.9: Simulated pumping schedule.

The simulation is performed with the 2D multi-fracture model with the fluid and proppant distribution calculation implicitly implemented. The simulated slurry injection rate into each cluster is shown in Fig. 5.10. In the pad stage (first 10 min of treatment),

cluster 1 (toe side cluster) receives less fluid, and cluster 4 receives more fluid, due to the stress shadow from the fracture of the previous stage.

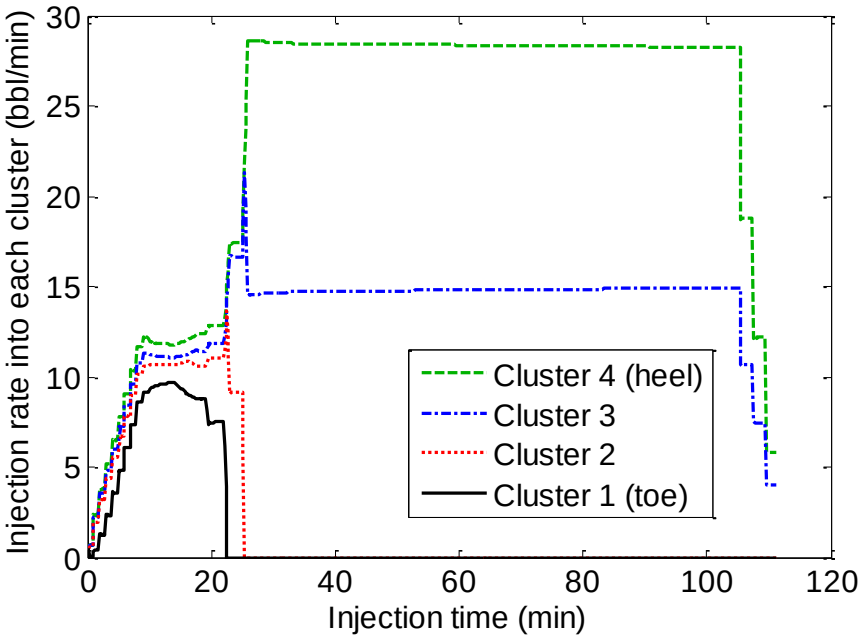

Figure 5.10: Simulated slurry rate into each cluster against time.

At early time of the proppant stage, the highly concentrated slurry flowing into the toe-side perforations increases the risk of premature screen-out. A critical proppant volume concentration (25%) is used as an empirical criterion for the beginning of proppant bridging in the near wellbore region. Perforations of cluster 1 (toe-side cluster) screened out gradually at the early time of proppant injection. And the fracturing fluid is re-distributed into the other active perforations. Eventually, all perforations in cluster 1 screened out. And shortly after that, cluster 2 also screens out, leaving only the two heel-side clusters to continue to receive treatment. In fact, 3 out of 5 perforations in cluster 3 reached the critical concentration and were plugged later in the treatment. And at the end of this

simulation, there were only 2 active perforations in cluster 3 while all 5 perforations of cluster 4 remained active.

Molenaar and Cox (2013) published the DAS and DTS results for this case, as shown in Fig. 5.11. It is clearly shown that the toe side clusters screened out early, and the heel side clusters dominate throughout the treatment.

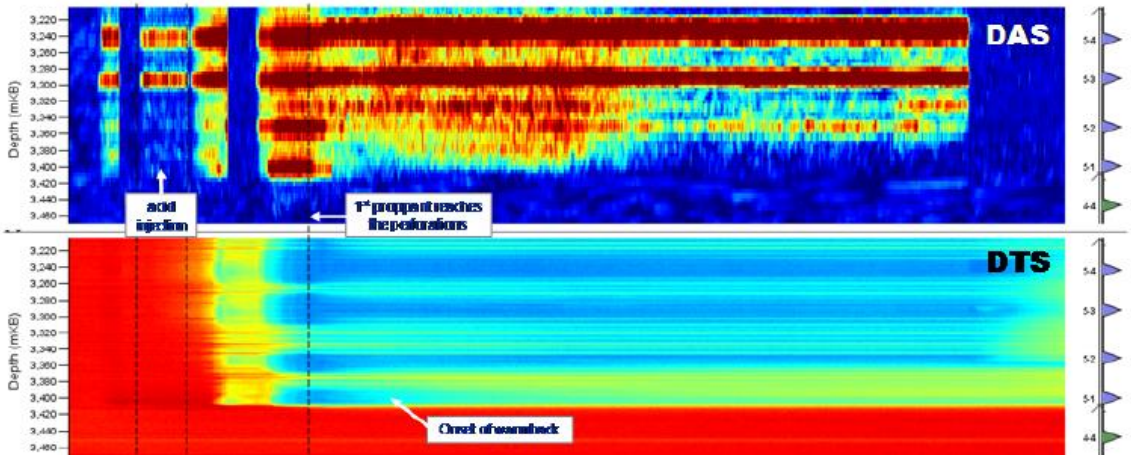

Figure 5.11: Field DAS, DTS observation. (Molenaar & Cox, 2013)

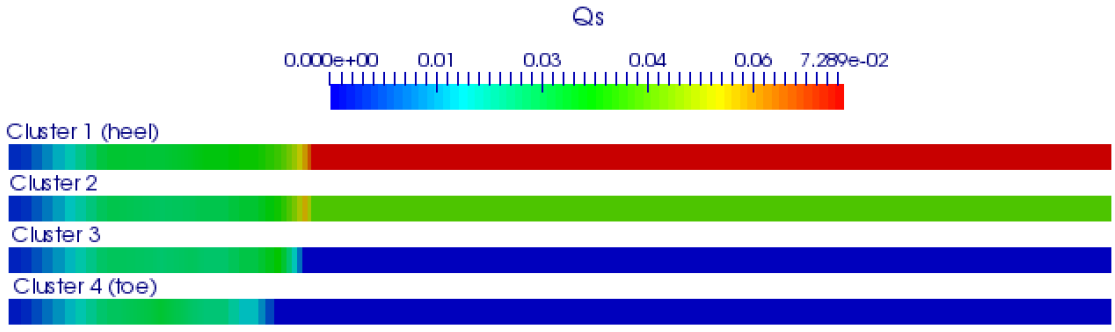

Figure 5.12: Simulated slurry distribution plotted in an analogous way as the DAS and DTS results.

We plotted our simulated slurry rate into each cluster in a comparable manner as shown in Fig. 5.12. The color scheme shows the injection rate. Warm (red) color shows high rate and cool (blue) color shows low rate. The comparison between Fig. 5.11 and 5.12 shows that we successfully captured pre-mature screen-out of the toe side clusters, as well as the dominant two heel side fractures. The simulated dynamic treatment partitioning agrees reasonably well with the field observation.

The simulated cumulative treatment distribution is shown in Fig. 5.13. It is shown that the toe side two clusters received little treatment due to premature screen-out while the heel side two clusters received about 90% of the treatment. Also, the proppant distribution and the fluid distribution is different. The heel side cluster received most of the fluid. And the second cluster from the heel received most proppant. This separation between fluid and proppant is because of the inertia of proppant. The inertial effect accumulates proppant towards to downstream of a perforation while fluid leaks off. Therefore, the heel side cluster receives more fluid than the second cluster. And the second cluster from the heel receives more proppant than the first.

The simulated cumulative fluid and proppant distribution can be validated with the field observation. The DTS observation is shown in Fig. 5.11. The blue color in the DTS plot means that the reservoir is cooled down because the injected fluid is of lower temperature than that of the formation. More fluid injection leads to more cool-down. And from the DTS result, we can see that little fluid went into the toe side clusters, and more fluid went into the heel cluster than the second cluster from the heel. Our simulation is consistent with the fluid distribution trend from the DTS observation.

The field sand distribution calculated from the DAS data is shown in Fig. 5.14. A comparison between Fig. 5.13 and 5.14 shows that the simulated proppant placement among the 4 clusters agrees with the field observed trend.

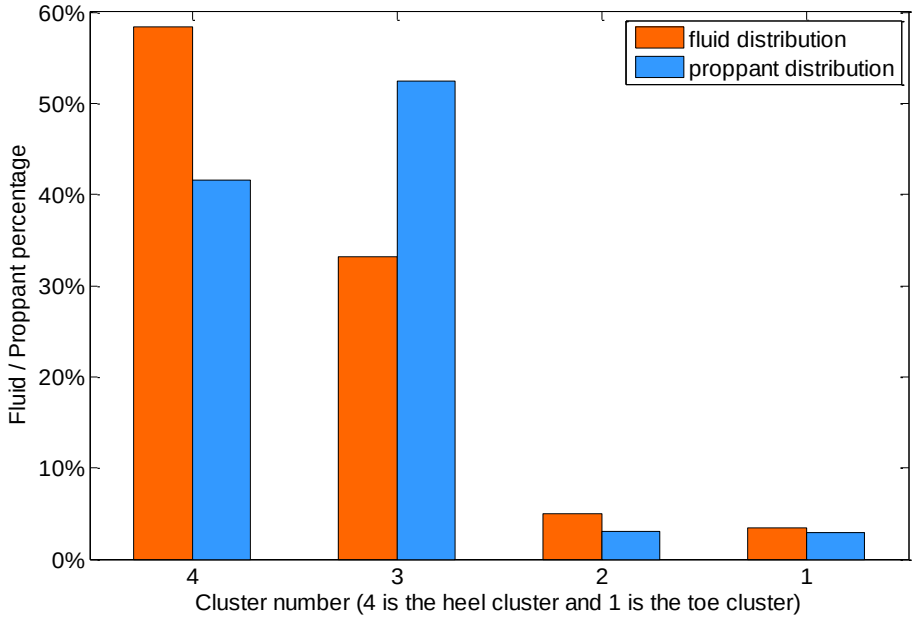

Figure 5.13: Simulated fluid and proppant distribution among the 4 clusters.

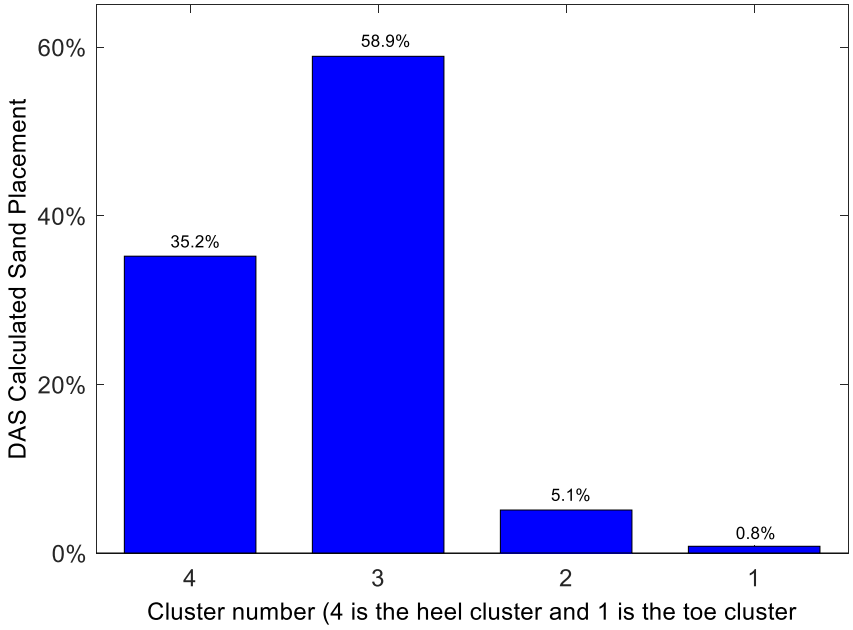

Figure 5.14: Field sand distribution among the 4 clusters calculated from DAS data. (Molenaar & Cox, 2013)

In the model, we used a simple empirical criterion for pre-mature screen-out in the near wellbore region: a critical proppant concentration. If the proppant concentration flowing into a perforation exceeds the critical proppant concentration, then, screen out happens in the near wellbore region. The perforation loses connection with the reservoir and no more fluid or proppant can flow into the perforation.

We have performed a sensitivity study to investigate the impact of the value of the critical proppant concertation on the final fluid and proppant distribution results. The same case has been performed with critical proppant concentration ranging from 6 to 7.5 ppa, and the results are shown in Fig. 5.15. In all cases, the final proppant distribution trend is consistent. The two toe side clusters are shown to screen out, and most proppant was placed in the heel side two clusters in all cases.

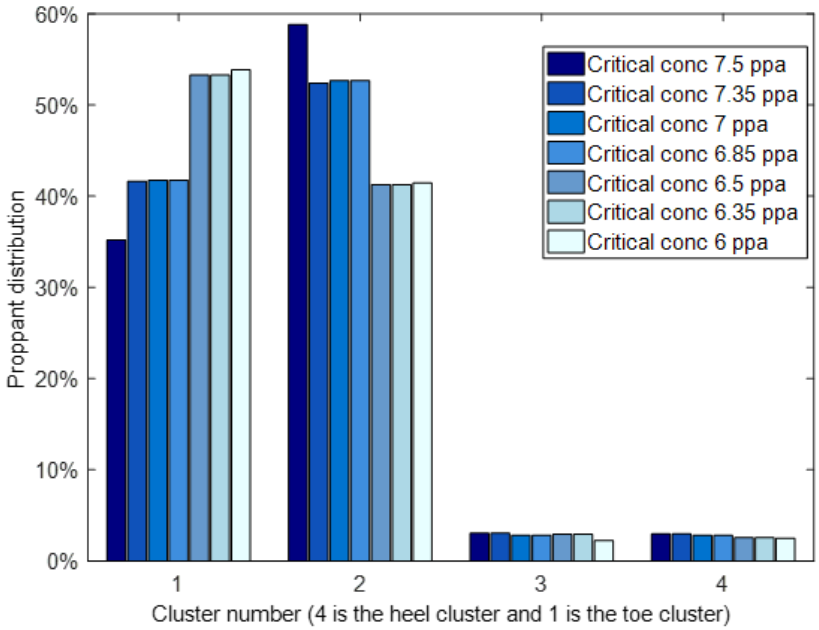

Figure 5.15: Impact of the critical proppant concentration value on final proppant distribution.

5.4. CONCLUSIONS

In the modeling of simultaneous propagation of multiple fractures, almost all previous simulators assumed that the proppant distribution ratio is the same as that of the fluid. However, both experimental work and simulation work in the literature have shown that this assumption is not valid. The inertia effect of solid particles can affect the transport of the proppant and cause some proppant to "miss the perforation exits". And this phenomenon can have a significant influence on the final fluid and proppant distribution among multiple fractures.

In this work, we try to quantify the distribution of fluid and proppant among multiple fractures, considering the inertia effect of proppant. Three steps were followed in this study. First, CFD-DEM simulations are performed to obtain PTE under different conditions. Secondly, the PTEs are statically analyzed to generate correlations of PTE versus PFR as a function of a series of parameters including wellbore and perforation properties, as well as fluid and proppant properties. Finally, the PTE correlations are incorporated into the muti-fracture model developed in the last three chapters to simulate the dynamic fluid and proppant partitioning among multiple clusters.

We validated our model with published field results. The simulated final fluid and proppant distribution agree well with the field observed trend by DAS and DTS. The treatment was heel biased with the two heel side clusters dominate and the toe side two clusters under-stimulated.

The heel biased treatment distribution in plug-and-perf stages have been observed consistently in many independent field studies. Results from Ugueto et al. (2016) and Wheaton et al. (2016) shown in Fig. 5.1 and 5.2 are two good examples. Although many factors can cause non-uniform treatment of multiple fractures, such as reservoir

heterogeneity, wellbore pressure drop and so on, it is difficult to explain the frequently observed heel-biased treatment distribution.

We propose an alternative explanation for the physics behind the heel biased treatment distribution. The inertia of the proppant particles accumulates proppant in the wellbore while fluid leaks off from the perforations. Thus, proppant concentration increases towards the toe side clusters. At the last perforation, the proppant concentration can be several times higher than the injection concentration. The highly concentrated slurry increases the risk of pre-mature screen-out at the toe side cluster. As the toe side clusters screen out, they stop receiving any fluid or proppant and the following treatment is re-distributed to other active clusters. Therefore, the final treatment distribution is heel biased.

The proppant transport model developed in this chapter is not restrained to the 2D and Pseudo-3D multi-fracture models. It can be applied to almost any fracture model with minor alteration.

In the following chapters, we apply the 2D and Pseudo-3D multi-fracture models to plug-and-perf designs and horizontal well refracturing studies. The goal is to develop strategies to improve the success of plug-and-perf stages and horizontal well refrac operations.

NOMENCLATURE

C_i	=	Fitting coefficients of a PTE versus PFR curve, i = 1 to 4
D_{perf}	=	Perforation diameter, L, m
D_{well}	=	Casing diameter, L, m
PFR	=	Perforation Flow Ratio
PTE	=	Proppant Transport Efficiency
$PTE_{perf,i}$	=	Proppant transport of efficiency of perforation i
Q_f	=	Wellbore fluid flow rate, L^3/T, m^3/s
$c_{proppant}$		Proppant concentration
$d_{proppant}$	=	Proppant diameter, L, m
m_{inj}	=	Total mass of proppant injected, M, kg
m_{perf}	=	Proppant mass flow through a perforation, M, kg
$m_{perf,i}$	=	Proppant mass flow through perforation i, M, kg
$m_{upstream}$	=	Proppant mass flow rate in the upstream of a perforation, M, kg
$m_{upstream,i}$	=	Proppant mass flow rate in the upstream of perforation I, M, kg
q_{perf}	=	Volumetric fluid flow rate through a perforation, L^3/T, m^3/s
$q_{upstream}$	=	Volumetric fluid flow rate upstream of a perforation, L^3/T, m^3/s
$\rho_{proppant}$	=	Proppant density, M/L3, kg/m3

REFERENCES

Goniva, C., Kloss, C., Deen, N.G., Kuipers, J.A.M., and Pirker, S. 2012. Influence of Rolling Friction on Single Spout Fluidized Bed Simulation. Particuology 10, no. 5, pp. 582–91. http://dx.doi.org/10.1016/j.partic.2012.05.002

Lafond, P.G., Gilmer, M.W., Koh, C.A., Sloan, E.D., Wu, D.T. and Sum, A.K., 2013. Orifice jamming of fluid-driven granular flow. *Physical Review E*, *87*(4), p.042204.

Molenaar, M.M. and Cox, B.E., 2013. Field cases of hydraulic fracture stimulation diagnostics using fiber optic distributed acoustic sensing (DAS) measurements and Analyses. Paper SPE 164030 presented at the SPE Unconventional Gas Conference and Exhibition, Muscat, Oman, 28-30 January 2013. http://dx.doi.org/10.2118/164030-MS

Mondal S., Wu C.-H., and Sharma M.M. 2016. Coupled CFD-DEM Simulation of Hydrodynamic Bridging at Constrictions. Int. J. Multiph. Flow, Volume 84, September 2016, pp. 245-263. http://dx.doi.org/10.1016/j.ijmultiphaseflow.2016.05.001.

Tran, T.V., Civan, F. and Robb, I.D., 2009. Correlating flowing time and condition for perforation plugging by suspended particles. SPE Drilling & Completion, 24(03), pp.398-403. SPE-120847-PA. http://dx.doi.org/10.2118/120847-PA

Ugueto, C., Gustavo, A., Huckabee, P.T., Molenaar, M.M., Wyker, B. and Somanchi, K., 2016, February. Perforation cluster efficiency of cemented plug and perf limited entry completions; Insights from fiber optics diagnostics. In *SPE Hydraulic Fracturing Technology Conference*. Society of Petroleum Engineers.

Wheaton, B., Haustveit, K., Deeg, W., Miskimins, J. and Barree, R., 2016, February. A case study of completion effectiveness in the eagle ford shale using DAS/DTS observations and hydraulic fracture modeling. In *SPE Hydraulic Fracturing Technology Conference*. Society of Petroleum Engineers.

Wu C.-H., Sharma, M.M. 2016. Effect of Perforation Geometry and Orientation on Proppant Placement in Perforation Clusters in a Horizontal Well. Paper SPE 179117 presented at the SPE Hydraulic Fracturing Technology Conference, The Woodlands, Texas, USA, 9-11 February 2016. http://dx.doi.org/10.2118/179117-MS

Wu, C.H., Yi, S. and Sharma, M.M., 2017, January. Proppant distribution among multiple perforation clusters in a horizontal wellbore. In *SPE Hydraulic Fracturing Technology Conference and Exhibition*. Society of Petroleum Engineers.

Yi, S.S., Wu, C.H. and Sharma, M.M., 2018. Proppant Distribution Among Multiple Perforation Clusters in Plug-and-Perforate Stages. *SPE Production & Operations*.

MAJOR SECTION 4: APPLICATIONS

In this section, we apply the multi-fracture models developed in the last two major sections to two important unconventional reservoir stimulation technologies: the plug-and-perf operation and horizontal well refracturing.

In Chapter 6, we study strategies to promote uniform fracture propagation in plug-and-perf operations with our model. We start by investigating how each design parameter such as the number of perforations per cluster, the size of the perforation, the injection rate and so on impact the final fluid and proppant distribution. After that, we developed an automated process to search for the optimum plug-and-perf design with multiple parameters. It is seen that the propped surface area can be improved greatly when multiple parameters are optimized together.

Chapter 7 presents the application of our models to the simulation of horizontal well refracturing employing diverting agents. Horizontal well refrac has many more fractures accepting fluid and a more complicated stress state in the reservoir compared to plug-and-perf stages. Two field cases were studied, and the workflow of initial completion – pore pressure depletion – refracturing was carried out for both cases. Our simulation results match the field diagnostic observations well. Strategies are developed to improve refrac success.

Chapter 6: Promoting Uniform Fracture Propagation in all Clusters in Plug-and-Perf Operations

6.1. INTRODUCTION

In Chapter 4 and 5, we solved the dynamic fluid and proppant partitioning among multiple clusters with novel methods. We have shown that the fluid and proppant distribution can be quite different. The inertial effect tends to accumulate the proppant towards the toe side clusters and causes pre-mature screen out. When the toe side clusters screen out, all the following treatment is distributed among the heel side clusters, and the final treatment proppant distribution is heel-biased.

This non-uniform proppant distribution has frequently been observed in the field with diagnostic methods including distributed acoustic sensing (DAS), distributed temperature sensing (DTS), tracers and micro seismic monitoring (Ugueto et al., 2016; Wheaton et al., 2016). The non-uniform distribution can affect final oil recovery negatively in several ways:

1). The under-stimulated clusters will not contribute to production as well as planned, limiting recovery from that part of the reservoir;

2). The over-stimulated clusters can receive many times the designed amount of treatment. The excessive amount of fluid and proppant creates big fractures and increases the chance of hitting offset wells. The interference between the treated well and the offset well can be detrimental to production from both wells.

In this chapter, we first quantitatively evaluate the impact of plug-and-perf design variables on the final proppant and fluid distribution. This analysis is applied to each variable, and directional suggestions are provided to improve plug-and-perf stage

efficiency. After that, we try to optimize the plug-and-perf design with multiple parameters being considered. An objective function is developed, and a Genetic Algorithm method is adopted for the optimization. This optimization process can be used to search for the optimum plug-and-perf design within a user provided parameter ranges.

6.2. Factors Affecting Final Treatment Distribution

The fluid and proppant placement among multiple clusters are affected by many factors as shown in Chapter 5. We organize the factors into two major categories: the perforation design and the pumping schedule. The perforation design parameters include the number of perforations per cluster (could be uniform or staggered), and perforation diameter. The pumping schedule design parameters include the proppant size and density, maximum injection rate and maximum proppant injection concentration, as well as the proppant concentration ramp-up speed. Both the perforation design and the pumping schedule can affect the final treatment distribution and fracture geometry significantly. Some other parameters are also investigated, including the wellbore diameter and cluster spacing. These factors are not found to dominate the final treatment distribution.

In this section, we examine how each parameter impacts the results and provide directional suggestions regarding each parameter.

6.2.1. Functions to Evaluate Plug-and-Perf Designs

To better understand how the parameters discussed above affect the treatment distribution of plug-and-perf stages, several functions are introduced to compare the results of different plug-and-perf stage designs. The Weighted Average and the Standard

Deviation describe the treatment distribution among clusters. The Hydraulic and Propped Surface Area are also calculated.

6.2.1.1. The Weighted Average

The Weighted Average (WA) is a function ranging from -1 to 1. It is an indicator of whether the treatment distribution is heel biased (-1 to 0) or toe biased (0 to 1). If WA is -1, it means all the treatment entered the heel cluster. On the other hand, if WA equals to 1, it means all the treatment entered the toe cluster. WA being 0 means that the treatment distribution is either uniform or symmetric.

The WA number is calculated as the summation of the fluid or proppant distribution multiplied by corresponding weight ratios, as shown in Equation 6.1.

$$wr(i) = -1 + \frac{2(i-1)}{n-1}, i = 1,2,\dots,n \tag{6.1a}$$

$$WA = \sum_{1}^{n} wr(i) * dis(i) \tag{6.1b}$$

Where n is the number of clusters, $wr(i)$ is the weight ratio for cluster i, and $dis(i)$ is the percentage of fluid/proppant distribution in cluster i.

The WA number is calculated for fluid and proppant distribution respectively. If the WA number of proppant is smaller than that of the fluid, it means the proppant distribution is more heel-biased than the fluid distribution, and vice versa.

6.2.1.2. The Standard Deviation

The Standard Deviation (SD) describes how uniform a treatment distribution is. An SD equal to 0 implies a uniform distribution. The larger the SD number, the more non-uniform the distribution is. The definition of SD is shown in Equation 6.2.

$$SD = \sqrt{\frac{\sum_{i=1}^{n}(dis(i) - \frac{1}{n})}{n-1}} \tag{6.2}$$

Where n is the number of clusters, and $dis(i)$ is the percentage of fluid/proppant distributed into cluster i. Like the WA number, the SD is calculated for both fluid and proppant.

The WA number or the SD number alone cannot describe the treatment distribution of a plug-and-perf stage completely. For both uniform and symmetric distributions (for example, 50% in the heel cluster, 50% in the toe cluster and 0 in the middle clusters), the WA number is 0. But the SD number for these two cases would be completely different. On the other hand, for a 100% heel biased distribution (all treatment ending up in the heel clusters), and a 100% toe biased distribution (all treatment ended up in the toe clusters), the SD number would be the same. But the WA number would be different.

Therefore, it is necessary to calculate both the WA and SD numbers to compare the results of different plug-and-perf designs. These two numbers combined, explain the change of the treatment distribution when a design parameter is changed.

6.2.1.3. The Hydraulic and Propped Surface Area

The Hydraulic Surface Area (HSA) is the total surface area created in all clusters, including both faces of both fracture wings, as shown in Equation 6.3.

$$HSA = 4 * \int_0^L h(x)dx \tag{6.3}$$

Where L is the length of one wing of the fracture and $h(x)$ is the height of the fracture.

The Propped Surface Area (PSA) is defined as the fracture surface area where proppant concentration exceeds 20% of maximum proppant concentration. The maximum

proppant concentration is 0.585 as defined in Chapter 2 and 3. The PSA is the total propped surface area created in all clusters.

For a good plug-and-perf stage, it is desired to have minimum values of WA and SD numbers, and maximum values for HSA and PSA.

6.2.2. The Base Case

We set up a Base Case similar to the case in Chapter 5. There are 4 perforation clusters with 50 m spacing. Each cluster has 5 perforations. The parameters used for the Base Case is shown in Table 6.1. The pumping schedule for the Base Case is shown in Fig. 6.1. And the simulated fluid and proppant distribution are shown in Fig. 6.2.

Parameter	Value	Parameter	Value
Wellbore ID (in.)	5.5	Res. Layer Thickness(ft)	164
Perforation Diameter (in.)	3/8	Res. Min Hz Stress (psi)	4227
Proppant Diameter (μm)	600	Stress Barrier (psi)	200
Proppant Density (lb/gal)	22.12	Res. Pore Pressure (psi)	3000
Fluid Density (lb/gal)	8.35	K_{Ic} (MPa $\sqrt{m}$)	1
Fluid Viscosity (cp)	3	Res. Permeability (μD)	50
Young's Modulus (MMpsi)	2.9	Res. Fluid Viscosity (cp)	5
Poisson's Ratio	0.23	Res. Porosity	0.08

Table 6.1: Parameters for the Base Case.

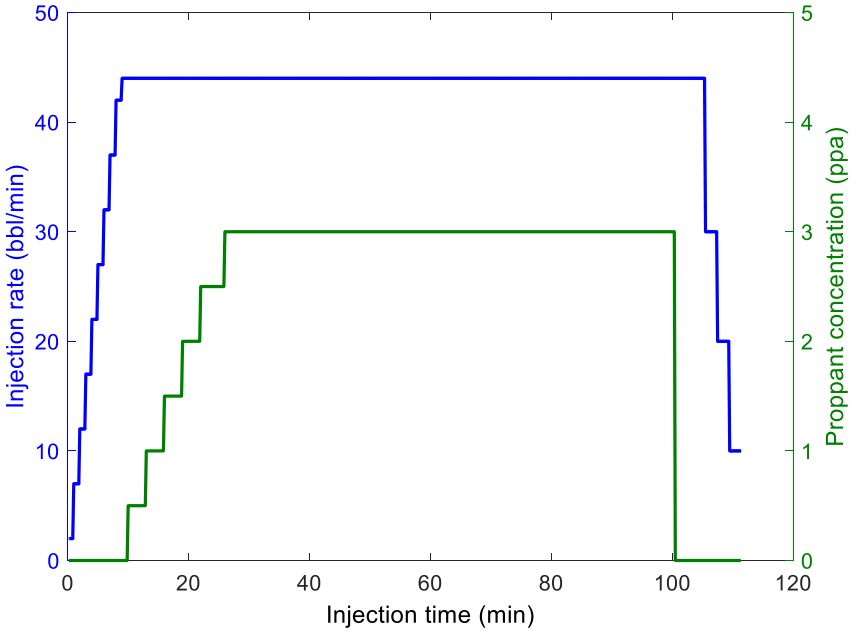

Figure 6.1: Pumping Schedule for the Base Case.

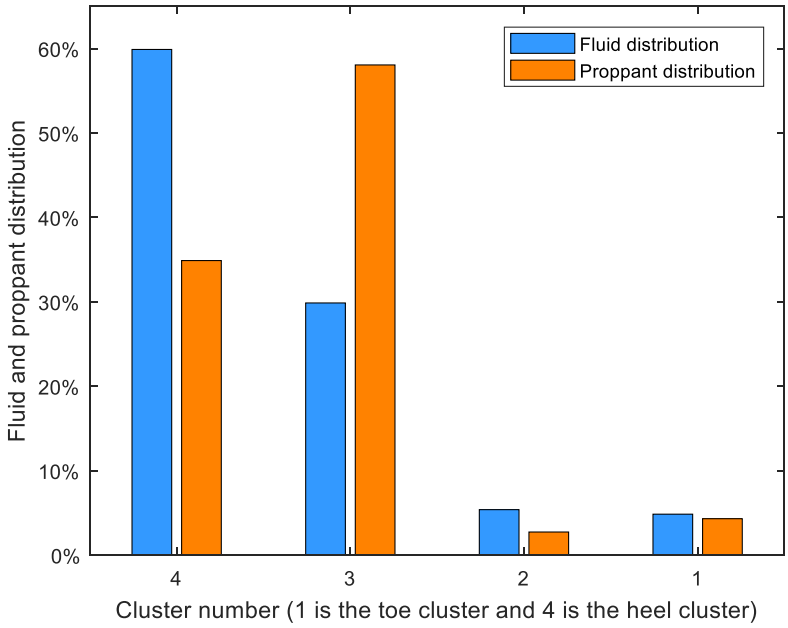

Figure 6.2: Simulated fluid and proppant distribution for the Base Case.

Note that this case is performed with the P3D multi-fracture model. And the final treatment distribution is very close to that obtained by the 2D PKN-Type multi-fracture model. This result is expected since the pressure drop in the fracture is only a small fraction of total pressure drop in the Resistance Model (please refer to Chapter 4). When the other parameters are the same, using 2D, P3D or fully 3D fracture models should provide very similar fluid and proppant distributions. All the simulations in this chapter are performed with the P3D multi-fracture model. The stress shadow effect is accounted for using the DDM method (please refer to Chapter 3, 4 and 5). Note that the stress shadow from the previous stages is not considered.

In the following study, the impact of each variable is studied by modifying the corresponding parameter from the Base Case. All other parameters remained the same as the Base Case.

One important thing to consider in the plug-and-perf design is the friction pressure drop in the perforation tunnel. In common plug-and-perf operations, the injection rate per perforation is usually 1 to 2 bpm, and the perforation pressure drop is in the order of several hundred psi. For the Limited Entry technique, the rates per perforation could be in the range of 3.3 to 3.6 bpm to generate over 1500 psi friction pressure differentials in the wellbore (Lagrone & Rasmussen, 1963; Somanchi et al., 2016). In this study, we keep the rate per cluster in all tested plug-and-perf designs within the range of 1 to 4 bpm to represent field conditions.

6.2.3. Effect of Perforation Design

Perforation designs include the number of perforations per cluster and perforation diameter. The perforation design has a significant impact on both fluid and proppant placement among multiple clusters.

6.2.3.1. Uniform Perforation Design

In a uniform perforation design, we put the same number of perforations in each cluster. Five cases are performed with perforations per cluster being 3, 5 (the Base Case), 8, and 10. All other parameters are the same as the Base Case. The final fluid and proppant distribution for the four cases are shown in Fig. 6.3 to Fig. 6.5.

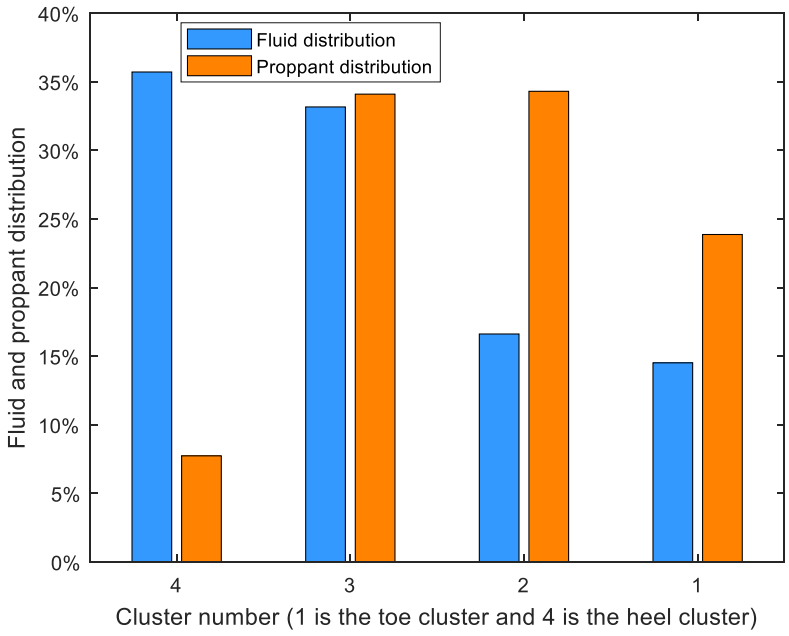

Figure 6.3: Simulated fluid and proppant distribution with 3 perforations per cluster.

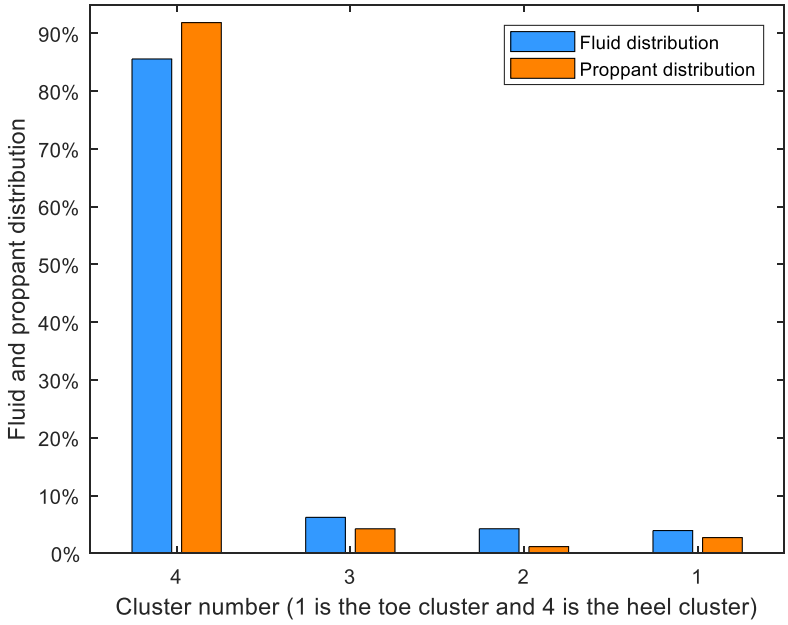

Figure 6.4: Simulated fluid and proppant distribution with 8 perforations per cluster.

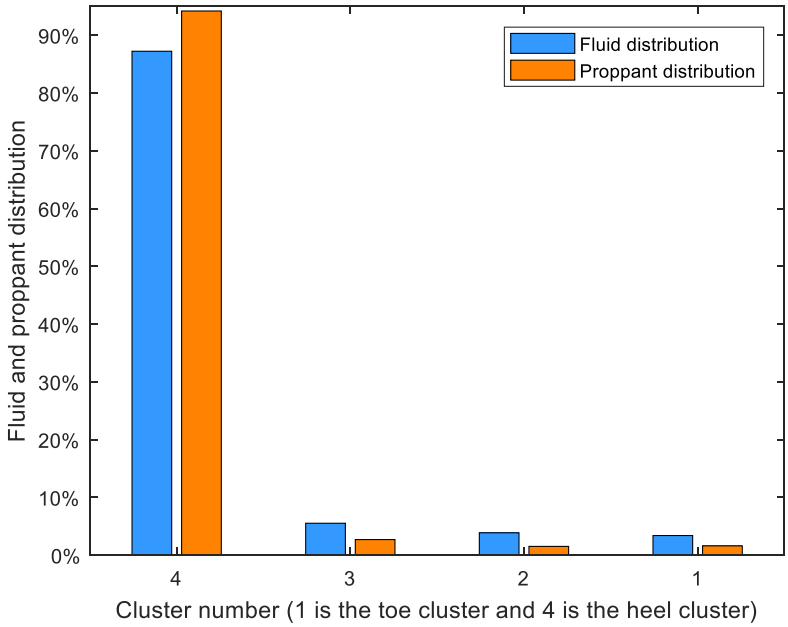

Figure 6.5: Simulated fluid and proppant distribution with 10 perforations per cluster.

Fig. 6.2 to Fig. 6.5 shows that as the number of perforations per cluster increases, the treatment is shifted towards the heel side clusters. When 3 perforations are designed for each cluster, all clusters got a noticeable amount of treatment. When 5 perforations are shot for each cluster, two heel-side clusters become dominant, and two toe-side clusters are under-stimulated. When each cluster has 8 or 10 perforation clusters, about 90% treatment ended up in the one heel-side clusters.

We can compare these cases more clearly with the WA and SD numbers. The WA and SD of these 4 cases are summarized in Fig. 6.6 and Fig. 6.7 below.

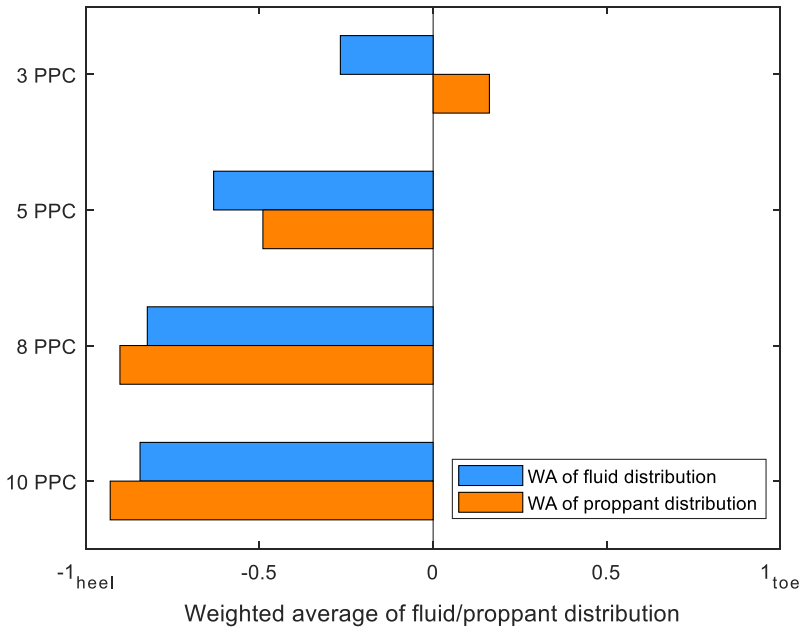

Figure 6.6: The WA numbers for the uniform perforation design cases. “PPC” is short for “perforations per cluster”.

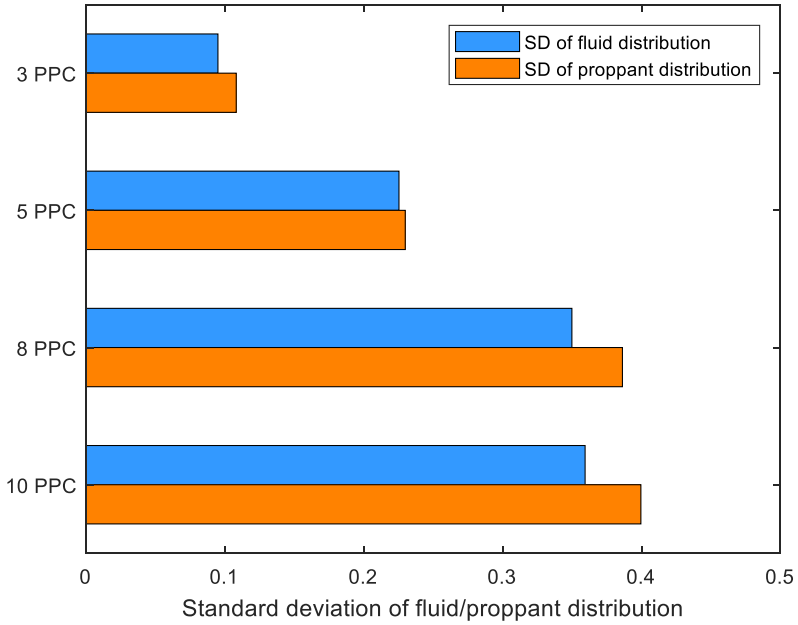

Figure 6.7: The SD numbers for the uniform perforation design cases. “PPC” is short for “perforations per cluster”.

Fig. 6.6 shows that as the number of perforations per cluster increases, both fluid and proppant distribution among the four clusters become more heel-biased. Similarly, Fig. 6.7 shows that as the number of perforation per cluster increases, both fluid and proppant distribution among the four clusters become more non-uniform.

The reason for the treatment distribution to become more heel-biased as the number of perforations per cluster increases can be explained by the inertia of the proppant. As the slurry flows through a perforation, more fluid leaks off than proppant. Therefore, slurry concentration is higher downstream of the perforation than upstream of it. As the perforation number increases, the slurry must flow past more perforations before it reaches the toe cluster, and the slurry concentration increases more. The higher slurry concentration at the toe side, the higher the risk of screen out. When the toe cluster screens out, it stops receiving any fluid or proppant, and the slurry is re-distributed to other clusters. Therefore,

more perforations per cluster magnify the inertial effect, and this increases the chance of pre-mature screen out at the toe side clusters.

The plots of the WA number and the SD number (Fig. 6.6 and Fig. 6.7) are good representations of the fluid and proppant distribution among multiple clusters (Fig. 6.2 to Fig. 6.5). For brevity, only the WA and SD plots are shown for most of the following cases. The fluid and proppant distribution figures not shown in this chapter can be found in **Appendix B**.

The HAS and PSA of the 5 cases with different perforation number are summarized in Fig. 6.8. It is shown that when the treatment distribution is closer to uniform, more hydraulic and propped surface areas are created. Compared to the case with 10 perforations per clusters, the case with 3 perforations per cluster created 8 % more HSA and 71.4% more PSA. The increase of PSA is related to the fracture geometry. In the case with 3 perforations per cluster, the treatment distribution is more uniform, and the maximum fracture width is 2.865 mm. While in the case with 10 perforations per cluster, more than 90% of the treatment ended up in the heel cluster and the maximum fracture width is 3.339 mm. For the wider fracture, more proppant is needed to reach the same proppant volumetric concentration, and less propped surface area is created.

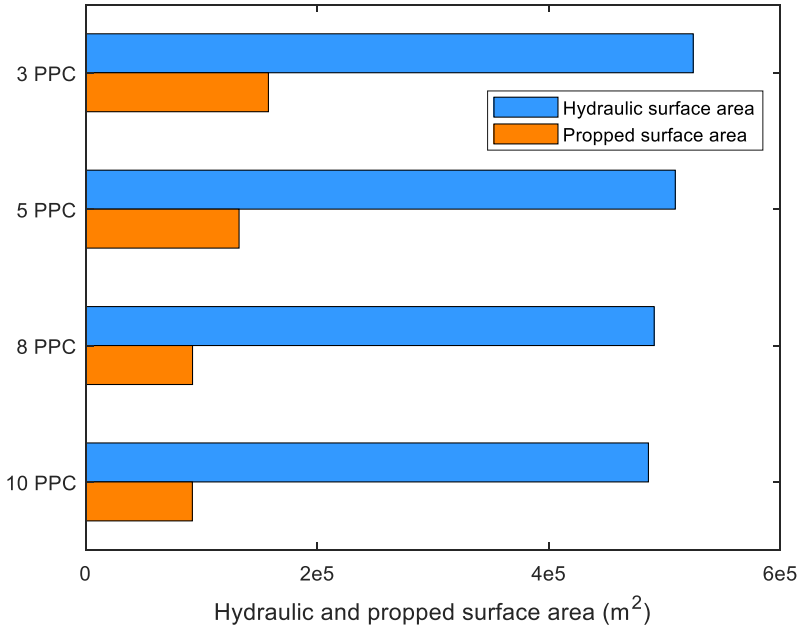

Figure 6.8: The HSA and PSA for the uniform perforation design case. "PPC" is short for "perforation per cluster".

6.2.3.2. Staggered Perforation Design

In the uniform perforation design, the number of perforations is the same for all clusters. For this section, we investigate a staggered perforation design. This design allows different numbers of perforations per cluster and can be used to investigate cases such as more perforations near the heel than near the toe, or more perforations near the toe than near the heel.

First, we investigate the impact of designing more perforations near the heel than the toe. The Base Case has 4 clusters with 5 perforations per cluster. We represent this design as 5-5-5-5. We can change this design to achieve new designs with more

perforations near the heel than the toe in two ways: 1) add more perforation near the heel (8-8-5-5) or 2) decrease perforation number near the toe (5-5-3-3).

The WA and SD numbers of these three cases are summarized in Fig. 6.9 and Fig. 6.10. The HSA and PSA are summarized in Fig. 6.11.

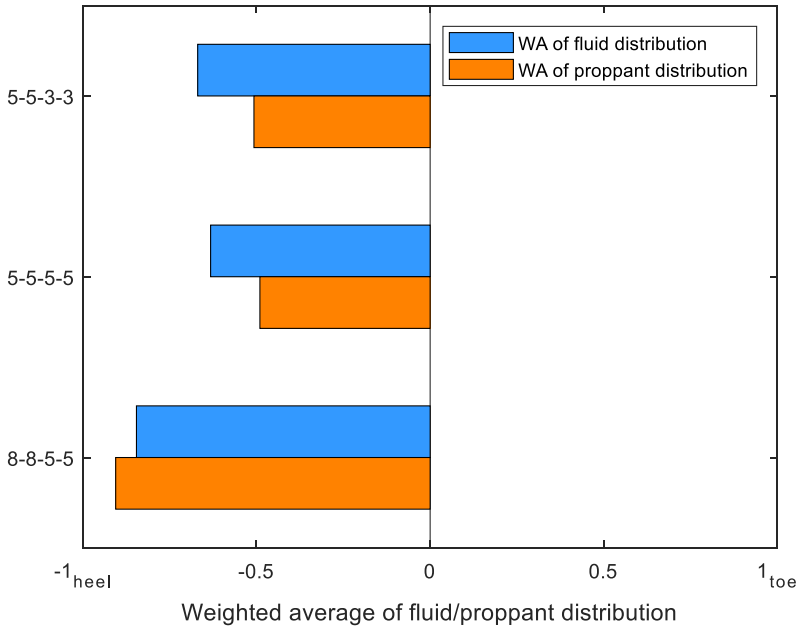

Figure 6.9: The WA numbers for the staggered perforation design cases, with more perforations near the heel than the toe.

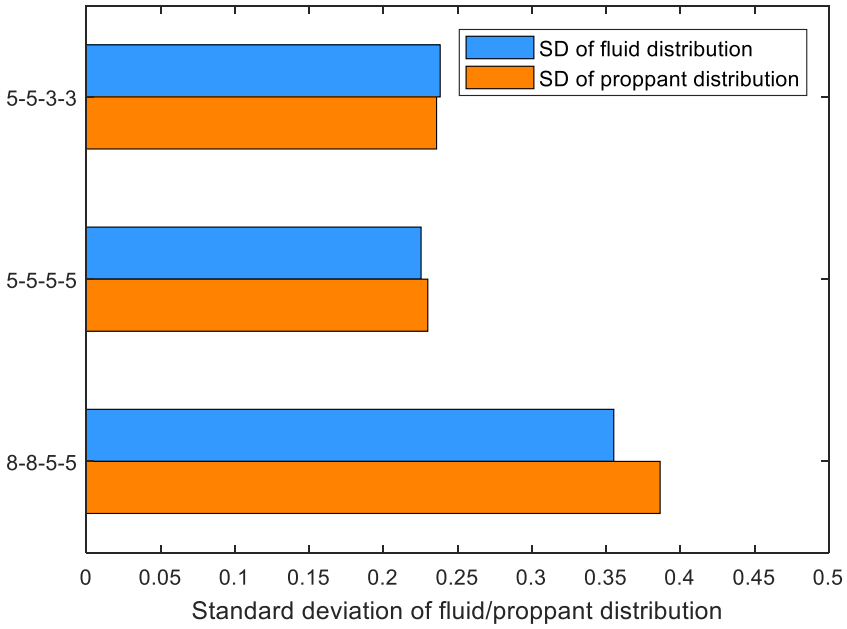

Figure 6.10: The SD numbers for the staggered perforation design cases, with more perforations near the heel than the toe.

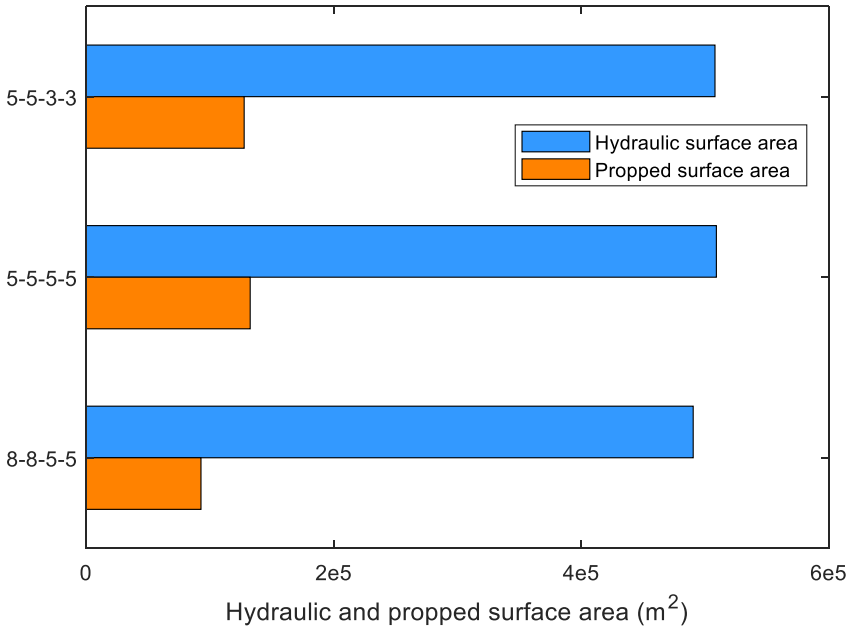

Figure 6.11: The HSA and PSA for the staggered perforation design cases, with more perforations near the heel than the toe.

It is shown that both cases with more perforations near the heel than the toe made the distribution more non-uniform, more heel-biased, and created less HSA and PSA than the uniform perforation case. The ranking of the three designs would be: 5-5-5-5 > 5-5-3-3 > 8-8-5-5.

Next, we investigate the impact of designing fewer perforations near the heel than the toe. Similarly, we can change the base design to achieve new designs in two ways: 1) add more perforation near the toe (5-5-8-8) or 2) decrease perforation number near the heel (3-3-5-5).

The WA and SD numbers of these three cases are summarized in Fig. 6.12 and Fig. 6.13. The HSA and PSA are summarized in Fig. 6.14.

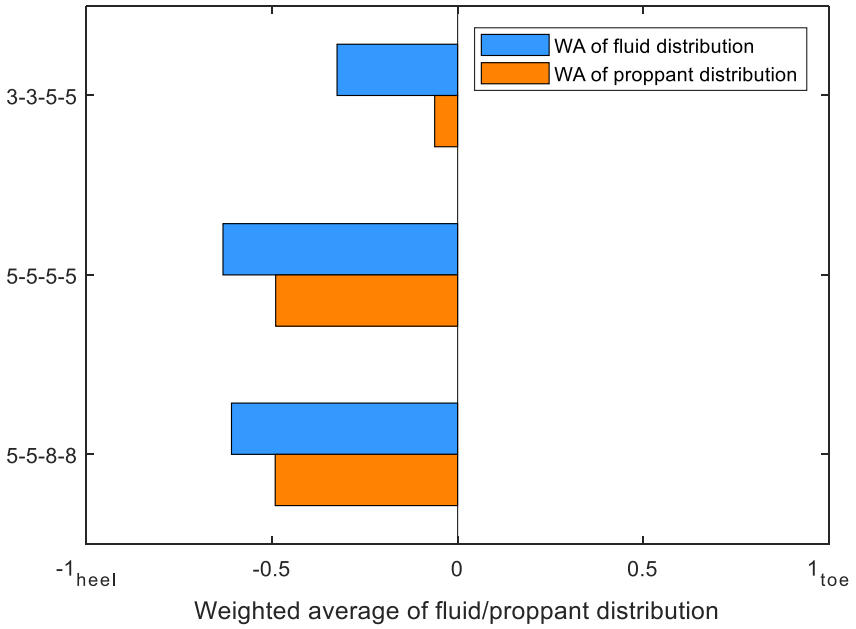

Figure 6.12: The WA numbers for the staggered perforation design cases, with fewer perforations near the heel than the toe.

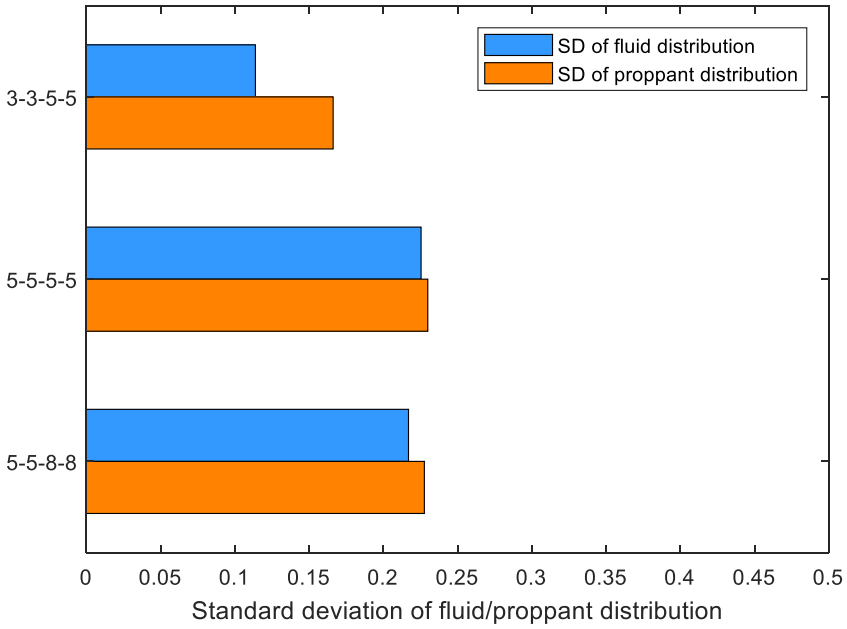

Figure 6.13: The SD numbers for the staggered perforation design cases, with fewer perforations near the heel than the toe.

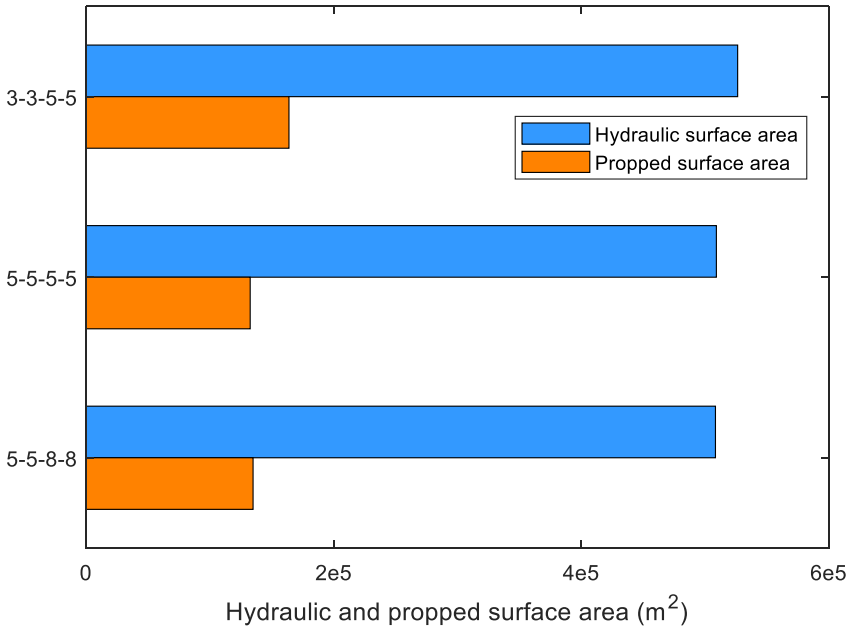

Figure 6.14: The HSA and PSA for the staggered perforation design cases, with fewer perforations near the heel than the toe.

It is shown that both cases with more perforations near the toe than the heel (3-3-5-5) and (5-5-8-8) made the distribution more uniform, less heel-biased, and created more HSA and PSA than the uniform perforation case (5-5-5-5). The case with design 3-3-5-5 is shown to improve both the treatment distribution and the surface area greatly. The ranking of the three designs would be: 3-3-5-5 > 5-5-8-8 > 5-5-5-5.

The results of staggered perforation design can be summarized. First, using fewer perforations near the heel than the toe is shown to have a positive impact on the efficiency of a plug-and-perf stage. Secondly, using more perforations near the heel than the toe is shown to impact the efficiency of a plug-n-perf stage negatively. Finally decreasing the perforation number for the heel side clusters can greatly improve the stimulation distribution of a plug-and-perf stage compared to a uniform perforation design. The fluid and proppant distribution plots for each case can be found in **Appendix B**.

6.2.3.3. Effect of Perforation Diameter

In this section, we investigate the impact of perforation diameter. The applicable range of the PTE correlation for perforation diameter is 0.375 to 0.5 inch. Beyond this range, the PTE correlation needs to be extrapolated (please refer to Chapter 5). The perforation size in the Base Case is 0.375 inch. Another case is performed with perforation size of 0.5 inch. The WA and SD numbers for these two cases are summarized in Fig. 6.15 and Fig. 6.16. The HSA and PSA are summarized in Fig. 6.17.

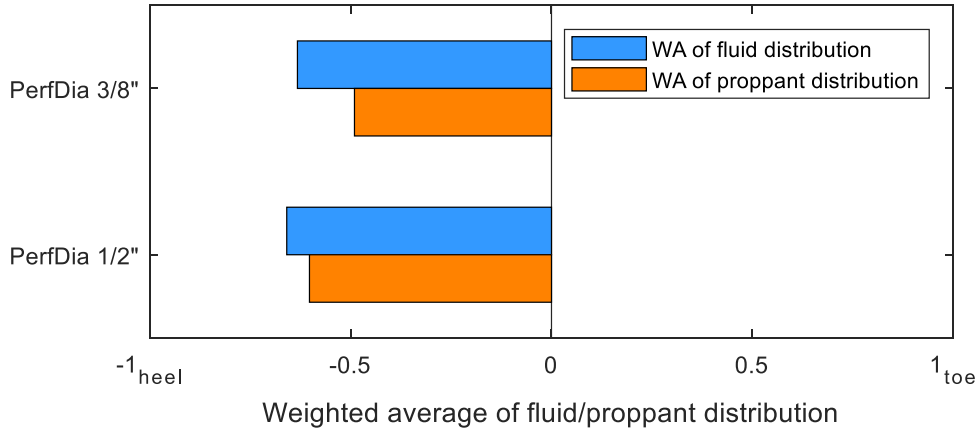

Figure 6.15: The WA numbers for plug-and-perf stages with different perforation diameters.

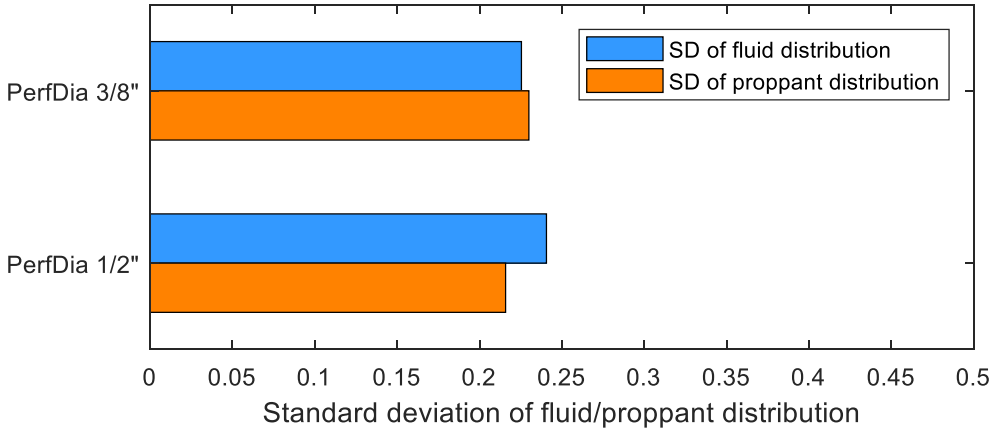

Figure 6.16: The SD numbers for plug-and-perf stages with different perforation diameters.

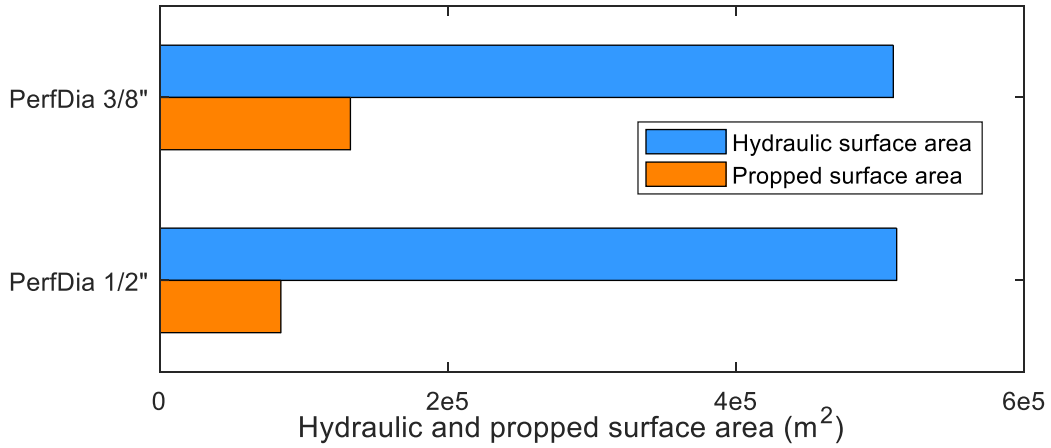

Figure 6.17: The HSA and PSA for plug-and-perf stages with different perforation diameters.

Fig. 6.15 shows that when the perforation size increases from 0.375 inch to 0.5 inch, the final distribution becomes more heel-biased. This can be explained by the PTE correlation, as shown in Fig. 6.18. When the perforation size changes from 0.375 inch to 0.5 inch, the Proppant Transport Efficiency (PTE value) increases when the PFR is between 0.4 to 0.6. Out of this PFR range, no significant increase in PTE can be observed. In fact, when PFR is equal to 0.2, the proppant intake is lower when the perforation diameter is 0.5 inch compared to 0.375 inch.

During multiple cluster stimulation, the PFR of the heel side perforations seldom exceeds 0.2. Therefore, the PTE for the 0.5-inch perforation could be lower than for the 0.375-inch perforation. More proppant is accumulated downstream, and this increases the risk of pre-mature screen out. Therefore, we observe from the simulations that when the perforation diameter is increased from 0.375 to 0.5 inch, the final treatment distribution is more heel-biased. We also observe that when the treatment is more heel-biased, less fracture area is created (HSA and PSA are lower). The fluid and proppant distribution for the 0.5-inch perforation case is given in **Appendix B**.

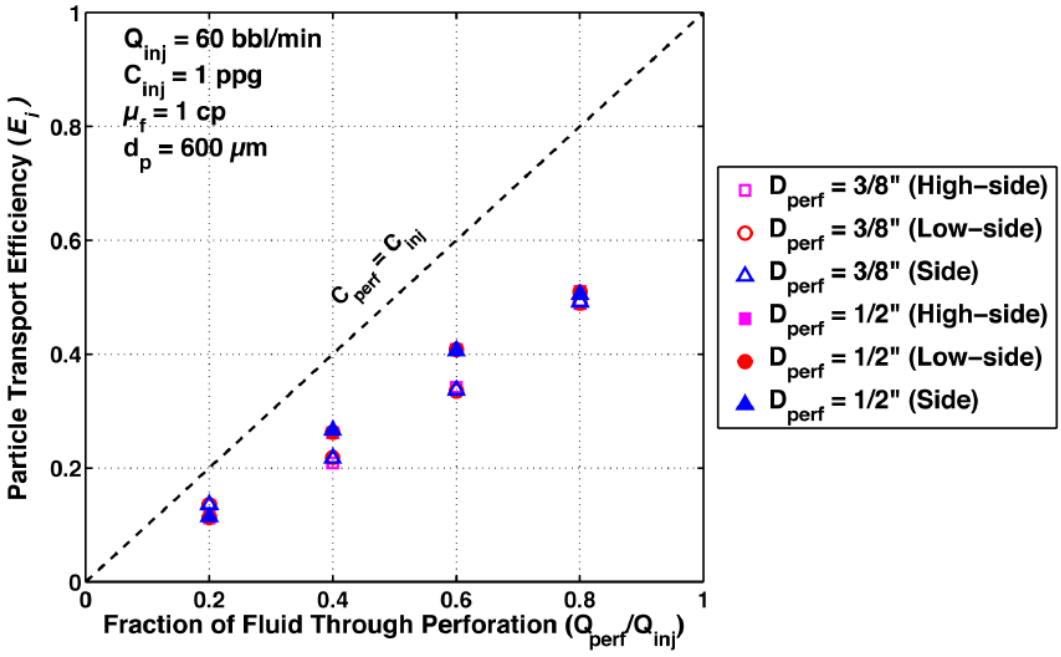

Figure 6.18: Impact of perforation size on PTE. (Wu & Sharma, 2016)

6.2.4. Effect of Pumping Schedule Designs

Pumping schedule designs include the proppant size and density, maximum slurry injection rate, maximum proppant injection concentration, as well as the proppant concentration ramp-up design. For the latter three parameters, it is difficult to study the impact of a single variable alone. The whole injection schedule needs to be updated to keep the total fluid and proppant volume conserved. For example, increasing the maximum slurry injection rate alone implies that a shorter time is needed to pump the designed volume. The pad stage would be shorter, and more proppant will be pumped at a lower concentration. Therefore, it is difficult to distinguish the impact of increasing maximum injection rate alone on the final treatment distribution. It is better to optimize multiple

parameters in the pumping schedule simultaneously than optimizing each one alone. The optimization of multiple variables will be discussed in the next section.

6.2.4.1. Effect of Proppant Size

In this section, we investigate the impact of proppant size. The applicable range of the PTE correlation for proppant size is 600 to 1260 μm. Beyond this range, the PTE correlation needs to be extrapolated (please refer to Chapter 5). Four different proppant sizes are tested by modifying the Base Case: 16-30 mesh (~800 μm), 35-50 mesh (~400 μm), 40-70 mesh (~300 μm), and 100 mesh (~150 μm). The proppant size used in the Base Case is 20-40 mesh (~600 μm).

The final treatment distribution as shown in Fig. 6.19 and 6.20. The simulation results show that different proppant sizes have a small impact on the WA and SD numbers. The reason is that when the injection rate is low (~ 0.6 bpm), increasing the proppant size magnifies the particle inertia and aggravates the non-uniform proppant distribution. But when the injection rate is high (~ 60 bpm), the effect of proppant size is less pronounced (Wu & Sharma, 2016). Another reason could be that the PTE correlation is extrapolated for some of the cases. Therefore, the results may not be very accurate.

However, differently sized proppants have considerable influence on the propped surface area created as shown in Fig. 6.21.

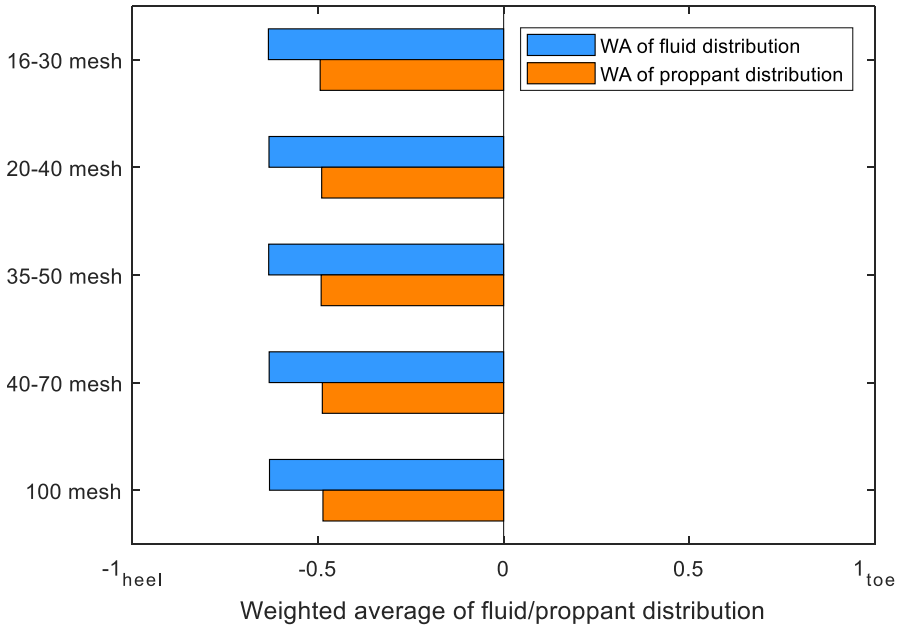

Figure 6.19: The WA numbers for plug-and-perf stages with different proppant sizes.

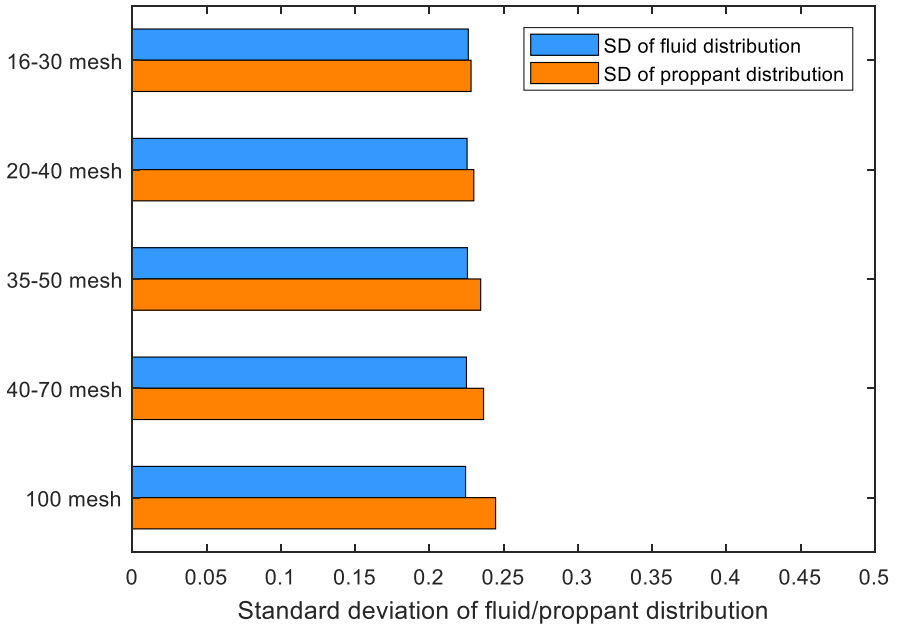

Figure 6.20: The SD numbers for plug-and-perf stages with different proppant sizes.

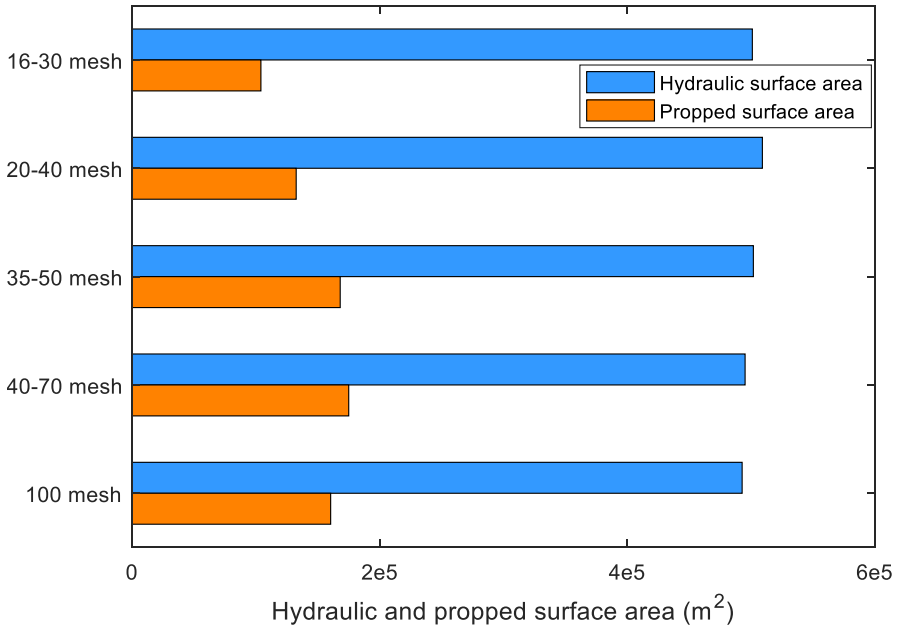

Figure 6.21: The HSA and PSA for plug-and-perf stages with different proppant sizes.

The proppant size affects the hydraulic and propped surface area in multiple ways:

1) Smaller proppant can travel deeper into the fracture and thus increase the propped surface area.

2) Smaller proppant settles less in the fracture than larger proppant. Less settling means higher proppant concentration in the slurry and more propped surface area.

3) Particle packs formed in the narrow section of the fracture with smaller proppant causes more pressure drop in the fracture than large proppant and can result in shorter fracture length.

Small sized proppants are commonly used in the development of unconventional reservoirs, to prop narrow fractures and natural fractures. The simulation results show that in general, using smaller sized proppant is beneficial for creating more PSA. The 100 mesh proppant is not performing better than the 40-70 mesh proppant for this case, because the

100 mesh proppant formed a high concentration pack near the tip of the fracture and caused a high pressure drop in the fracture. The fluid and proppant distribution figures for these cases can be found in **Appendix B**.

6.2.4.2. Effect of Proppant Density

In this section, we investigate the impact of proppant density. Three proppant density values are tested: 1540 kg/m^3, 2650 kg/m^3 (the Base Case) and 3560 kg/m^3. Changing proppant density has a big impact on the WA and SD numbers regarding final treatment distribution as shown in Fig. 6.22 and 6.23. The HSA and PSA plots comparison of the three cases are shown in Fig. 6.24.

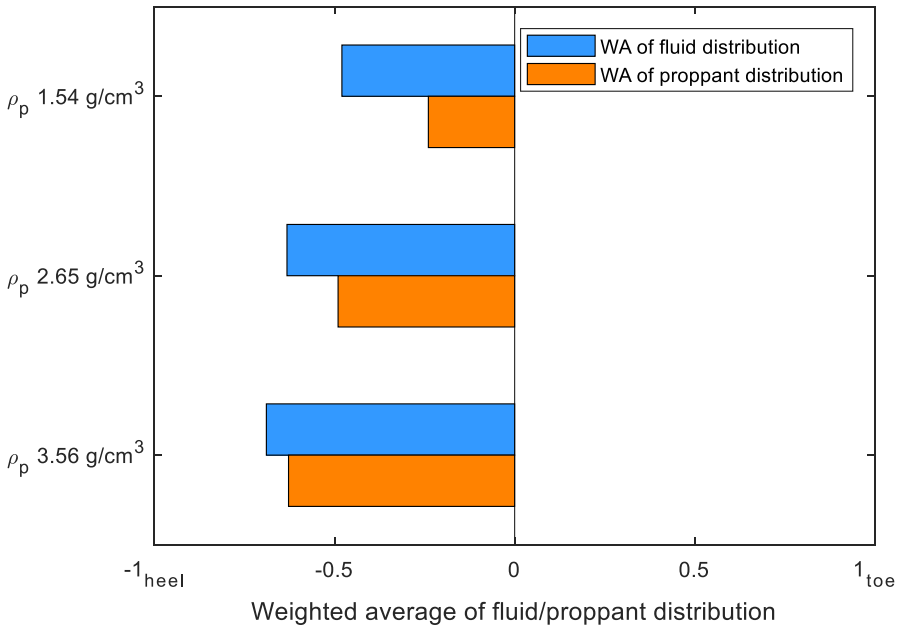

Figure 6.22: The WA numbers for plug-and-perf stages with different proppant densities.

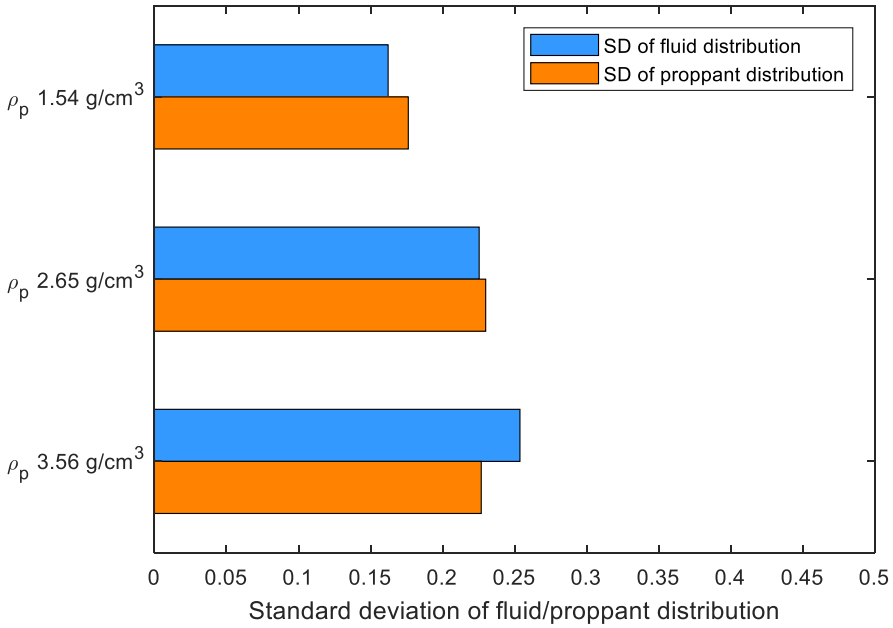

Figure 6.23: The SD numbers for plug-and-perf stages with different proppant densities.

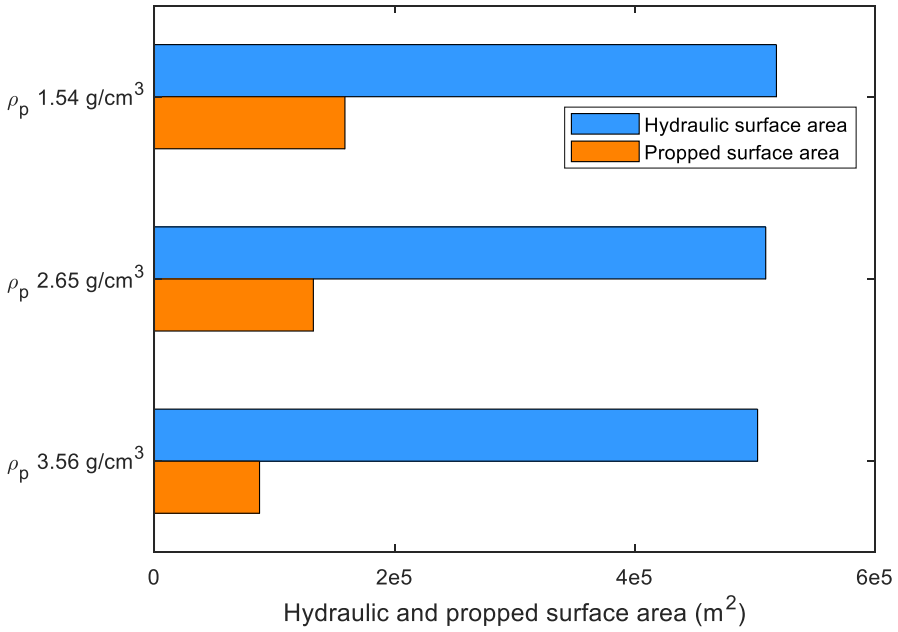

Figure 6.24: The HSA and PSA for plug-and-perf stages with different proppant densities.

It is seen that decreasing the proppant density makes the final treatment distribution more uniform, less heel-biased, and creates more propped surface area. The PSA increased 81.2% by changing the proppant concentration from 3560 kg/m^3 to 1540 kg/m^3 and keeping everything else the same. The fluid and proppant distribution figures for these cases can be found in **Appendix B**.

6.2.4.3. Effect of Maximum Injection Rate

In this section, we investigate the impact of maximum slurry injection rate. Five cases are designed with the maximum slurry injection rate being 30, 44 (the Base Case), 60, and 80 bpm. The total volumes of fluid and proppant are conserved. The maximum proppant injection concentration and ramp-up rate remain the same. It is important to point out that, changing the maximum slurry injection rate requires changing some other aspects of the pumping schedule at the same time. For example, the design with a larger injection rate takes less time to inject the designed volume.

The WA and SD numbers for the final treatment distribution are shown in Fig. 6.25 and 6.26. And the HSA and PSA plots of the three cases are shown in Fig. 6.27.

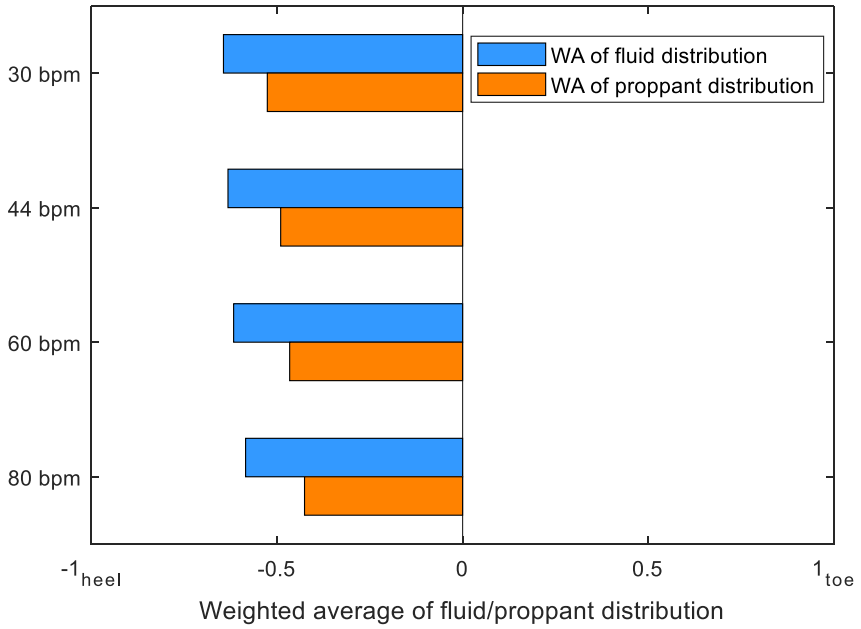

Figure 6.25: The WA numbers for plug-and-perf stages with different maximum slurry injection rates.

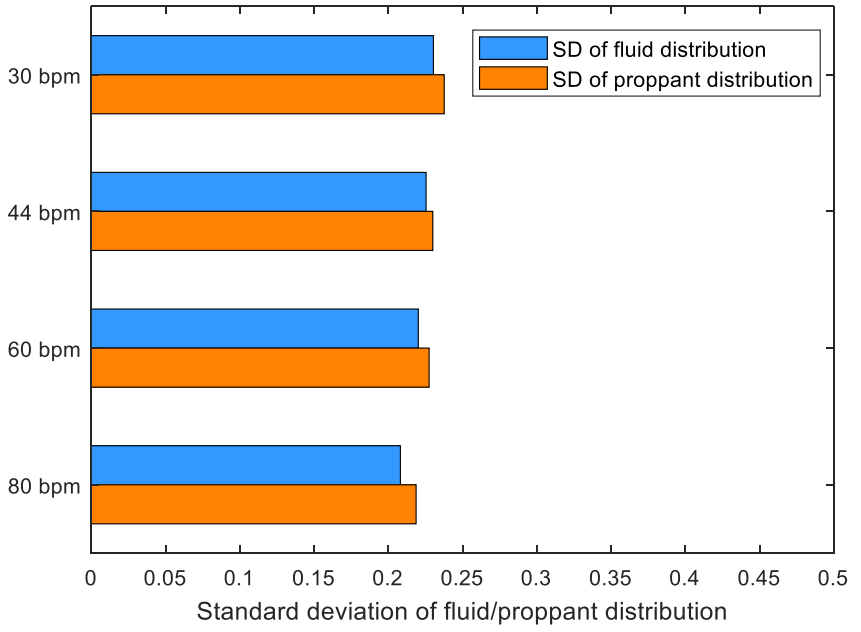

Figure 6.26: The SD numbers for plug-and-perf stages with different maximum slurry injection rates.

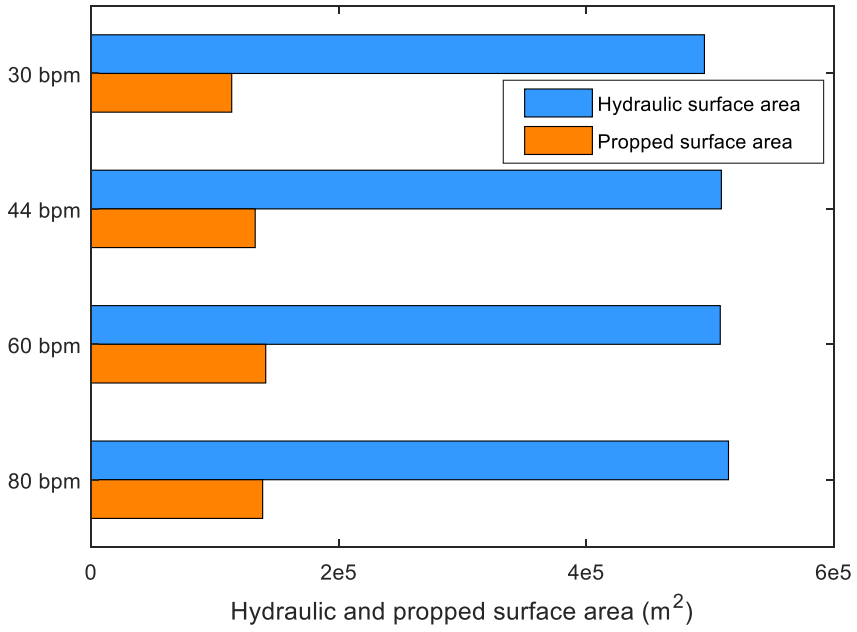

Figure 6.27: The HSA and PSA for plug-and-perf stages with different maximum slurry injection rates.

The PTE correlation shows that larger injection rate tends to magnify the inertial effect of proppant and result in more heel-biased treatment distribution (Wu & Sharma, 2016). However, the simulation results in Fig. 6.25 to 6.27 show that a larger injection rate seems to promote more uniform treatment distribution and create more hydraulic and propped surface area. The reason is that the total fluid and proppant volumes are conserved. And the proppant injection concentration and proppant concentration ramp-up rate remained constant for cases with different injection rate. Therefore, when a higher injection rate is used, more proppant is injected at a lower concentration, and this resulted in a more uniform final treatment distribution.

Due to constraints in designing the plug-and-perf stage pumping schedule, such as conserving total fluid and proppant volume, the effect of different maximum injection rate

on final treatment distribution is more complicated than the PTE correlation. The fluid and proppant distribution figures for these cases can be found in **Appendix B**.

6.2.4.4. Effect of Maximum Proppant Concentration

In this section, we investigate the impact of maximum proppant injection concentration. The applicable range of the PTE correlation is 1 to 3 ppa. Out of this range, the PTE correlation needs to be extrapolated (please refer to Chapter 5). Three cases are designed with maximum proppant injection concentration being 2.5, 3, 4 ppa. The total volume of fluid and proppant are conserved. And the rate of injection is constant at 44 bpm.

The WA and SD are shown in Fig. 6.28 and 6.29. And the HSA and PSA plots comparing the three cases are shown in Fig. 6.30. It is shown that higher proppant concentration makes the final treatment distribution more heel-biased, less uniform and decreases the created propped surface area.

As before, changing the maximum proppant injection concentration also requires changing the injection time. The impact of maximum proppant concentration on final treatment distribution can be complicated. As a rule of thumb, injecting at a smaller proppant concentration has a higher chance of reaching uniform treatment distribution. The fluid and proppant distribution figures for these cases can be found in **Appendix B**.

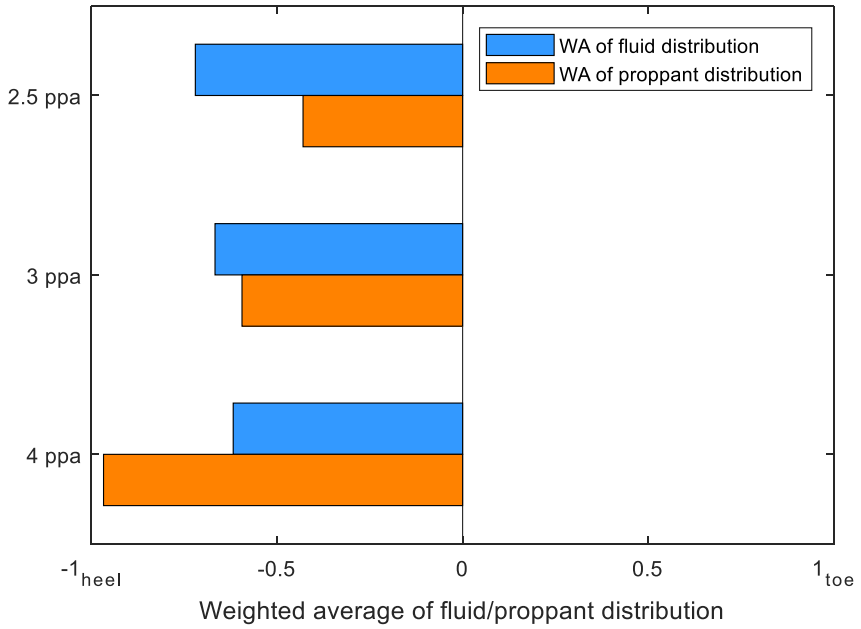

Figure 6.28: The WA numbers for plug-and-perf stages with different maximum proppant concentration.

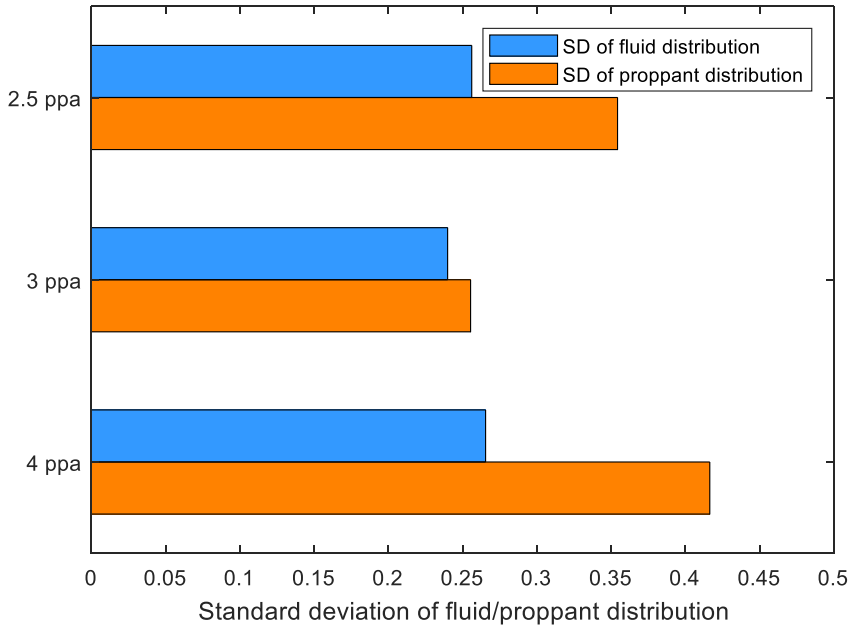

Figure 6.29: The SD numbers for plug-and-perf stages with different maximum proppant concentration.

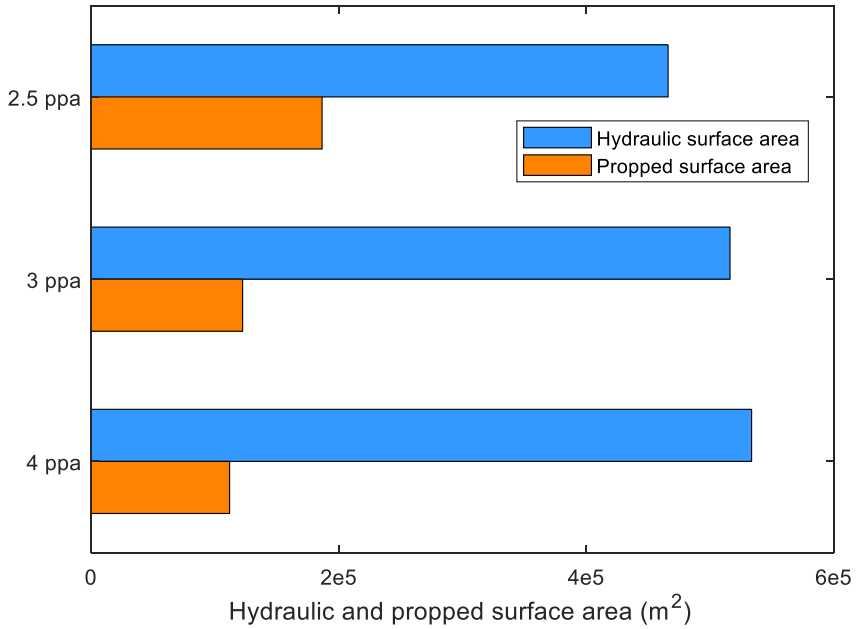

Figure 6.30: The SD numbers for plug-and-perf stages with different maximum proppant concentration.

6.2.4.5. Effect of Rate of Proppant Concentration Ramp-up

In this section, we investigate the impact of the rate of proppant concentration ramp-up. Three cases are considered: slow, modest and fast ramp-up. The total volume of fluid and proppant are conserved. The maximum injection rate and maximum proppant concentration are the same for all cases. In the slow ramp-up case, it takes 30 minutes for proppant concentration to ramp-up from 0 to 3 ppa. In the modest ramp-up case, it takes 15 minutes (the Base Case), and in the fast ramp-up case, it takes 2.5 minutes.

Ramp-up can affect final treatment distribution in two ways: 1) slow ramp-up injects more proppant at lower concentration, this can help the proppant distribution to be more uniform, and 2) in the slow ramp-up design, the proppant injected at a lower

concentration has more time to erode the perforation and the near wellbore region. The erosion process helps reduce the risk of pre-mature screen out and promotes more uniform treatment distribution.

The WA and SD numbers for the final treatment distribution are shown in Fig. 6.31 and 6.32. The HSA and PSA plots for the three cases are shown in Fig. 6.33. It is shown that slow ramp-up promotes uniform treatment distribution and creates more propped surface area. The fluid and proppant distribution figures for these cases can be found in **Appendix B**.

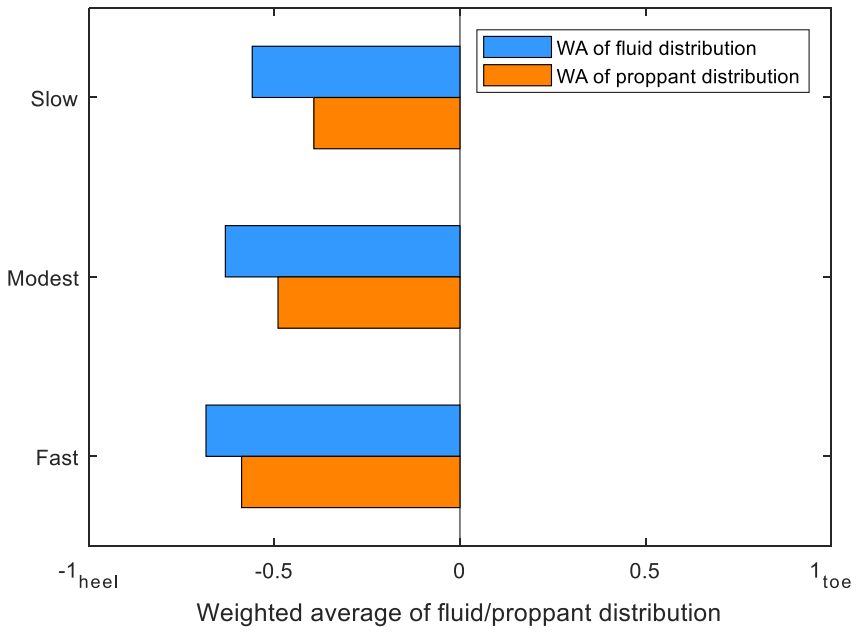

Figure 6.31: The WA numbers for plug-and-perf stages with different rates of proppant concentration ramp-up.

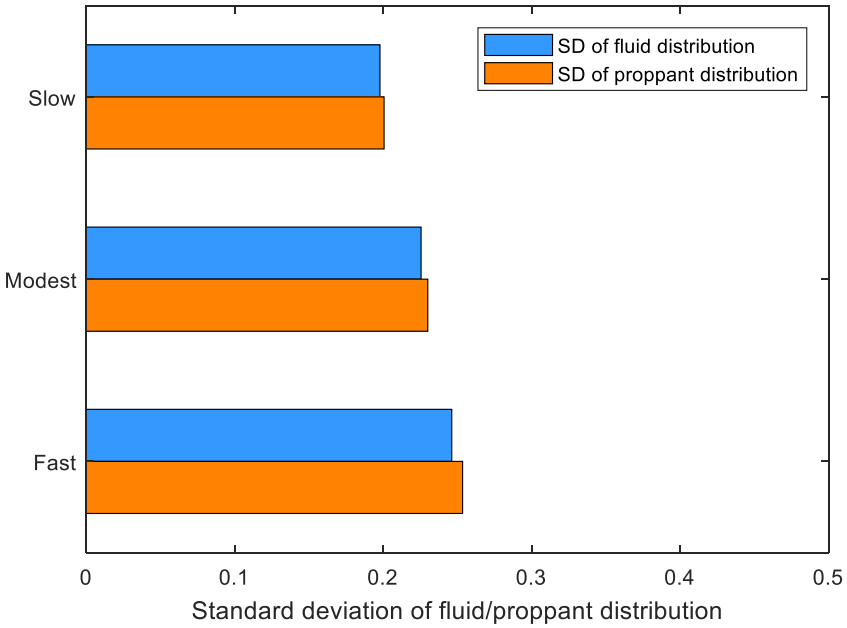

Figure 6.32: The WA numbers for plug-and-perf stages with different rates of proppant concentration ramp-up.

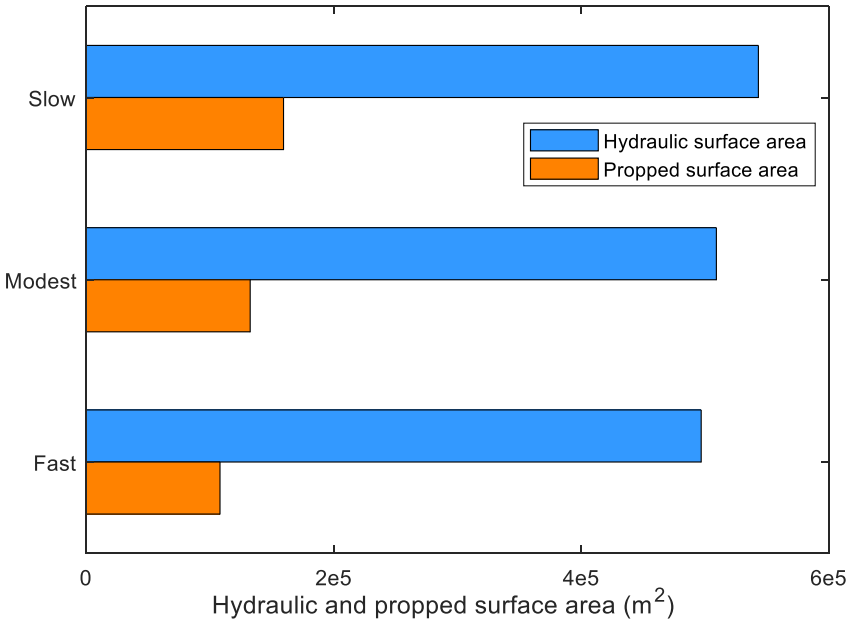

Figure 6.33: The HSA and PSA for plug-and-perf stages with different rates of proppant concentration ramp-up.

6.2.5. Effect of Other Parameters

The impact of two other parameters on the final treatment distribution and surface area has been investigated: the cluster spacing and the wellbore diameter. The final treatment distribution is shown to be not very sensitive to these parameters, as shown in Fig. 6.34 to Fig. 6.35. The fluid and proppant distribution figures for these cases can be found in **Appendix B**.

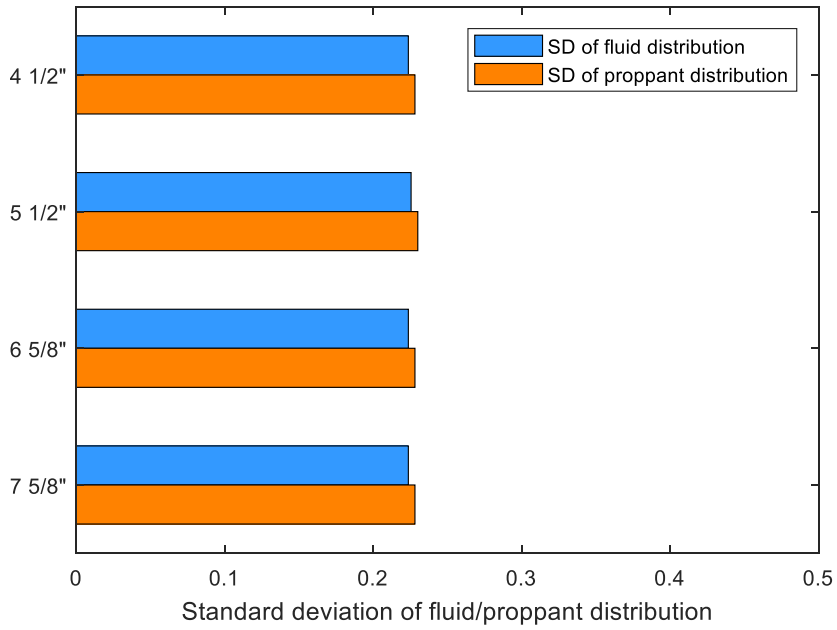

Figure 6.34: The SD number for plug-and-perf stages with different wellbore size.

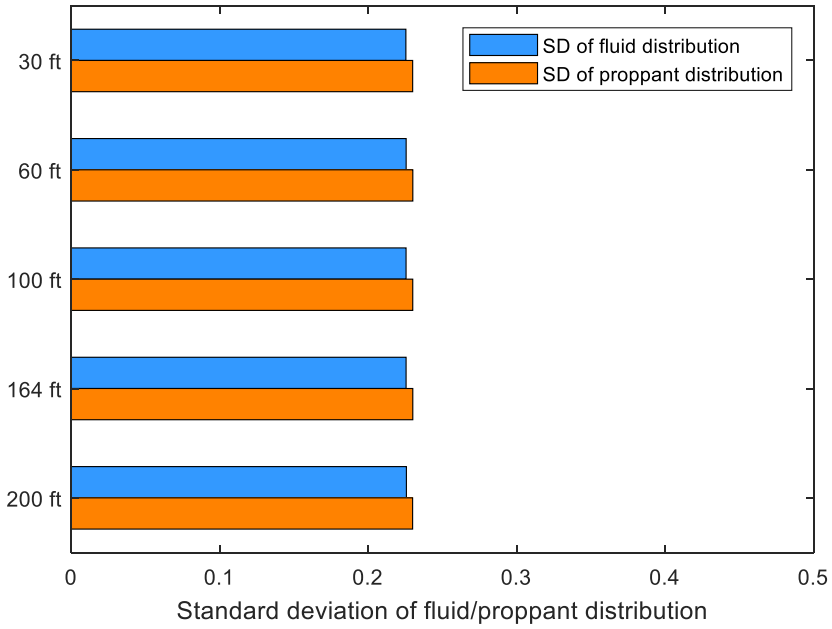

Figure 6.35: The SD number for plug-and-perf stages with different cluster spacing.

It might be a little surprising that the cluster spacing did not make a big difference in the final fluid and proppant distribution.

The reason is that when fractures are closer (smaller spacing), the fracture width reduces due to the stress shadow effect. This increases the pressure drop in the fractures. However, the fracture pressure drop is not a dominant factor in the fluid distribution because it is much smaller than perforation friction. Moreover, the inertia effect accumulates proppant towards the toe side clusters. The two toe side clusters screened out in all cases tested with cluster spacing ranging from 30 to 200 ft. And the final treatment distribution is heel-biased. Therefore, in these 5 cases of different cluster spacing, the inertial effect of proppant dominates and the stress shadow is not a first order effect.

Some field DAS and DTS observations can help validate the conclusion discussed above. A heel-biased treatment distribution has been observed in many cases with cluster

spacing varying between 40 ft to 164 ft. (Molenaar & Cox, 2013; Somanchi et al., 2016; Shen et al., 2017; Wheaton et al., 2016).

Two things should be noted with this conclusion. First, the stress shadow of previous stages is not considered for these cases. The stress shadow induced by previous stages could favor the treatment distribution towards the heel side, especially with small cluster spacing. Second, the fracture model used in this study assumes planar fractures. If fracture turning is allowed, the stress shadow may have a larger influence.

6.3. Optimization of Plug-and-Perf Stages

In the previous section, the impact of individual parameters on the final treatment distribution was investigated. In this section, we try to optimize the plug-and-perf stage design with multiple parameters. The goal is to develop an automated process to search for the optimum solution of multiple variables within the given parameter range.

6.3.1. The Genetic Algorithm

A Genetic Algorithm (GA) method is adopted to search for the optimum plug-and-perf stage design with multiple parameters. GA is a meta-heuristic method inspired by the natural selection process that solves the optimization problem using operators inspired by biology such as elite selection, crossover, and mutation. The main concepts of GA are explained briefly here for ease of understanding of this chapter (Toolbox, G.O., 2011).

The Genetic Algorithm begins with a randomly generated initial population. In each step, the current generation is used to create children that form the next generation. Three types of children are created for the next generation: elite, cross over and mutation as shown in Fig. 6.36. Elite children are the best performing solutions of the parent generation.

Crossover children are generated by combining parameters of some good performing parents. And mutation children are created by randomly changing some variables of the parent solution.

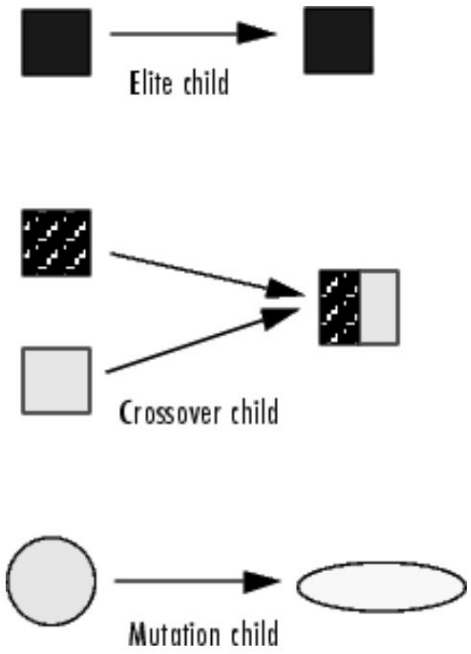

Figure 6.36: Illustration of the GA method: Three types of children created in each generation. (Toolbox, G.O., 2011)

A graphical example of the Genetic Algorithm process is shown in Fig. 6.37 and Fig. 6.38. The initial population is shown in Fig. 6.37. The population after 60, 80, 95 and 100 iterations are shown in Fig. 6.38.

It is shown that through the “natural selection process”, the individuals in the population gradually evolve from scattered points to groups near the optimum solution.

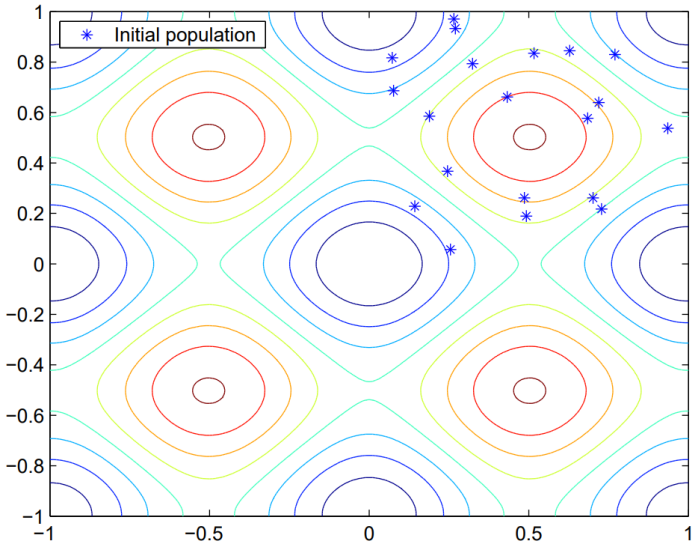

Figure 6.37: Illustration of the GA method: Initial population. (Toolbox, G.O., 2011)

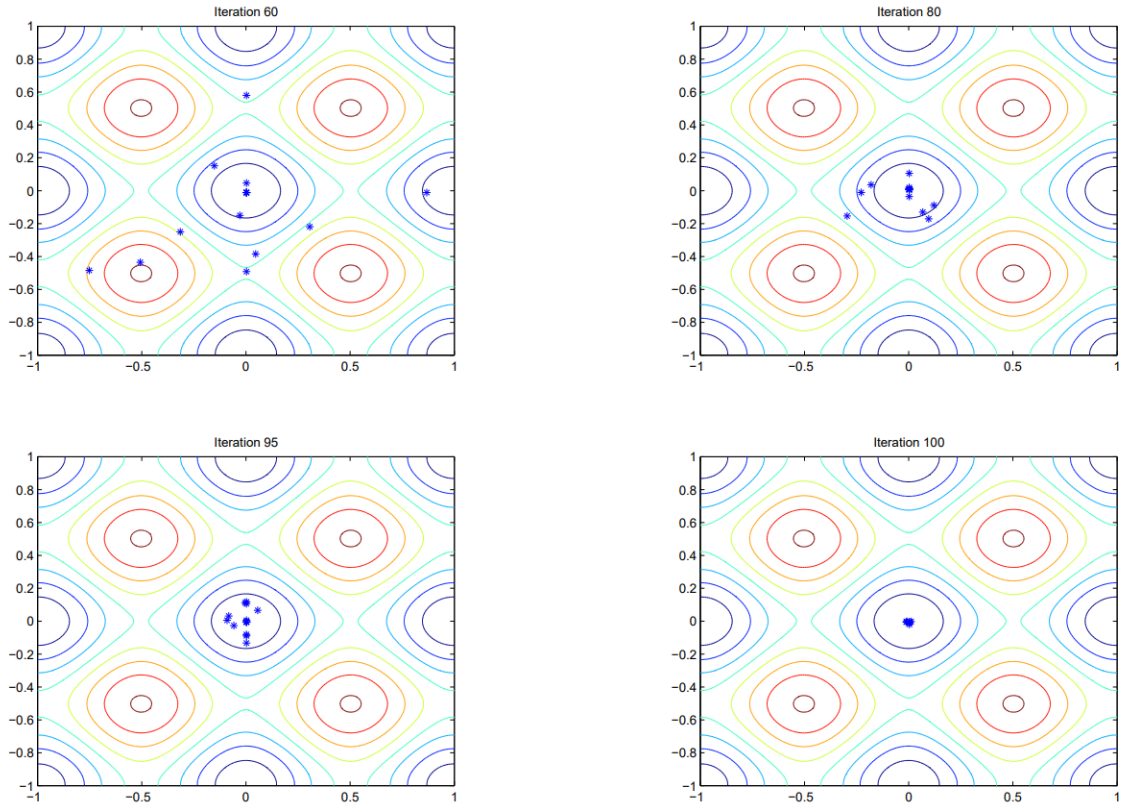

Figure 6.38: Illustration of the GA method: Population after 60, 80, 95, and100 iterations. (Toolbox, G.O., 2011)

6.3.2. Objective Functions

The goal of optimizing a plug-n-perf stage design is to promote uniform fluid and proppant distribution, as well as to maximize the propped surface area. In other words, it is desired to minimize the standard deviation of fluid and proppant distribution, as well as to maximize the propped surface area.

The objective function is defined to be (Equation 6.4).

$$Obj\ Func = \frac{SD_{fluid} + SD_{proppant}}{PSA} * 1e6 \tag{6.4}$$

Since *PSA* is about 6 orders of magnitude larger than SD_{fluid} and $SD_{proppant}$ as shown in Section 6.2, a scaling factor of 1e6 is used in Equation 6.4.

6.3.3. Optimization of a Four-Cluster Plug-and-Perf Stage

The Genetic Algorithm method has been applied to search for the optimum solution for the Base Case. The wellbore diameter, number of clusters and cluster spacing remain the same as the Base Case. The parameter space over which the optimization is conducted is summarized in Table 6.2. The goal of the optimization is to minimize the objective function shown in Equation 6.4.

Two constraints are applied to limit the parameters in the optimization search. First, the total fluid and proppant amount are conserved as in the Base Case. The proppant amount per clusters is 100,000 lbs, and the total fluid injected is 4,400 bbls. The other constraint is that the injection rate per perforation is in the range of 1 to 4 bpm.

Variable	Range
Perforation No. per Cluster	1, 2, 3, 4, 5, 6, 7, 8
Perforation Diameter	0.375”, 0.5”
Max Inj. Rate	30-120 (bpm)
Max Prop Conc.	1-5 (ppa)
Proppant Density	1.54, 2.65, 3.54 (g/cm^3)
Proppant Size	16-30, 20-40, 35-50, 40-70, 100 (mesh)
Ramp-up Time of Each Prop Conc	1 – 15 (min)

Table 6.2: The range of variables in the optimization search.

The initial population is set to be 100. The function tolerance is set to be 1e-10, and the stall generation is set to be 10. The simulation is considered to be converged if the average relative change of the best objective function in the latest 10 generations (stall generation) is smaller than the tolerance (1e-10). The maximum generations allowed is 200. The search will stop when the maximum number of generations is reached, regardless of whether it converged or not.

The solution process of the Genetic Algorithm is shown in Fig. 6.39. The best and the average values of the objective function are plotted against the generation number. It is shown that after 110 generations, the function tolerance is satisfied, and the optimum solution has been determined. For this case, it takes about 20 hours under a Mac OS system using one core (16 GB memory, Intel Core i7).

The search for the optimum solution has been performed 13 times, and 13 sets of optimum solution have been obtained. The average values and the uncertainty of each variable are summarized in Table 6.3. The uncertainty of a variable is defined as the standard deviation of the 13 sets of optimum solutions divided by the average value.

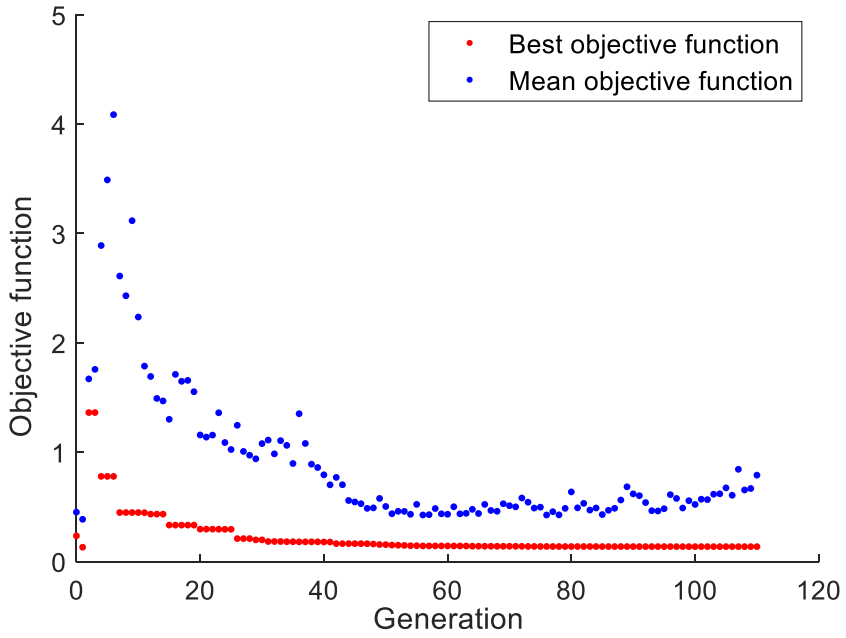

Figure 6.39: The best and the average value of the objective function of each generation.

Parameter	Optimum (Uncertainty)	Base Case
Perforation No. per Cluster	2-3-6-6 (0)	5-5-5-5
Perforation Diameter (inch)	1/2- 3/8- 1/2-1/2 (0)	3/8- 3/8- 3/8-3/8
Max Inj. Rate (bpm)	40.2 (0.97%)	44
Proppant Concentration (ppa)	3.7 (0.14%)	3
Proppant Density (g/cm^3)	1.54 (0)	2.65
Proppant Size (mesh)	40-70 (0)	20-40
Ramp-up Time for Each Prop Conc (min)	1.45 (1.3%)	3

Table 6.3: The optimum solution compared to the Base Case.

It is shown that the uncertainty of the optimum solution is very small, meaning that the optimum solution is unique under the specified conditions. One of the reasons is that some of the parameters are discontinuous and have limited options. For example, the perforation diameter has only two choices: 0.375” and 0.5”. The proppant density has only three possible values: 1.54, 2.65 and 3.56 g/cm^3. And the proppant size also has limited choices. Another reason for the low uncertainty could be that the objective function is sensitive to the parameters.

The pumping schedule is shown in Fig. 6.40. According to the optimum solution, the maximum injection rate is 40.2 bpm, the maximum proppant concentration is 3.7 ppa. The proppant concentration ramps up in steps of 0.5 ppa, and the injection time for each proppant concentration step is 1.45 minutes.

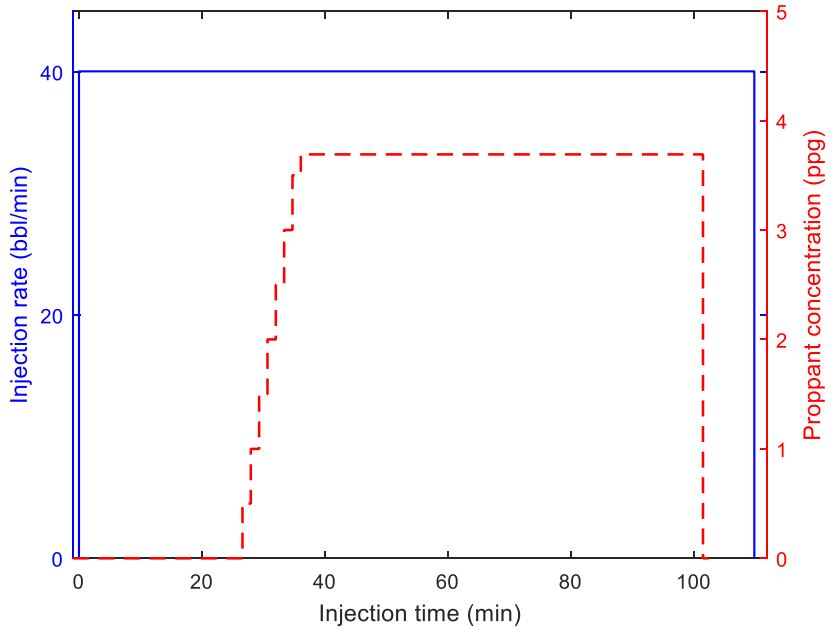

Figure 6.40: Pumping schedule for the optimum solution.

Fig. 6.41 shows the final fluid and proppant distribution for the optimum solution. Compared to the treatment distribution for the Base Case shown in Fig. 6.2, the treatment distribution has been improved greatly.

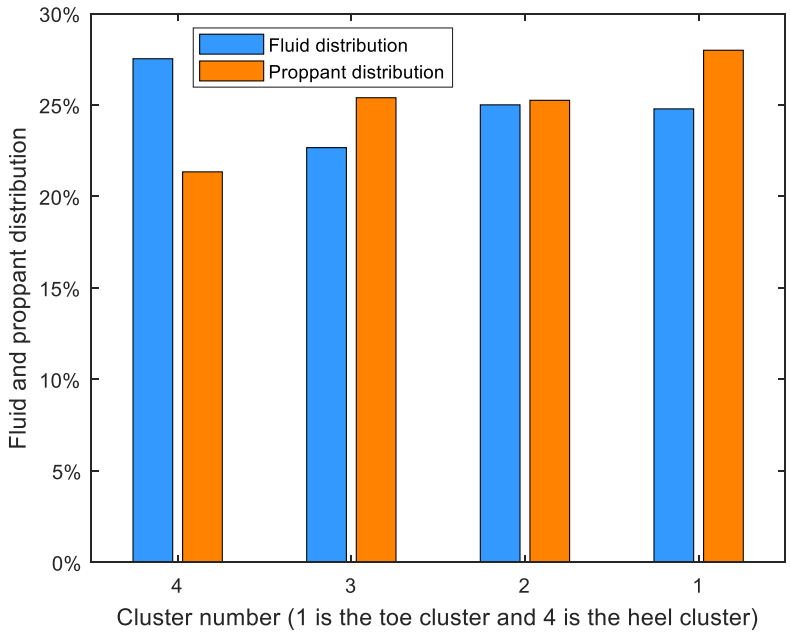

Figure 6.41: Final fluid and proppant distribution among the 4 clusters of the optimum solution.

Fig. 6.42 compares the WA number, the SD numbers, and the hydraulic and propped surface area of the Base Case and the optimum solution. It is shown that the optimum solution promoted more uniform treatment distribution and created much more hydraulic and propped fracture surface area. The propped surface area of the optimum solution is about 2.3 times of that in the Base Case.

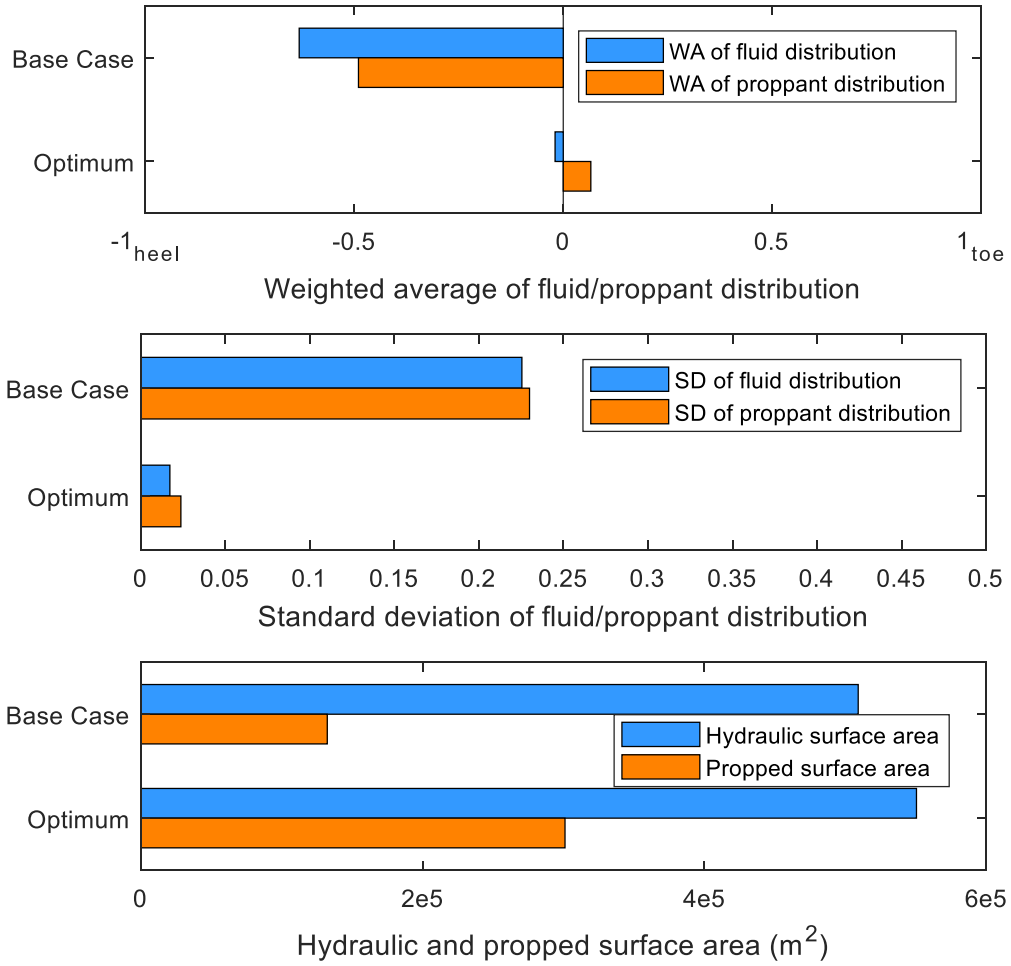

Figure 6.42: Comparing the WA, SD numbers and the hydraulic and propped surface area of the Base Case and the optimum solution.

The parameters in the optimum solution are reasonable choices for promoting uniform proppant and fluid distribution. For example, according to the analysis in Section 6.2, fewer perforations near the heel than the toe, smaller proppant size and lighter proppant can lead to a more uniform treatment distribution. The parameters obtained in the optimum solution represent these trends well. The parameters of the pumping schedule are optimized together including the injection rate, maximum proppant concentration and so on. Because of the interdependency of the pumping schedule parameters, the optimized solution may

lead to an outcome that may seem contradictory to conclusions for the sensitivity study presented in the former section. It is illustrated in this optimization example that when multiple parameters are optimized simultaneously, the propped fracture surface area can be greatly improved.

In this example problem for the optimum solution, the variables are allowed to vary over in a relatively wide range. For example, proppant density of 1.54 g/cm^3 is allowed, and different perforation size for each cluster is allowed. For the design of real fracture treatment, more restrictions will usually need to be set for the variables due to economic and operational considerations.

6.4. CONCLUSIONS

In this chapter, we applied the multi-fracture model developed in the last 4 chapters to calculate the fluid and proppant distribution among multiple clusters quantitatively. It is shown that proppant placement into fractures depends on many completion factors including the perforation design and pumping schedule. By investigating the sensitivity of the proppant distribution to different operational parameters, specific design recommendations are provided that will promote uniform proppant placement in all clusters leading to better production.

We have also for the first time developed a process to automate the optimization of operational parameters by varying multiple parameters simultaneously using a Genetic Algorithm approach. The optimum plug-and-perf stage design that promotes uniform treatment distribution and maximizes propped surface area can be obtained using this process.

To summarize, both the perforation design and pumping schedule variables are found to have a significant impact on the final treatment distribution. The impact of each variable is summarized below:

1. Uniform perforation design: with the same number of clusters, fewer perforations per cluster were found to promote uniform treatment distribution and create more surface area.
2. Staggered perforation design: a design with fewer perforations near the heel than the toe was found to promote uniform treatment distribution and create more fracture surface area. More perforations near the heel than the toe was found to impact the final treatment distribution negatively.
3. Perforation diameter: the 3/8” perforation diameter was found to be better than the 1/2” perforation diameter in terms of final treatment distribution.
4. Proppant size and density: changing the proppant density was found to have a much bigger impact on final treatment distribution than changing the proppant size. Using lighter proppant is found to promote uniform treatment distribution and create more propped surface area. Using a smaller proppant is found to create more propped surface area.
5. Injection rate, proppant concentration and rate of proppant ramp-up: due to constraints in designing the pumping schedule such as conserving the volume of fluid and proppant, these three parameters should be optimized together. As a rule of thumb, smaller proppant concentration and slow proppant ramp-up help to promote more uniform treatment distribution and create more propped surface area.

A new Genetic Algorithm based method is presented to obtain the optimum plug-and-perf design. The treatment distribution in the optimum case is much more uniform than

the Base Case. It is also shown that when multiple operational parameters are optimized simultaneously, the propped surface area can be greatly improved. The optimization process can be applied to search for optimum plug-and-perf stage designs with variables within a specified range.

NOMENCLATURE

HSA	=	Hydraulic surface area, L^2, m^2
L	=	Length of one fracture wing, L, m
PSA	=	Propped surface area, L^2, m^2
SD	=	The Standard Deviation number
WA	=	The Weighted Average number
dis	=	Percentage of fluid/proppant distribution
n	=	Number of clusters
wr	=	Weight ratio in WA number calculation

REFERENCES

Lagrone, K.W. and Rasmussen, J.W., 1963. A new development in completion methods-the limited entry technique. *Journal of Petroleum Technology*, 15(7), pp.695-702.

Molenaar, M.M. and Cox, B.E., 2013. Field cases of hydraulic fracture stimulation diagnostics using fiber optic distributed acoustic sensing (DAS) measurements and Analyses. In *SPE Unconventional Gas Conference and Exhibition*. Society of Petroleum Engineers.

Shen, Y., Holley, E., and Jaaskelainen, M., 2017. Quantitative Real-Time DAS Analysis for Plug-and-Perf Completion Operation. Unconventional Resources Technology Conference. doi:10.15530/URTEC-2017-2668525

Somanchi, K., O'Brien, C., Huckabee, P. and Ugueto, G., 2016. Insights and observations into limited entry perforation dynamics from fiber-optic diagnostics. *Unconventional Resources Technology Conference* (URTEC).

Toolbox, G.O., 2011. *User's Guide* (r2011b). The MathWorks Inc.

Ugueto, C., Gustavo, A., Huckabee, P.T., Molenaar, M.M., Wyker, B. and Somanchi, K., 2016. Perforation cluster efficiency of cemented plug and perf limited entry completions; Insights from fiber optics diagnostics. In *SPE Hydraulic Fracturing Technology Conference*. Society of Petroleum Engineers.

Wheaton, B., Haustveit, K., Deeg, W., Miskimins, J. and Barree, R., 2016. A case study of completion effectiveness in the eagle ford shale using DAS/DTS observations and hydraulic fracture modeling. In *SPE Hydraulic Fracturing Technology Conference*. Society of Petroleum Engineers.

Wu C.-H., Sharma, M.M. 2016. Effect of Perforation Geometry and Orientation on Proppant Placement in Perforation Clusters in a Horizontal Well. Paper SPE 179117 presented at the *SPE Hydraulic Fracturing Technology Conference*, The Woodlands, Texas, USA, 9-11 February 2016. http://dx.doi.org/10.2118/179117-MS

Chapter 7: Proppant and Fluid Distribution in Horizontal Well Refracturing Operations

7.1. INTRODUCTION

Refracturing refers to the process of doing a second hydraulic fracturing treatment after some time of production. Many reported horizontal well refracs in the literature today are done in the most widely explored unconventional reservoirs, such as the Haynesville, Eagle Ford, Bakken, and Barnett shales (Jacobs, 2014).

Direct simulation of refracturing treatments in horizontal wells has seldom been conducted in the published literature. In this Chapter, we applied the multi-fracture simulator to simulate horizontal well refracturing employing diverting agents. The goal is to quantitatively model the fluid and proppant distribution and fracture propagation when re-stimulating the entire wellbore with many clusters of perforations accepting fluid. The model has been used to study field refracturing cases and provide recommendations for refrac treatment design.

7.1.1. Motivation of Refracturing

Horizontal well drilling and multi-stage hydraulic fracturing have boosted US oil production over 65% through the development of unconventional reservoirs (Murtaugh et al., 2014). However, not all the clusters of the horizontal wellbore contribute to production. Several production evaluations have shown that only 64% of the perforated clusters were producing, leaving almost 40% of the wellbore not contributing to production; a vast opportunity for refracturing (Fragachan et al., 2015; Denney 2011; Sinha & Ramakrishnan 2011). A typical successful refracturing treatment can bring up the production rate beyond

the well's initial production rate and sustain the improved production. Fig. 7.1 shows an example of production improvement after refracturing. The well is in the Woodford Shale, and it was refractured with ball sealers. In this case, the refracturing operation almost doubled the production.

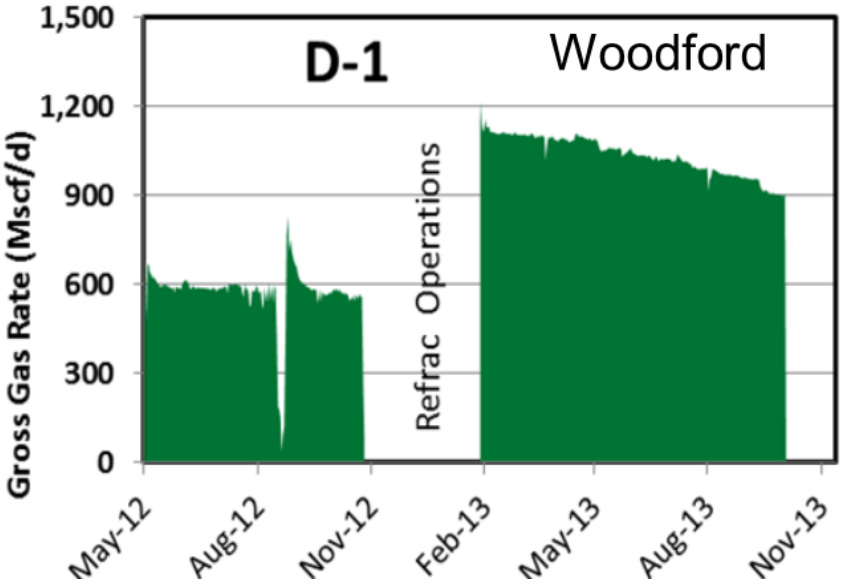

Figure 7.1: Refrac improved production. (French et al., 2014)

Another important motivation of horizontal well refracturing is to protect the parent well from child well stimulation. As the development of unconventional plays mature, the drilling and completion of child wells become an important aspect of field development. Pore pressure depletion of the parent wells creates low pressure and stress regions that attract the fluid and proppant injected during the child well stimulation and results in frac-hits. Fig. 7.2 shows an analysis of frac-hits observed in the Eagle Ford. Most frac-hits have a negative impact on the oil and gas recovery. The production from both the parent and the child wells could be compromised due to frac-hits.

Refracturing the parent well before the stimulation of the child well could re-pressurize and re-stress the reservoir around the parent well, to avoid frac-hits and protect the parent well from the treatment of child well. Applying refracturing treatment to the parent well has become a common practice in the development of unconventional basins. Lindsay et al. (2016) analyzed refracturing operations in the Eagle Ford. Among the 20 re-fractured wells they investigated, 12 of them were done for parent well protection.

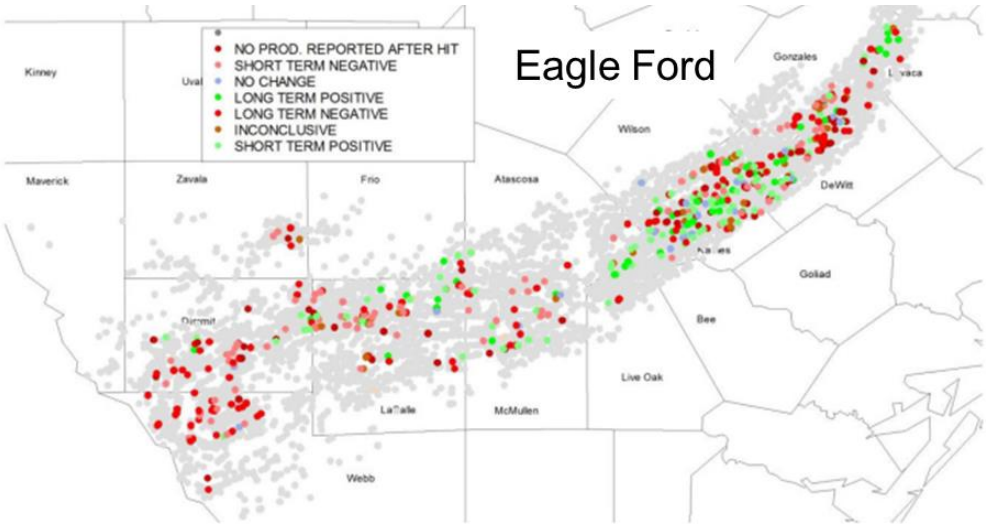

Figure 7.2: Frac-hits in the Eagle Ford (Miller et al., 2016)

7.1.2. Diagnostics of Refracturing

In common refracturing treatments, no mechanical isolation is installed along the lateral, and all fractures are stimulated simultaneously. This kind of refrac is also referred to as bull-heading refrac treatments. In this case, it is important to know the treatment distribution among multiple fractures.

Many diagnostic methods have been applied to evaluate the treatment distribution, such as micro seismic mapping, proppant tracer, and production logging. The conclusion is that the treatment distribution in refracs is usually heel-biased. In other words, most of the treatment fluid and sand end up in the heel section of the wellbore while the toe side of the wellbore receives very little treatment.

Leonard et al. (2015) studied refracturing of 43 horizontal wells in 7 producing formations in the US, including the Barnett, Haynesville and Eagle Ford formations. The primary diagnostic method used in their study is proppant tracer. The results show that a large fraction of refrac preferentially treated the heel section. Figure 7.3 shows the proppant tracer results of a refracturing treatment in the Haynesville shale (Leonard et al., 2016). It is a typical case that shows that the heel section is preferentially stimulated. Early proppant (shown in blue) is visible in the toe section. But the middle proppant (yellow) and late proppant (red) are focused in the heel section. The middle proppant was concentrated within 1000 ft from the heel. And the late proppant was concentrated within 300 ft from the heel.

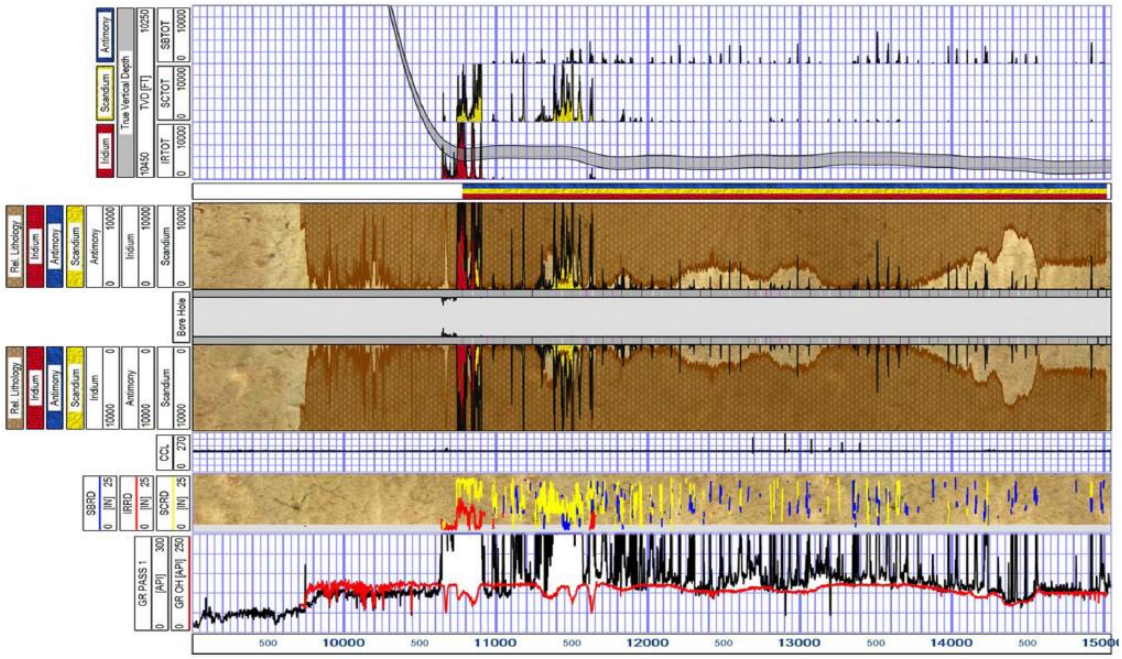

Figure 7.3: Proppant tracer results show that the refrac treatment distribution is heel-biased. (Leonard et al., 2016)

Besides the heel-biased treatment distribution trend, several other important conclusions can be inferred from refracturing diagnostics.

First, new clusters do effectively break down during refracs. In the analysis presented by Leonard et al. (2015), effectively stimulated new perforations are observed in all the wells studied.

Secondly, although some field evidence shows that diverting agent can successfully divert the treatment (Potapenko et al., 2009; Fragachan et al., 2005), the performance of diverting agents is not consistent. This conclusion was confirmed by Evans et al. (2016)'s work. They injected diverting agent in the middle of plug-and-perf stages, hoping to stimulate all clusters effectively, and DAS and DTS technology were used to monitor these treatments. Fig. 7.4 shows a successful fluid diversion. The treatment was heel-biased pre-diverter, with most treatment going into the heel clusters. Then, the diverting agent plugged

the dominant fracture at the heel and promoted the propagation of the toe side clusters. Fig. 7.5 shows another stage where the diverting agent was not as effective. The dominant fracture pre-diverter still received the most treatment after the application of the diverting agent.

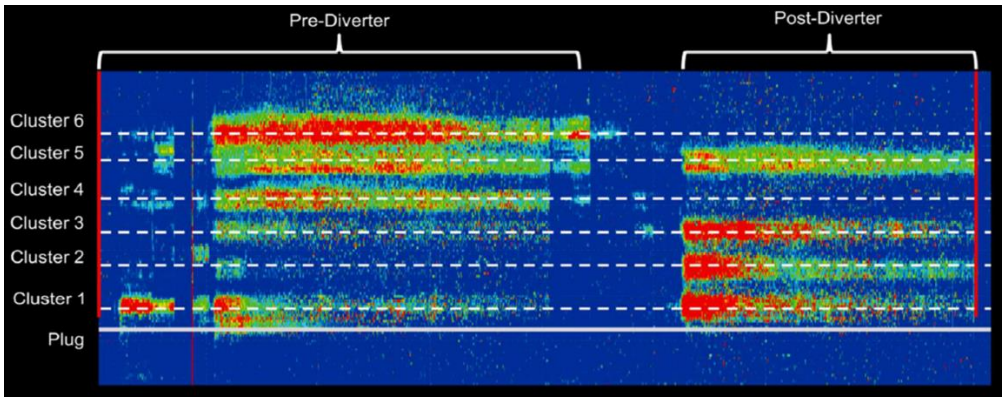

Figure 7.4: Effective treatment diversion by particulate diverting agents. (Evans et al., 2016)

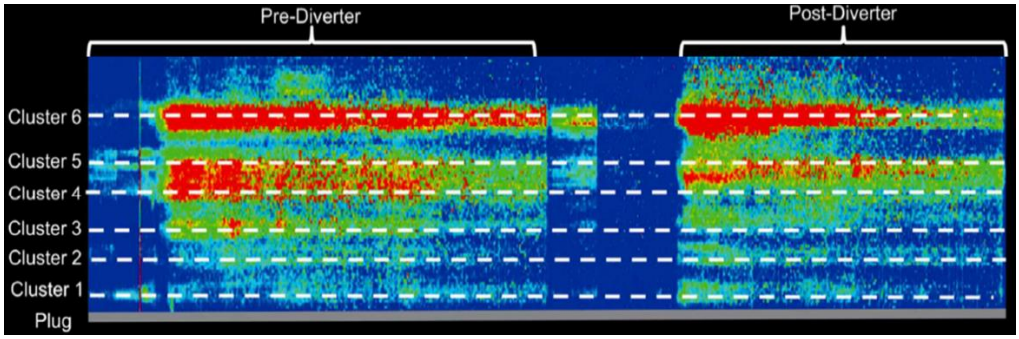

Figure 7.5: Diverting agents are less effective in some cases. (Evans et al., 2016)

Mechanical isolation is the best option in terms of controlling the injection point and fracture initiation. However, it can cause considerable operational difficulties, and the

cost of this method may exceed the gains. Therefore, diverting agents are the most economical and most popular fluid diversion method for horizontal well refracturing.

Finally, the refrac performance is highly field and case dependent. There is no clear correlation between refrac success with production time before refrac or percentage of new and old clusters treated as shown in Fig. 7.6. Analysis needs to be applied case by case to understand refracturing performance.

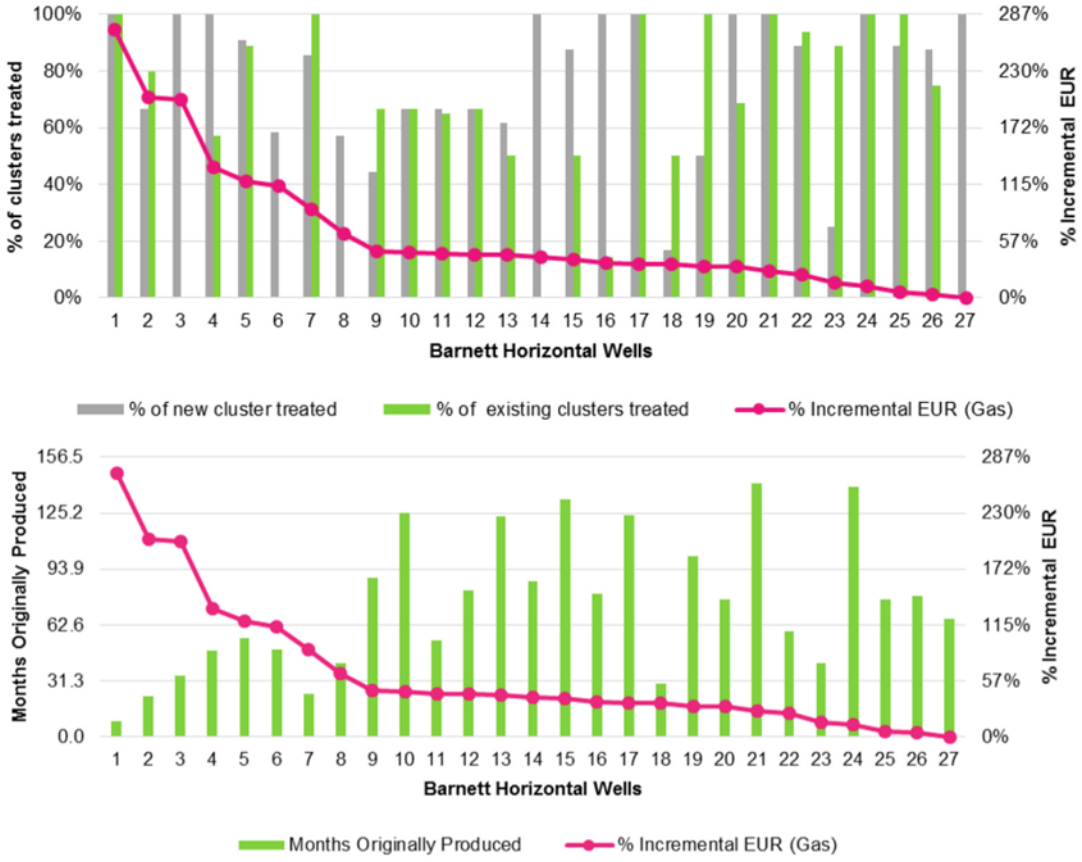

Figure 7.6: Refracturing performance is case dependent. (Leonard et al., 2015)

7.1.3. The Main Challenge of Refracturing

The objective of refracturing is to create more reservoir contact (create more fractures) in the under-stimulated region and to protect the parent well by re-pressurizing/re-stressing the depleted zones. The main challenge of horizontal well refracturing is to prevent the heel-biased refrac treatment distribution.

When the treatment is heel-biased, it could impact both the refrac well and the offset wells negatively. On the one hand, the toe half of the refrac well gets little treatment and contribute little to production. On the other hand, the over-stimulated heel section could hit the offset wells, and the under-stimulated toe section can attract treatment from offset wells. Wellbore communication could compromise production from both wells.

Therefore, preventing heel-biased treatment distribution and diverting more treatment to the toe side of the wellbore could have a significant positive impact on refrac success. This is the main challenge horizontal well refracturing faces today.

7.2. FACTORS CONTROLLING REFRAC SUCCESS

Horizontal well refracturing is a complicated process where a large number of fractures (from 10 to over 100) propagate simultaneously in a reservoir with highly non-uniform pore pressure and in-situ stress. Many factors and physical mechanisms affect the results of the refrac. In this section, we analyze key factors that control refrac success. We consider these factors from two perspectives: the perspective of pressure and stress heterogeneity in the field due to pore pressure depletion, and the perspective of wellbore hydrodynamics. Many researchers have looked into the first perspective, and methods have been established to quantitatively study the non-uniform pressure and stress caused by production (Fisher et al. 2004, Wright & Connant 1995, Roussel & Sharma 2012, to cite a

few). The second perspective has been overlooked in the past. It has been shown to have a significant impact on refrac success as well.

7.2.1. Pressure and Stress Heterogeneity in the Field

Pore pressure depletion prior to the refrac leads to non-uniform pore pressure and stress distribution in the region around the wellbore. The combined effect of mechanical and poro-elastic stress changes determine the distribution of fluids and proppant in the refrac treatment.

The non-uniform pressure and stress along the wellbore could favor either existing or new clusters to propagate. First, it is important to note that the stress and pore pressure near existing fractures are lower than near the new clusters. This phenomenon favors the propagation of fractures in existing clusters which have older, depleted fractures. However, the existing fractures have a finite propped width, and additional hydraulic pressure in the fracture is required to widen them to accommodate additional proppant. Moreover, the proppant pack in the existing fracture causes a higher pressure drop in the fracture. These two mechanisms limit the widening and propagation of existing fractures. Whether the reservoir conditions favor the propagation of existing clusters or new clusters depends on factors such as the initial treatment design, the amount of depletion, the spacing of the clusters, etc. A detailed quantitative analysis needs to be performed to analyze the combined result of all the mechanical and poro-elastic effects.

The non-uniform pressure and stress in the longitudinal direction (along with the fracture length direction) could also impact refrac treatment distribution. The pore pressure depletion decreases as the distance from the well increases. The depleted region near the well forms a “stress cage”. In the stress cage, the pore pressure and stresses are low, while

away from the wellbore, the pore pressure and stresses are high (closer to their in-situ value). The fractures propagated early during the refracturing treatment could reach the boundary of the "stress cage" and feel the high pressure and stress outside of the cage. In this case, the "stress cage" could act as a natural diverter that limits the propagation of fractures propagating further from the well and promote the propagation of fractures that have not received as much fluid.

The pore pressure and stress heterogeneity in the reservoir is a crucial factor in terms of controlling the treatment distribution and fracture growth. However, it is difficult to use the non-uniform pressure or stress field to explain the fact that most refracs are heel-biased. Another important aspect of the problem needs to be considered to explain this observation and better understand the refracturing process: wellbore hydrodynamics.

7.2.2. Wellbore Hydrodynamics

In Chapter 5 and 6, we have shown that wellbore hydrodynamics could have a significant impact on the final fracture geometry in plug-and-perf stages. The same applies to refracturing. The effect of proppant inertia results in accumulation of proppant in the wellbore while fluid leaks off from the heel side clusters, resulting in high slurry concentration near the toe side clusters that can cause pre-mature screen out. When the toe side fractures screen out, the following treatment is re-distributed in the heel section of the wellbore.

Many factors impact the fluid and proppant distribution among multiple clusters as discussed in Chapter 6. Quantitative dynamic fluid and proppant partitioning among multiple fractures during refracturing treatment can be solved using the fluid and proppant distribution model developed in Chapter 4 and 5. The one big difference in refrac

operations is that there are a much larger number of perforations and fractures that can receive the fluid and proppant. This magnifies the non-uniform fluid distribution problem significantly.

7.3. MODEL FORMULATION

The 2D multi-fracture model with dynamic fluid and proppant partitioning is applied to the refracturing simulation. Several new features are added to the model to account for the re-opening of existing fractures during refrac and the impact of diverting agents.

7.3.1. Model for Reopening of Existing Fractures

The dimension of the existing fracture and the proppant pack in the fracture need to be accounted for in order to simulate existing fracture re-opening during a refracturing treatment.

During production, the pore pressure depletes, and the effective stress increases as the fractures close on the proppant. Therefore, it is assumed that the existing fractures are filled with proppant at the time of a refrac. The permeability of the proppant pack in the fracture can be estimated by the Carman-Kozeny equation as shown in Equation 7.1 (Peters, 2012).

$$k_{pp} = \frac{4\varphi^3 a^2}{(1-\varphi)^2} \tag{7.1}$$

Where k_{pp} represents the permeability of the proppant pack, a is the proppant radius and φ is the porosity of the proppant pack.

The process of an existing fracture re-opening is illustrated in Fig. 7.7. The proppant particles close to the fracture wall (indicated by red color) are assumed to be

embedded during production and cannot move during the refracturing process. The proppant near the center of the existing fracture (shown by orange color) can be picked up by the slurry pumped during the refrac and can be moved deeper into the fracture.

As the treating pressure increases during the refrac, the existing fracture widens and propagates, and a channel is assumed to form in the center of the fracture to accommodate new fluid and proppant. This process is illustrated in the bottom figure of Fig. 7.7. The slurry in the channel picks up the movable old proppant in the center and takes it deeper as the fracture propagates.

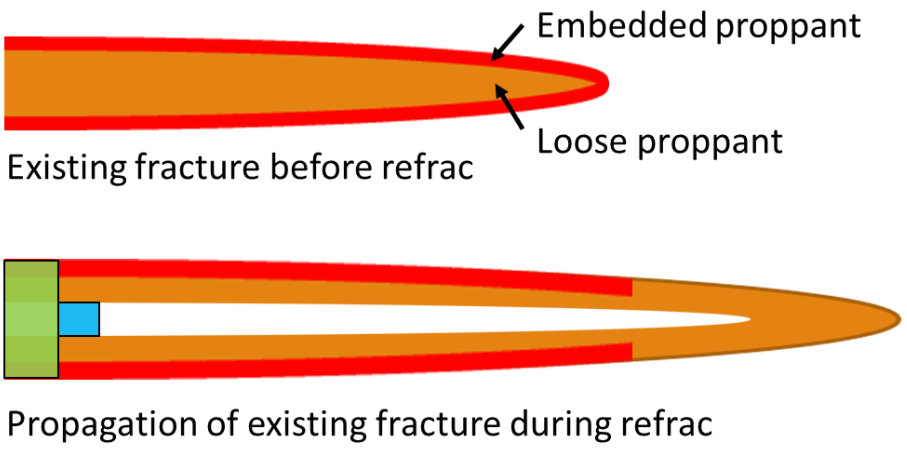

Figure 7.7: Illustration of existing fractures re-open during a refrac treatment.

Two kinds of computation cells are used in the model to describe the process of existing fracture re-opening: the fracture cell and the channel cell. The fracture cell includes both the old proppant and the channel in the middle of the fracture, as shown by the green box in Fig. 7.7. The channel cells only include the channel formed in the center during refracturing as shown by the blue box. The transport of the new proppant is solved

in the channel cells. The fracture geometry, fluid leak-off, and global mass balance are solved on the fracture cell.

In other words, both the fracture width (w_f) and the channel width ($w_{channel}$) are stored at fracture nodes. The fracture geometry, local mass balance and the global mass balance are solved with the fracture width

$$\frac{\partial q}{\partial x} + \frac{\partial w_f}{\partial t} + u_L = 0 \tag{7.2}$$

$$w_f = -\frac{\pi P_{net} h_f (1-v)}{4G} \tag{7.3}$$

$$\int_0^{L(t)} w_f(x,t)dx + \int_0^t \int_0^{L(t')} u_L(x,t')\,dxdt' = \int_0^t q_o(t')dt' \tag{7.4}$$

The transport of the new proppant is solved with the channel width

$$\frac{\partial w_{channel}\overline{\emptyset}}{\partial t} + \frac{\partial q_p}{\partial x} = 0 \tag{7.5}$$

The fluid momentum (pressure drop in the fracture) is calculated using an average permeability of the existing proppant and the channel as shown in Equation 7.6.

$$q = -\frac{k_{avg}}{\mu}\frac{\partial P_f}{\partial x} \tag{7.6}$$

The permeability of the existing proppant (k_{pp}) is calculated according to the Carman-Kozeny equation shown in Equation 7.1. The permeability of the channel ($k_{channel}$) is calculated using Equation 7.7. And the average permeability is calculated using Equation 7.8 (Peters, 2012)

$$k_{channel} = \frac{w_{channel}^3}{12}\hat{Q}^s\left(\overline{\emptyset}, \frac{w_{channel}}{a}\right) \tag{7.7}$$

$$k_{avg} = \frac{w_{channel} * k_{channel} + \left(w_f - w_{channel}\right) * k_{pp}}{w_f} \tag{7.8}$$

For the value of $\hat{Q}^s\left(\overline{\emptyset}, \frac{w}{a}\right)$, please refer to Chapter 2.

7.3.2. Modeling Diverting Agent

Diverting agents consist of self-degradable particulates of different sizes as shown in Fig. 7.8. The plugging mechanism of the diverting agent is conceptually thought to be as follows: the large particles first form a plug, and then the small particles filter through the plug and significantly reduce the porosity and permeability of the plug.

Diverting agents are generally designed to plug perforations. However, the amount of diverting agent used in many treatments is much larger than the capacity of all the perforations. This suggests that the diverting agent probably enters the fractures as the fractures grow and widen. The diverting agent plug causes an additional pressure drop in the fracture and diverts treatment into other fractures.

The diverting agent is designed to degrade with time. Therefore, the temporarily plugged fractures (during the refracturing treatment) can produce once the material degrades.

Figure 7.8: Diverting Agent particulates. (Evans et al., 2016)

The density of diverting agent particulates is close to water. Therefore, we assume that the diverting agent follows the fluid. In other words, the fracture receiving more fluid would also receive more diverting agent. We also assume that the diverting agent forms a radial plug near the wellbore as shown in Fig. 7.9. The diverting agent plug has a permeability of 0.03-2.7 D as measured in our lab. And the pressure drop through the plug is simulated using Darcy's Law as shown in Equation 7.9 (Peters, 2012).

$$\Delta p_{DA,i} = \frac{\mu}{k_{DA} w} \ln\left(\frac{r_{DA}}{r_w}\right) \tag{7.9}$$

Where $\Delta p_{DA,i}$ is the pressure drop due to the diverting agent plug per unit flow rate, μ is the viscosity of the fracturing fluid, k_{DA} is the permeability of the diverting agent plug, w is the width of the fracture, r_{DA} is the outer radius of the diverting agent plug, determined simply by mass balance, and r_w is the radius of the wellbore. When the treating pressure increases and the fracture widens, the pressure drop due to diverting agent decreases.

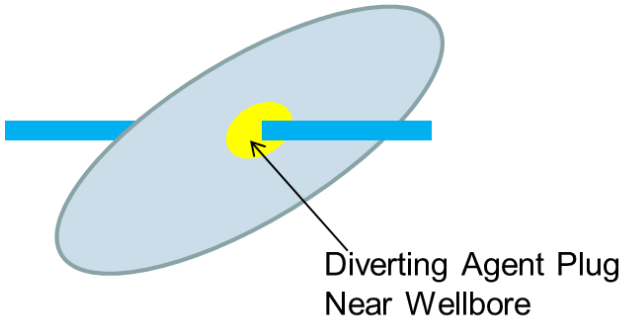

Figure 7.9: The diverting agent plug.

The additional pressure drop caused by diverting agent is added in the Resistance Model developed in Chapter 4. The updated Resistance Model is shown in Equations 7.10 to 7.12.

$$R_i = \frac{BHP - S_{hmin,i}}{Q_i} = \frac{\Delta p_{f,i} + \Delta p_{DA,i} + \Delta p_{pf,i} + \Delta p_{w,i}}{Q_i} \tag{7.10}$$

$$\frac{1}{R_{tot}} = \sum_{i=1}^{n} \frac{1}{R_i} \tag{7.11}$$

$$Q_i = \frac{R_{tot}(Q_T + \sum_{i=1}^{n} \frac{S_{hmin,i}}{R_i}) - S_{hmin,i}}{R_i} \tag{7.12}$$

Where R_i is the resistance of fracture *i*, BHP is the bottom hole pressure, $S_{hmin,i}$ is the minimum horizontal stress near fracture *i*, Q_i is the injection rate of fracture *i*, $\Delta p_{f,i}, \Delta p_{DA,i}, \Delta p_{pf,i}, \Delta p_{w,i}$ are the pressure drop in the fracture, in the diverting agent plug, in the perforation and in the wellbore for fracture *i*, R_{tot} is the total resistance of all the fractures, and Q_T is the total injection rate.

When diverting agent forms a plug in fracture *i*, $\Delta p_{DA,i}$ increases and R_i increases. And so less fluid is distributed to fracture *i* in the following time step according to Equation 7.12. The fluid diversion is a dynamic process affected by the stress heterogeneity, the mass of diverting agent, the fracture width and so on. Usually, several hundred psi to over one thousand psi pressure increase is observed after the application of a diverting agent.

7.4. RESULTS

In this section, we first illustrate how the diverting agent affects treatment distribution among multiple fractures with a synthetic case. Following that, we present two field refracturing cases studies. For both cases, the simulation workflow of initial completion – pore pressure depletion – the refracturing process is carried out. We learned valuable lessons working on these two field cases. Strategies to improve refrac success are discussed.

7.4.1. Fluid Diversion by Diverting Agent

A synthetic three fracture case is presented to show how diverting agent affects treatment distribution in the simulation. The parameters used in the simulation are summarized in Table 7.1. The main difference among the three fractures is the minimum horizontal stress (S_{hmin}). The closure stress of fracture 2 is 100 psi lower than that of fracture 1, and the closure stress of fracture 3 is 100 psi lower than that of fracture 2. Fluid is injected into the three fractures at a constant rate of 10 bpm for 30 minutes.

Parameter	Value	Parameter	Value
Young's Modulus (MMpsi)	3.5	Wellbore Diameter (in)	4
Poisson's Ratio	0.22	Perforation Diameter (in)	0.375
Porosity	0.07	Perforation per Cluster	12
Reservoir Permeability (μD)	10	Inject Fluid Density (lb/gal)	8.35
Number of Fractures	3	Inject Fluid Viscosity (cp)	1
Pore pressure (psi)	7200	S_{hmin} of fracture 2 (psi)	10100
S_{hmin} of fracture 1 (psi)	10200	S_{hmin} of fracture 3 (psi)	10000

Table 7.1: Parameters for the diverting agent illustration case.

In the first case, no diverting agent was injected. The fluid injection rate into each fracture versus time is plotted in Fig. 7.10. A large fraction of the fluid flowed into fracture 3, the fracture with the lowest S_{hmin}. A small fraction of the injected fluid went into fracture 2. And the fracture with the highest S_{hmin} (fracture 1) got very little treatment fluid.

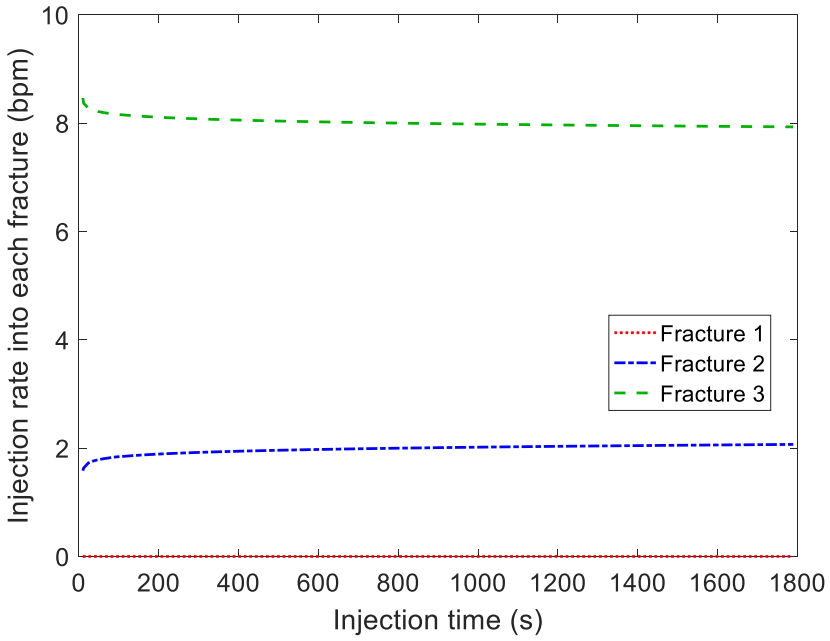

Figure 7.10: Injection rate into each fracture without diverting agents.

In the second case, diverting agents were injected after 10 minutes of treatment. It is assumed that diverting agent follows the distribution of treating fluid, and most diverting agent ends up in the fracture that gets the most treating fluid. The diverting agent in the fracture causes additional resistance and fluid is diverted to other fractures that have less flow resistance, as shown in Fig. 7.11. The fluid distribution after the application of diverting agent is much more uniform compared to the first case.

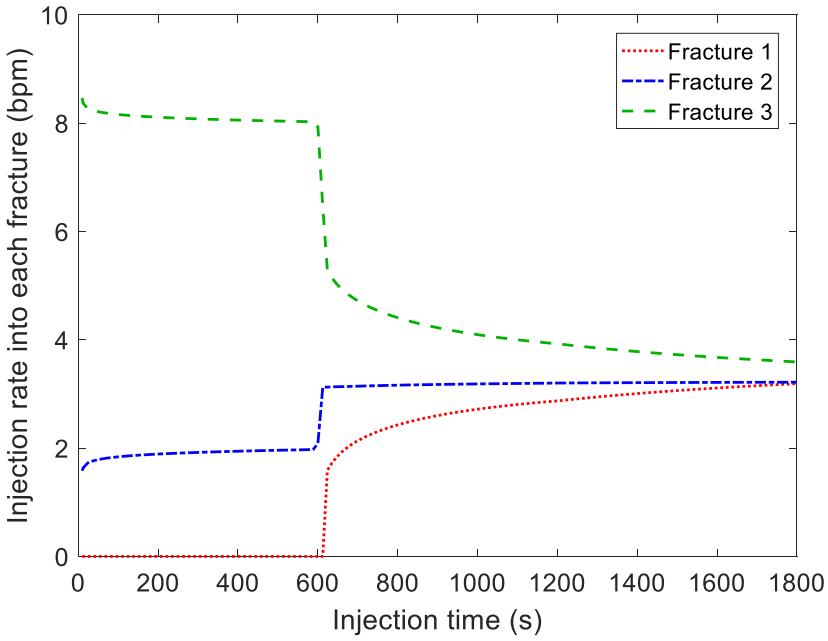

Figure 7.11: Injection rate into each fracture under the influence of diverting agents.

The bottom hole pressure (BHP) of these two cases are plotted in Fig. 7.12. Without diverting agent, the BHP remained almost constant throughout the stimulation. The application of diverting agent increased the BHP by about 1000 psi. Later in the treatment, as the fractures widen and propagate, the BHP gradually drops.

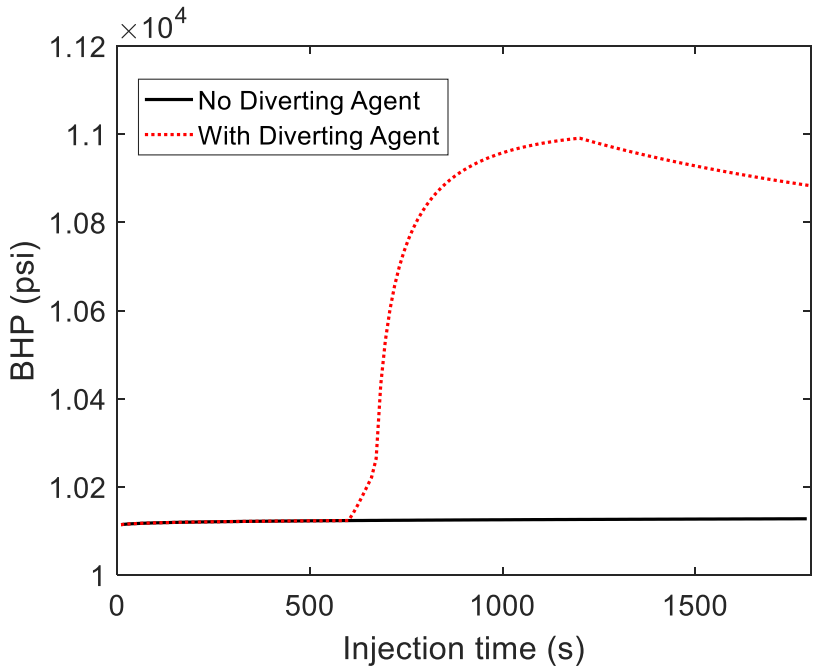

Figure 7.12: BHP of the synthetic case.

7.4.2. Field Case Study 1[3]

A refracturing treatment using a poly-lactic acid diverting agent was carried out in the Haynesville shale to improve production. Before the refracturing treatment, the well had been on production for about one year. Then it was shut in for about one and a half years. The production rate and tubing pressure history of the well are shown in Fig.7.13. Immediately after the refrac, the production rate was comparable to the initial production.

[3]This field case study is based on a collaboration project with Shell. It has been presented in the following conference: Yi, S. and Sharma, M., 2016, August. A model for refracturing operations in horizontal wells employing diverting agents. In SPE Asia Pacific Hydraulic Fracturing Conference. Society of Petroleum Engineers.

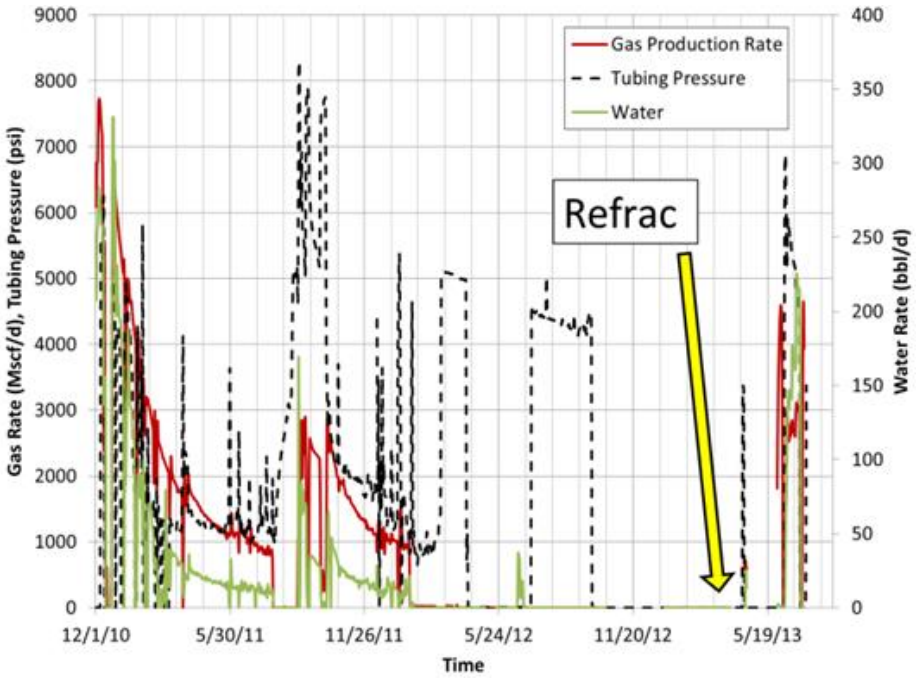

Figure 7.13: Production history of the re-fractured well.

The wellbore trajectory and the location of old and new perforation clusters are plotted in Fig. 7.14. The well has 21 original perforation clusters (plotted as black squares) from the initial stimulation, and 13 new perforation clusters (plotted as red dots) were added at the time of refracturing. The average cluster spacing for refrac is about 69 ft. During the refracturing treatment, no mechanical isolation was installed in the wellbore and the only fluid diversion method applied is diverting agent.

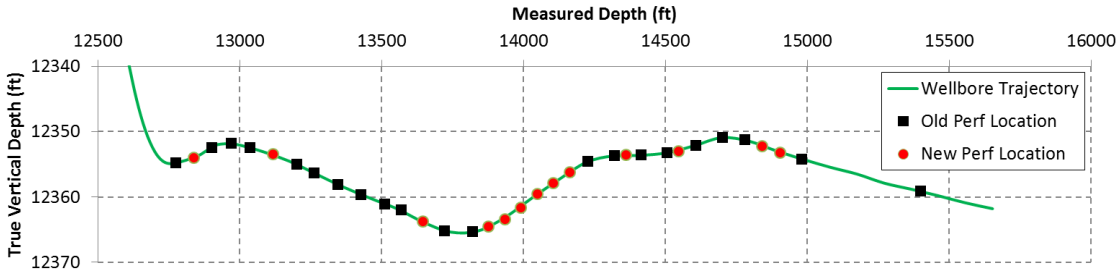

Figure 7.14: Wellbore trajectory and the location of old and new perforation clusters.

We followed this workflow to simulate the refracturing process:

1. The original fracture dimensions were estimated by simulating propagation of the original fractures and matching the net pressure data.
2. A reservoir simulator was used to history match the production data and to estimate the SRV properties. Fig. 7.15 shows the field and simulated data of bottom hole pressure and cumulative gas production. The simulated production matches the field results reasonably well.
3. A coupled geomechanical reservoir simulator was used to capture the influence of production on the reservoir pressure and stress. Fig. 7.16 shows the pore pressure and minimum horizontal stress along the wellbore after depletion. Near each existing fracture, the pore pressure and minimum horizontal stress are low due to depletion. The depletion effect is relatively local because of the short production time and the low reservoir permeability in the Haynesville Shale. Far from the fractures, the pressure and stress are close to the initial reservoir state.
4. The non-uniform pore pressure and stress state after depletion were used as inputs for the refracturing simulation. The minimum horizontal stress and the pore pressure values used for each cluster are marked by blue diamonds and green dots respectively in Fig. 7.16. The stress and pressure near new clusters are higher than those near existing fractures. The stress variation along the longitudinal direction (the fracture length direction) is simplified to account for the "stress cage" effect. In the SRV box, the stresses for each cluster is un-even as shown in Fig. 7.16. And out of the SRV box, the stresses are equal to the initial reservoir value.

The first three steps of this work were accomplished by Dr. Manchanda. And the refracturing simulation (step 4) is carried out with the model developed in this Chapter.

It is important to clearly state one word of caution in the application of this model (or any similar model). Reservoir heterogeneity will have a significant impact on the results of the simulation. In most cases data on rock heterogeneity is not available, and it is, therefore, not considered in the results presented here. As such the results obtained will be subject to some degree of uncertainty and should not be expected to predict the performance of each perforation cluster. Instead, the simulation results provide clear directional trends and guidelines that are expected to be correct. If more information on reservoir heterogeneity was available, more precise predictions could be made.

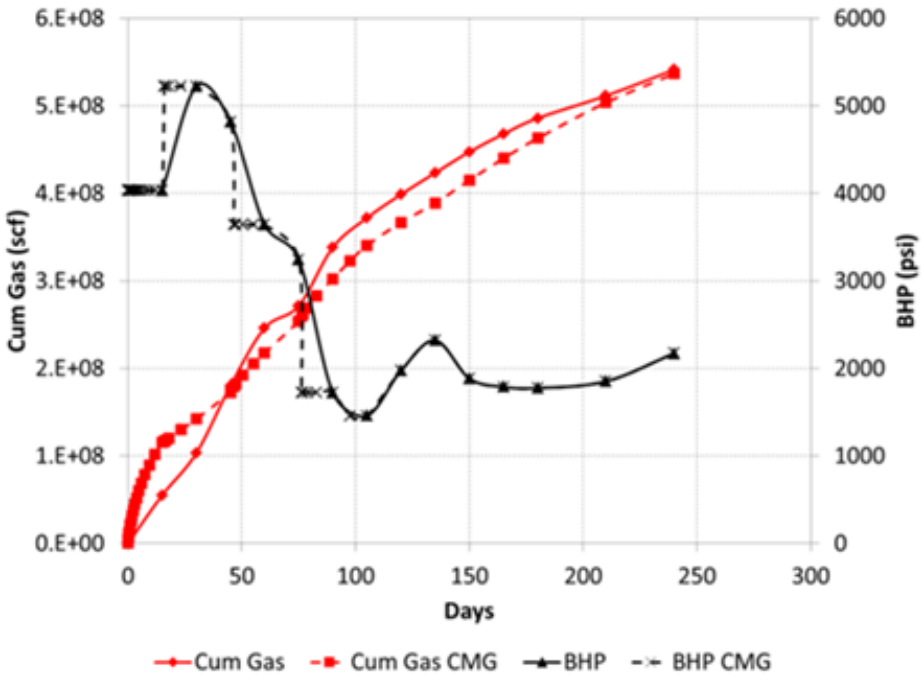

Figure 7.15: History match of gas production and bottom hole pressure. (Courtesy of Dr. Manchanda)

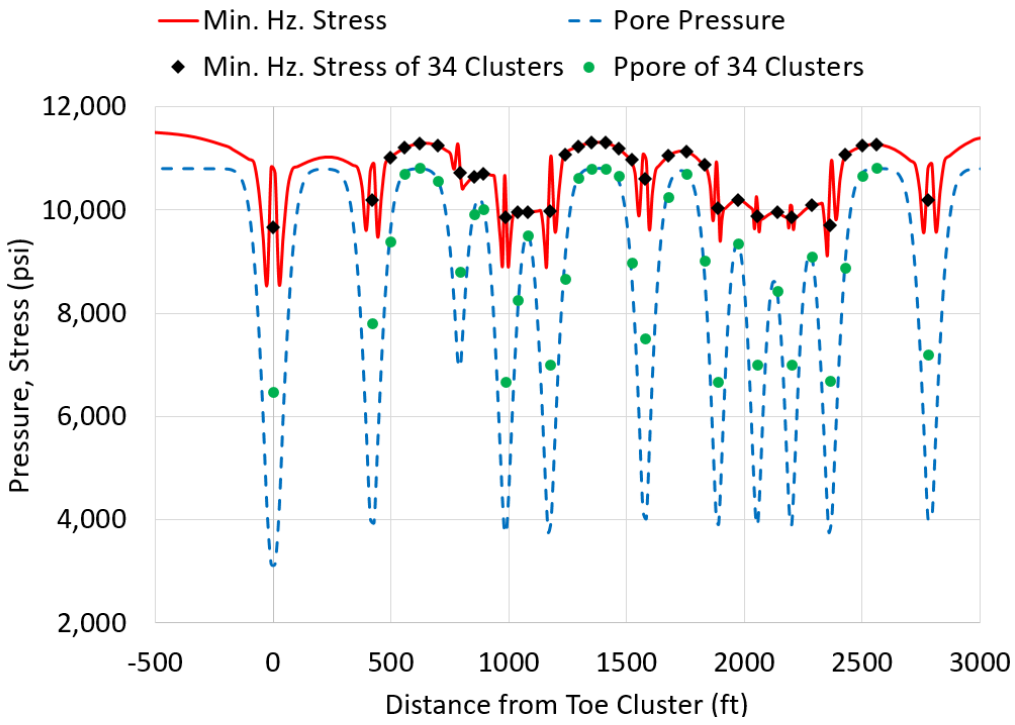

Figure 7.16: Pore pressure and minimum horizontal stress along the wellbore after depletion. (Courtesy of Dr. Manchanda)

A typical refracturing treatment cycle starts with a diverting agent stage to plug the fractures treated in the last stage, followed by a pad stage, a proppant stage and finishes with a shut-in. In this refrac treatment, 14 such refrac cycles were completed. The whole treatment lasted over 32 hours.

The BHP calculated from field treating pressure and the simulated bottom hole pressure during refracturing treatment are plotted in Fig. 7.17. In the figure, the field BHP data is plotted with marks. Different marks represent different stages in the refrac cycle: green triangles indicate diverting agent stages; blue diamonds represent pad stages; red squares are proppant stages, and crosses are shut-ins. The grey line in Fig. 7.17 is the simulation result.

It is shown that the simulated BHP matches the field BHP trend reasonably well. In each refrac cycle, the bottom-hole pressure rises due to the application of the diverting agent and the increase of injection rate. As the fractures widen and propagate, the bottom-hole pressure drops and maintains at a certain level. As more refracturing cycles are injected, the reservoir gets re-pressurized and re-stressed, and the bottom-hole pressure shows an overall climbing trend.

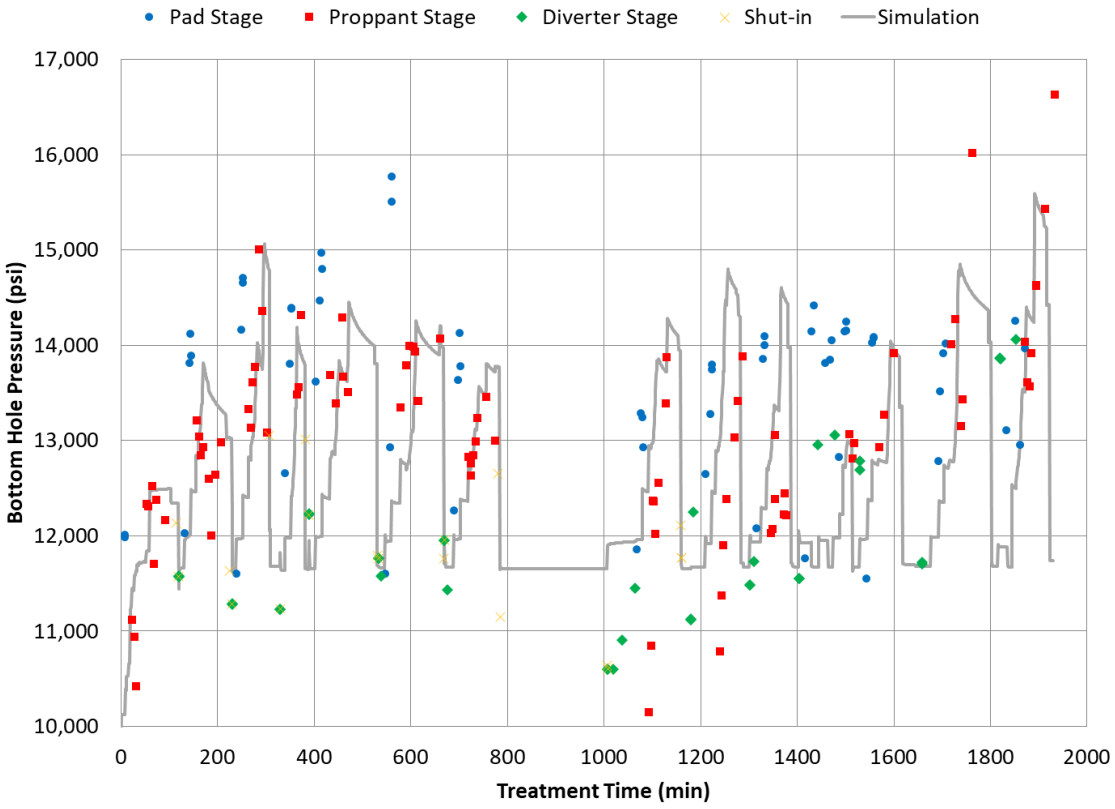

Figure 7.17: The field and simulated bottom hole pressure during the refracturing treatment.

One thing to be noted is that the well was shut-in for about 4 hours in the middle of the refracturing treatment. The bottom-hole pressure was observed to drop by over thousand psi when the injection was initiated after the shut-in.

The reason for this is that before the shut-in, the reservoir was supercharged due to injection. Both the pore pressure and the stress around the fractures increase due to fluid injection. During shut-in, fluid dissipates into the surrounding reservoir and releases the pressure and stress near the fractures. Thus, the pressure needed to open fractures after shut-in is lower than before. However, the reservoir permeability is very low in the Haynesville Shale, and 4 hours is a relatively brief time for the fluid to leak off and achieve a reduction in BHP on the order of thousand psi. Therefore, this information might be indicative of an induced unpropped fracture network created during refracturing that helped the fluid to dissipate during shut-in.

The final fluid and proppant distribution among multiple clusters are shown in Fig. 7.18. It is shown that the refrac treatment is heavily heel-biased. Most treatments ended up in the 5 clusters near the heel, and little treatment was distributed near the toe half of the well. Production logging was performed to evaluate the performance of different clusters. The main conclusion was that most production comes from the heel and the toe half of the wellbore contributed very little. The simulated treatment distribution trend is consistent with the production logging.

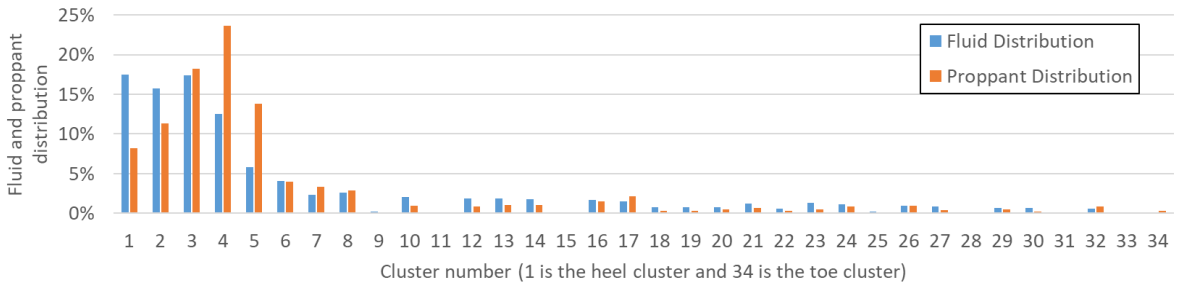

Figure 7.18: Simulated fluid and proppant distribution after refrac.

One of the main reasons for the heel biased refrac treatment distribution is the inertial effect of proppant. This effect has been discussed in detail in Chapter 5 and 6. Another likely reason is the wellbore trajectory. As shown in Fig. 7.14, there is an obvious dip in the middle of the wellbore. The slurry needs to climb up the slope in the middle of the wellbore before it reaches the toe half. It could be difficult to transport proppant through this dip as proppant particles may settle out due to gravity. Therefore, the toe side clusters received little treatment. Other reasons that could contribute to the heel biased treatment distribution includes wellbore pressure drop, plugs of proppant or diverting agent in the wellbore.

7.4.3. Field Case Study 2[4]

The second refrac case study is carried out on a horizontal well with more recent completion designs. This well is a parent well, and it is refractured for parent well protection. The well has been on production for two and half years, produced about 330 MBOE before refrac. The refrac treatment was successful in terms of improving the production of the parent well and protect the parent well from the child well stimulation. However, the refrac was also unsuccessful because only limited sections of the wellbore were effectively stimulated. The production pre- and post- refrac is shown in Fig. 7.19. Good production improvement was achieved after the refrac.

[4]This field case study is based on a collaboration project with ConocoPhillips.

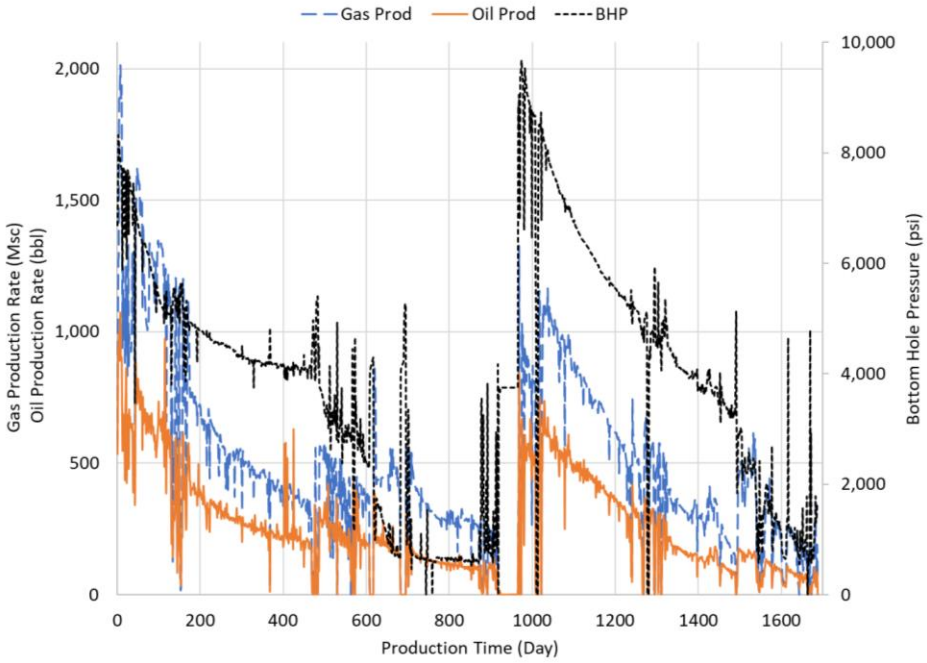

Figure 7.19: Production history of the re-fractured well.

Some key features of the refrac treatment are summarized in Table 7.2. The wellbore length of the horizontal section is about 4400 ft. The well was initially fractured with a plug-and-perf completion design. The initial treatment created 40 clusters with 112 ft cluster spacing. And at the time of refrac, 72 new clusters were perforated. The cluster spacing for refrac is 40 ft. The refracturing design injected almost twice the amount of proppant compared to the initial completion.

Parameters	Initial	Refrac
Perf to Perf	4439	4439
No. of Clusters	40	112
Cluster Spacing (ft)	112	40
Prop Amount (lb/ft)	831	1507
Pump Rate (bpm)	50	55
Max Prop Conc (ppa)	3	5

Table 7.2: Important parameters for the refrac field study.

A similar workflow as that in field case 1 is followed for the simulation. In the first step, fracture geometry created from the initial treatment was estimated. It is assumed that all the initial fractures are planar and are of the same dimension. Then, a reservoir simulator is used to match the production history and obtain the pore pressure distribution in the reservoir before refrac. This step was accomplished by ConocoPhillips's in-house reservoir simulator. SRV boxes are assumed around each fracture to represent the enhanced permeability near the fracture. And stress dependent permeability is adopted to simulate the permeability reduction due to the increase in effective stress during production.

Illustration of the simulation set up for the production history match is shown in Fig. 7.20. The historical oil production and the simulation results are plotted in Fig. 7.21. The historical bottom hole pressure and the simulation results are shown in Fig. 7.22. The simulated production matches the historical data well.

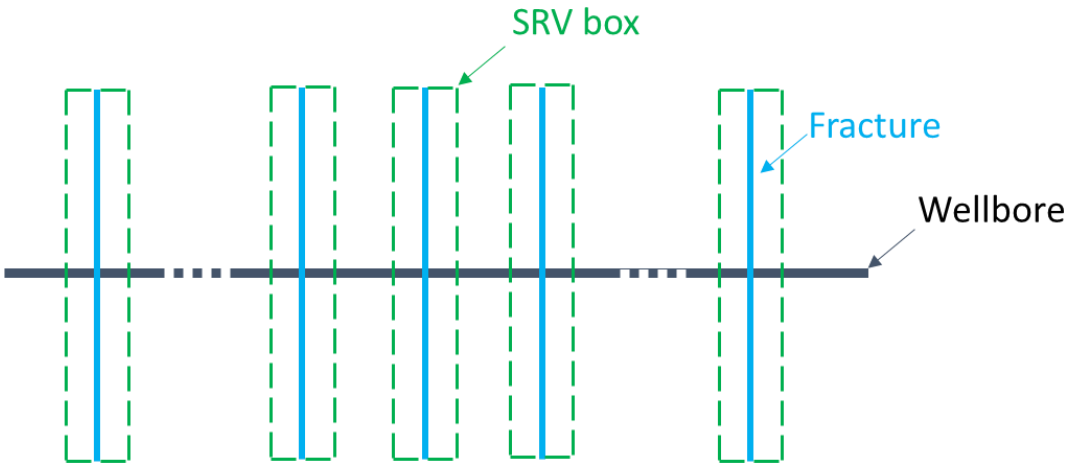

Figure 7.20: Illustration of the simulation domain for the production history match.

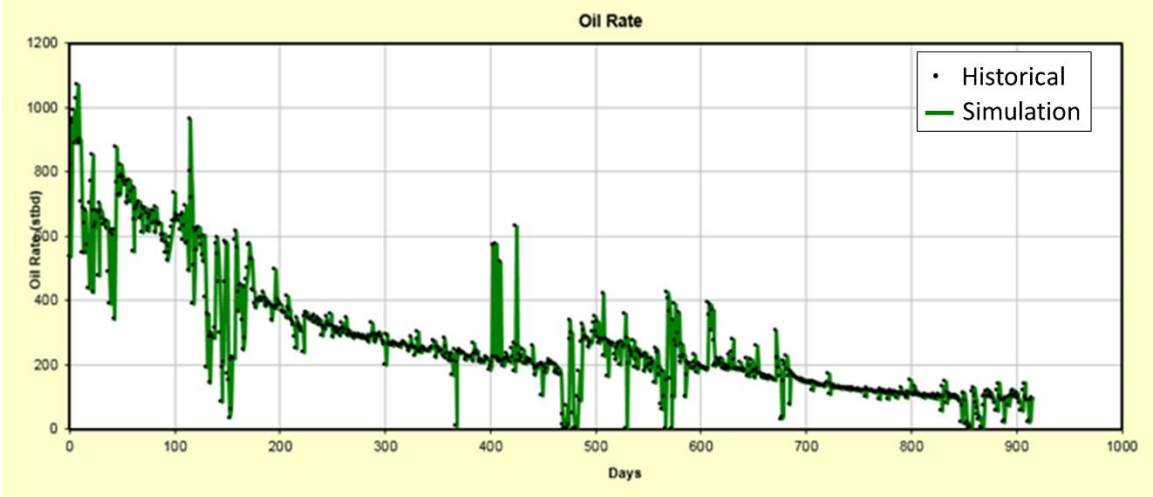

Figure 7.21: Historical and simulated oil production.

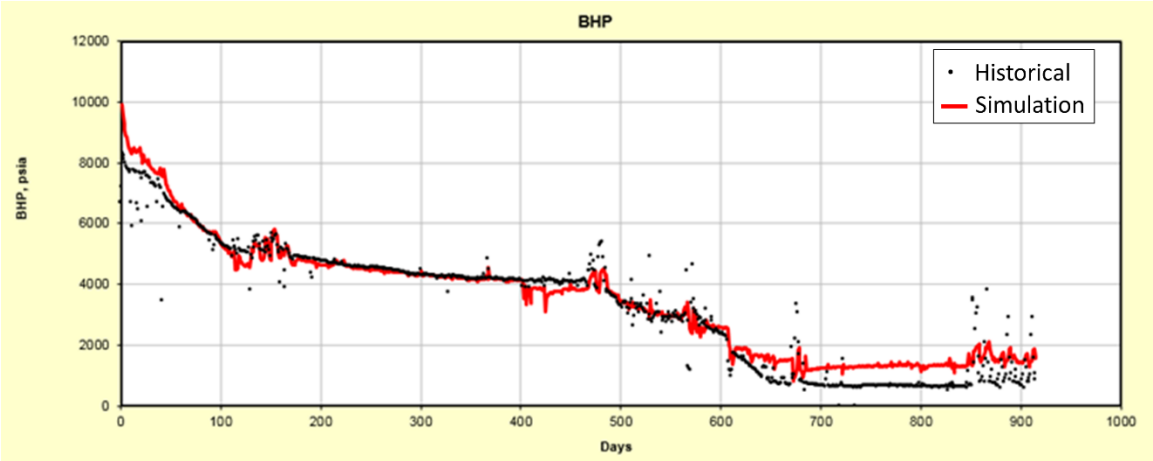

Figure 7.22: Historical and simulated bottom hole pressure during production.

Next, the pressure field obtained through the production history simulation was introduced into a coupled reservoir-geomechanical simulator to calculate the stress change in the reservoir due to poro-elastic effects. It is assumed that all the initial fractures experienced the same pore pressure depletion process. Therefore, only one fracture is simulated in a sector model as shown in Fig. 7.23. Symmetric boundary conditions (zero-normal displacement) were set on the four vertical boundaries surrounding the fracture. At the top of the reservoir, constant stress is applied to represent the overburden. At the bottom of the reservoir, zero-normal displacement is assumed.

Both ConocoPhillips's in-house geomechanical simulator and Multi-Frac-Res (Manchanda, 2015) were used to calculate the stress field. The results from the two different simulators compare well with each other as shown in Fig. 7.24. As pore pressure decreases, the effective stress increases to balance the total stress away from the depleted region. The pore pressure is the lowest near the existing fracture due to depletion. And the effective stress is the highest near the existing fracture.

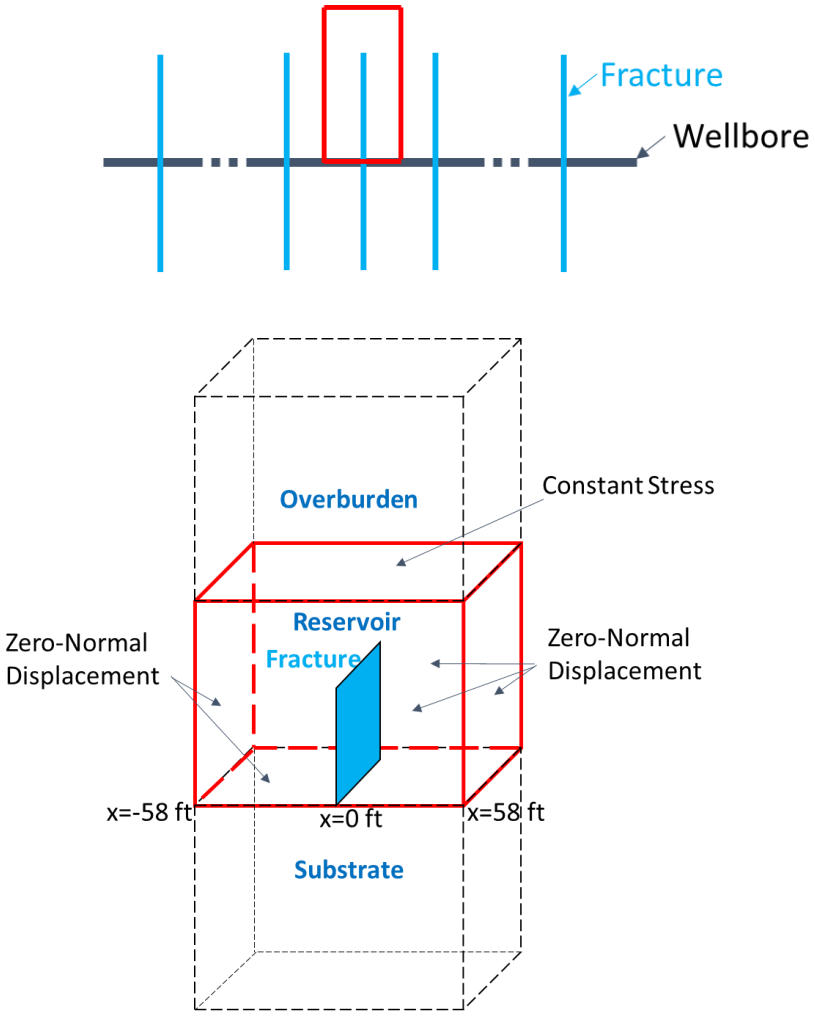

Figure 7.23: Illustration of the simulation domain for the coupled reservoir-geomechanical simulators.

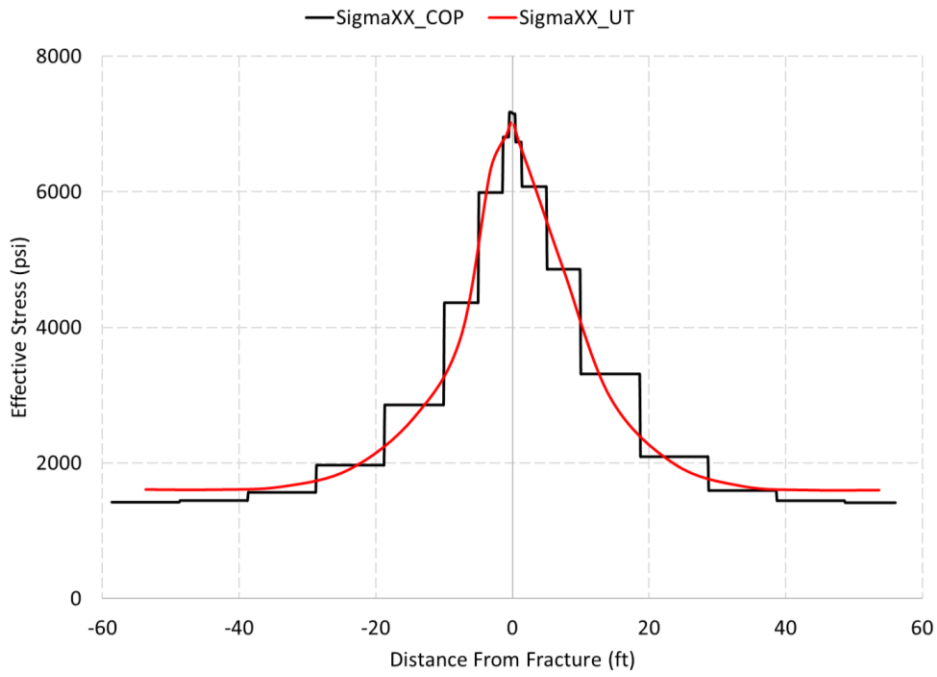

Figure 7.24: Effective stress profile. (Courtesy of Dr. Manchanda and Dr. Roussel)

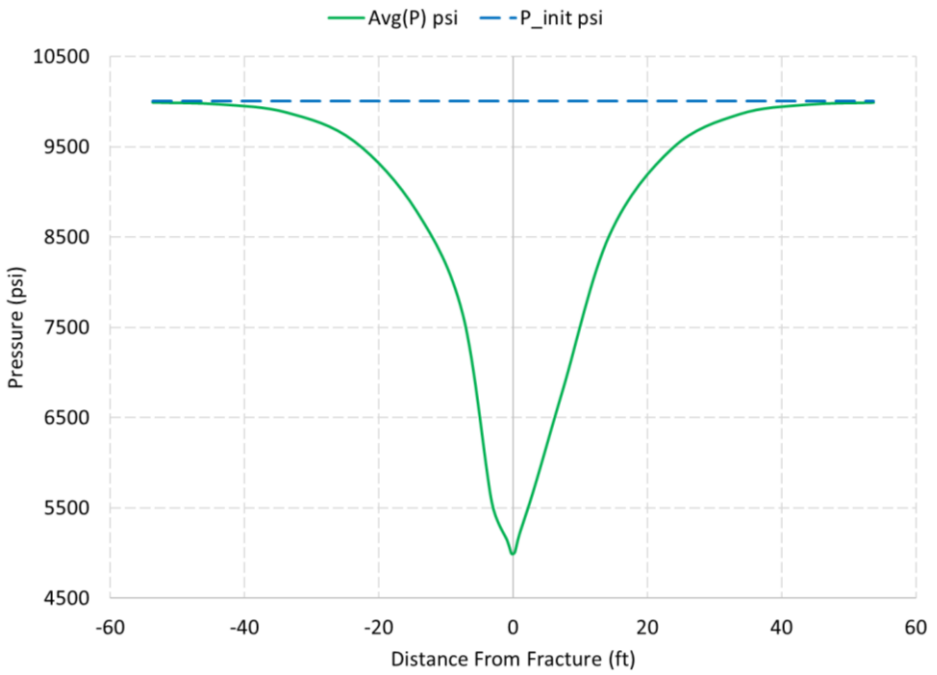

Figure 7.25: Pore pressure profile after depletion. (Courtesy of Dr. Roussel)

The pore pressure profile after depletion is plotted in Figure 7.25. The initial pore pressure in the reservoir is shown by the dashed blue line. And the pore pressure after depletion is shown by the solid green line. After production, the pore pressure distribution in the reservoir has a steep slope. The lowest pore pressure is found near the fracture with over 4,500 psi pressure reduction. And in the middle of two fractures (at the boundary of the simulation domain), the pore pressure is close to the initial value.

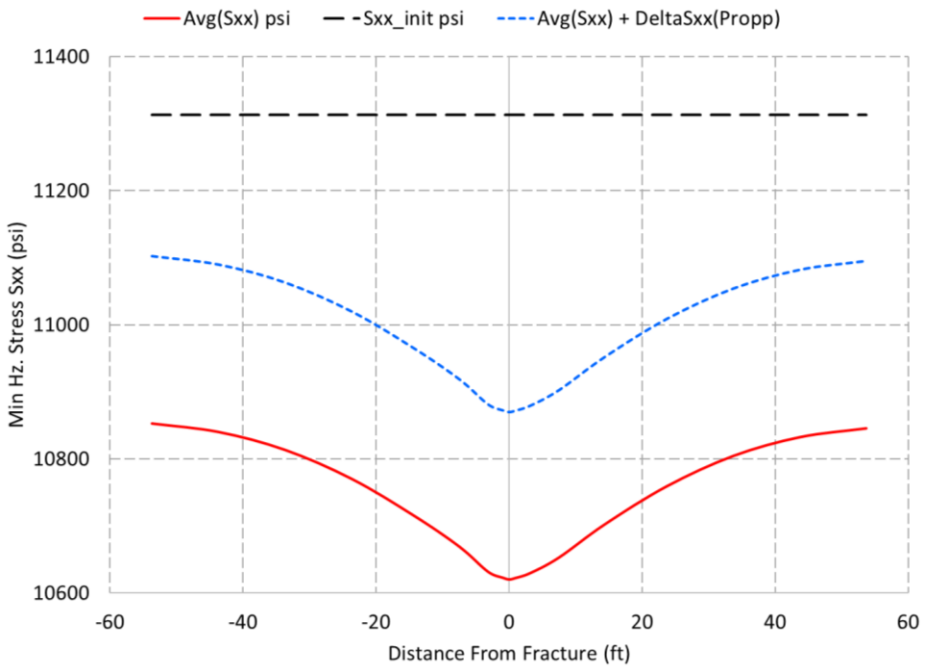

Figure 7.26: Stress profile after depletion. (Courtesy of Dr. Manchanda and Dr. Roussel)

The stress profile in the reservoir is plotted in Fig. 7.26. The dashed black line plots the initial stress in the reservoir, and the solid red line shows the stress profile after depletion. While the pore pressure reduction is limited near the fracture, the stress value decreased everywhere in the reservoir. The reason is that the stress change spreads much further than the pore pressure change. The reservoir redistributes the stress reduction

caused by pore pressure depletion, and the stress field gradually evens itself out in the reservoir. Compared to the pore pressure curve after depletion, the stress profile curve seems much more flat. The lowest stress is found near the fracture with about 700 psi reduction. And the minimum stress reduction in the reservoir is over 450 psi.

The mechanical stress caused by the opening of the fracture was also considered. When a fracture has a finite propped width in the reservoir, it deforms the rock nearby and introduces additional stress in the reservoir (Roussel, 2011). The mechanical opening of the fracture is simulated by a discrete fracture mesh in Multi-Frac-Res. The fracture is propped open in the simulation, and this process caused an increase of about 250 psi in the minimum horizontal stress. The final stress profile including both the pore pressure depletion and the mechanical stress shadow effect is shown by the dashed blue line in Fig. 7.26.

The pore pressure profile in Fig. 7.25 and the stress profile in Fig. 7.26 are expanded throughout the wellbore by applying the same pattern to each fracture. And the stress values at each existing and new cluster are interpolated from this profile and used as inputs in the refracturing simulation.

The last step of the workflow is the refracturing simulation. It is performed with the refrac model developed in this Chapter. The important parameters used in the refrac modeling are summarized in Table 7.3.

Reservoir Parameter	Value	Wellbore and Perforation Parameter	Value
Young's Modulus (GPa)	20	Wellbore Diameter (in)	5
Poisson's Ratio	0.25	Perforation Diameter (in)	0.375
Porosity	0.1	Perforation per Cluster	8
Reservoir Permeability (nD)	100	Initial Fracture Length (ft)	200
Reservoir Fluid Compressibility (Pa^{-1})	9.674e-10	Initial Fracture Height (ft)	100
Reservoir Fluid Viscosity (cp)	1	Fracture Half Height (ft)	82
Height (ft)	100	Initial Fracture Width at Wellbore (mm)	0.75
		Number of Existing Clusters	40
Fluid and Proppant Parameter	**Value**	Number of New Clusters	72
Fluid Density (g/cm^3)	1	Existing Cluster S_{hmin} (psi)	~10977
Fluid Viscosity (cp)	1	Existing Cluster P_{pore} (psi)	~4093
Proppant Density (g/cm^3)	2.65	New Cluster S_{hmin} (psi)	~10818
Proppant Diameter (μm)	400	New Cluster P_{pore} (psi)	~9891

Table 7.3: Parameters for Refrac simulation.

The refracturing process consists of 6 short refrac cycles (~40 minutes each) and 17 long refrac cycles (~100 minutes each). Each refrac cycle consists of diverting agent, pad, proppant and flush stages. The whole treatment lasted over 30 hours. The pumping schedule is shown in Fig. 7.27.

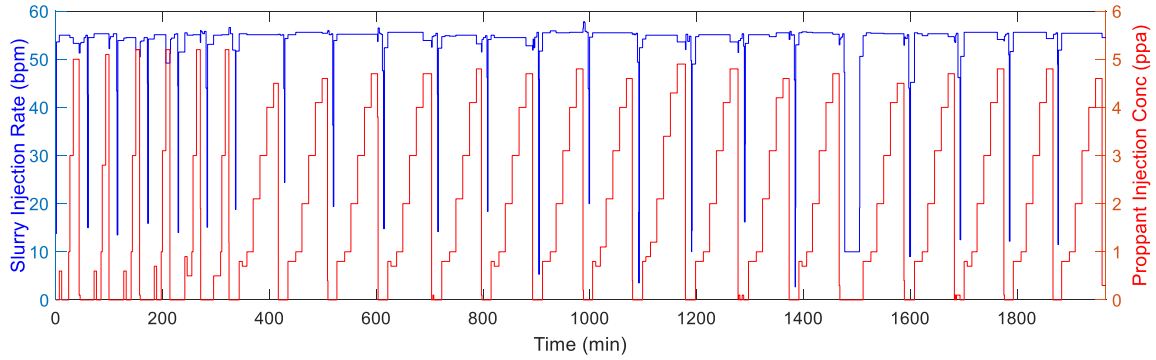

Figure 7.27: Refracturing treatment schedule.

The simulated fracture geometry after refrac is shown in Fig. 7.28. Fractures near the heel of the well grow the most. Fractures in the middle of the wellbore showed some propagation. And fractures near the toe section of the well propagated very little.

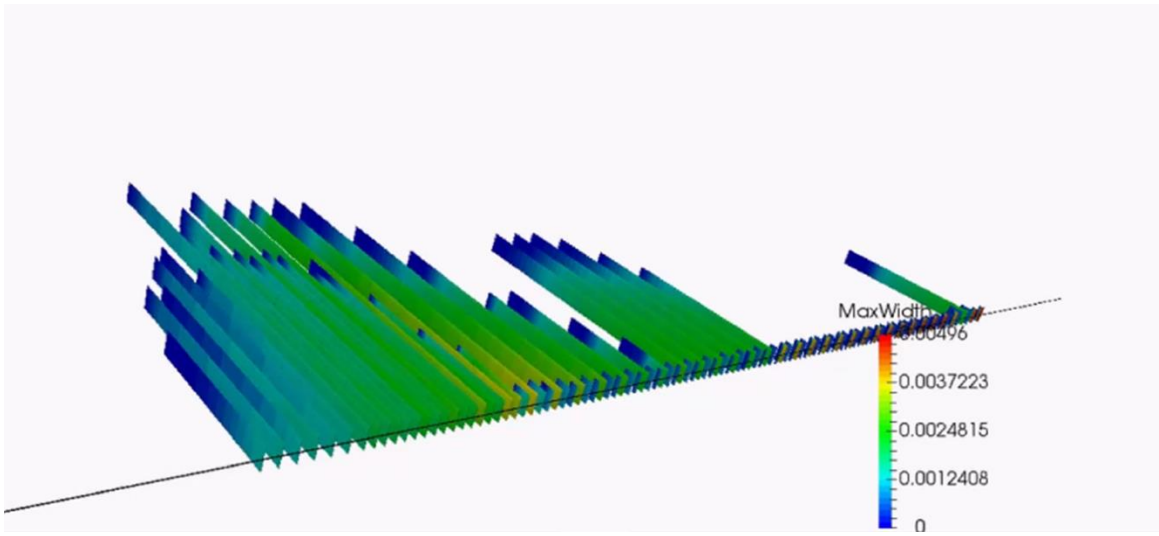

Figure 7.28: Simulated fracture geometry after the refracturing process.

The fluid and proppant distribution among all the clusters is shown in Fig. 7.29. The heel side 20 clusters took most of the treatment, the middle clusters received some,

and the toe side clusters got very little treatment. The final refrac treatment distribution is heel biased.

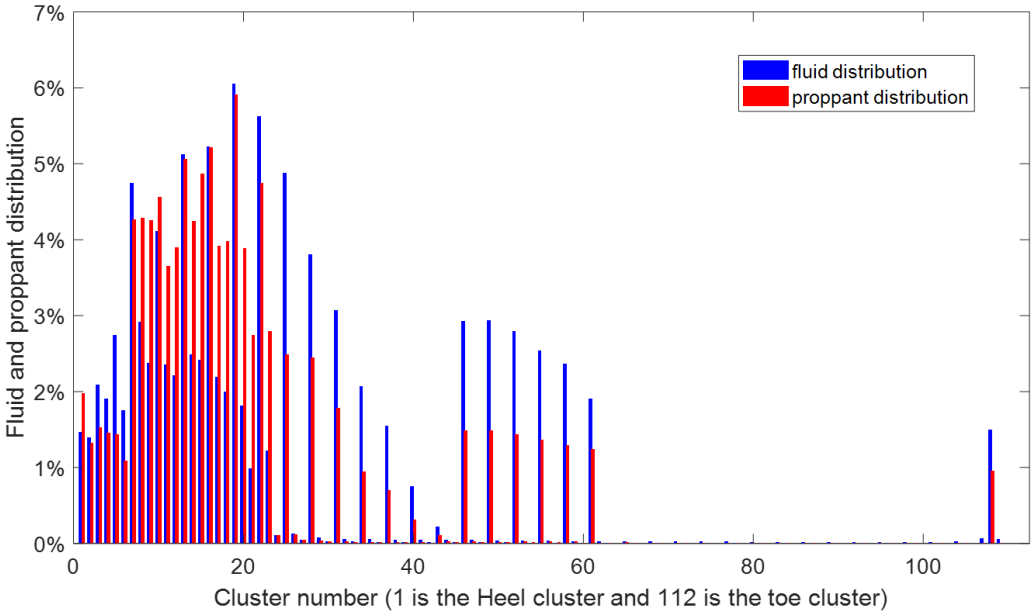

Figure 7.29: The fluid and proppant distribution among all fractures after the refracturing treatment.

A close-up view of the well-stimulated 20 heel-side clusters is shown in Fig. 7.30. The fractures marked by yellow arrows on the top are existing fractures, and the fractures without yellow arrows are new clusters perforated before the refrac. It is shown that both existing and new clusters can effectively break down during the refracturing treatment.

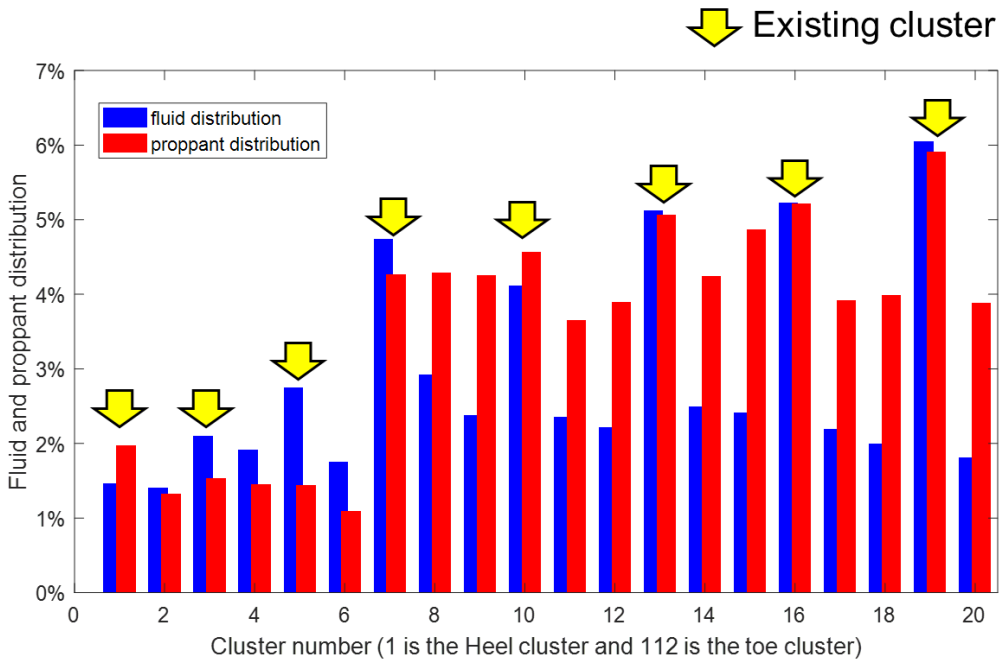

Figure 7.30: Fluid and proppant distribution among the well-treated 20 heel side clusters.

Diagnostics including proppant tracer imaging and quantitative production profile are performed about three months after the refracturing treatment. The main conclusions from the diagnostics show that the heel half of the wellbore contributes about 87% of total production. The heel section of the wellbore contributed the most to the production. Some production comes from the middle of the wellbore, and very little came from the toe. The simulated treatment distribution trend is consistent with the diagnostic results.

Furthermore, about 24% of the total clusters are producing at detectable flow rates according to the production profile. In the simulation results, it is observed that about 30% of the clusters received a substantial amount of the treatment. It is also observed in both the diagnostics and the simulations that new perforations can effectively break down during refracturing treatment.

7.4.4. Strategies to Promote Refrac Success

Through the analysis in the last several sections, we learned that the refracturing treatment is usually heel biased, with the heel side of the wellbore over-stimulated and the toe side of the wellbore under-stimulated. This uneven treatment distribution leads to under-performance of the refrac well and increases the risk of frac-hits. In this section, we provide some strategies to promote uniform treatment distribution in refracs and minimize interference between wellbores.

7.4.4.1. Short Refrac Cycles with More Frequent Diversion

The first strategy we propose to promote uniform treatment distribution among multiple fractures in refrac is to use short refrac cycles with more frequent diversion. In other words, we propose to divide the pumping schedule into shorter refrac cycles and apply diverting agent between each refrac cycle.

When multiple fractures are stimulated simultaneously, we observe from the simulation that only a few fractures dominate; and they remain dominant throughout the treatment unless the fracture screens out or some diversion method is applied.

This conclusion can be confirmed from the field DAS and DTS observations. Fig. 7.31 shows three independent studies of plug-and-perf treatments monitored by DAS and DTS. It is shown that the dominant fractures keep receiving most of the treatment until the end of the stage. Fig. 7.4 and 7.5 from another plug-and-perf study also show that most treatments went in the dominant fracture until some diversion method is applied.

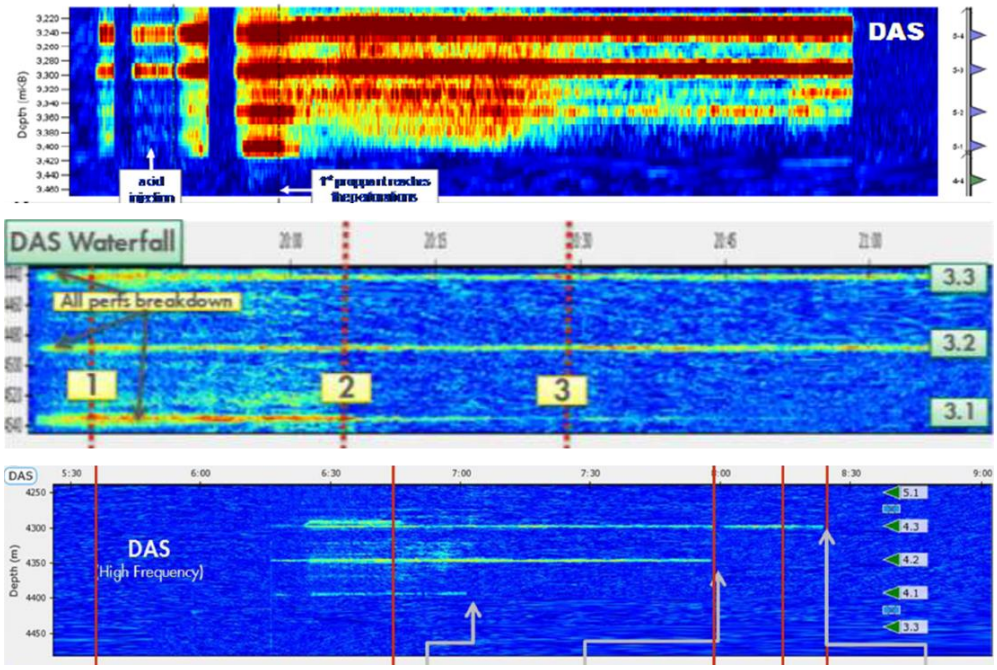

Figure 7.31: DAS observations show that dominant fractures remain dominant throughout the treatment unless screen out happens. (Molenaar & Cox, 2013; Somanchi et al., 2016; Ugueto et al., 2016)

Therefore, long refracturing cycles could over-stimulate the dominant fractures and leave the other fractures under-stimulated. We propose to target only a small number of fractures (about 3 to 5) in each refrac cycle, design each cycle to be short with less fluid and proppant volume, and apply diverting agent at the end of each refrac cycle to temporarily plug the dominant fractures.

We modified the pumping schedule of the second field refrac case to show the potential results of this strategy. In the original design, there were 6 short refrac cycles, each lasting about 30 minutes, and 17 long refrac cycles, each lasting about 100 minutes. We designed a new pumping schedule to inject the same amount of fluid and proppant in 30-minute short refrac cycles. The pumping schedule of the first three short refrac cycles is shown in Fig. 7.32.

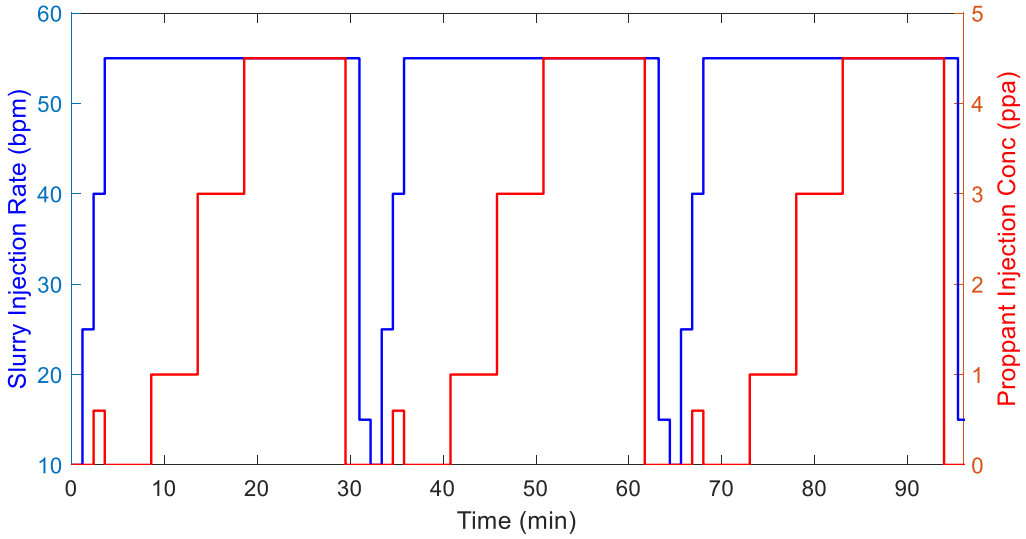

Figure 7.32: Illustration of short refrac cycles.

In the new design, the refrac cycles shown in Fig. 7.32 are repeated until all the planned fluid and proppant are pumped. In total, 66 such short refrac cycles were needed. The total treatment lasts around 35 hours, which is about 5 hours longer than the original design. Diverting agents are pumped between every stage to plug fractures treated in the last refrac cycle. The total amount of diverting agent is conserved.

All other parameters remained the same as the second field case except for the pumping schedule. The fluid and proppant distribution with the new pumping schedule design is shown in Fig. 7.33. The new design is shown to successfully shift a lot of the treatment to the toe side of the wellbore, and the final treatment distribution is much more uniform compared to the original design shown in Fig. 7.29. The most dominant fracture in the original design received about 6% of the total treatment. And the most dominant fracture in the new design received less than 3%. In the original design, about 30% of the clusters were effectively stimulated according to the simulation (effectively stimulated

fractures are defined as those received more than 100%÷112 = 0.89% of the total proppant). While in the new design, more than 55% of clusters were effectively stimulated. The number of effectively stimulated clusters increased by more than 80%.

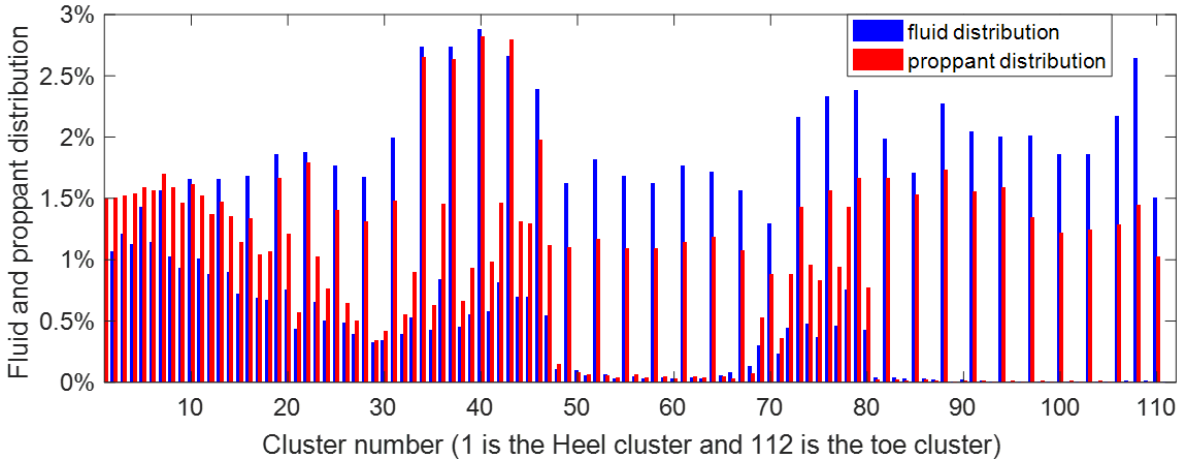

Figure 7.33: Fluid and proppant distribution of the new pumping schedule design with short refrac cycles.

To sum up, both the simulation and the field observation suggest that when many fractures are stimulated simultaneously, only a few fractures dominate. The dominant fractures receive most of the treatment, and they remain dominant unless the fractures screen out or a diversion method is applied. Long refrac cycles could over-stimulate the dominant fractures, leave other clusters under-stimulated, and increase the risk of affecting nearby wells.

We propose to target only a few fractures in each refracturing cycle, use shorter refrac cycles and divert more frequently. Simulation results show that this strategy could help prevent the heel-biased refrac treatment distribution and promote uniform fracture propagation.

7.4.4.2. Wellbore Arrangement

While different strategies may be used to promote uniform treatment distribution among multiple fractures during refrac, the heel-biased distribution trend may not be avoided completely, especially for long horizontal wells. In this case, we propose to arrange the child wells and the parent wells in a heel-to-toe pattern, in order to minimize the wellbore interaction.

Fig. 7.34 a) is an illustration of arranging the parent and child wells heel-to-heel. And Fig. 7.34 b) is an illustration of arranging the wells heel-to-toe. The yellow and red elliptical areas are the heel section of the two parent wells respectively. They are the wellbore sections that could potentially receive most of the refracturing treatment.

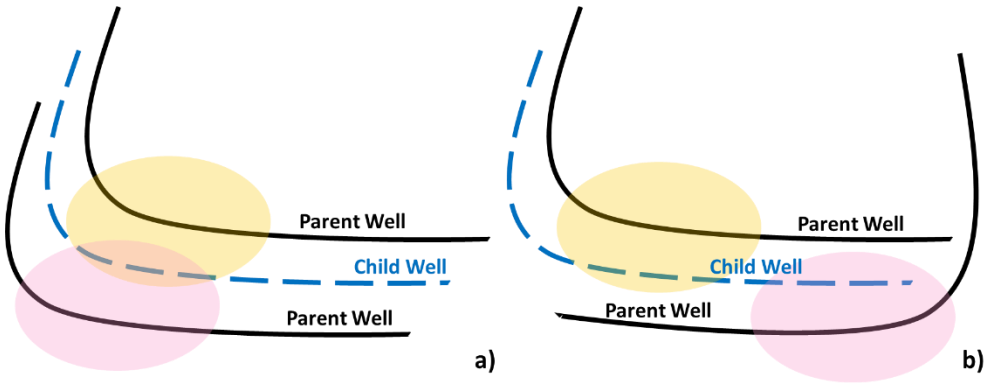

Figure 7.34: Illustration of a) arranging the wellbores heel-to-heel and b) arranging the wellbores heel-to-toe.

With the heel-to-heel wellbore arrangement pattern, the yellow and red ellipse could overlap. The heel sections of these wells are over-stimulated, and the toe sides are under-stimulated. Refracturing the parent wells could lead to serious wellbore communication among the parent and child wells and affect the final oil recovery negatively.

On the other hand, with the heel-to-toe pattern as shown in Fig. 7.25 b), the overlap of the yellow and red area is avoided. The interaction among the wells decreases compared to the heel-to-heel pattern. And refracturing the parent wells could improve oil recovery from different regions of the reservoir. Using this strategy may require modifications of pad arrangement and may not be practical or economical to accomplish in some cases.

7.4.4.3. Other Strategies

Some researchers have suggested injecting fluid into the well before the refrac treatment to overcome the impact of reservoir depletion, equalize the pressure and stress around the wellbore to improve the refrac efficiency (Manchanda et al., 2017). Although our model is not able to investigate such a strategy because the reservoir is not simulated, we can qualitatively see why this is a sound idea.

First, equalizing the pressure and stress by injecting fluid can help divert the following treatment to fractures with higher pressure and stress, prevent packing sand in the depleted fractures. Secondly, at the time of refrac, stress and pressure are the lowest near the wellbore, and as fractures propagate further from the wellbore, they will face higher stress regions. Increasing the pressure and stress by injecting fluid can help the fractures propagate beyond the depleted region and reach high-pressure zones of the reservoir. Thirdly, delaying the injection of proppant can help some fractures grow wider and longer, and decrease the risk of pre-mature screen out during refrac. This could also help the final treatment distribution to be more uniform.

Some other strategies suggested in Chapter 6 that promote uniform treatment distribution among multiple clusters could also be applied here. For example, create fewer

perforations, use lighter, smaller proppant, ramp up slowly to allow proppant to erode the near wellbore region and so on.

However, it should be noted that the situation in refracturing is much more complicated than in a plug-and-perf operation. Horizontal well refrac has many more fractures accepting fluid and a more complicated stress state in the reservoir. Directional suggestions are provided from the simulation, and these are very useful in designing a refrac treatment. We recognize that many uncertainties exist in many of the input parameters such as the efficiency of the diverting agent, heterogeneity in the reservoir, interaction among multiple wells and many others. The simulations, however, provide a very useful tool to direct our efforts before testing them in the field.

7.5. CONCLUSIONS

In this chapter, we developed a model to simulate a horizontal well refractuing process employing diverting agents. The model is capable of solving the simultaneous propagation of many fractures efficiently. The re-opening of existing fractures, the propagation of fractures in new clusters, the effect of diverting agents, and the dynamic fluid and proppant partitioning among multiple fractures are accounted for in the model.

We have applied this model to two refracturing field cases. The workflow of simulating the initial fracturing job – production history match – refracturing process has been presented for both cases. Our simulated refrac treatment distribution trend matches the field observation reasonably well. Some valuable conclusions can be drawn from this study:

1. The refracturing treatment distribution is usually heel-biased, with the heel side of the wellbore over-stimulated and the toe side under-stimulated. This has been

confirmed by the two field cases we studied and other published diagnostic results. The non-uniform treatment distribution can negatively impact the oil recovery from the refractured well and increase the risk of hitting offset wells. The main challenge in refracturing horizontal wells is to mitigate the heel-biased treatment distribution and stimulate more sections of the wellbore.

2. Our simulation results show that both existing and new perforations can effectively break down during refracturing treatment. This conclusion is consistent with field diagnostic results. Therefore, we can contact new zones of the reservoir by stimulating new perforations during the refrac.
3. Diverting agents can help promote a uniform treatment distribution by plugging the dominant fractures. The application of diverting agent usually introduces several hundred to a thousand psi pressure drop. The performance of diverting agent is not always consistent according to DAS and DTS observations. And despite the low permeability the diverting agent plugs offer, the inertial effect of proppant plays a crucial role in determining the slurry partitioning.
4. When multiple fractures are stimulated simultaneously, only some of the fractures dominate. And these fractures remain dominant until screen out or some diversion method is applied. Long refrac cycles could over-stimulate the dominant fractures.

We have also proposed some strategies to improve the efficiency of refracturing treatments and to promote a more uniform treatment distribution:

1. Use shorter refrac cycles and divert more frequently. In other words, target only a few fractures (3 to 5) in each refracturing cycle. Design short refrac cycles and apply diverting agents between each cycle. The simulation results show that

this strategy promotes more uniform treatment distribution and greatly increases the number of effectively treated clusters.

2. Arrange the parent and child wellbores in a heel-to-toe manner, so that the refracturing of two parent wells will not overlap at the child well. This will reduce wellbore interference but may require modifications of drilling pad designs.
3. Inject fluid prior to refracturing treatment to equalize the pressure and stress in all perforation clusters near the wellbore. This will help fractures reach beyond the depleted region and decrease the risk of pre-mature screen out.

7.6. ACKNOWLEDGMENT

I would like to acknowledge Shell and ConocoPhillips for providing the field case data and allowing us to publish the work. I am in debt to many people who have provided kind advice for building the model. Special thanks to people who have provided crucial suggestions and comments: Ripudaman Manchanda (UT Austin), Nicolas Roussel (ConocoPhillips), Mark Fissell (ConocoPhillips), Victoria Qiu (Assure Oilfield Testing), Liang Jin (Shell), Xu Li (Shell), David Nesse (Shell). And many thanks to people who worked on history matching and obtaining the pressure and stress profile for the two field cases: Ripudaman Manchanda (UT Austin), Nicolas Roussel (ConocoPhillips), Sergei Solonitsyn (ConocoPhillips), Yueming Liang (ConocoPhillips).

NOMENCLATURE

BHP	=	Bottom hole pressure, M/LT^2, Pa
G	=	Shear Modulus, M/LT^2, Pa
L	=	Fracture length (one wing), L, m
P_f	=	Pressure in the fracture, M/LT^2, Pa
P_{net}	=	Net pressure in the fracture, M/LT^2, Pa
Q_i	=	Injection rate into fracture i, L^3/T, m^3/s
$\hat{Q}^s$	=	Function representing transition of flow
Q_T	=	Total injection rate, L^3/T, m^3/s
R_i	=	Fracture resistance for fracture i, M/(L^{4}T), Pa·s/m^3
R_{tot}	=	Total resistance of all fractures, M/(L^{4}T), Pa·s/m^3
$S_{hmin,i}$	=	Closure stress of fracture *i*, M/LT^2, Pa
a	=	Radius of existing proppant, L, m
h_f	=	Fracture height, L, m
k_{DA}	=	Permeability of the diverting agent plug, L^2, m^2
k_{avg}	=	Average permeability of the fracture cell, L^2, m^2
$k_{channel}$	=	Permeability of the channel in the middle of the fracture, L^2, m^2
k_{pp}	=	Proppant pack permeability, L^2, m^2
q	=	Slurry flow rate per unit fracture height, L^2/T, m^2/s
q_o	=	Injection rate to one wing of the fracture per unit fracture height, L^2/s, m^2/s
q_p	=	Proppant flux per unit fracture height, L^2/T, m^2/s
r_{DA}	=	Outer radius of the diverting agent plug, L, m
r_w	=	Wellbore radius, L, m
u_L	=	Leak-off velocity, L/T, m/s
v	=	Poisson's Ratio
$w_{channel}$	=	Width of the channel in the middle of the fracture, L, m
w_f	=	Fracture width, L, m
$\Delta p_{DA,i}$	=	Pressure drop due to diverting agent plug for fracture *i*, M/LT^2, Pa
$\Delta p_{f,i}$	=	Pressure drop in fracture i, M/LT^2, Pa
$\Delta p_{pf,i}$	=	Pressure drop in perforations of fracture i, M/LT^2, Pa
$\Delta p_{w,i}$	=	Pressure drop in wellbore of fracture i, M/LT^2, Pa
$\overline{\emptyset}$	=	Normalized proppant concentration
μ	=	Viscosity of the fracturing fluid, M/LT, Pa·s
φ	=	Proppant pack porosity

REFERENCES

Denney, D., 2011. Screening Method To Select Horizontal-Well Refracturing Candidates in Shale-Gas Reservoirs. *Journal of Petroleum Technology*,63(11), pp.102-106.

Evans, S., Holley, E., Dawson, K., Garrison, N., Montes, M., Preston, G. and Hudson, S., 2016. Eagle Ford Case History: Evaluation of Diversion Techniques to Increase Stimulation Effectiveness. *Unconventional Resources Technology Conference* (URTEC).

Fisher, M.K., Heinze, J.R., Harris, C.D., Davidson, B.M., Wright, C.A. and Dunn, K.P., 2004. Optimizing Horizontal Completion Techniques in the Barnett Shale Using Microseismic Fracture Mapping. Paper SPE 90051 presented at the *SPE Annual Technical Conference and Exhibition*, Houston, Texas, 26–29 September.

Fragachan, F.E., Babey, A.G., Arnold, D.M., Heminway, E.M. and Yuan, F., 2015, September. Secret Weapon Against the Red Queen: Using Chemical Packers and Degradable Mechanical Diverters in Refracturing Operations. In *SPE Annual Technical Conference and Exhibition*. Society of Petroleum Engineers.

French, S., Rodgerson, J. and Feik, C., 2014, February. Re-fracturing horizontal shale wells: case history of a Woodford Shale pilot project. In *SPE Hydraulic Fracturing Technology Conference*. Society of Petroleum Engineers.

Jacobs, T., 2014. Renewing Mature Shale Wells Through Refracturing. *Journal of Petroleum Technology*, 66(04), pp.52-60.

Leonard, R.S., Moore, C.P., Woodroof, R.A. and Senters, C.W., 2015, September. Refracs-Diagnostics provide a second chance to get it right. In *SPE Annual Technical Conference and Exhibition*. Society of Petroleum Engineers.

Leonard, R.S., Woodroof, R.A., Senters, C.W., Wood, T.M. and Drylie, S.W., 2016, September. Evaluating and optimizing refracs-what the diagnostics are telling us. In *SPE Annual Technical Conference and Exhibition*. Society of Petroleum Engineers.

Lindsay, G.J., White, D.J., Miller, G.A., Baihly, J.D. and Sinosic, B., 2016, February. Understanding the applicability and economic viability of refracturing horizontal wells in unconventional plays. In *SPE Hydraulic Fracturing Technology Conference*. Society of Petroleum Engineers.

Manchanda, R., 2015. A general poro-elastic model for pad-scale fracturing of horizontal wells (Doctoral dissertation).

Manchanda, R., Sharma, M., Rafiee, M. and Ribeiro, L., 2017. Overcoming the Impact of Reservoir Depletion to Achieve Effective Parent Well Refracturing. *Unconventional Resources Technology Conference* (URTEC).

Miller, G., Lindsay, G., Baihly, J. and Xu, T., 2016, May. Parent Well Refracturing: Economic Safety Nets in an Uneconomic Market. In *SPE Low Perm Symposium*. Society of Petroleum Engineers.

Molenaar, M.M. and Cox, B.E., 2013, January. Field cases of hydraulic fracture stimulation diagnostics using fiber optic distributed acoustic sensing (DAS) measurements and Analyses. In *SPE Unconventional Gas Conference and Exhibition*. Society of Petroleum Engineers.

Murtaugh, D., Cao, J. 2014. U.S. Shale Oil Output Seen Growing Even as Prices Drop. Retrieved from http://www.bloomberg.com/news/articles/2014-10-14/u-s-shale-oil-output-growing-even-as-prices-drop-eia

Peters, E.J., 2012. *Advanced Petrophysics: Volume 1: Geology, Porosity, Absolute Permeability, Heterogeneity and Geostatistics*. Live Oak Book Co, Austin, Texas.

Potapenko, D.I., Tinkham, S.K., Lecerf, B., Fredd, C.N., Samuelson, M.L., Gillard, M.R., Le Calvez, J.H. and Daniels, J.L., 2009, January. Barnett Shale refracture stimulations using a novel diversion technique. In *SPE Hydraulic Fracturing Technology Conference*. Society of Petroleum Engineers.

Roussel, N.P., 2011. Stress reorientation in low permeability reservoirs (Doctoral dissertation).

Roussel, N.P. and Sharma, M.M., 2012. Role of stress reorientation in the success of refracture treatments in tight gas sands. *SPE Production & Operations*, 27(04), pp.346-355.

Sinha, S. and Ramakrishnan, H., 2011, January. A novel screening method for selection of horizontal refracturing candidates in shale gas reservoirs. In *North American Unconventional Gas Conference and Exhibition*. Society of Petroleum Engineers.

Somanchi, K., O'Brien, C., Huckabee, P. and Ugueto, G., 2016. Insights and observations into limited entry perforation dynamics from fiber-optic diagnostics. *Unconventional Resources Technology Conference* (URTEC).

Ugueto, C., Gustavo, A., Huckabee, P.T., Molenaar, M.M., Wyker, B. and Somanchi, K., 2016, February. Perforation cluster efficiency of cemented plug and perf limited entry completions; Insights from fiber optics diagnostics. In *SPE Hydraulic Fracturing Technology Conference*. Society of Petroleum Engineers.

Wright, C.A., Conant, R.A., Stewart, D.W. and Byerly, P.M., 1994, January. Reorientation of propped refracture treatments. In *Rock Mechanics in Petroleum Engineering*. Society of Petroleum Engineers.

Yi, S. and Sharma, M., 2016, August. A model for refracturing operations in horizontal wells employing diverting agents. In *SPE Asia Pacific Hydraulic Fracturing Conference*. Society of Petroleum Engineers.

MAJOR SECTION 5: CONCLUSIONS

Chapter 8: Conclusions and Future Work

This chapter summarizes the computationally efficient multi-fracture models presented in the dissertation. Strategies and insights for promoting uniform fracture propagation in plug-and-perf operations and horizontal well refracturing are drawn from the simulation results. New directions for extending these research topics are proposed for further research.

8.1. SUMMARY AND CONCLUSIONS

8.1.1. The Computationally Efficient Multi-Fracture Model

A multi-fracture model has been developed to simulate the propagation of multiple hydraulic fractures from a horizontal wellbore. The model captures most of the major features of fracture propagation with a small computational cost. This is essential if a large number of fractures are to be simulated in a reasonable amount of time. The main components and ideas used in the model are summarized below:

Single Fracture Modeling:

1. A 2-D PKN-type fracture model is first used to simulate a fracture that is well contained in the reservoir layer with a constant fracture height.
2. Next a pseudo-3D fracture model is developed. This model allows a series of reservoir and fluid properties to vary with depth, including the minimum horizontal stress, pore pressure, reservoir porosity and permeability, reservoir

fluid viscosity and compressibility. The mechanical properties such as Young's Modulus and Poisson's Ratio are assumed to remain constant.

3. The equilibrium height and the width profile of the pseudo-3D fracture are calculated using superposition of an exact, analytical solid mechanics solution. This method is much faster than the integral method or the 2D displacement discontinuity method (DDM).
4. For both the PKN-Type and the pseudo-3D fracture models, plane strain is assumed. This assumption is shown to be fairly accurate when the fracture length (tip to tip) is larger than three times the fracture height.
5. For both models, fracture propagation is solved on a moving mesh, and the number of elements remains constant throughout the simulation.
6. For both models, proppant transport in the fracture is simulated using a continuous constitutive model. A smooth transition from Poiseuille flow to Darcy flow is used for low and high proppant concentration (Dontsov & Peirce, 2014).
7. In the PKN-type model, proppant settling is ignored. In the pseudo-3D model, proppant settling and the development of a proppant bank is solved on a separate, fixed mesh.
8. Both models were validated with published solutions. Sensitivity studies were used to study the minimum number of elements required to obtain accurate solutions when using the moving mesh.

Multi-Fracture Modeling:

1. A new approach is developed to calculate fluid distribution among multiple fractures. We refer to this method as the Resistance Method. This new method

defines the resistance to flow into a fracture and distributes fluid among fractures in reverse proportion to fracture resistance, using an analogy of current distribution in a circuit network.

2. In the new fluid distribution method, the original N+1 non-linear equations for mass balance and pressure continuity are reformulated to eliminate one unknown and form a system of N non-linear equations with N unknowns ($Q_1, Q_2, \dots, Q_n$). The new system of N equations has been proved to converge locally at least linearly.
3. Compared to the commonly adopted Newton-Raphson method, the Resistance Method has several advantages: 1) it is easy to implement; 2) it does not require the evaluation of derivatives and a Jacobian matrix; 3) it is computationally efficient; 4) it can be implicitly integrated with almost any fracture model to create multi-fracture simulators.
4. The interaction between fractures due to stress shadow effects is accounted for in two ways: 1) a simple analytical solution and 2) a DDM method. We applied the first method to the 2D multi-fracture model and the DDM method to the psedueo-3D multi-fracture model.
5. Proppant Transport Efficiency (PTE) correlations developed in our group are incorporated into the muti-fracture model developed here to calculate the proppant partitioning among multiple clusters.
6. It is shown that the proppant distribution among multiple fractures can be quite different from that of the fluid. The inertia of the proppant particles results in proppant accumulating in the wellbore while fluid leaks off from the perforations. Thus, proppant concentration increases towards the toe side clusters. The highly concentrated slurry increases the risk of pre-mature screen-

out for the toe side clusters. As the toe side clusters screen out, they stop receiving any more fluid or proppant. All subsequent fluid and proppant is re-distributed to other active clusters, resulting in a heel-biased treatment distribution.

7. The heel-biased treatment distribution has frequently been observed in the field (Ugueto et al., 2016; Wheaton et al., 2016). The simulated treatment distribution predicted by our model matches the field observations well.
8. The proppant transport model is not limited to the 2D and pseudo-3D multi-fracture models. It can be applied to almost any fracture model with minor alteration.

8.1.2. Plug-and-Perf Operations

The multi-fracture model is applied to quantitatively calculate the fluid and proppant distribution among multiple clusters in plug-and-perf operations. It is shown that proppant placement into fractures depends on many completion factors including the perforation design and pumping schedule. By investigating the sensitivity of the proppant distribution to different operational parameters, specific design recommendations are provided that will promote uniform proppant placement in all clusters leading to better production.

To summarize, both the perforation design and pumping schedule variables are found to have a significant impact on the final treatment distribution. The impact of each variable is summarized below:

6. For a uniform perforation design, with the same number of perforations per cluster, fewer perforations per cluster were found to promote uniform treatment distribution and create more surface area.
7. A staggered perforation design, a design with fewer perforations near the heel than the toe, was found to promote a more uniform treatment distribution and create a lot more propped fracture surface area. Shooting more perforations near the heel than the toe was found to impact the final treatment distribution negatively.
8. Perforation diameter: A 3/8" perforation diameter was found to perform better than the 1/2" perforation diameter with respect to the final treatment distribution.
9. Proppant size and density: Changing the proppant density was found to have a much bigger impact on final treatment distribution than changing the proppant size. Using lighter proppant is found to promote a much more uniform treatment distribution and create more propped fracture surface area. Using a smaller proppant is also found to create more propped surface area.
10. Injection rate, proppant concentration and rate of proppant ramp-up: Due to constraints in designing the pumping schedule such as conserving the volume of fluid and proppant, these three parameters should be optimized together. As a rule of thumb, smaller proppant concentration and a more gradual proppant ramp-up help to promote more uniform treatment distribution and create more propped surface area.

We have also for the first time developed a process to automate the optimization of operational parameters by varying multiple parameters simultaneously using a Genetic Algorithm approach. The optimum plug-and-perf stage design that promotes uniform

treatment distribution and maximizes propped surface area can be obtained using this algorithm. It is also shown that when multiple operational parameters are optimized simultaneously, the propped surface area can be greatly improved.

8.1.3. Horizontal Well Refracturing

The multi-fracture model is applied to simulate horizontal well refracturing. The re-opening of existing fractures as well as the propagation of new perforations and the effect of diverting agents are accounted for. In refracturing operations employing diverting agents, a large number of clusters (and perforations) are open to the injected fracturing fluid. This makes the proppant transport efficiency even more important and a heel-biased proppant distribution much more likely.

We have applied this model to two field refracturing cases. The workflow that we follow is as follows:

1. Simulate the initial fracture treatment
2. Production history match all prior production and obtain the new stress state in the reservoir
3. Simulate the refracturing process.

Our simulated refrac treatment distribution trend matches the field observation reasonably well. Valuable conclusions can be drawn from this study:

1. The refracturing treatment distribution is usually heel-biased, with the heel side of the wellbore over-stimulated and the toe side under-stimulated. This has been confirmed by the two field cases we studied and other published diagnostic results. The non-uniform treatment distribution can negatively impact the oil recovery from the refrac well and increase the risk of hitting the offset wells. The main challenge of refracturing horizontal

wells is to mitigate the heel-biased treatment distribution and stimulate more sections of the wellbore.

2. Our simulation results show that both existing and new perforations can effectively break down during a refracturing treatment. This conclusion is consistent with the diagnostic results. Therefore, we can possibly contact new zones of the reservoir by creating new perforations.

3. Diverting agents can help promote a more uniform treatment distribution by plugging the dominant fractures. The application of diverting agent usually introduces several hundred to thousand psi pressure drop. The performance of diverting agent is not always consistent according to DAS and DTS observations. And despite the low permeability the diverting agent plugs offer, the inertia of the proppant particles still plays a crucial role in determining the slurry partitioning, and the final treatment distribution.

4. When multiple fractures are stimulated simultaneously, only some of the fractures dominate. And these fractures remain dominant until screen out or some diversion method is applied. Long refrac cycles could over-stimulate the dominant fractures.

We proposed some strategies to improve the efficiency of refracturing treatment, promote a more uniform treatment distribution and minimize wellbore interference:

1. Use shorter refrac cycles and divert more frequently. In other words, target only a few fractures (3 to 5) in each refracturing cycle. Design short refrac cycles and apply diverting agents between each cycle. The simulation results show that this strategy promotes a more uniform treatment distribution and greatly increases the number of effectively treated clusters.

2. Arrange the parent and child wellbores in a heel-to-toe manner, so that the refracturing of the parent wells wouldn’t overlap at the child well and reduces wellbore

interference. This may not be economically feasible if the pad design has to be modified for this purpose.

3. Inject fluid prior to the refracturing treatment to equalize the pressure and stress near the wellbore for all perforation clusters (new and old). This will partly mitigate the effect of reservoir depletion and allow fractures to propagate in regions other than the depleted region and decrease the risk of pre-mature screen out.

8.2. FUTURE WORK

The research work presented in this dissertation could be extended to study many interesting topics, including but not limited to:

1. More work can be done to improve the simulation of perforation erosion. The current model uses Romero's correlation (Romero et al., 1995) to calculate the perforation pressure drop. In this model, the perforation erosion only considers the impact of the total proppant mass flowing through perforation on the discharge coefficient. In more recent work, other authors (Long & Xu, 2017) have identified that injection rate and proppant concentration also play a role in perforation erosion.
2. The multi-fracture model can be extended to simulate fracture turning and fracture interaction with natural fractures (Kresse et al., 2013). Two potential methods could be used to determine the fracture propagation direction: the principal stress direction ahead of the fracture tip (Kresse et al., 2013), or the maximum circumferential stress criterion (Wu, 2014). The fracture cell size increases as the fracture propagates in the moving mesh algorithm. Proper

interpolation or re-meshing methods need to be adopted to model fracture turning and fracture interaction with natural fractures.

3. The fluid and proppant transport in the fracture could be extended to the 2D model and further extended to study proppant transportation in fracture and natural fracture networks.
4. Further development of the PTE correlations is recommended. Potential topics include: (1) Develop PTE correlations for Non-Newtonian fluids. (2) Current PTE correlations are perforation-based. In other word, current PTE correlations are applied to each perforation in each cluster. Cluster-based PTE correlations can be developed to calculate proppant distribution more accurately. (3) Study the impact of wellbore trajectory on PTE correlations. The gravity effect could affect proppant transport in the wellbore when the wellbore is not perfectly horizontal. (4) Study the impact of shooting perforations 45 degrees from the flow direction. This strategy might help mitigate the proppant inertia and promote uniform proppant distribution among multiple clusters. But the impact of this type of perforation on fracture initiation and near wellbore effects needs to be considered.
5. It will be useful to take economics into consideration in the optimization of plug-and-perf operations. In Chapter 6 it is shown that when multiple parameters are optimized simultaneously, the propped fracture surface area can be greatly improved. A cash flow and internal rate of return (IRR) analysis can be applied to analyze the cost of applying the design and the benefit in terms of improved production rates. The best plug-and-perf design should be based on such the economic analysis.

6. The current model simulates the diverting agent in a simple way. Additional experimental and simulation work on diverting agent placement can be conducted to better explain and estimate the extent of fluid diversion by diverting agents.
7. The effects of stress reorientation from poroelastic and mechanical effects during horizontal well depletion, and how it impacts horizontal well refracturing can be studied in more detail to investigate fracture turning and intersection (Roussel, 2011).
8. Study candidate well selection for horizontal well refracturing.

REFERENCES

Dontsov, E.V. and Peirce, A.P., 2014. Slurry flow, gravitational settling and a proppant transport model for hydraulic fractures. Journal of Fluid Mechanics, 760, pp.567-590.

Kresse, O., Weng, X., Gu, H. and Wu, R., 2013. Numerical modeling of hydraulic fractures interaction in complex naturally fractured formations. Rock mechanics and rock engineering, 46(3), pp.555-568.

Long, G. and Xu, G., 2017. The effects of perforation erosion on practical hydraulic-fracturing applications. *SPE Journal*, *22*(02), pp.645-659.

Romero, J., Mack, M.G. and Elbel, J.L., 1995. Theoretical model and numerical investigation of near-wellbore effects in hydraulic fracturing. Presented at the SPE Annual Technical Conference and Exhibition, Dallas, Texas, 22-25 October. SPE-30506-MS. http://dx.doi.org/10.2118/30506-MS

Roussel, N.P., 2011. Stress reorientation in low permeability reservoirs (Doctoral dissertation).

Ugueto, C., Gustavo, A., Huckabee, P.T., Molenaar, M.M., Wyker, B. and Somanchi, K., 2016, February. Perforation cluster efficiency of cemented plug and perf limited entry completions; Insights from fiber optics diagnostics. In *SPE Hydraulic Fracturing Technology Conference*. Society of Petroleum Engineers.

Wheaton, B., Haustveit, K., Deeg, W., Miskimins, J. and Barree, R., 2016, February. A case study of completion effectiveness in the eagle ford shale using DAS/DTS observations and hydraulic fracture modeling. In *SPE Hydraulic Fracturing Technology Conference*. Society of Petroleum Engineers.

Wu, K., 2014. Numerical modeling of complex hydraulic fracture development in unconventional reservoirs (Doctoral dissertation).

Appendix A: Convergence of the Resistance Method

Here we discuss convergence properties of the new fluid distribution method.

According to the Ostrowski's Theorem (Ortega (1990)), for a general iteration as shown in Equation A-1:

$$\boldsymbol{x^{k+1}} = G(\boldsymbol{x^k}), k = 0, 1, \ldots \tag{A-1}$$

Where $G: R^n \to R^n$. A solution of the Equation A-1: $\boldsymbol{x}^* = G(\boldsymbol{x}^*)$ is called a fixed point of *G*. If $G: R^n \to R^n$ is differentiable at the fixed point $\boldsymbol{x}^*$ and the spectral radius $\rho\big(G'(\boldsymbol{x}^*)\big) < 1$ (where G' is the Jacobian matrix of *G*), then $\boldsymbol{x}^*$ is a point of attraction for the iteration (A-1), and the iteration converges locally at least linearly. The smaller $\rho\big(G'(\boldsymbol{x}^*)\big)$, the faster the system converges. We prove the convergence of the new slurry distribution method using this theorem.

The new slurry distribution method consists of N non-linear equations for slurry distribution among N fractures, as shown in Equation A-2.

$$\begin{aligned} Q_1 &= \frac{BHP - S_{hmin,1}}{R_1} \\ Q_2 &= \frac{BHP - S_{hmin,2}}{R_2} \\ &\cdots \\ Q_n &= \frac{BHP - S_{hmin,n}}{R_n} \end{aligned} \tag{A-2}$$

Where the bottom hole pressure (*BHP)*, fracture resistance for fracture *i* (R_i), and total resistance (R_{tot}) are defined as below:

$$BHP = R_{tot}(Q_T + \sum_{i=1}^{n} \frac{S_{hmin,i}}{R_i}) \tag{A-3}$$

$$R_i = \frac{\Delta p_{f,i} + \Delta p_{pf,i} + \Delta p_{w,i}}{Q_i} = \frac{\Delta P_i}{Q_i} \tag{A-4}$$

$$\frac{1}{R_{tot}} = \sum_{i=1}^{n} \frac{1}{R_i} \tag{A-5}$$

First, we estimate the relationship between ΔP_i and Q_i. The pressure drop for a fracture is the summation of pressure drop in the wellbore, in perforations and in the fracture. The pressure drop in the horizontal section of the wellbore ($\Delta p_{w,i}$) is small compared to pressure drop in perforations and in the fracture (for a wellbore of 5.5" diameter, injecting slurry with $\rho = 1000\, kg/m^3$, $\mu = 1\, cP$ at rate $30\, bpm$, pressure drop is $\approx 0.085\, psi/ft$ according to Equation 20, while pressure drop in the perforations and in the fracture is in the order of hundreds of psi). Thus, pressure drop in the horizontal wellbore is ignored in the following analysis. According to Equation 16 and Equation 19, we can simplify the expression for pressure drop in the fracture and in perforation as Equation A-6 and Equation A-7 below.

$$\Delta P_{f,i} = A_i * Q_i^{\frac{1}{4}} \tag{A-6}$$

$$\Delta P_{pf,i} = B_i * Q_i^{\,2} \tag{A-7}$$

Where A_i and B_i are constants for fracture *i*.

Therefore, pressure drop corresponding to fracture *i* can be expressed as Equation A-8.

$$\Delta P_i = A_i * Q_i^{\frac{1}{4}} + B_i * Q_i^{\,2} \tag{A-8}$$

Now, Equations A-2, A-3, A-4, A-5 and A-8 consist of a complete system of non-linear equations. We re-organize the equation system to be Equation A-9, A-10, and A-8.

$$\begin{aligned} Q_1 &= \frac{BHP - S_{hmin,1}}{\Delta P_1} Q_1 = F_1 \\ Q_2 &= \frac{BHP - S_{hmin,2}}{\Delta P_2} Q_2 = F_2 \\ &\cdots \\ Q_n &= \frac{BHP - S_{hmin,n}}{\Delta P_n} Q_n = F_n \end{aligned} \tag{A-9}$$

$$BHP = \frac{1}{\frac{Q_1}{\Delta P_1} + \frac{Q_2}{\Delta P_2} + \cdots + \frac{Q_n}{\Delta P_n}} \tag{A-10}$$

$$* \left(Q_T + \frac{S_{hmin,1} * Q_1}{\Delta P_1} + \frac{S_{hmin,2} * Q_2}{\Delta P_2} + \cdots + \frac{S_{hmin,n} * Q_n}{\Delta P_n}\right)$$

Equation A-9 is a system of N non-linear equations with N unknowns in the form of fixed point iteration. And the Jacobian matrix of this equation system is shown in Equation A-11.

$$[\boldsymbol{Jac}] = \begin{bmatrix} \frac{\partial F_1}{\partial Q_1} & \frac{\partial F_1}{\partial Q_2} & \cdots & \frac{\partial F_1}{\partial Q_n} \\ \frac{\partial F_2}{\partial Q_1} & \frac{\partial F_2}{\partial Q_2} & \cdots & \frac{\partial F_2}{\partial Q_n} \\ \vdots & \vdots & \ddots & \vdots \\ \frac{\partial F_n}{\partial Q_1} & \frac{\partial F_n}{\partial Q_2} & \cdots & \frac{\partial F_n}{\partial Q_n} \end{bmatrix} \tag{A-11}$$

Next we evaluate each term in the Jacobian matrix in Equation A-11.

The evaluation of the first row of the Jacobian matrix is shown in Equation A-12.

$$\begin{aligned} \frac{\partial F_1}{\partial Q_1} &= \frac{BHP - S_{hmin,1}}{\Delta P_1} - \frac{Q_1}{\Delta P_1} * \frac{\partial \Delta P_1}{\partial Q_1} * \frac{BHP - S_{hmin,1}}{\Delta P_1} \\ &\quad - \frac{Q_1}{\Delta P_1} * R_{tot} * \left(1 - \frac{Q_1}{\Delta P_1} * \frac{\partial \Delta P_1}{\partial Q_1}\right) * \frac{BHP - S_{hmin,1}}{\Delta P_1} \\ \frac{\partial F_1}{\partial Q_2} &= -\frac{Q_1}{\Delta P_1} * R_{tot} * \left(1 - \frac{Q_2}{\Delta P_2} * \frac{\partial \Delta P_2}{\partial Q_2}\right) * \left(\frac{BHP - S_{hmin,2}}{\Delta P_2}\right) \\ \frac{\partial F_1}{\partial Q_3} &= -\frac{Q_1}{\Delta P_1} * R_{tot} * \left(1 - \frac{Q_3}{\Delta P_3} * \frac{\partial \Delta P_3}{\partial Q_3}\right) * \left(\frac{BHP - S_{hmin,3}}{\Delta P_3}\right) \\ &\cdots \\ \frac{\partial F_1}{\partial Q_n} &= -\frac{Q_1}{\Delta P_1} * R_{tot} * \left(1 - \frac{Q_n}{\Delta P_n} * \frac{\partial \Delta P_n}{\partial Q_n}\right) * \left(\frac{BHP - S_{hmin,n}}{\Delta P_n}\right) \end{aligned} \tag{A-12}$$

To simplify Equation A-12, we define two sets of parameters as Equation A-13 and A-14.

$$\alpha_i = \frac{\frac{1}{R_i}}{\sum_{j=1}^{n} \frac{1}{R_j}} = \frac{1}{R_i} * R_{tot} \tag{A-13}$$

$$X_i = \frac{Q_i}{\Delta P_i} * \frac{\partial \Delta P_i}{\partial Q_i} \tag{A-14}$$

It is obvious that $\alpha_i \in (0,1)$, $\sum_{i=1}^{n} \alpha_i = 1$ and $X_i \in \left(\frac{1}{4}, 2\right)$. Moreover, at the solution (the fixed point) of the system, $\Delta P_i = BHP - S_{hmin,i}$. As a result, we can simplify Equation A-12 as Equation A-15 below:

$$\begin{aligned} \frac{\partial F_1}{\partial Q_1} &= (1-\alpha_1) * (1-X_1) \\ \frac{\partial F_1}{\partial Q_2} &= -\alpha_1 * (1-X_2) \\ \frac{\partial F_1}{\partial Q_3} &= -\alpha_1 * (1-X_3) \\ &\cdots \\ \frac{\partial F_1}{\partial Q_n} &= -\alpha_1 * (1-X_n) \end{aligned} \tag{A-15}$$

The second row of the Jacobian matrix at the fixed point can be calculated similarly and is shown in equation A-16 below:

$$\begin{aligned} \frac{\partial F_2}{\partial Q_1} &= -\alpha_2 * (1-X_1) \\ \frac{\partial F_2}{\partial Q_2} &= (1-\alpha_2) * (1-X_2) \\ \frac{\partial F_2}{\partial Q_3} &= -\alpha_2 * (1-X_3) \\ &\cdots \\ \frac{\partial F_2}{\partial Q_n} &= -\alpha_2 * (1-X_n) \end{aligned} \tag{A-16}$$

And finally we get the Jacobian matrix expression at the fixed point as Equation A-17:

$$[\boldsymbol{Jac}] = \begin{bmatrix} (1-X_1)(1-\alpha_1) & -(1-X_2)\alpha_1 & \cdots & -(1-X_n)\alpha_1 \\ -(1-X_1)\alpha_2 & (1-X_2)(1-\alpha_2) & \cdots & -(1-X_n)\alpha_2 \\ \vdots & \vdots & \ddots & \vdots \\ -(1-X_1)\alpha_n & -(1-X_2)\alpha_n & \cdots & (1-X_n)(1-\alpha_n) \end{bmatrix} \tag{A-17}$$

Recall that $\alpha_i \in (0,1)$ and $X_i \in \left(\frac{1}{4}, 2\right)$. Thus, all elements of the Jacobian matrix satisfy $\left|Jac_{i,j}\right| < 1$.

It is very difficult to obtain the spectral radius of the Jacobian matrix analytically. Instead, numerical experiments are applied to estimate the bounds of the spectral radius. In the numerical experiments, random numbers of $\alpha_i\ (i = 1, 2, \dots, n)$ and $X_i\ (i = 1, 2, \dots, n)$ that satisfy $\alpha_i \in (0, 1)$, $\sum_{i=1}^{n} \alpha_i = 1$ and $X_i \in \left(\frac{1}{4}, 2\right)$ are generated to form the Jacobian matrix. And then the spectral radius of the Jacobian matrix is calculated.

More than 100 million numerical experiments have been carried out by generating random sets of α_i, X_i for fracture number n ranging from 2 to over 500. For all the Jacobian matrix tested, the spectral radius is smaller than 1. Results of 5000 numerical experiments for fracture systems consist of 2, 5, 10, 20, 100 and 500 fractures respectively are shown in Fig. A-1 below.

Fig. A-1 shows that the spectral radius of the Jacobian matrix distributes around an average value for a system of fixed fracture number. As fracture number increases, the average spectral radius increases. The upper bound of the spectral radius is 1. According to Ostrowski's Theorem introduced at the beginning of this section, this implies that the Resistance Method converges locally at least linearly in the tested range.

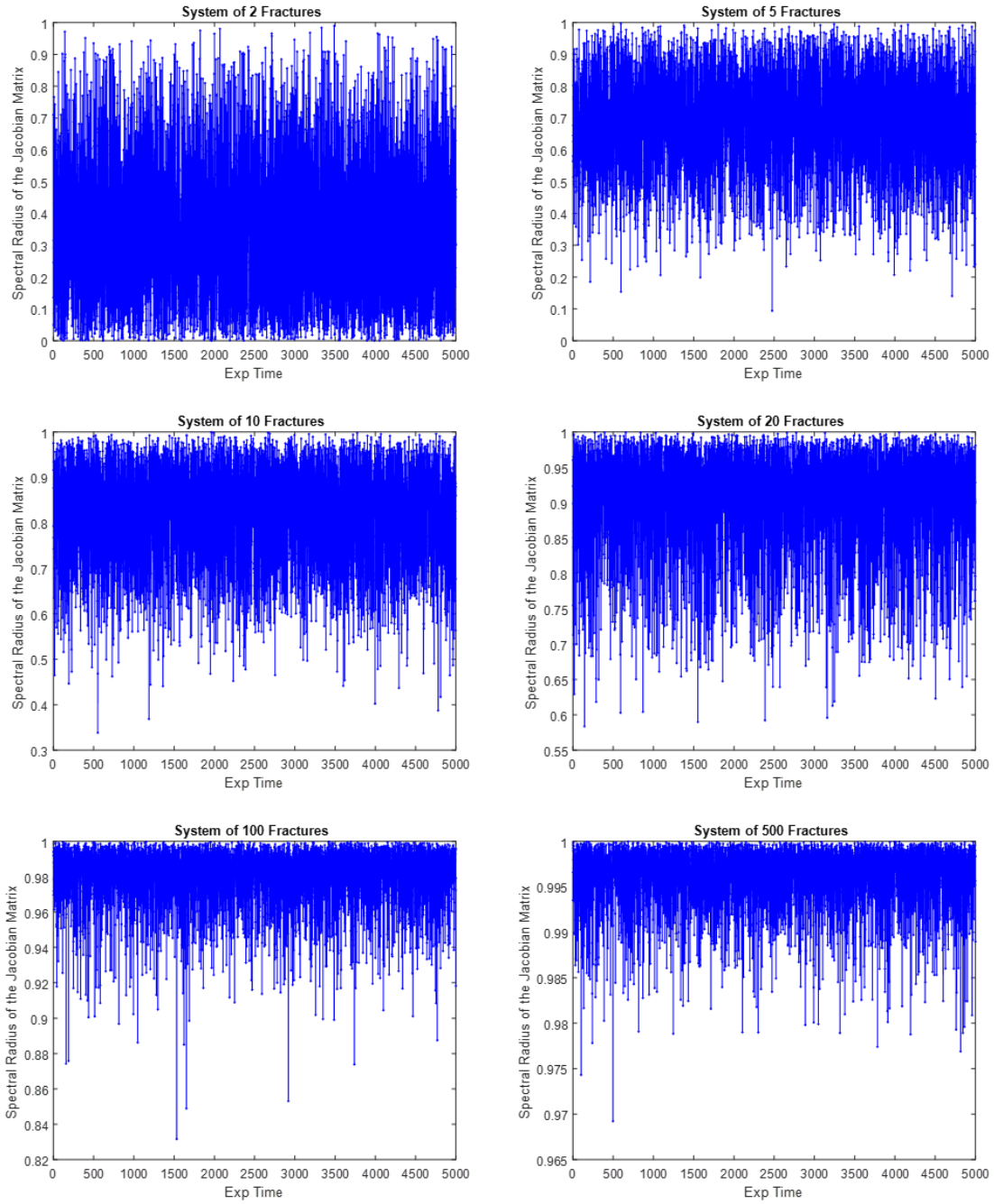

Figure A-1: Spectral radius of the Jacobian matrix generated in the numerical experiments for fracture systems with 2, 5, 10, 20, 100 and 500 fractures respectively. As the number of fracture increase, the average value of the spectral radius also increases and the max limit of the spectral radius is 1.

Appendix B: Fluid and Proppant Distribution Plots

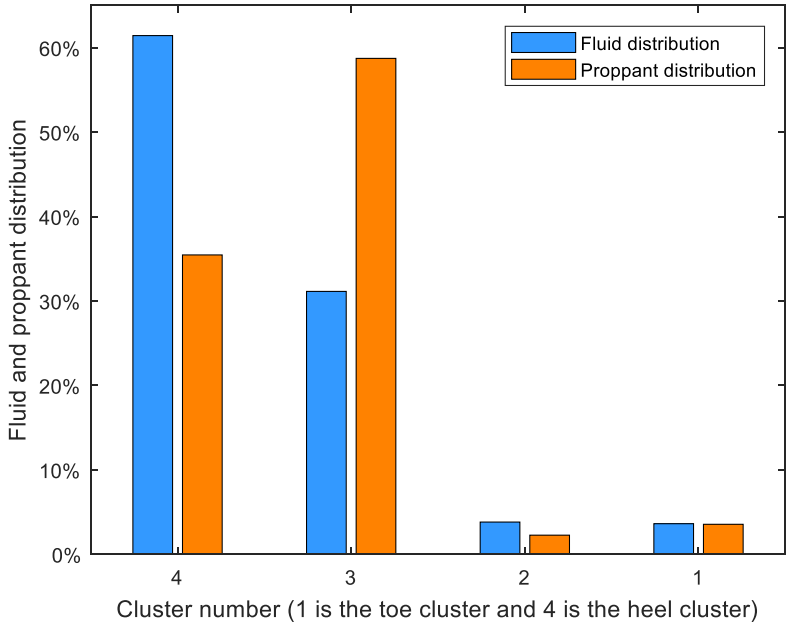

Figure B.1: Final fluid and proppant distribution among the 4 clusters with staggered perforation design of 5-5-3-3.

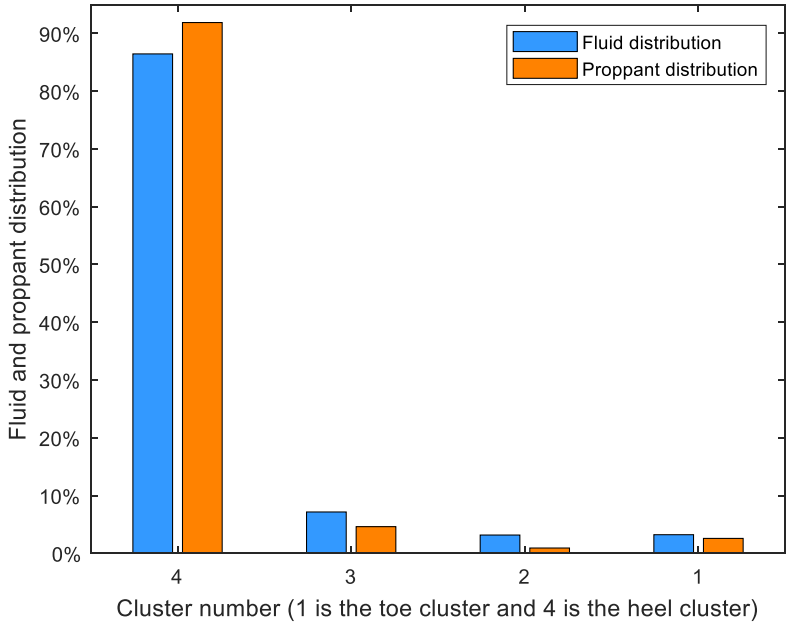

Figure B.2: Final fluid and proppant distribution among the 4 clusters with staggered perforation design of 8-8-5-5.

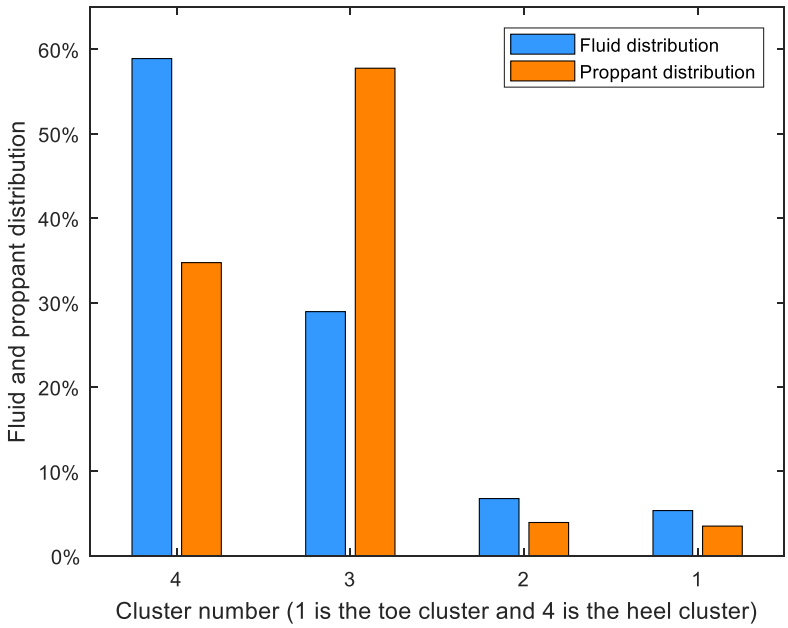

Figure B.3: Final fluid and proppant distribution among the 4 clusters with staggered perforation design of 5-5-8-8.

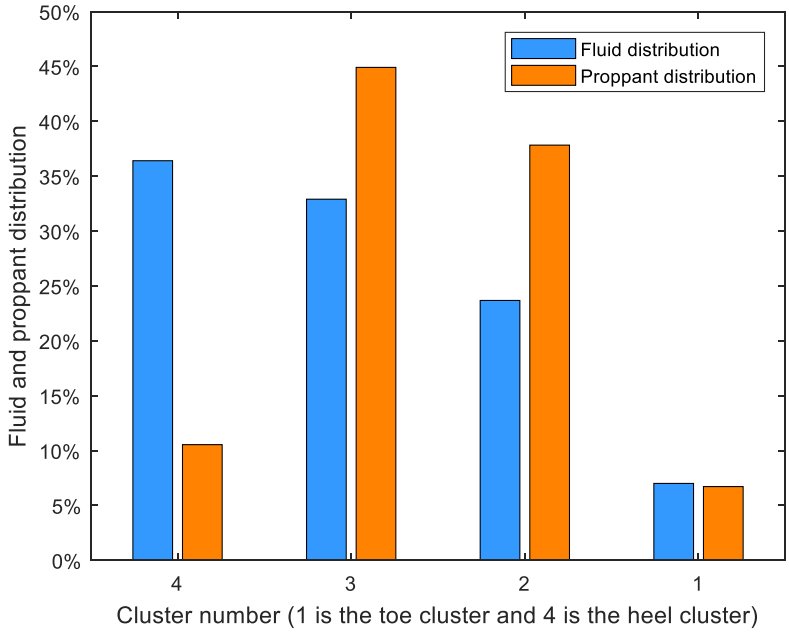

Figure B.4: Final fluid and proppant distribution among the 4 clusters with staggered perforation design of 3-3-5-5.

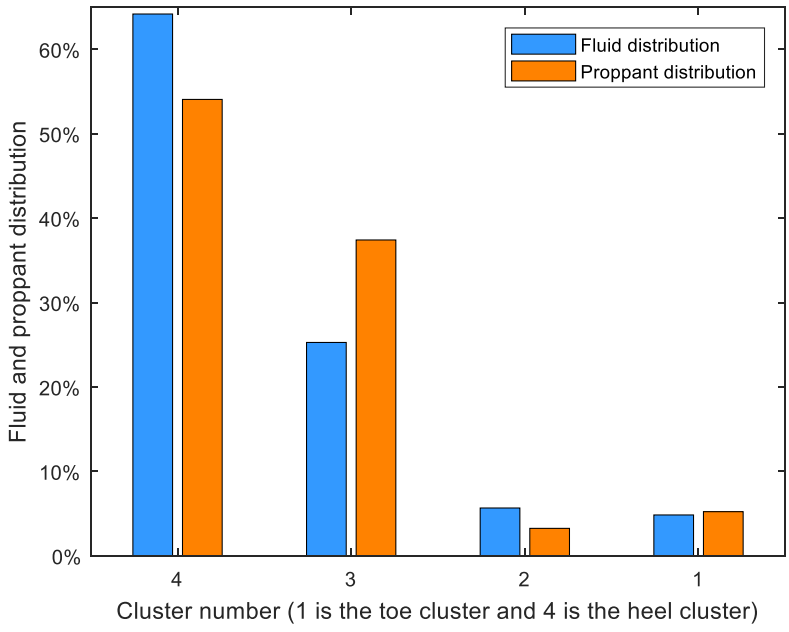

Figure B.5: Final fluid and proppant distribution among the 4 clusters with perforation diameter being 0.5 inch.

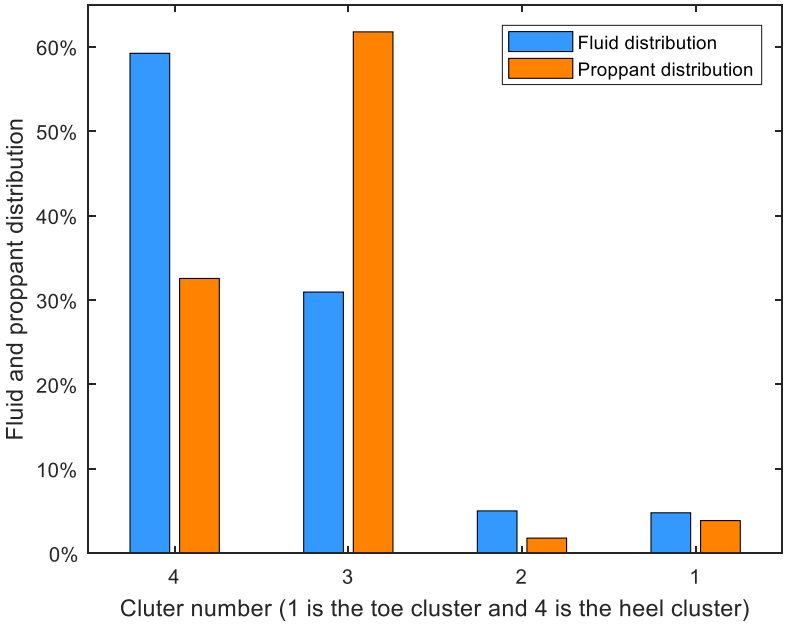

Figure B.6: Final fluid and proppant distribution among the 4 clusters with proppant size being 100 mesh (150 μm).

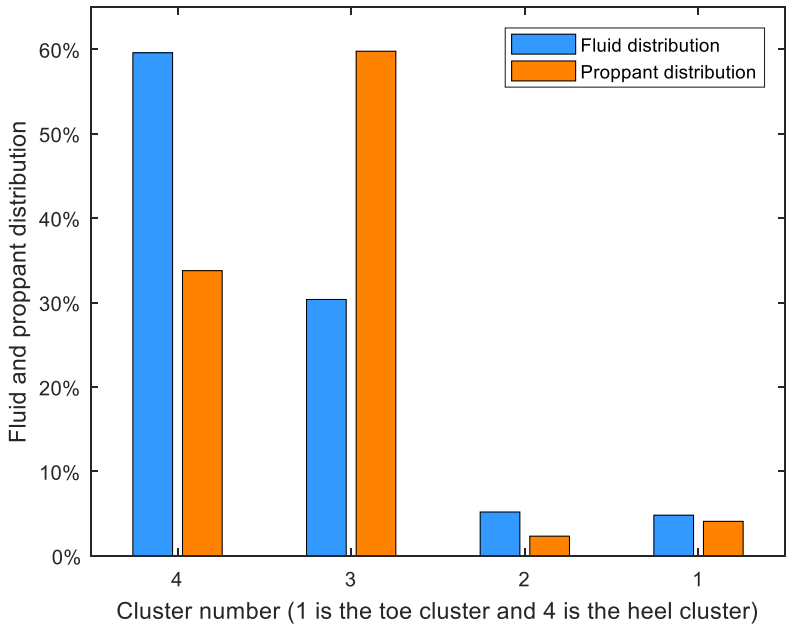

Figure B.7: Final fluid and proppant distribution among the 4 clusters with proppant size being 40-70 mesh (300 μm).

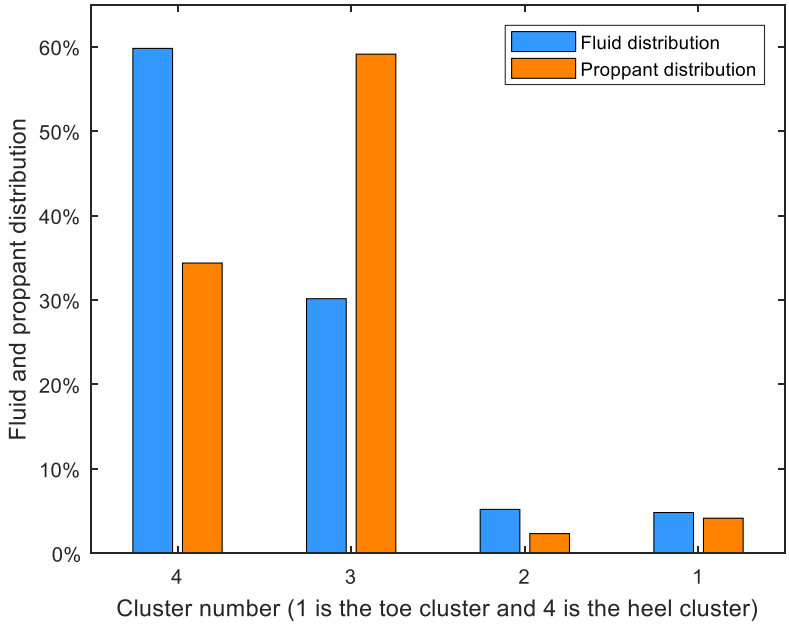

Figure B.8: Final fluid and proppant distribution among the 4 clusters with proppant size being 35-50 mesh (400 μm).

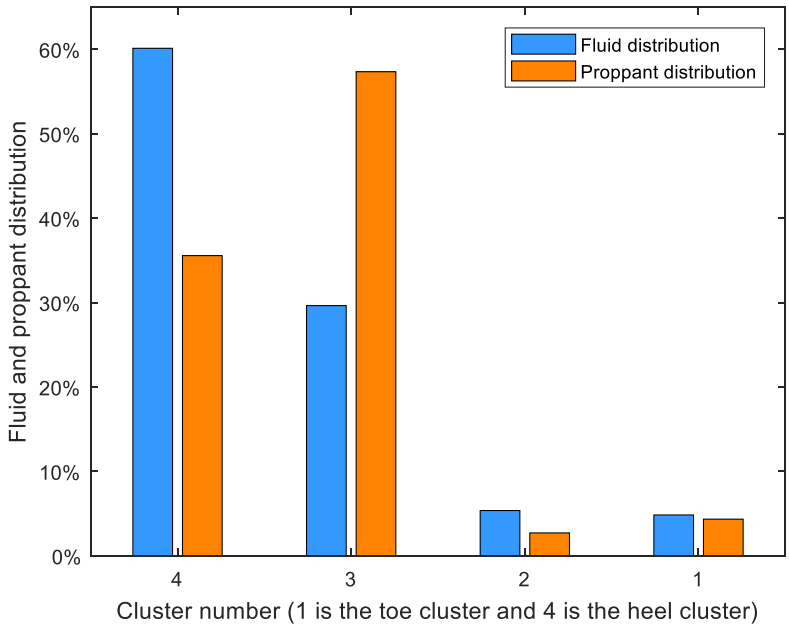

Figure B.9: Final fluid and proppant distribution among the 4 clusters with proppant size being 16-30 mesh (800 μm).

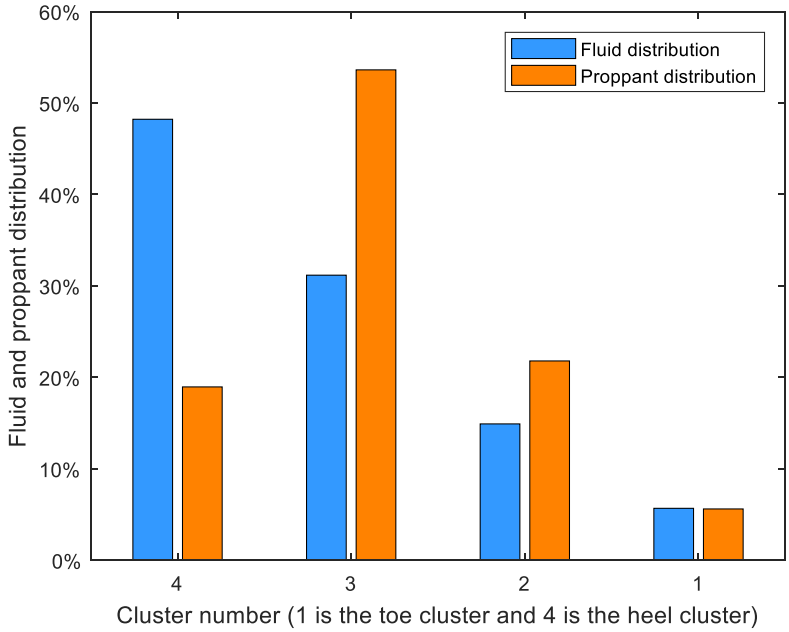

Figure B.10: Final fluid and proppant distribution among the 4 clusters with proppant density being 1.54 g/cm^3.

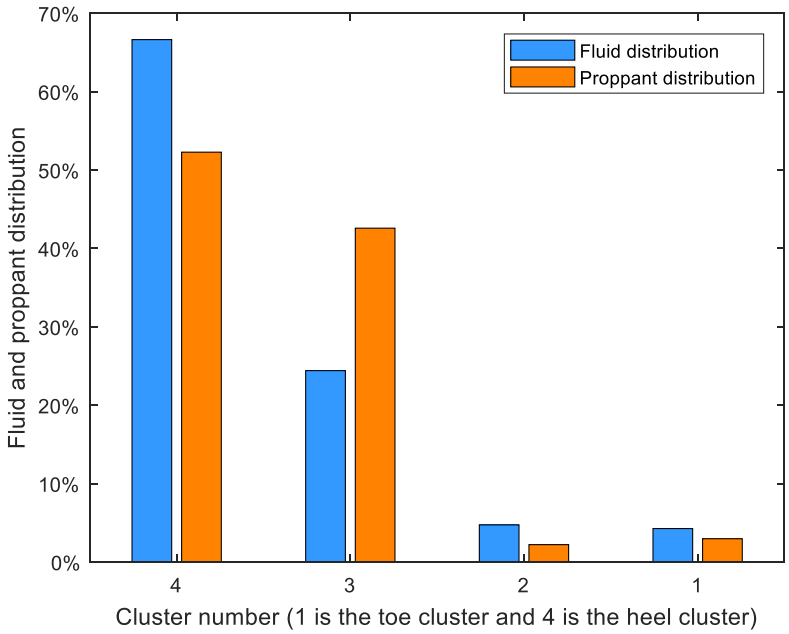

Figure B.11: Final fluid and proppant distribution among the 4 clusters with proppant density being 3.65 g/cm^3.

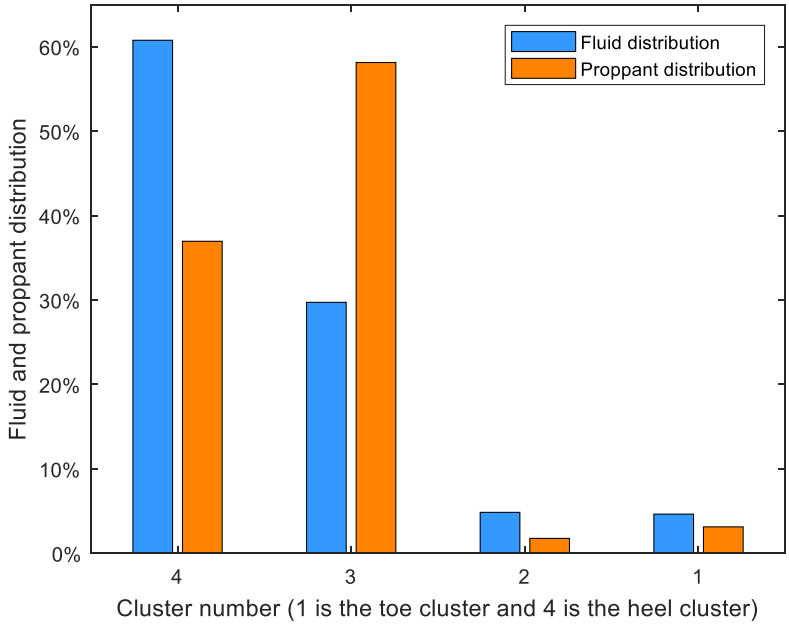

Figure B.12: Final fluid and proppant distribution among the 4 clusters with maximum slurry injection rate being 30 bpm.

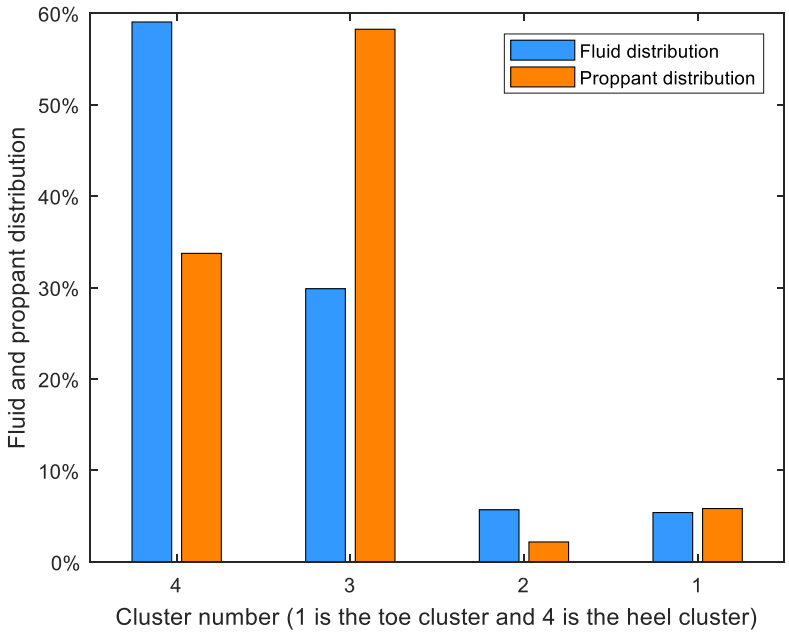

Figure B.13: Final fluid and proppant distribution among the 4 clusters with maximum slurry injection rate being 60 bpm.

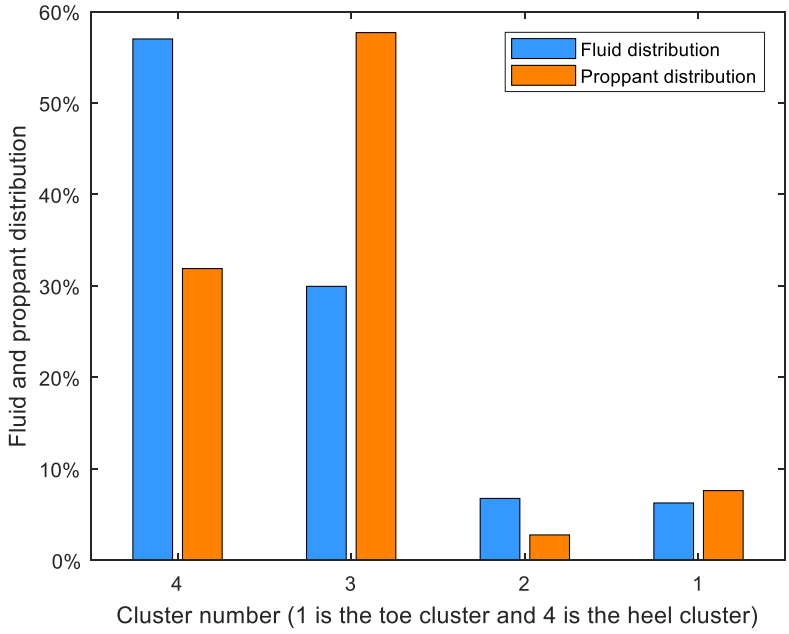

Figure B.14: Final fluid and proppant distribution among the 4 clusters with maximum slurry injection rate being 80 bpm.

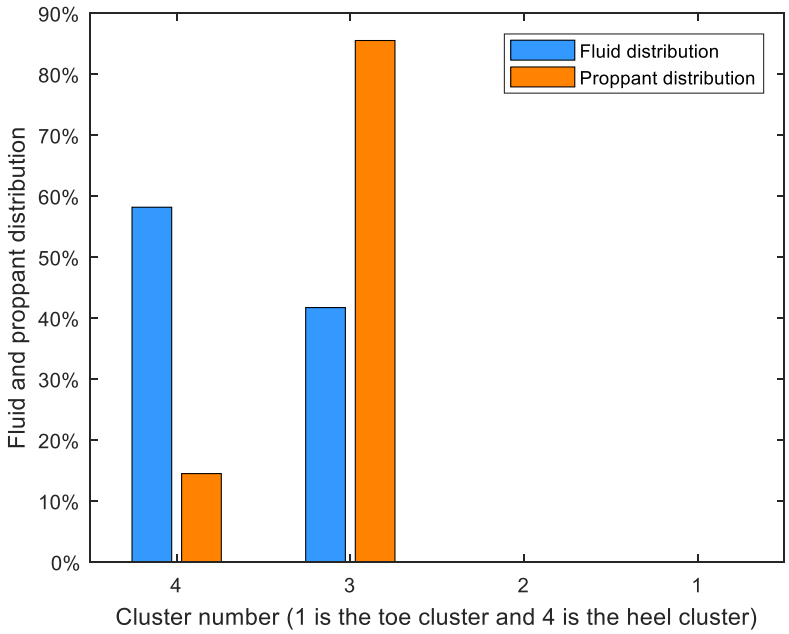

Figure B.15: Final fluid and proppant distribution among the 4 clusters with maximum proppant concentration being 2.5 ppa.

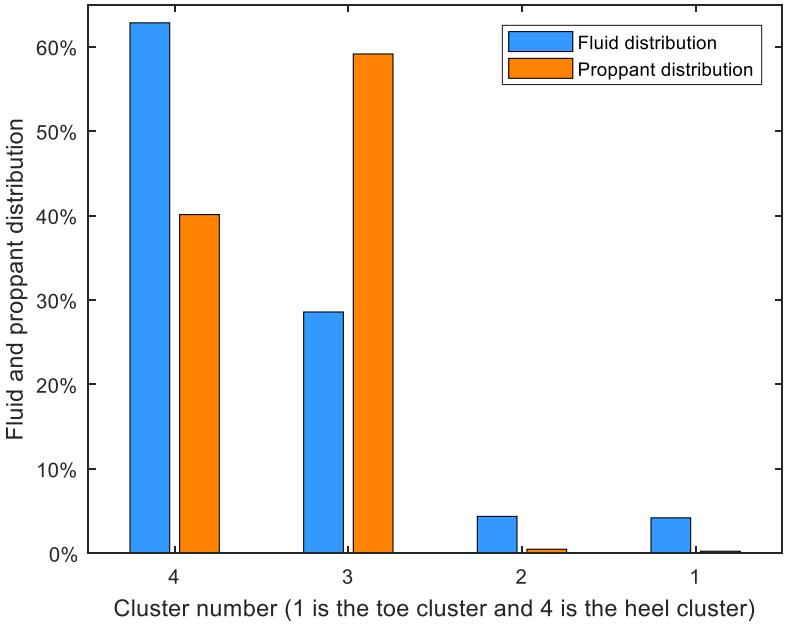

Figure B.16: Final fluid and proppant distribution among the 4 clusters with maximum proppant concentration being 3 ppa.

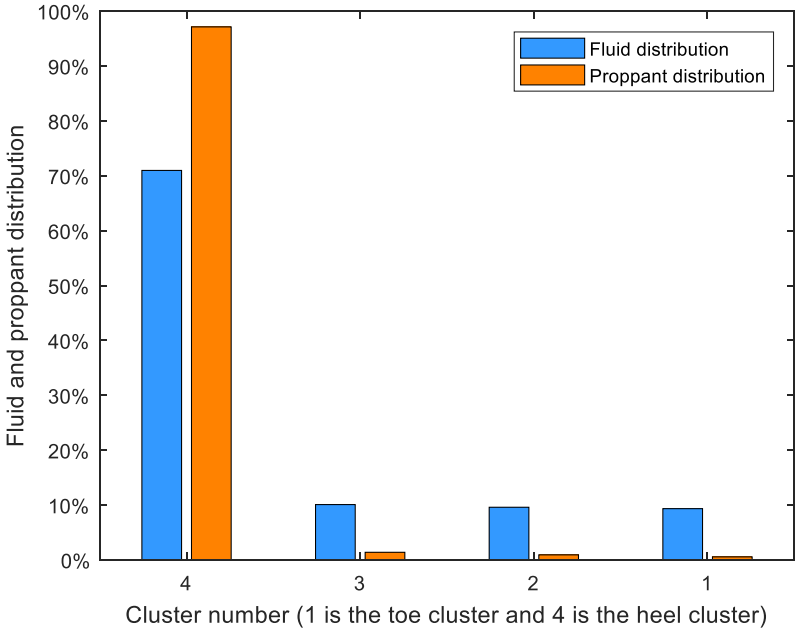

Figure B.17: Final fluid and proppant distribution among the 4 clusters with maximum proppant concentration being 4 ppa.

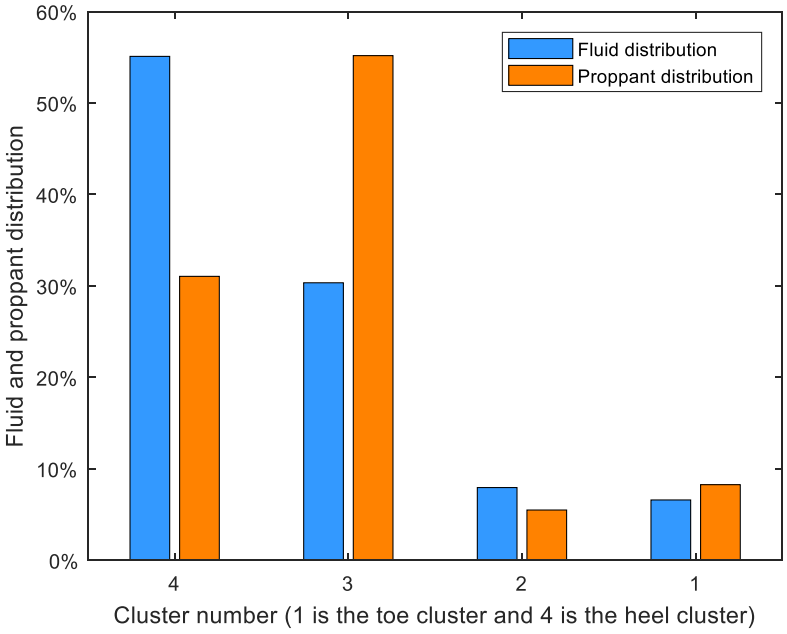

Figure B.18: Final fluid and proppant distribution among the 4 clusters with slow proppant concentration ramp up speed.

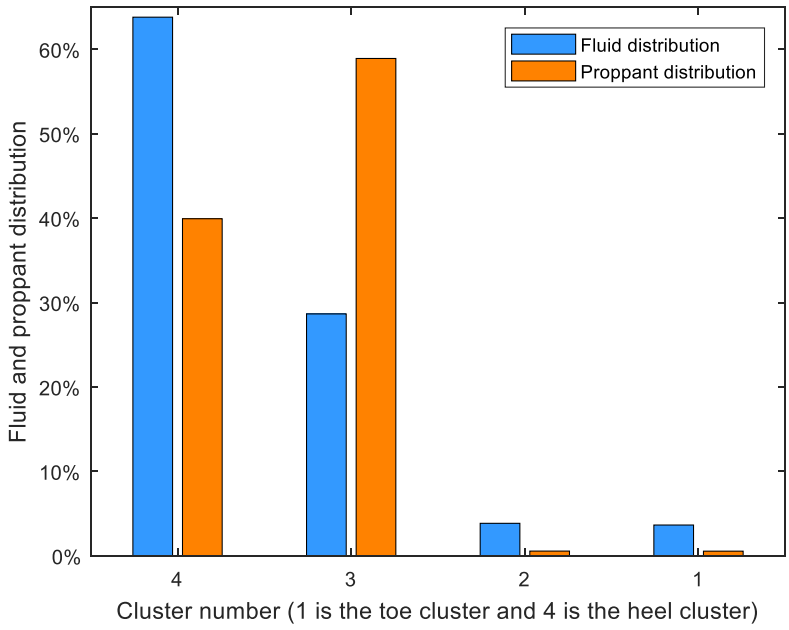

Figure B.19: Final fluid and proppant distribution among the 4 clusters with fast proppant concentration ramp up speed.

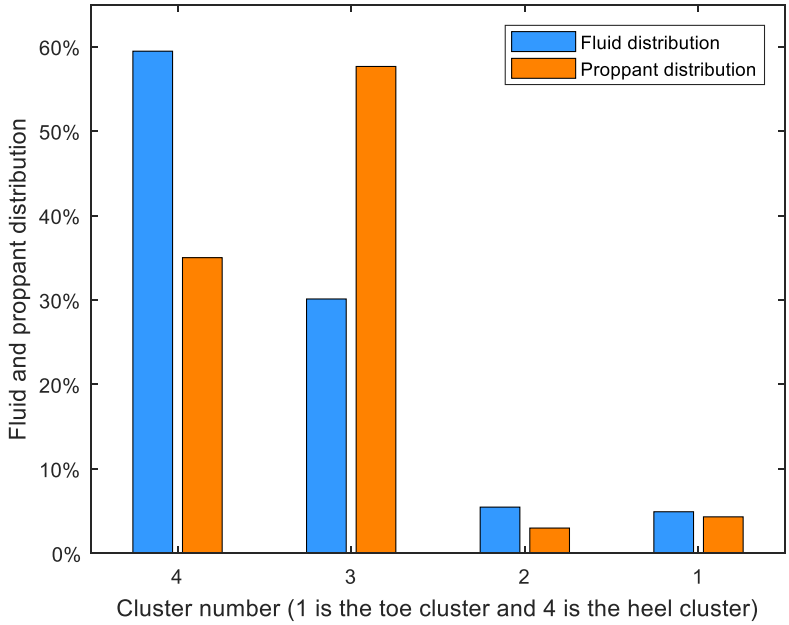

Figure B.20: Final fluid and proppant distribution among the 4 clusters with wellbore diameter being 4 1/2".

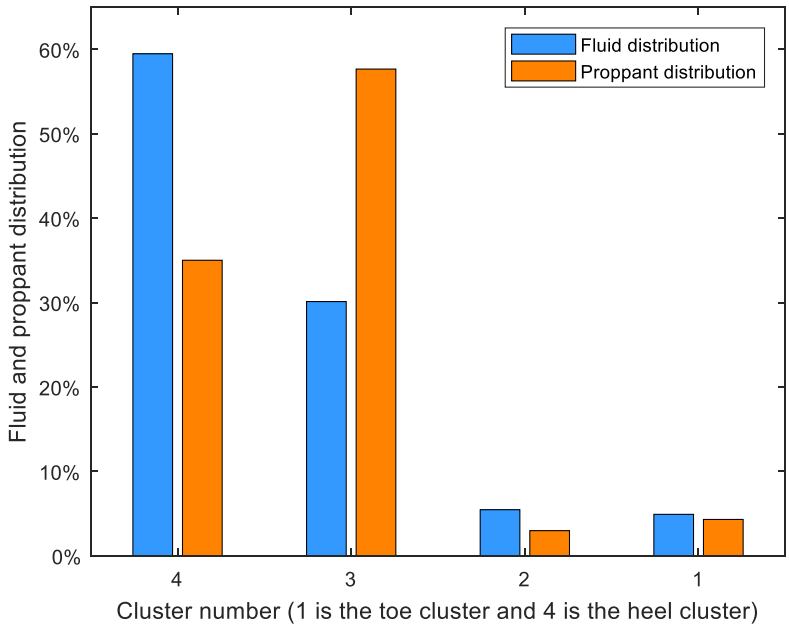

Figure B.21: Final fluid and proppant distribution among the 4 clusters with wellbore diameter being 6 5/8".

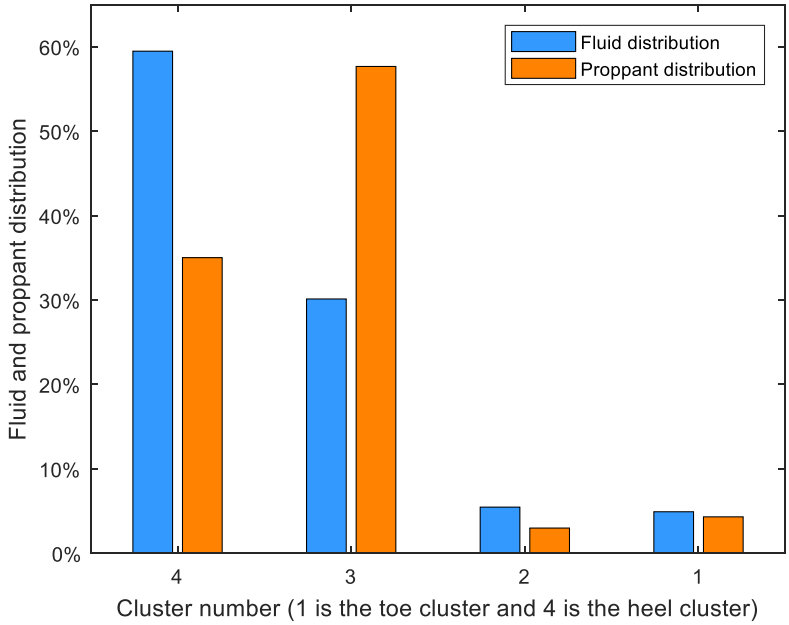

Figure B.22: Final fluid and proppant distribution among the 4 clusters with wellbore diameter being 7 5/8".

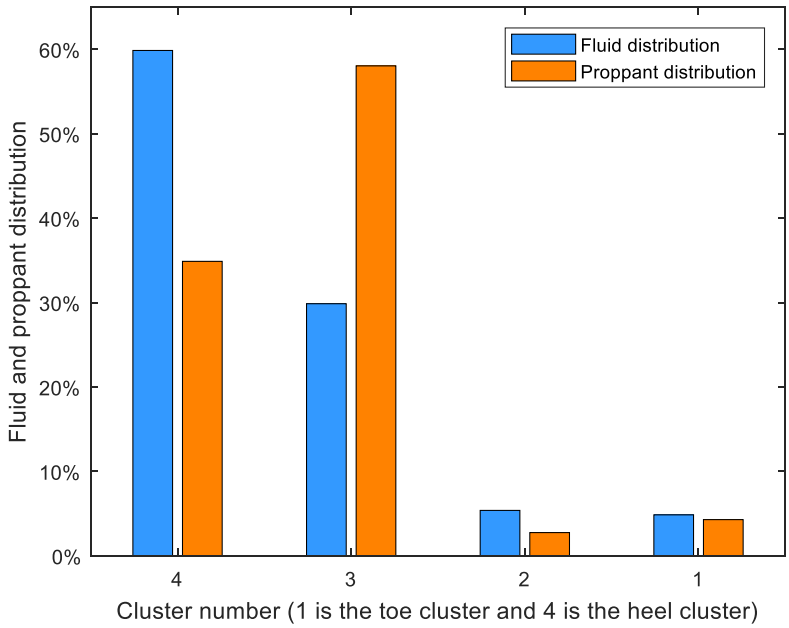

Figure B.23: Final fluid and proppant distribution among the 4 clusters with cluster spacing being 30 ft.

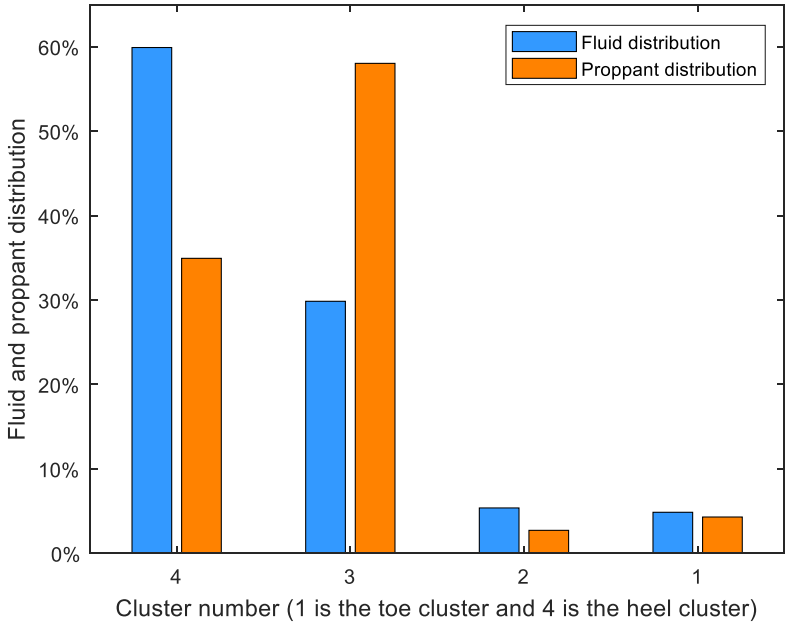

Figure B.24: Final fluid and proppant distribution among the 4 clusters with cluster spacing being 60 ft.

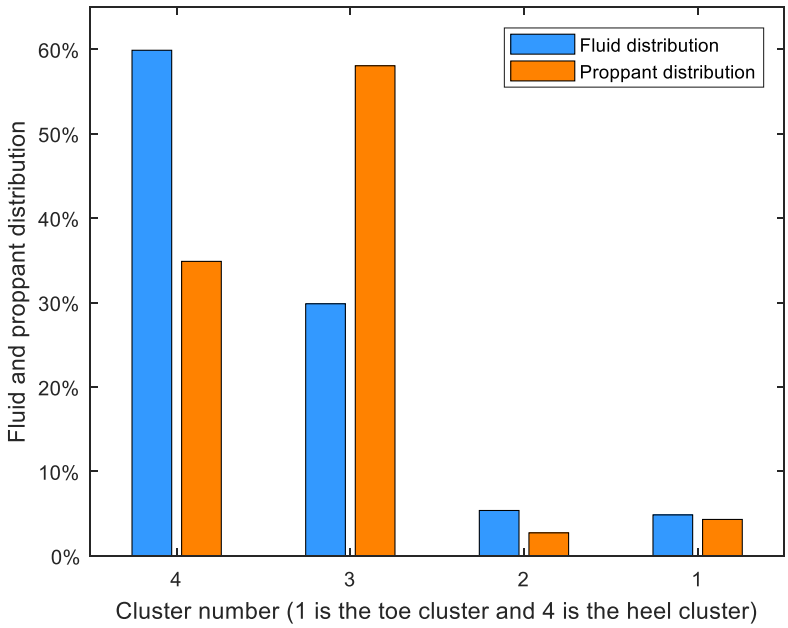

Figure B.25: Final fluid and proppant distribution among the 4 clusters with cluster spacing being 100 ft.

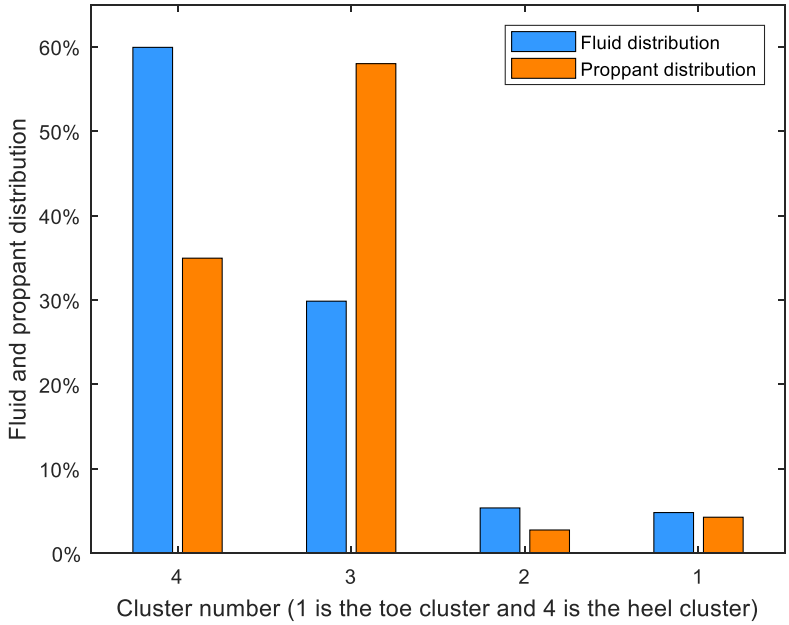

Figure B.26: Final fluid and proppant distribution among the 4 clusters with cluster spacing being 200 ft.

References

Adachi, J., Siebrits, E., Peirce, A. and Desroches, J., 2007. Computer simulation of hydraulic fractures. *International Journal of Rock Mechanics and Mining Sciences*, *44*(5), pp.739-757.

Avila, L.S., Barre, S., Blue, R., Geveci, B., Henderson, A., Hoffman, W.A., King, B., Law, C.C., Martin, K.M. and Schroeder, W.J., 2010. *The VTK User's Guide*. New York: Kitware.

Azar, J.J. and Samuel, G.R., 2007. *Drilling engineering*. PennWell Books.

Barree, R.D., 1983. A practical numerical simulator for three-dimensional fracture propagation in heterogeneous media. In *SPE Reservoir Simulation Symposium*. Society of Petroleum Engineers.

Bhardwaj, P., Hwang, J., Manchanda, R. and Sharma, M.M., 2016, September. Injection Induced Fracture Propagation and Stress Reorientation in Waterflooded Reservoirs. In *SPE Annual Technical Conference and Exhibition*. Society of Petroleum Engineers.

Bird, R.B., Stewart, W.E. and Lightfoot, E.N. 2007. Interphase Transport in Isothermal Systems. In Transport Phenomena, Revised 2nd ed, Chap 6, 177-196. New York: Wiley.

Britt, L.K., Smith, M.B., Haddad, Z.A., Lawrence, J.P., Chipperfield, S.T. and Hellman, T.J., 2006, January. Waterfracs: We do need proppant after all. In *SPE Annual Technical Conference and Exhibition*. Society of Petroleum Engineers.

Bryant, E.C., Hwang, J. and Sharma, M.M., 2015, February. Arbitrary fracture propagation in heterogeneous poroelastic formations using a finite volume-based cohesive zone model. In *SPE Hydraulic Fracturing Technology Conference*. Society of Petroleum Engineers.

Cardiff, P., Manchanda, R., Bryant, E.C., Lee, D., Ivankovic, A. and Sharma, M.M., 2015. Simulation of fractures in OpenFOAM: from adhesive joints to hydraulic fractures. In *10th OpenFOAM Workshop*.

Carter, R.D., 1957. Derivation of the general equation for estimating the extent of the fractured area. *Appendix I of "Optimum Fluid Characteristics for Fracture Extension," Drilling and Production Practice, GC Howard and CR Fast, New York, New York, USA, American Petroleum Institute*, pp.261-269.

Cipolla, C. L., Lolon, E., Mayerhofer, M. J., & Warpinski, N. R., 2009. The Effect of Proppant Distribution and Un-Propped Fracture Conductivity on Well Performance in Unconventional Gas Reservoirs. Society of Petroleum Engineers. doi:10.2118/119368-MS

Cipolla, C.L., 2009. Modeling production and evaluating fracture performance in unconventional gas reservoirs. *Journal of Petroleum Technology*, 61(09), pp.84-90.

Cohen, C.E., Kresse, O. and Weng, X., 2017, January. Stacked height model to improve fracture height growth prediction, and simulate interactions with multi-layer DFNs and ledges at weak zone interfaces. In *SPE Hydraulic Fracturing Technology Conference and Exhibition*. Society of Petroleum Engineers.

Crouch, S.L., Starfield, A.M. and Rizzo, F.J., 1983. Boundary element methods in solid mechanics. *Journal of Applied Mechanics*, *50*, p.704.

Daneshy, A.A., 2011. Hydraulic Fracturing of Horizontal Wells: Issues and Insights. Paper SPE 140134 presented at the *SPE Hydraulic Fracturing Technology Conference and Exhibition* held in The Woodlands, Texas, USA, 24-26 January 2011.

Denney, D., 2011. Screening Method To Select Horizontal-Well Refracturing Candidates in Shale-Gas Reservoirs. *Journal of Petroleum Technology*,63(11), pp.102-106.

Detournay, E., Cheng, A.D. and McLennan, J.D., 1990. A poroelastic PKN hydraulic fracture model based on an explicit moving mesh algorithm. *Journal of energy resources technology*, *112*(4), pp.224-230.

Dontsov, E.V. and Peirce, A.P., 2014. Slurry flow, gravitational settling and a proppant transport model for hydraulic fractures. *Journal of Fluid Mechanics*, *760*, pp.567-590.

Dontsov, E.V. and Peirce, A.P., 2015. Proppant transport in hydraulic fracturing: crack tip screen-out in KGD and P3D models. *International Journal of Solids and Structures*, *63*, pp.206-218.

Economides, M.J. and Nolte, K.G., 1989. *Reservoir stimulation* (Vol. 2). Englewood Cliffs, New Jersey: Prentice Hall.

Elbel, J.L. 1993. A method to estimate multizone injection profiles during hydraulic fracturing. SPE Prod & Fac 8 (02): 117-122. SPE-21869-PA. https://doi.org/10.2118/21869-PA

Elbel, J.L., Piggott, A.R. and Mack, M.G. 1992. Numerical modeling of multilayer fracture treatments. Presented at the Permian Basin Oil and Gas Recovery Conference, Midland, Texas, 18-20 March. SPE-23982-MS. https://doi.org/10.2118/23982-MS

England, A.H. and Green, A.E., 1963, April. Some two-dimensional punch and crack problems in classical elasticity. In *Mathematical Proceedings of the Cambridge Philosophical Society* (Vol. 59, No. 2, pp. 489-500). Cambridge University Press.

Evans, S., Holley, E., Dawson, K., Garrison, N., Montes, M., Preston, G. and Hudson, S., 2016. Eagle Ford Case History: Evaluation of Diversion Techniques to Increase Stimulation Effectiveness. *Unconventional Resources Technology Conference* (URTEC).

Ferziger, J.H. and Peric, M., 2012. *Computational methods for fluid dynamics*. Springer Science & Business Media.

Fisher, M.K. and Warpinski, N.R., 2012. Hydraulic-fracture-height growth: Real data. *SPE Production & Operations*, *27*(01), pp.8-19.

Fisher, M.K., Heinze, J.R., Harris, C.D., Davidson, B.M., Wright, C.A. and Dunn, K.P., 2004, January. Optimizing horizontal completion techniques in the Barnett shale using microseismic fracture mapping. In *SPE Annual Technical Conference and Exhibition*. Society of Petroleum Engineers.

Fragachan, F.E., Babey, A.G., Arnold, D.M., Heminway, E.M. and Yuan, F., 2015, September. Secret Weapon Against the Red Queen: Using Chemical Packers and Degradable Mechanical Diverters in Refracturing Operations. In *SPE Annual Technical Conference and Exhibition*. Society of Petroleum Engineers.

French, S., Rodgerson, J. and Feik, C., 2014, February. Re-fracturing horizontal shale wells: case history of a Woodford Shale pilot project. In *SPE Hydraulic Fracturing Technology Conference*. Society of Petroleum Engineers.

Fung, R.L., Vilayakumar, S. and Cormack, D.E., 1987. Calculation of vertical fracture containment in layered formations. *SPE formation evaluation*, *2*(04), pp.518-522.

Gadde, P.B., Liu, Y., Norman, J., Bonnecaze, R. and Sharma, M.M., 2004, January. Modeling proppant settling in water-fracs. In *SPE annual technical conference and exhibition*. Society of Petroleum Engineers.

Gala, D.P., Manchanda, R., Sharma, M.M., 2018. Modeling of Fluid Injection in Depleted Parent Wells to Minimize Damage due to Frac-Hits. In *Unconventional Resources Technology Conference*. URTeC: 2881265

Geertsma, J. and De Klerk, F., 1969. A rapid method of predicting width and extent of hydraulically induced fractures. *Journal of Petroleum Technology*, *21*(12), pp.1-571.

Gold, R., 2014. *The boom: How fracking ignited the American energy revolution and changed the world*. Simon and Schuster.

Goniva, C., Kloss, C., Deen, N.G., Kuipers, J.A.M., and Pirker, S. 2012. Influence of Rolling Friction on Single Spout Fluidized Bed Simulation. Particuology 10, no. 5, pp. 582–91. http://dx.doi.org/10.1016/j.partic.2012.05.002

Gruesbeck, C. and Collins, R.E. 1982. Particle Transport Through Perforations. Society of Petroleum Engineers Journal 22, no. 06, pp. 857-865. doi: 10.2118/7006-PA

Gu, H. and Siebrits, E., 2006, January. Effect of formation modulus contrast on hydraulic fracture height containment. In *International Oil & Gas Conference and Exhibition in China*. Society of Petroleum Engineers.

Gu, H., Desroches, J. and Elbel, J.L. 2000. Computer simulation of multilayer hydraulic fractures. Presented at the International Oil and Gas Conference and Exhibition in China, Beijing, 7-10 November. SPE-64789-MS. https://doi.org/10.2118/64789-MS

Indras, P. and Blankenship, C., 2015, September. A Commercial Evaluation of Refracturing Horizontal Shale Wells. In *SPE Annual Technical Conference and Exhibition*. Society of Petroleum Engineers.

Jacobs, T., 2014. Renewing Mature Shale Wells Through Refracturing. *Journal of Petroleum Technology*, 66(04), pp.52-60.

Khristianovic, S. and Zheltov, Y., 1955, June. Formation of vertical fractures by means of highly viscous fluids. In *Proc. 4th world petroleum congress, Rome* (Vol. 2, pp. 579-586).

Kresse, O., Weng, X., Gu, H. and Wu, R., 2013. Numerical modeling of hydraulic fractures interaction in complex naturally fractured formations. *Rock mechanics and rock engineering*, *46*(3), pp.555-568.

Lafond, P.G., Gilmer, M.W., Koh, C.A., Sloan, E.D., Wu, D.T. and Sum, A.K., 2013. Orifice jamming of fluid-driven granular flow. *Physical Review E*, *87*(4), p.042204.

Lagrone, K.W. and Rasmussen, J.W., 1963. A new development in completion methods-the limited entry technique. Journal of Petroleum Technology, 15(7), pp.695-702.

Lamb, H., 1932. *Hydrodynamics*. Cambridge university press.

Le Calvez, J.H., Craven, M.E., Klem, R.C., Baihly, J.D., Bennett, L.A. and Brook, K., 2007, January. Real-time microseismic monitoring of hydraulic fracture treatment: A tool to improve completion and reservoir management. In *SPE Hydraulic Fracturing Technology Conference*. Society of Petroleum Engineers.

Lecampion, B. and Desroches, J. 2015. Simultaneous initiation and growth of multiple radial hydraulic fractures from a horizontal wellbore. *Journal of the Mechanics and Physics of Solids*, 82: 235-258.

Leonard, R.S., Moore, C.P., Woodroof, R.A. and Senters, C.W., 2015, September. Refracs-Diagnostics provide a second chance to get it right. In *SPE Annual Technical Conference and Exhibition*. Society of Petroleum Engineers.

Leonard, R.S., Woodroof, R.A., Senters, C.W., Wood, T.M. and Drylie, S.W., 2016, September. Evaluating and optimizing refracs-what the diagnostics are telling us. In *SPE Annual Technical Conference and Exhibition*. Society of Petroleum Engineers.

Lindsay, G.J., White, D.J., Miller, G.A., Baihly, J.D. and Sinosic, B., 2016, February. Understanding the applicability and economic viability of refracturing horizontal

wells in unconventional plays. In *SPE Hydraulic Fracturing Technology Conference*. Society of Petroleum Engineers.

Liu, Y. and Sharma, M.M., 2005, January. Effect of fracture width and fluid rheology on proppant settling and retardation: an experimental study. In *SPE Annual Technical Conference and Exhibition*. Society of Petroleum Engineers.

Liu, Y., 2006. *Settling and hydrodynamic retardation of proppants in hydraulic fractures* (Doctoral dissertation).

Long, G. and Xu, G., 2017. The effects of perforation erosion on practical hydraulic-fracturing applications. *SPE Journal*, *22*(02), pp.645-659.

Mack, M.G., Elbel, J.L. and Piggott, A.R. 1992. Numerical representation of multilayer hydraulic fracturing. Presented at the 33rd US Symposium on Rock Mechanics (USRMS), Santa Fe, New Mexico, 3-5 June. ARMA-92-0355.

Manchanda, R., 2015, A general poro-elastic model for pad-scale fracturing of horizontal wells. (Doctoral dissertation).

Manchanda, R., Bhardwaj, P., Hwang, J. and Sharma, M.M., 2018, January. Parent-Child Fracture Interference: Explanation and Mitigation of Child Well Underperformance. In SPE Hydraulic Fracturing Technology Conference and Exhibition. Society of Petroleum Engineers.

Manchanda, R., Roussel, N.P. and Sharma, M.M., 2012, June. Factors influencing fracture trajectories and fracturing pressure data in a horizontal completion. In *Paper ARMA 12-633 presented at the 46th US Rock Mechanics/Geomechanics Symposium, Chicago, Illinois* (pp. 24-27).

Manchanda, R., Sharma, M., Rafiee, M. and Ribeiro, L., 2017. Overcoming the Impact of Reservoir Depletion to Achieve Effective Parent Well Refracturing. *Unconventional Resources Technology Conference* (URTEC).

McDaniel, B.W., 2010, January. Horizontal Wells with Multi-Stage Fracs Provide Better Economics for Many Lower Permeability Reservoirs. In *SPE Asia Pacific Oil and Gas Conference and Exhibition*. Society of Petroleum Engineers.

McDaniel, B.W., 2012, March. Can We Achieve Acceptable Fracture Conductivity Using WaterFracs?. In *SPE/EAGE European Unconventional Resources Conference & Exhibition-From Potential to Production*.

Miller, G., Lindsay, G., Baihly, J. and Xu, T., 2016, May. Parent Well Refracturing: Economic Safety Nets in an Uneconomic Market. In *SPE Low Perm Symposium*. Society of Petroleum Engineers.

Molenaar, M.M. and Cox, B.E., 2013, January. Field cases of hydraulic fracture stimulation diagnostics using fiber optic distributed acoustic sensing (DAS) measurements and Analyses. In *SPE Unconventional Gas Conference and Exhibition*. Society of Petroleum Engineers.

Mondal S., Wu C.-H., and Sharma M.M. 2016. Coupled CFD-DEM Simulation of Hydrodynamic Bridging at Constrictions. Int. J. Multiph. Flow, Volume 84, September 2016, pp. 245-263. http://dx.doi.org/10.1016/j.ijmultiphaseflow.2016.05.001.

Murtaugh, D., Cao, J. 2014. U.S. Shale Oil Output Seen Growing Even as Prices Drop. Retrieved from http://www.bloomberg.com/news/articles/2014-10-14/u-s-shale-oil-output-growing-even-as-prices-drop-eia

Nolte, K.G., 1979, January. Determination of fracture parameters from fracturing pressure decline. In *SPE Annual Technical Conference and Exhibition*. Society of Petroleum Engineers.

Nordgren, R.P., 1972. Propagation of a vertical hydraulic fracture. *Society of Petroleum Engineers Journal*, *12*(04), pp.306-314.

Olson, J.E., 2004. Predicting fracture swarms—The influence of subcritical crack growth and the crack-tip process zone on joint spacing in rock. Geological Society, London, Special Publications, 231(1), pp.73-88.

Ortega, J.M. 1990. Numerical analysis: a second course. Society for Industrial and Applied Mathematics.

Ouchi, H., Foster, J.T. and Sharma, M.M., 2017. Effect of reservoir heterogeneity on the vertical migration of hydraulic fractures. *Journal of Petroleum Science and Engineering*, *151*, pp.384-408.

Ouchi, H., Katiyar, A., Foster, J. and Sharma, M.M., 2015a, February. A peridynamics model for the propagation of hydraulic fractures in heterogeneous, naturally fractured reservoirs. In *SPE Hydraulic Fracturing Technology Conference*. Society of Petroleum Engineers.

Ouchi, H., Katiyar, A., York, J., Foster, J.T. and Sharma, M.M., 2015b. A fully coupled porous flow and geomechanics model for fluid driven cracks: a peridynamics approach. *Computational Mechanics*, *55*(3), pp.561-576.

Patankar, N.A., Joseph, D.D., Wang, J., Barree, R.D., Conway, M. and Asadi, M., 2002. Power law correlations for sediment transport in pressure driven channel flows. *International Journal of Multiphase Flow*, *28*(8), pp.1269-1292.

Perkins, T.K. and Kern, L.R., 1961. Widths of hydraulic fractures. *Journal of Petroleum Technology*, *13*(09), pp.937-949.

Peters, E.J., 2012. *Advanced Petrophysics: Volume 1: Geology, Porosity, Absolute Permeability, Heterogeneity and Geostatistics*. Live Oak Book Co, Austin, Texas.

Potapenko, D.I., Tinkham, S.K., Lecerf, B., Fredd, C.N., Samuelson, M.L., Gillard, M.R., Le Calvez, J.H. and Daniels, J.L., 2009, January. Barnett Shale refracture stimulations using a novel diversion technique. In *SPE Hydraulic Fracturing Technology Conference*. Society of Petroleum Engineers.

Romero, J., Mack, M.G. and Elbel, J.L., 1995. Theoretical model and numerical investigation of near-wellbore effects in hydraulic fracturing. Presented at the SPE Annual Technical Conference and Exhibition, Dallas, Texas, 22-25 October. SPE-30506-MS. http://dx.doi.org/10.2118/30506-MS

Roussel, N.P. and Sharma, M.M., 2010. Quantifying transient effects in altered-stress refracturing of vertical wells. SPE Journal, 15(03), pp.770-782.

Roussel, N.P. and Sharma, M.M., 2011. Optimizing fracture spacing and sequencing in horizontal-well fracturing. SPE Production & Operations, 26(02), pp.173-184.

Roussel, N.P. and Sharma, M.M., 2012. Role of stress reorientation in the success of refracture treatments in tight gas sands. SPE Production & Operations, 27(04), pp.346-355.

Roussel, N.P., 2011. Stress reorientation in low permeability reservoirs. (Doctoral dissertation).

Roussel, N.P., 2017, January. Analyzing ISIP Stage-by-Stage Escalation to Determine Fracture Height and Horizontal-Stress Anisotropy. In *SPE Hydraulic Fracturing Technology Conference and Exhibition*. Society of Petroleum Engineers.

Roussel, N.P., Manchanda, R. and Sharma, M.M., 2012, January. Implications of fracturing pressure data recorded during a horizontal completion on stage spacing design. In *SPE Hydraulic Fracturing Technology Conference*. Society of Petroleum Engineers.

Safari, R., Lewis, R., Ma, X., Mutlu, U. and Ghassemi, A., 2017. Infill-Well Fracturing Optimization in Tightly Spaced Horizontal Wells. *SPE Journal*, 22(02), pp.582-595.

Schechter, R.S., 1992. Oil well stimulation.

Shen, Y., Holley, E., and Jaaskelainen, M., 2017. Quantitative Real-Time DAS Analysis for Plug-and-Perf Completion Operation. Unconventional Resources Technology Conference. doi:10.15530/URTEC-2017-2668525

Shiozawa, S. and McClure, M., 2016, February. Comparison of pseudo-3D and fully-3D simulations of proppant transport in hydraulic fractures, including gravitational settling, formation of proppant banks, tip-screen out, and fracture closure. In *SPE hydraulic fracturing technology conference*. Society of Petroleum Engineers.

Shrivastava, K., Blyton, C.A. and Sharma, M.M., 2017. Local Linearization Method for Efficient Solution of Coupled Fluid Flow and Geomechanics Problem. In *51st US Rock Mechanics/Geomechanics Symposium*. American Rock Mechanics Association.

Simonson, E.R., Abou-Sayed, A.S. and Clifton, R.J., 1978. Containment of massive hydraulic fractures. *Society of Petroleum Engineers Journal*, *18*(01), pp.27-32.

Sinha, S. and Ramakrishnan, H., 2011, January. A novel screening method for selection of horizontal refracturing candidates in shale gas reservoirs. In *North American Unconventional Gas Conference and Exhibition*. Society of Petroleum Engineers.

Siriwardane, H.J. and Layne, A.W. 1991. Improved model for predicting multiple hydraulic fracture propagation from a horizontal well. Presented *at the SPE Eastern Regional Meeting, Lexington, Kentucky*, 22-25 October. SPE-23448-MS. https://doi.org/10.2118/23448-MS

Sneddon, I., 1946. The distribution of stress in the neighbourhood of a crack in an elastic solid. *Proc. R. Soc. Lond. A*, *187*(1009), pp.229-260.

Sneddon, I.N. and Elliot, H.A., 1946. The opening of a Griffith crack under internal pressure. *Quarterly of Applied Mathematics*, *4*(3), pp.262-267.

Somanchi, K., O'Brien, C., Huckabee, P. and Ugueto, G., 2016. Insights and observations into limited entry perforation dynamics from fiber-optic diagnostics. *Unconventional Resources Technology Conference* (URTEC).

Strother, D., Valadares, R., Nakhwa, A.D. and Pitcher, J.L., 2013, November. Challenges of refracturing horizontal wells in unconventional and tight reservoirs. In *SPE Unconventional Resources Conference and Exhibition-Asia Pacific*. Society of Petroleum Engineers.

Tada, H., Paris, P.C. and Irwin, G.R., 1973. The stress analysis of cracks. *Handbook, Del Research Corporation*.

Thiercelin, M., Jeffrey, R.G. and Naceur, K.B., 1987, January. The Influence of Fracture Toughness on the Geometry of Hydraulic Fractures. In *Low Permeability Reservoirs Symposium*. Society of Petroleum Engineers.

Toolbox, G.O., 2011. *User's Guide (r2011b)*. The MathWorks Inc.

Tran, T.V., Civan, F. and Robb, I.D., 2009. Correlating flowing time and condition for perforation plugging by suspended particles. *SPE Drilling & Completion*, 24(03), pp.398-403. SPE-120847-PA.

U.S. Energy Information Administration. 2016. from, https://www.eia.gov/maps/maps.htm

U.S. Energy Information Administration. 2018. *Annual Energy Outlook 2018 with projections to 2050*.

Ugueto, C., Gustavo, A., Huckabee, P.T., Molenaar, M.M., Wyker, B. and Somanchi, K., 2016, February. Perforation cluster efficiency of cemented plug and perf limited entry completions; Insights from fiber optics diagnostics. In *SPE Hydraulic Fracturing Technology Conference*. Society of Petroleum Engineers.

Valko, P. and Economides, M.J., 1995. *Hydraulic fracture mechanics* (Vol. 28). Chichester: Wiley.

Van Eekelen, H.A.M., 1982. Hydraulic fracture geometry: fracture containment in layered formations. *Society of Petroleum Engineers Journal*, *22*(03), pp.341-349.

Wang, H., Yi, S. and Sharma, M.M., 2018. A computationally efficient approach to modeling contact problems and fracture closure using superposition method. *Theoretical and Applied Fracture Mechanics*, *93*, pp.276-287.

Wang, J., Joseph, D.D., Patankar, N.A., Conway, M. and Barree, R.D., 2003. Bi-power law correlations for sediment transport in pressure driven channel flows. *International journal of multiphase flow*, *29*(3), pp.475-494.

Warpinski, N.R., 2009, January. Stress amplification and arch dimensions in proppant beds deposited by waterfracs. In *SPE Hydraulic Fracturing Technology Conference*. Society of Petroleum Engineers.

Westergaard, H.M., 1939. Bearing pressures and cracks. *Journal of applied mechanics*, *6*(2), pp.A49-A53.

Wheaton, B., Haustveit, K., Deeg, W., Miskimins, J. and Barree, R., 2016, February. A case study of completion effectiveness in the eagle ford shale using DAS/DTS observations and hydraulic fracture modeling. In *SPE Hydraulic Fracturing Technology Conference*. Society of Petroleum Engineers.

Wright, C.A., Conant, R.A., Stewart, D.W. and Byerly, P.M., 1994, January. Reorientation of propped refracture treatments. In *Rock Mechanics in Petroleum Engineering*. Society of Petroleum Engineers.

Wu, C.H., Yi, S. and Sharma, M.M., 2017, January. Proppant distribution among multiple perforation clusters in a horizontal wellbore. In *SPE Hydraulic Fracturing Technology Conference and Exhibition*. Society of Petroleum Engineers.

Wu, C.H., Yi, S. and Sharma, M.M., 2017, January. Proppant distribution among multiple perforation clusters in a horizontal wellbore. In *SPE Hydraulic Fracturing Technology Conference and Exhibition*. Society of Petroleum Engineers.

Wu, K. and Olson, J.E., 2015a. A simplified three-dimensional displacement discontinuity method for multiple fracture simulations. *International Journal of Fracture*, *193*(2), pp.191-204.

Wu, K. and Olson, J.E., 2015b. Simultaneous multifracture treatments: fully coupled fluid flow and fracture mechanics for horizontal wells. *SPE journal*, *20*(02), pp.337-346.

Wu, K., 2014. *Numerical modeling of complex hydraulic fracture development in unconventional reservoirs* (Doctoral dissertation).

Xiang, J., 2012. *A PKN hydraulic fracture model study and formation permeability determination* (Master Thesis, Texas A & M University).

Yi, S. and Sharma, M., 2016, August. A model for refracturing operations in horizontal wells employing diverting agents. In *SPE Asia Pacific Hydraulic Fracturing Conference*. Society of Petroleum Engineers.

Yi, S.S., and Sharma, M.M., 2018. A New Method to Calculate Slurry Distribution Among Multiple Fractures During Fracturing and Refracturing. *Journal of Petroleum Science and Engineering*.

Yi, S.S., Wu, C.H. and Sharma, M.M., 2018. Proppant Distribution Among Multiple Perforation Clusters in Plug-and-Perforate Stages. *SPE Production & Operations*.

Yue, K., Olson, J. and Schultz, R., 2018, July. Layered Modulus Effect on Fracture Modeling and Height Containment. In *SPE/AAPG/SEG Unconventional Resources Technology Conference*. Unconventional Resources Technology Conference.